Advanced Oxy-fuel Combustion for Carbon Capture and Sequestration

János Szuhánszki

BEng (Hon) Energy and Environmental Engineering

Submitted in accordance with the requirements for the degree of
Doctor of Philosophy

The University of Leeds

Energy Technology and Innovation Initiative (ETII)

School of Chemical and Process Engineering

Faculty of Engineering

May 2014

The candidate confirms that the work submitted is his own, except where work which has formed part of jointly-authored publications has been included. The contribution of the candidate and the other authors to this work has been explicitly indicated below. The candidate confirms that appropriate credit has been given within the thesis where reference has been made to the work of others.

J Szuhánszki, S Black, A Pranzitelli, L Ma, PJ Stanger, DB Ingham, M Pourkashanian. 2013. Evaluation of the Performance of a Power Plant Boiler Firing Coal, Biomass and a Blend Under Oxy-fuel Conditions as a CO_2 Capture Technique. Energy Procedia, **37**, 1413-1422.

S Black, J Szuhánszki, A Pranzitelli, L Ma, PJ Stanger, DB Ingham, M Pourkashanian. 2013. Effects of firing coal and biomass under oxy-fuel conditions in a power plant boiler using CFD modelling. Fuel, **113**, 780-786.

Acknowledgements

I would like to express my gratitude to my supervisors Dr Bill Nimmo and Prof Mohamed Pourkashanian for the opportunity to research this exciting subject and their support and guidance throughout the PhD. I am also grateful for the help of the research technicians, Bob Harries, Gus Morrison and Martin Murphy, building and maintaining the rig as well as providing technical support during the experimental trials. I also owe my thanks to my colleagues, Sandy Black, Sam Pickard and Ray Edmunds, with whom I shared many discussion about each other's experiences in our respective fields of experimental research and CFD modelling as well as completing a 100 km trail walking challenge raising a substantial sum for charity.

I wish to thank my parents and my godmother for their constant and never tiring support and encouragement throughout my journey in life.

Lastly, but not the least, I would like to thank Simon who has stayed by my side through the good and joyful times of the PhD as well as through the harder moments.

Abstract

This dissertation assesses the contribution of CCS in mitigating climate change, investigates Computational Fluid Dynamics (CFD) in aiding the development of CCS technology, and presents the results of air and oxy-fuel combustion experiments conducted in a 250 kW furnace.

Coal combustion was investigated using non-preheated and preheated air. Preheating increased the heat input to the flame and the radiative heat transfer near the flame region, enhancing flame stability and burnout. Radiative and convective heat transfer measurements showed that the total heat transfer is mainly influenced by thermal radiation, data on which is essential in validating newly developed radiation models.

Oxy-fuel experiments produced flue gas with over 90% CO_2 concentration (allowing CCS without chemical scrubbing). Exit concentrations of NO and SO_2 increased with reduced recycle ratio, largely due to the reduction in dilution. However, total NO emissions reduced by ~50% compared to air-firing, which was attributed to low levels of atmospheric N_2 in the oxidiser and significant reductions in fuel NO formation.

Air and oxy-fired peak radiative heat transfer corresponded to a range typical of coal-fired boilers. For the oxy-cases, in-furnace temperatures and heat flux increased with total O_2 concentration. Radiative heat transfer increased with higher gas emissivity. The results indicated that the air-fired temperature profiles can be matched when retrofitting to oxy-firing by modifying the recycle ratio, and the optimum ratio lies between the investigated cases of 27% and 30% O_2 concentrations (using a dry recycle). The radiative heat flux profiles can also be adjusted. Temperature and heat flux measurements indicated delayed combustion due to the higher heat capacity of CO_2 and delayed mixing between the Primary and Secondary/Tertiary streams.

CFD modelling was undertaken on 250 kW and 2.4 MW coal-fired furnaces under air-firing conditions, and a $500MW_e$ utility boiler firing coal, a biomass blend, and 100% biomass under air and oxy-fuel conditions. Using wet recycle, the optimum total O_2 concentration lies between 25 and 30%, where air-fired heat transfer characteristics can be matched without significant modifications when firing coal or the biomass blend, but not 100% biomass.

Table of Contents

List of Figures

List of Tables

Nomenclature

Roman letters

a (m)	coal injector diameter (inner diameter of the secondary)
A (m)	burner throat diameter (outer diameter of the secondary)
A (m^2)	area
A (kg m^{-2} s^{-1})	Arrhenius pre-exponential factor
A_g (m^2)	specific internal surface area
A_i (g)	dry ash content of the ash
A/F (dimensionless)	air to fuel ratio
B (%)	burnout
B (m)	quarl throat diameter
c (m)	core air tube diameter (inner diameter of the primary)
C (mol m^{-3})	molar concentration of the gas
C_1 (kg m^{-2} s^{-1} Pa^{-1})	binary diffusion coefficient of O_2 in the air
C_2 (kg m^{-2} s^{-1} Pa^{-1})	Arrhenius pre-exponential factor
C_D (dimensionless)	drag coefficient
c_p (J kg^{-1} K^{-1})	specific heat
C_{SW} (dimensionless)	swelling coefficient
CV (MJ kg^{-1})	calorific value
d (m)	diameter
D_0 (kg m^{-2} s^{-1})	diffusion limited reaction rate
D_{im} (m^2 s^{-1})	diffusion coefficient of oxidant in the bulk
E (J mol^{-1})	activation energy
f_{ann} (dimensionless)	factor considering the effect of char annealing
f_{mac} (dimensionless)	factor considering the effect of coal maceral content

h (W m^{-2} K^{-1})	film heat transfer coefficient
h_{fg} (J kg^{-1})	latent heat of vaporisation
I (W sr^{-1})	radiation intensity
k (m^2 s^{-2})	turbulent kinetic energy/ rate constant
k (kg m^{-2} s^{-1})	rate constant
k_c (m s^{-1})	film mass transfer coefficient
k_i	intrinsic reactivity
L (m)	length
m (kg)	mass
$\dot{M}_O$ (kg s^{-1})	original mass flow
$\dot{M}_R$ (kg s^{-1})	recalculating mass flow
M_W (g mol^{-1})	molecular weight
N_i (kmol m^{-2} s^{-1})	molar flux of vapour i
p_{ox} (Pa)	partial pressure of the oxidiser
r (m)	radius
$\mathscr{R}$ (kg m^{-2} s^{-1})	chemical kinetics reaction rate
R (J mol^{-1} K^{-1})	universal gas constant
$R_{i,r}$	net rate of production of species i
Re (dimensionless)	Reynolds number
S_b (dimensionless)	stoichiometry (mass of oxidant per mass of char)
SF (dimensionless)	shape factor
t (s)	time
T (K)	temperature
v (m s^{-1})	velocity
ν (dimensionless)	fraction of volatiles evolved

v^* (dimensionless)	initial volatile fraction
V (kg s^{-1})	volatile yield
W (g)	dry weight of the ash
X_P (dimensionless)	Impingement point
Y_{ox} (dimensionless)	local mass fraction of oxidant in the bulk
Y_P (dimensionless)	mass fraction of any product species P
$Y_{\mathcal{R}}$ (dimensionless)	mass fraction of reactant species $\mathcal{R}$

Greek letters

α (dimensionless)	constant
ε (m^2 s^{-3})	dissipation of turbulent kinetic energy
η (dimensionless)	effectiveness factor
ϵ (dimensionless)	emissivity
Θ_R (K)	radiation temperature
ν' (dimensionless)	stoichiometric coefficients of reactants
ν'' (dimensionless)	stoichiometric coefficients of products
ρ (kg m^{-3})	density
σ (W m^{-2} K^{-4})	Stefan-Boltzmann constant
ω (1 s^{-1})	specific dissipation rate

Common Subscripts

0	initial
p	Particle
∞	bulk

Abbreviations

AASB	Aerodynamically Air Staged Burner
AD	Axial Distance
AFT	Adiabatic Flame Temperature
APGTF	Advanced Power Generation Technology Forum
ASU	Air Separation Unit
BS	British Standard
CAC	CO_2 Avoidance Cost
CAD	Computer Aided Design
CBK	Carbon Burnout Kinetics
CCS	Carbon Capture and Sequestration
CFB	Circulating Fluidised Bed
CFD	Computational Fluid Dynamics
CIA	Carbon In Ash
COE	Cost of Electricity
CPD	Chemical Percolation Devolatilisation
CPU	CO_2 Processing Unit
CTF	Combustion Test Facility
DNS	Direct Numerical Simulation
DO	Discrete Ordinates
DP	Differential Pressure
DPS	Doosan Power Systems
DTF	Drop Tube Furnace
ECBM	Enhanced Coal Bed Methane
EDC	Eddy Dissipation Concept

EDM	Eddy Dissipation Model
EOR	Enhanced Oil Recovery
ERZ	External Recirculation Zone
ETII	Energy Technology and Innovation Initiative
FC	Fixed Carbon
FG-DVC	Functional-Group Depolymerization, Vaporization, Crosslinking
FGD	Flue Gas Desulphurisation
FGR	Flue Gas Recycle
FRH	Final Reheater
FSCK	Full Spectrum Correlated K-Distributions
FSD	Full Scale Deflection
GFC	Gas Filter Correlation
HMI	Human Machine Interface
I/O	Input/Output
IEA	International Energy Agency
IFRF	International Flame Research Foundation
IGCC	Integrated Gasification Combined Cycle
IPCC	Intergovernmental Panel on Climate Change
IR	Infra Red
IRZ	Internal Recirculation Zone
ISO	International Organization for Standardization
LCPD	Large Combustion Plant Directive
LDV	Laser Doppler Velocimetry
LES	Large Eddy Simulation
LHS	Left Hand Side

LIF	Laser Induced Fluorescence
NDIR	Non-dispersive Infrared
NMR	Nuclear Resonance Magnetometer
NS	Navier-Stokes
P&I D	Process & Instrumentation Diagram
PACT	Pilot-scale Advanced Capture Technology
PDF	Probability Density Function
PIV	Particle Image Velocimetry
pk pk	Peak To Peak
PLC	Programmable Logic Controller
ppm	Parts Per Million
RANS	Reynolds Averaged Navier-Stokes
RCP	Representation Concentration Pathways
RFG	Recycled Flue Gas
RHS	Right Hand Side
RNG	Re-Normalisation Group
RR	Rosin-Rammler
RSM	Reynolds Stress Equation Model
RTE	Radiative Transfer Equation
SCADA	System Control And Data Acquisition
SCR	Selective Catalytic Reduction
sd	Standard Deviation
SNCR	Selective Non-Catalytic Reduction
SSH	Secondary Superheater
UDF	User Defined Function

UKCCSRC	UK Carbon Capture and Storage Research Centre
UV	Ultra Violet
VM	Volatile Matter
WSGG	Weighted Sum of Grey Gases
ZEP	Zero Emissions Platform

Chapter 1

Introduction

1.1 The Issue of Climate Change

The broader context for this project is the continuing global effort to mitigate the effects of Climate Change. In 2013 the Intergovernmental Panel on Climate Change (IPCC) published its 5th assessment report, which reconfirmed that human activity – primarily the burning of fossil fuels, industrial activity and land use changes – has led to a dramatic increase in the concentration of CO_2 in the atmosphere which, along with other so-called greenhouse gases (CH_4, N_2O, CFCs), is largely responsible for climate change (IPCC, 2013). Figure 1.1 shows the increase in global anthropogenic CO_2 emissions since the industrial revolution. There is a particularly dramatic rise since circa 1950, with current annual CO_2 emissions stand at over 30 thousand gigatonnes. This increase correlates to changes in atmospheric CO_2 concentration shown in Figure 1.2, which when compared to the data from ice core records over a 400,000 year period, illustrates the historic nature of the increase that has occurred over the last century.

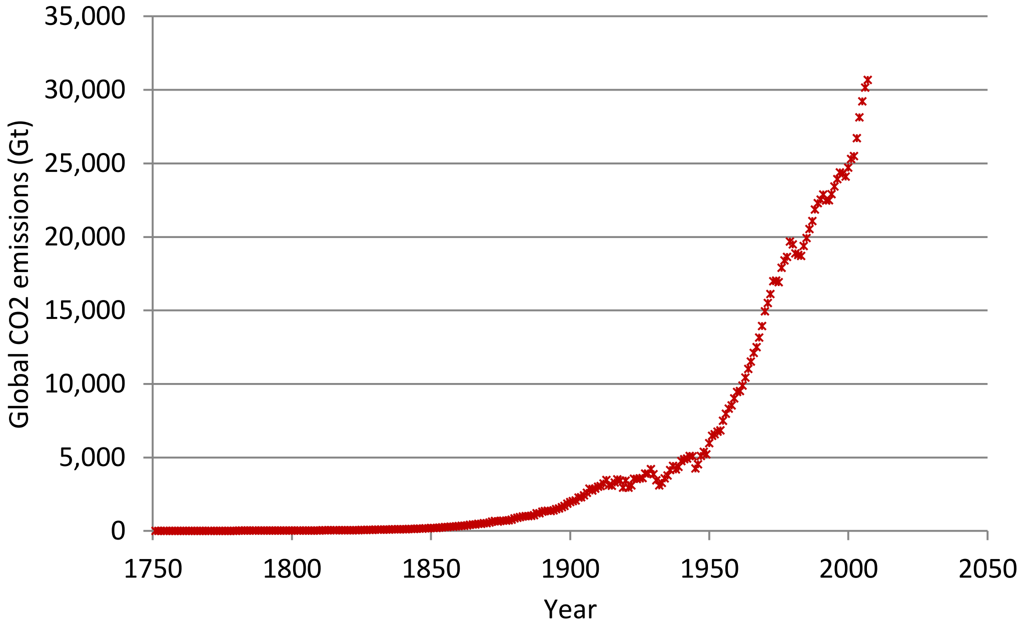

Figure 1.1. Global CO_2 emissions from Fossil-Fuel Burning, Cement Manufacture, and Gas Flaring, in gigatonnes (CDIAC, 2014).

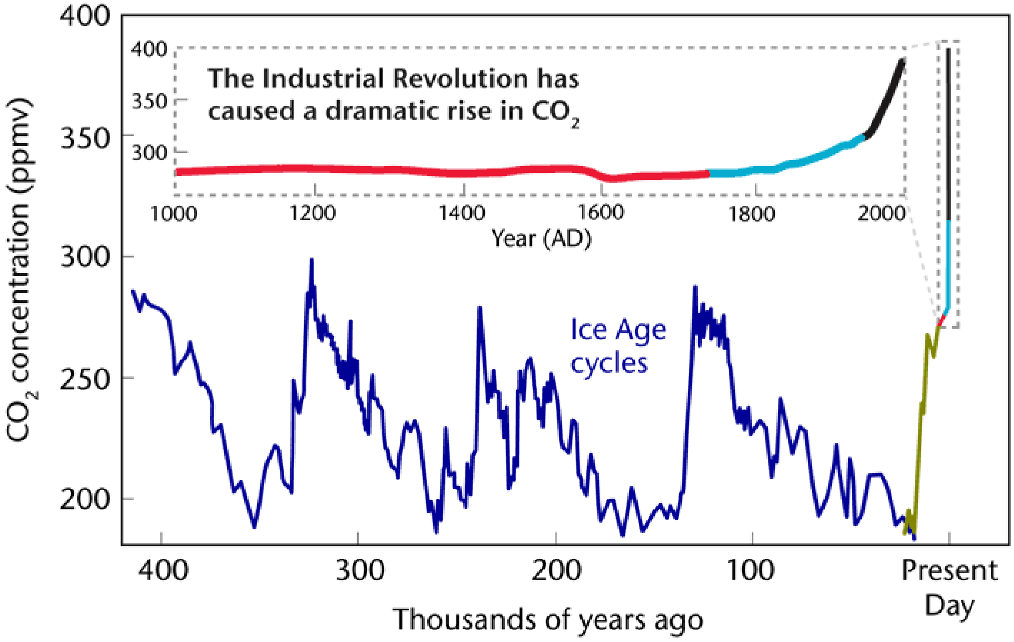

Figure 1.2. Record of past variations in atmospheric CO_2 concentrations from ice core records (Met Office, 2011).

The level of CO_2 concentration in the atmosphere currently stands at 398 ppm (USNOAA, 2014), which is an almost 40% increase since the beginning of the industrial revolution and is substantially higher than levels recorded in ice cores from the last 800,000 years (IPCC, 2013). The level is predicted to reach 550 ppm by 2050 (Stern, 2006). In order to avoid the most dangerous effects of climate change – which includes the melting of glaciers and arctic ice sheets, the acidification of the World's oceans, extreme weather conditions such as droughts and floods and other possible consequences such as food supply shortage (Royal Society, 2005; Stern, 2006), which could even lead to civil unrest and the destabilisation of developing countries, mass migrations of refugees etc. – it is recognised by the Copenhagen Accord that the global average temperature rise must not exceed 2°C (ZEP, 2010b). According to Stern (2006), at the current emissions trends, there is a 77 to 99% chance that this 2°C rise will be exceeded. Therefore, in order to keep the temperature rise below this critical 2°C, global emissions must be stabilised before 2020 (PIK, 2009) and reduced by 50% below 1990 levels by 2050 (CCC, 2009).

When modelling future climate change for its Fifth Assessment Report (2013), the IPCC identified four scenarios (Representation Concentration Pathways, or RCPs), which were identified by their estimated total radiative forcing in year 2100 relative to 1750: RCP2.6 (2.6 W/m^2); RCP4.5 (4.5 W/m^2); RCP6.0 (6.0 W/m^2); and RCP8.5 (8.5 W/m^2). These corresponded to one mitigation scenario (RCP 2.6), two stabilization scenarios (RCP 4.5 & RCP 6.0), and one scenario with very high levels of greenhouse gas emissions (RCP 8.5). These were chosen to represent a range of likely climate policies (or lack thereof) during the course of the coming century, each resulting in different land use practices and levels of greenhouse emissions leading to 2100. The predictions for global surface temperature increases are shown in Figure 1.3. It shows starkly that a policy of 'business as usual', with continuing high levels of CO_2 emissions (RCP8.5), is projected to lead to temperature rises well in excess of the 2°C target identified above.

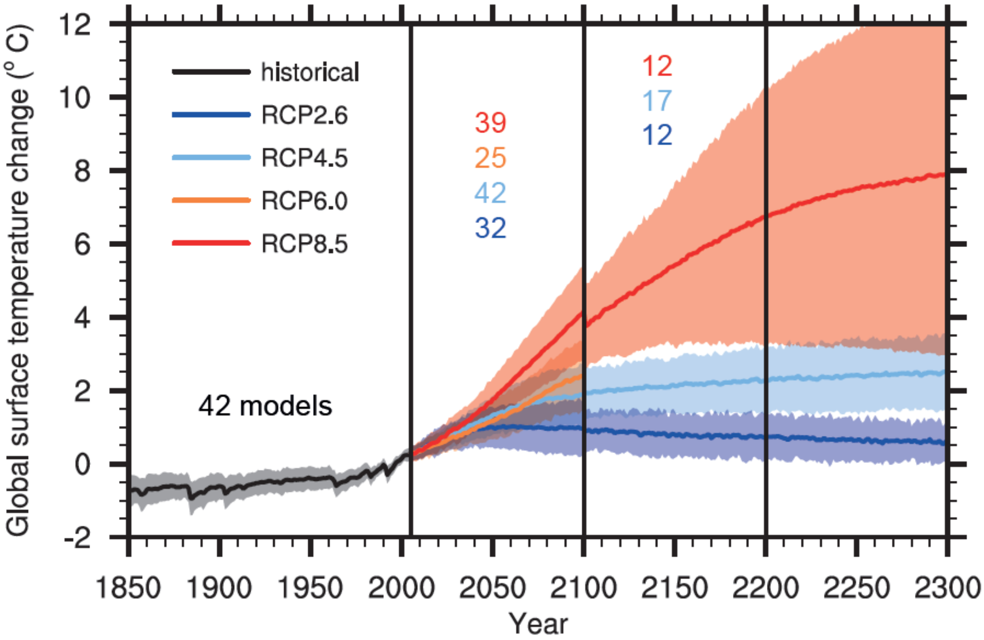

Figure 1.3. Time series of global annual mean surface air temperatures (IPCC, 2013).

Given our continuing reliance on fossil fuels (in 2007 they provided over 80% of the world's total primary energy supply) (ZEP, 2010a), the burning of which produces large quantities of CO_2 emissions, mitigating climate change will be a major challenge. Indeed, recent figures suggest that fossil fuel power plants, together with heavy industry, produce 52% of global CO_2 emissions - approximately 15 billion tonnes of CO_2 per year (ZEP, 2010a).

1.2 Energy Sector

The 4th IPCC report showed that the energy sector is a key contributor to CO_2 emissions. In 2004 it was responsible for 26% of the total anthropogenic CO_2 equivalent emissions (IPCC, 2007). This is due to the major part of the electricity being generated from fossil fuels, with over 41% coming from coal. In the UK coal provided 29% of the electricity in 2012 (World Coal Association, 2014). Figure 1.4 shows the projected electricity generation trends for the next two decades, indicating a significant increase in energy demand, which is predicted to rise by 50% over the next 20 years alone. This increase is driven primarily by population growth (the world population is predicted to grow from 7 billion to 9 billion by 2050), economic development and rising standards of living in the developing parts of the World (ZEP, 2010a).

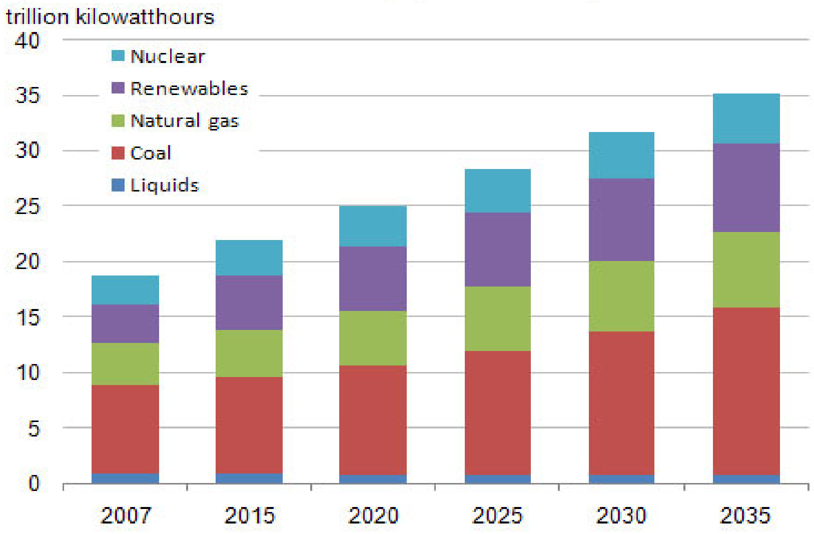

Figure 1.4. World net electricity generation by fuel (IEA, 2010).

It is clear that to meet this demand a combination of improved energy efficiency (both in the generation sector and at end use), and increased reliance on low carbon energy sources will be needed to mitigate climate change (Pielke, 2009). Over the longer term this increased demand is expected to be met entirely from low carbon energy sources. These technologies include renewables (such as solar, wind, hydroelectric and geothermal power as well as sustainably farmed biomass) and nuclear power (and in many decades to come perhaps power provided by fusion reactors). However, each of these technologies face unique challenges. Nuclear power, for example, is very expensive, due to the high cost of construction and decommissioning, and also has issues regarding safety and the difficulty of long term waste disposal (Fyfe, 1999).

Although many renewable technologies share the problems of high cost, the main challenges derive from their unreliable and unpredictable nature. Figure 1.5, which shows the significant changes in the UK's daily energy demand, illustrates the importance of technologies that are reliable, flexible and capable of adjusting to sudden changes in consumption. Balancing an intermittent demand with generation technologies that are inherently intermittent is too great of a challenge to be met in the near future.

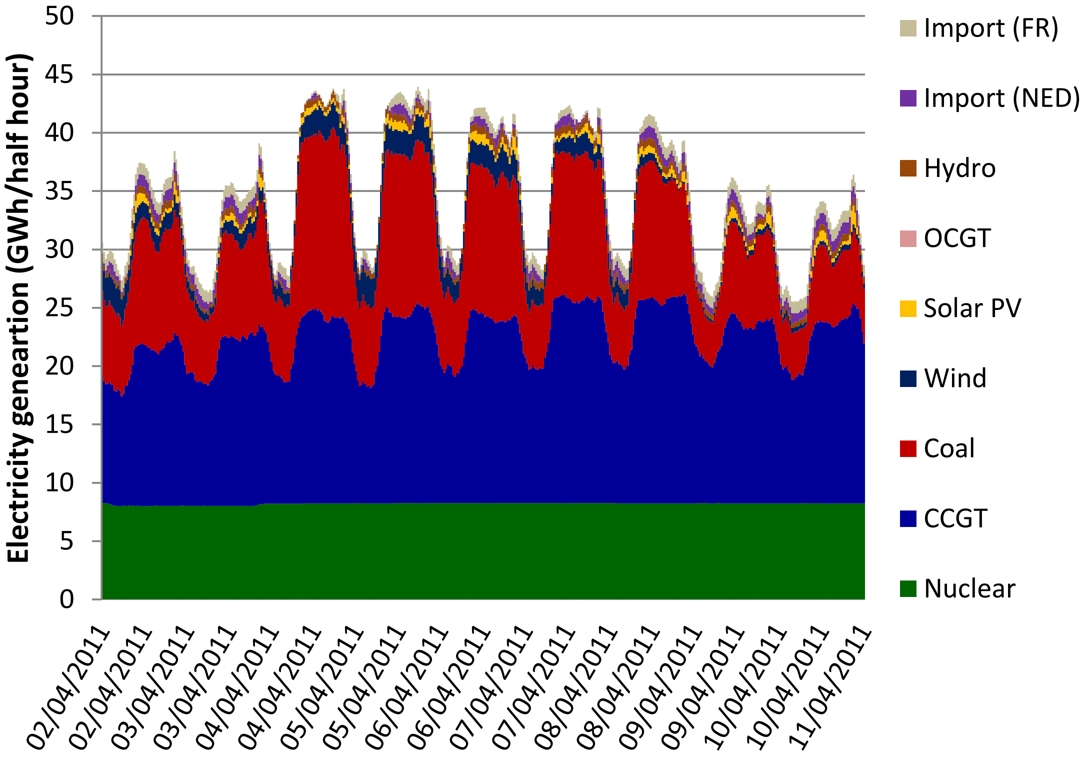

m

Figure 1.5. UK electricity demand & generation by fuel type - over a period of 9 days (ELEXON, 2011).

Therefore the IEA's predictions (Figure 1.4) that energy generation will continue to rely on fossil fuels over the short and medium term are justified.

From the major fossil fuel sources, coal is the most abundant with proven reserves of 109 years, whereas natural gas reserves are estimated to last for 56 years, and oil for 53 years (based on 2012 reserves and production rates) (BP, 2013).

As a first step towards reducing the carbon intensity of fossil fuel-based power generation, increasing the efficiency of existing technologies is required. Although efficiency increases alone cannot reduce emissions to near zero, they will help to lower CO_2 emissions per unit of energy generated. While numerous cost effective end-user efficiency improvements, such as home insulation, have been identified and are being promoted, these fail to realise carbon savings on the scale required to mitigate global CO_2 emissions (Figure 1.6). On the other hand, this figure shows the substantial abatement potential of CCS technologies, although these come at much higher costs.

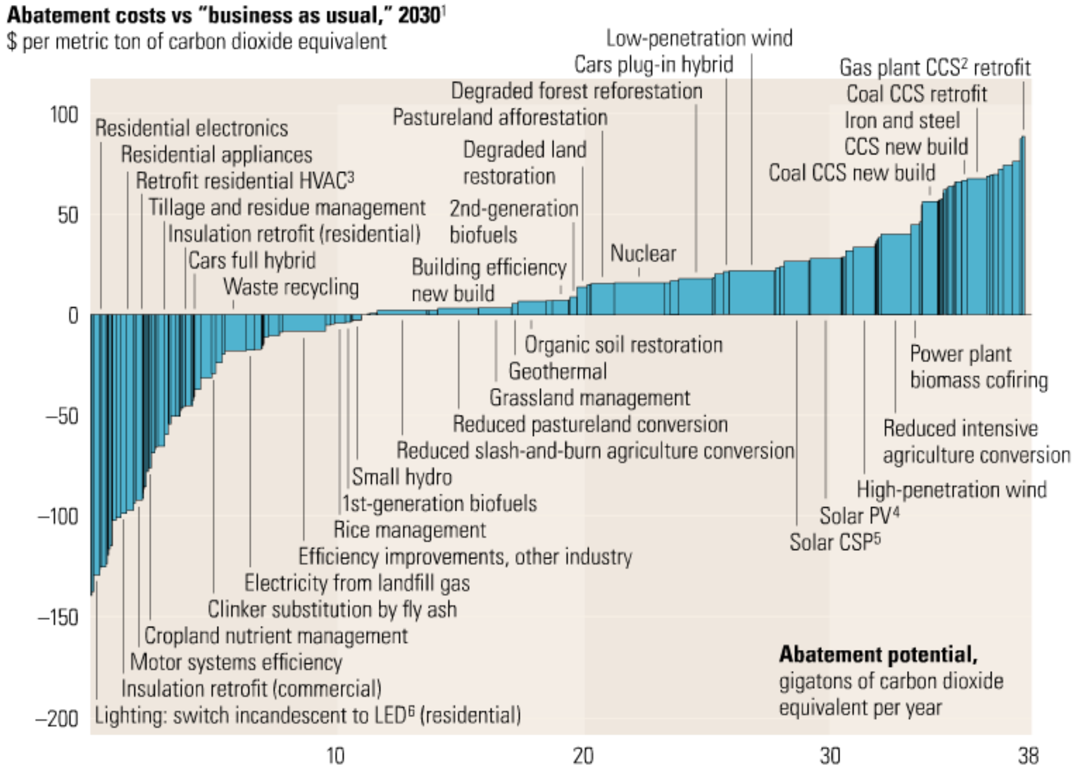

Figure 1.6. CO_2 abatement cost and potential of a range of technologies (McKinsey & Company, 2014).

Biomass is a promising alternative fuel source that can be co-fired with or replace, coal in pulverised fuel boilers. When sustainably produced, the process can be considered close to carbon neutral because the CO_2 released during the combustion of the biomass is removed from the atmosphere by a new generation of crops. Biomass also contains less sulphur and nitrogen, lowering both SO_x and NO_x emission compared to coal firing. Furthermore, as part of a balanced energy mix, biomass can increase energy security (DECC, 2012b). There is considerable experience of co-firing small amounts of biomass with coal in coal-fired power stations; and in the UK, the government has provided additional incentives for full conversion to biomass firing in the form of Renewable Obligation Certificates (DECC, 2012a). However, given the constraints (such as the availability of suitable land, and concerns that switching agricultural production away from food will lead to higher prices, or even shortages of staple foodstuffs), it is clear that coal will remain a key part of the energy mix for at least several decades (see IEA predictions in Figure 1.4). This is because substantial reserves of coal remain (see above), and many countries, both advanced and developing countries, currently rely heavily on coal (see Table 1.1). Therefore, CCS technologies for coal-firing will be essential for any successful effort to mitigate global climate change.

Table 1.1. Share of coal in the worldwide energy generation mix in 2012 (World Coal Association, 2014).

South Africa	94%	Indonesia	44%
Poland	86%	USA	43%
PR China	81%	Germany	43%
Australia	69%	UK	29%
India	68%	Japan	27%

1.3 Carbon Capture and Sequestration

CCS is widely regarded as having the potential to enable the continued use of fossil fuels over the coming decades whilst also reducing the CO_2 emissions of the sector to near zero. Thus, it promises to enhance the energy security of nations with significant fossil fuel reserves, and enable those nations that rely on energy imports to maintain a more diverse range of supply. Another advantage of CCS is its technological maturity for short term deployment (Florin and Fennell, 2010). Stern (2006) stresses the economic benefits of early action in climate change mitigation, as opposed to a reactive approach of dealing with the consequences down the line. According to the IEA (2010), CCS is an essential part of the strategy to achieve substantial CO_2 reductions by 2050. They estimate that the cost of mitigation is considerably higher if CCS is not included in the strategy to decarbonise the energy sector. In the IEA's

‘Blue Map scenario’, 19% of the emissions reductions are met by CCS (a mixture of 35 coal fired and 20 gas fired CCS units of 500 MW capacity).

When it comes to the UK, CCS has been endorsed by both the UK Government (2009) and the industry lead coalition of the APGTF (2014). In order to achieve the 2050 target of reducing the emissions of the power generation sector to close to zero, while maintaining energy security and diversity, HM Government (2009) plans the implementation of CCS, with the potential to secure close to 90% CO_2 reductions across the energy sector, as well as significant reductions within heavy industry (e.g. cement manufacture) and even transport (if widespread electrification of vehicles is introduced). As of 2009, all new coal and gas fired plants, over the 300 MW net generation capacity, have to be built ready for retrofitting with a CCS plant.

CCS involves three technological components:

- first, the technology to capture the CO_2 emissions of large point source emitters such as power stations (these are discussed in Chapter 2).
- second, the means to transport the captured CO_2 to the storage site. The cost of storage is nonlinear with increasing scale (Katzer, 2007), therefore newly built power stations should be placed close to a storage site and ideally in clusters, possibly together with heavy industry plants suitable to CCS such as cement manufacturing or refineries, to take advantage of economies of scale. In the UK there are many such suitable areas, dense in power stations and heavy industry and relatively close to depleted natural gas reservoirs under the North and Irish Sea, for example in the Yorkshire and Humber region.
- and thirdly, its injection to deep geological formations, such as deep saline aquifers or depleted oil and gas reservoirs, where it is initially trapped in the small pores of the porous rock, then it migrates through the formations and over the longer term it undergoes mineralisation and it is considered immobile.

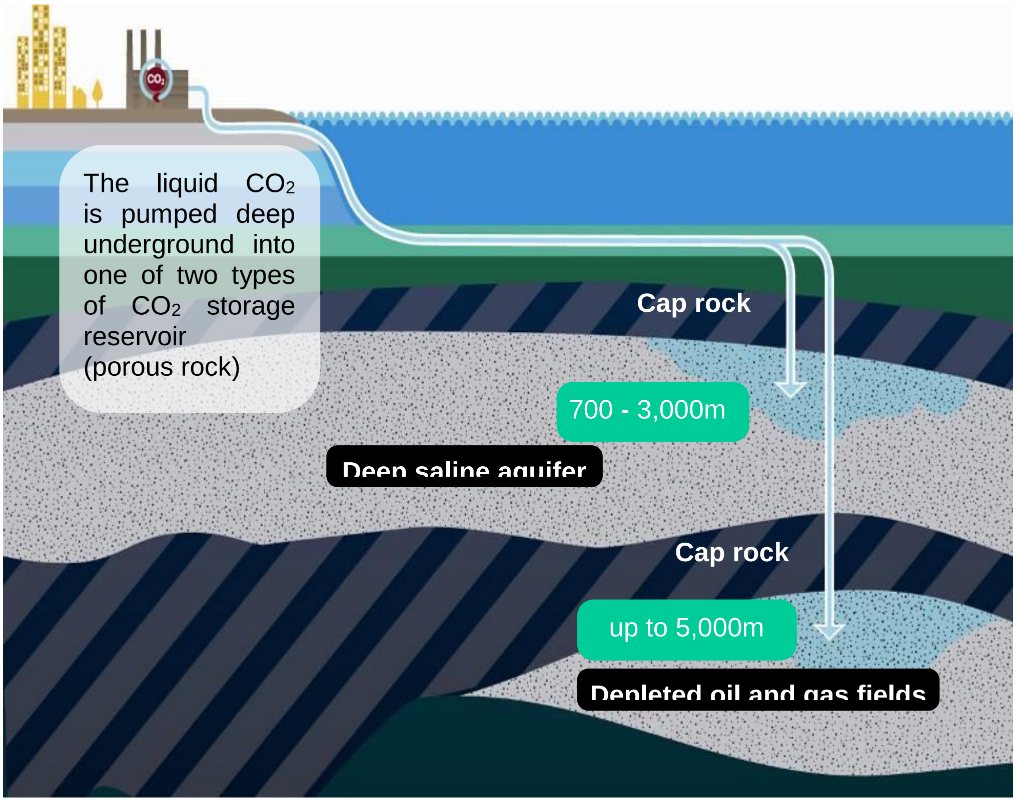

Figure 1.7. Schematics of CCS (ZEP, 2010a).

Each of these 3 components is a separate scientific field in its own right, and this thesis looks only at the first part of this process. However all technologies have now been developed sufficiently to allow the deployment of CCS in the near future. These can be categorised as pre-combustion, post-combustion and oxy-fuel combustion (Florin and Fennell, 2010), and will be explored in more detail in Chapter 2.

1.4 Objectives and Aims

This thesis helps advance our understanding of the oxy-fuel combustion process, and the role that it may play in the development of technologies for Carbon Capture and Sequestration. It presents the results of an experimental programme conducted on a 250 kW solid fuel combustion test facility (located at the PACT national facilities near Sheffield), and investigates CFD modelling for oxy-fuel combustion.

Chapter 2 presents a literature review of experimental oxy-fuel research. It describes the physical processes taking place during combustion, as well as their applicability to oxy-fuel Computational Fluid Dynamics (CFD) modelling, which can be an important tool in aiding the design and development of this promising technology.

Chapter 3 provides a detailed description of the facilities and measurement devices. It describes the fuel used and the experimental conditions investigated. Experimental practices and estimation of measurement errors are also presented, along with the experimental schedule.

Chapter 4 describes the combustion of coal under both air- and oxy-fired conditions in a state-of-the-art 250 kW CTF. A range of measurement techniques were used to obtain a detailed picture of the combustion process, with a particular focus on flame characterisation and heat transfer performance.

Measurements presented and discussed include radiative and total heat flux taken along the length of the furnace, flame temperature profiles, flue gas emissions of O_2, CO_2, CO, SO_2 and NO_x as well as burnout.

Chapter 5 describes the CFD modelling studies, beginning with pilot scale simulation work on the 250 kW facility. The CFD results are compared to the results obtained from the experimental programme. In addition, modelling work conducted on a commercial 500 MW power station is outlined. The investigated cases on this include the validation of the air-fired base case against data provided by the power station. Then the theoretical cases of converting to biomass co-firing and oxy-fuel operation are analysed.

Chapter 6 summarises the major findings and makes suggestions for future work.

Chapter 2

Literature Review and Combustion Modelling

2.1 Chapter Overview

This chapter outlines the literature that relates to both the experimental and the CFD modelling aspects of the research into air and oxy-fuel combustion. A brief summary of the three major CCS technologies is provided. Then, the chapter describes the physical processes taking place during combustion, as well as their applicability to the two methods that were utilised: experimental investigations, and Computational Fluid Dynamics (CFD) modelling. These are important in aiding the design and development of commercial-scale CCS technology.

2.2 Commercial CCS Technologies

Three technologies, pre-combustion, post-combustion and oxy-fuel combustion, have been developed to a sufficient extent to allow the deployment of CCS in the near future (Florin and Fennell, 2010).

2.2.1 Pre-combustion

A schematic of the technology is shown in Figure 2.1. The main feature of the process is the conversion of solid fuel sources (including coal) to gaseous fuel, called synthesis gas or ‘syngas’, in a gasifier. During the conversion process, the fuel undergoes partial oxidation to provide energy for the conversion process. The produced syngas consists mainly of CO, H_2, CH_4, CO_2 (plus tars and other trace components, the exact nature and amount of which will depend on the composition of the fuel source). In the next step, the syngas is reacted with steam in a water-gas shift reactor where the CO is converted to CO_2, which produces a stream with a high CO_2 concentration, typically 50%. The CO_2 then can be separated from the stream at high temperature and pressure. At the end of this process a gas mixture, consisting primarily of H_2, is produced which can be combusted in a gas turbine or used to run a fuel cell.

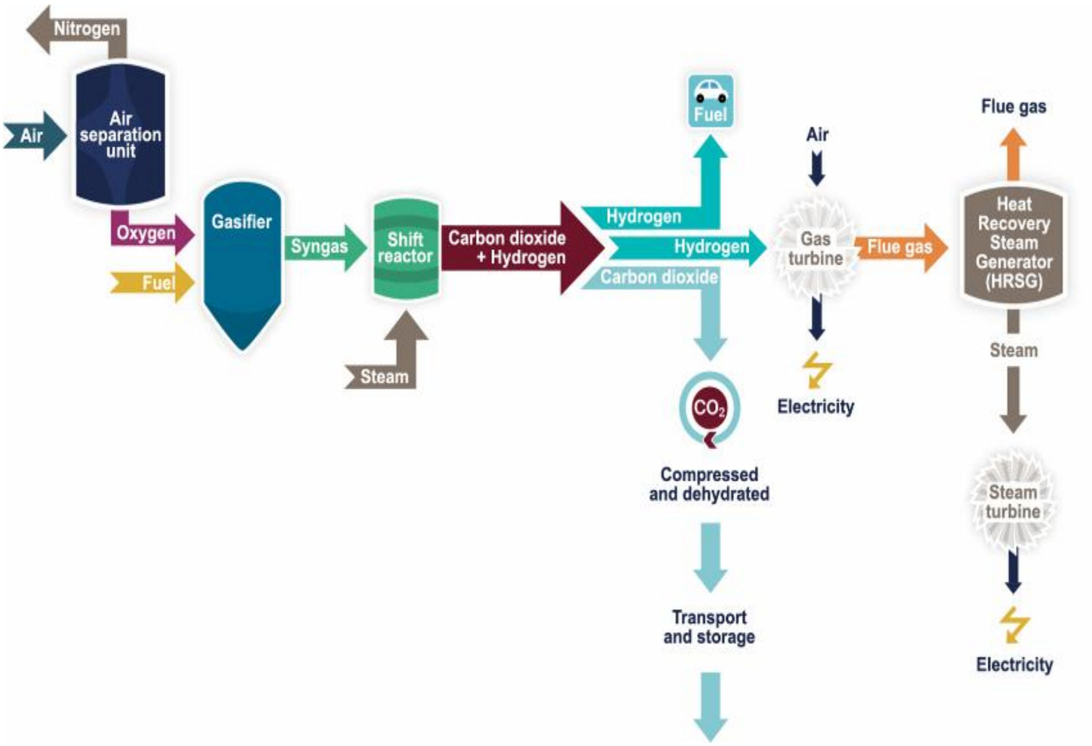

Figure 2.1. Schematic of the pre combustion process (ZEP, 2010a).

One of the main disadvantages of the process is the high cost of the gasifier, which requires continuous operation of the unit in order to be cost effective. This reduces the flexibility of this technology and makes it more suitable only for base line operation (unless, at times of low electricity demand, the excess hydrogen can be stored on site or used as a feedstock for chemical manufacture process) (Florin and Fennell, 2010).

Another problem of the process is the issue of complexity, which imposes challenges for flexible operation. Even the commercially available IGCC plants still have issues with the operability and availability of the plant (Katzer, 2007).

However, an advantage of the process (over post combustion) is that the scrubbing plant runs at high temperature and pressure and the partial pressure of CO_2 in the treated stream is high, and thus enables the use of physical scrubbing agents, which bind to the CO_2 less strongly than chemical agents and therefore their regeneration requires less energy. The current energy penalty of pre-combustion plants is approximately 7-9% (APGTF, 2011).

2.2.2 Post-combustion

This technology is the least intrusive option. It does not require modifications to the power plant and its boilers, and involves attaching a scrubber at the end of the generation plant. Thus one of the main advantages of the process is retaining operational flexibility of the power plant. A schematic of the process is shown in Figure 2.2.

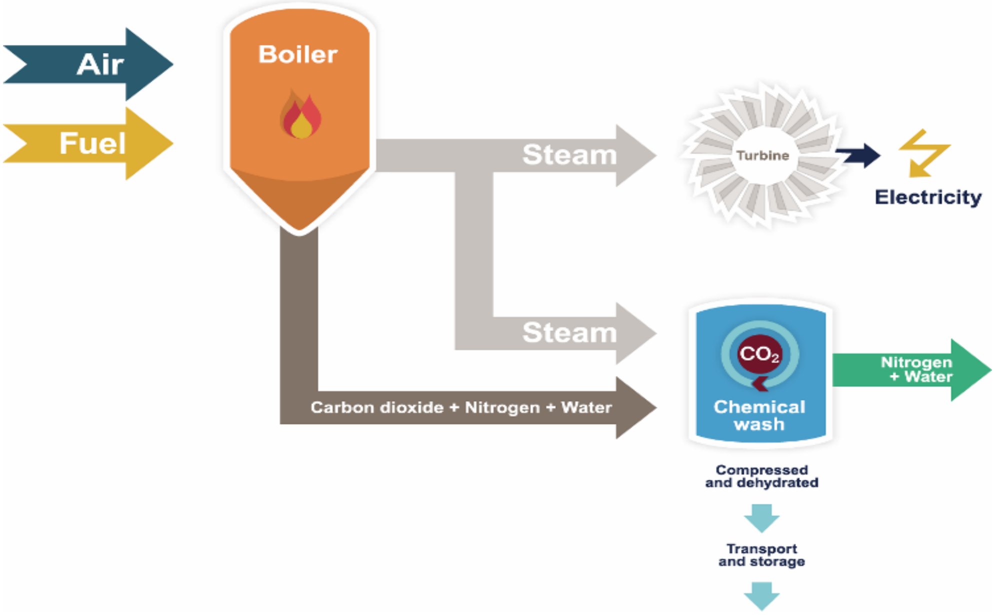

Figure 2.2. Schematic of the post combustion process (ZEP, 2010a).

The flue gas from the boiler needs to be cleaned as the scrubbing process is particularly sensitive to the impurities that are present. The flue gas is then drawn through the scrubbing unit at typically 80°C and atmospheric pressure where approximately 90% of the CO_2 is removed and the remaining flue gas, which consists largely of N_2 and H_2O and some CO_2, is sent to the chimney.

Due to the low concentration of CO_2 in the flue of conventional power stations (typically 12-14%), the process requires the use of chemical scrubbers, which bind to the CO_2 and carry it to a second unit where the CO_2 is recovered and the scrubbing solvent is regenerated. However, regeneration requires large amounts of heat (20% of the generated power), thus imposing a parasitic load on the power plant which lowers its overall efficiency by 12% (APGTF, 2011). Another disadvantage of the process is that the scale up and capital and operational cost of the capture plant is significant, due to the large volume of flue gas which needs to be treated.

2.2.3 Oxy-fuel Combustion

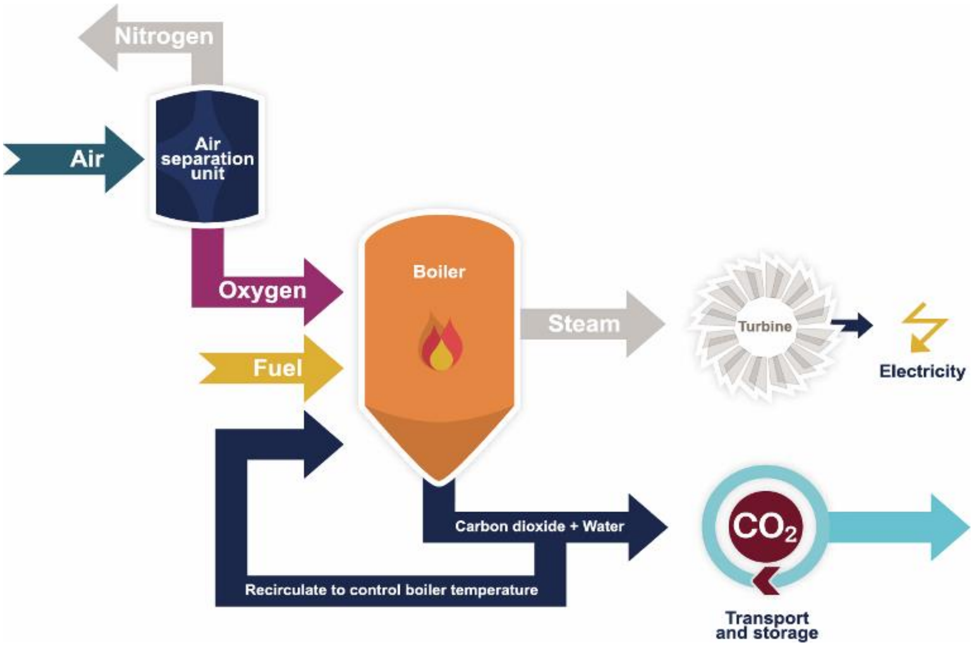

Figure 2.3. Schematic of the oxy-fuel combustion process (ZEP, 2010a).

Oxy-fuel technology is one of the leading contenders for CCS. The main difference from conventional air firing is that the fuel is burned in a mixture of O_2 and recycled flue gases. Flue gas recycle (FGR) is necessary as burning coal in pure O_2 (without N_2 acting as a diluent) would produce furnace temperatures which could not be withstood by conventional furnace materials. By removing the N_2 upstream of the process, a flue gas rich in CO_2 and water vapour is produced. The water vapour can be removed simply by condensation, leaving a product stream of high purity CO_2 which, after subsequent purification and dehydration, is ready to be pumped away to a geological storage site. This eliminates the need for a costly post-combustion capture plant, although the extra cost is now shifted to the oxygen plant.

2.3 Economic and Feasibility Issues

The question of which of these technologies will ultimately be widely adopted depends on numerous factors, including the economy, technological maturity, expected plant availability and operational flexibility, and environmental performance.

All the technologies offer above 90% CO_2 capture efficiency (Dhungel, 2010). The maximum efficiency that each technology can achieve will be especially important in the event that a carbon tax is introduced. Post- and oxy-fuel combustion are both suited to retrofit existing plants, whereas pre-combustion is only applicable for newly built facilities (Florin and Fennell, 2010).

The main economic challenge of the carbon capture technologies is to reduce the overall plant efficiency loss, which is caused by the parasitic energy requirement of CO_2 separation (for pre- and post-combustion), of O_2 separation (for oxy-fuel), and of CO_2 processing (for all of the above). For a supercritical unit, this results in approximately 9% reduction in overall efficiency (e.g. from 38% to 29%), which requires a 32% increase in coal consumption to maintain the same output (Katzer, 2007). This means that CCS will result in significantly increased CO_2 production, although most of this CO_2 can be captured and stored, thus resulting in overall reductions in CO_2 emissions.

A way to reduce the cost associated with CCS is the sale of the captured CO_2. So far, CO_2 is utilised on a large scale for enhanced oil recovery (EOR) or enhanced coal bed methane (ECBM) extraction. High purity CO_2 can also be used as feedstock for various chemical processes, e.g. urea or methanol production. As an alternative, CO_2 is being investigated as a feedstock for 3rd generation biofuel production (i.e. large scale bioreactors, where algae transform the CO_2 rich flue to bio-oils). However there are a number of issues with all of the above technologies. For example, given the quantities of emissions around the globe only a fraction of this CO_2 can be viably recycled as a chemical feedstock, and also when considering the life cycle assessment, the overall CO_2 reduction may be drastically reduced.

As Toftegaard *et al.* (2010) have pointed out, techno-economic studies have shown that based on current knowledge there is no significant cost difference between the three available CCS technologies (although some early studies suggested that oxy-fuel technology might be the most cost efficient). However, there exists a degree of uncertainty concerning the configuration and cost assumptions that have been built into these assessments.

A number of detailed studies have explored the potential cost effectiveness of oxy-fuel technology compared to a conventional air-blown power station. For example Xiong *et al.* (2009) explored the economic feasibility of oxy-fuel technology for retrofit in China. Taking into account both the cost of electricity (COE) and CO_2

avoidance cost (CAC). They predicted that the COE is comparable to conventional air firing as long as the unit price of CO_2 is within 17-22 $/t (according to the authors 15-25 $/t sale price is acceptable in China) or, if a carbon tax is considered, when the unit CO_2 tax is between 29-36 $/t. They also found the cost of CAC to decrease with increasing power output by 1-3 $/t (from 300 to 600 MW), which is due to the scale dependence of the economic viability of steam cycles. Thus oxy-fuel technology is more suitable to large scale power plants with advanced steam cycles.

MIT's *The Future of Coal* report found that a 500 MW oxy-fuel combustion plant may offer 10% lower COE and 25% lower CAC than supercritical post combustion plant of the same unit size (Katzer, 2007).

Oxy-fuel technology can lead to increased efficiency associated with the reduced flue gas losses, as the overall volume of the flue gas is lower, it is cooled further, and the latent heat of water vapour is recovered during the condensation step. Furthermore, due to significantly lower total NO_x production, the costly de-NO_x plants are often omitted from the cost estimates of oxy-fuel plants, along with de-SO_x units when the co-storage of SO_2 along with CO_2 is assumed. Although it should be noted that this latter option has not been proven, and raises serious concerns for transport and storage due to the corrosive nature of SO_2.

When considering oxy-fuel technology, the major cost is associated with the O_2 production. Shah (2006) estimates this to be 57% of the overall cost, and the CO_2 processing unit (CPU) and FGR accounting for 36% and 7%, respectively. At present, on a large scale, cryogenic air separation is the most viable option (though as part of the ENCAP project other innovative technologies are also being investigated, including membrane separation and chemical looping). Darde *et al*. (2009) found that the efficiency of cryogenic air separation units (ASU) has more than doubled since 1971, and project a continued increase due to technological learning advances, "since the overall energy of separation is still significantly greater than the theoretically required separation energy".

The operational cost of the ASU also depends on the purity of O_2 required, and Shah (2006) found that 95-97.5% purity is optimal, but also recognised the need for minimising air ingress to the system). Jordal (2004) notes that this may be particularly challenging for retrofit purposes for boilers where the level of air leakage into the boiler or downstream may already be significant. Another way of reducing the energy penalty of the ASU plant is by successful heat integration of the ASU and the low temperature heat sources of an oxy-fuel plant (flue gas condensation, CO_2 compression, steam cycle) (Jordal *et al*., 2004) - though higher degree of integration poses additional process control challenges, which will need further investigation.

van der Broek *et al*. (2009) noted the significant potential that, over time, technological learning curves may decrease the capital and operational cost of separation and CO_2 processing technologies. However, overall it is difficult to assess fully the cost effectiveness of any of the CCS technologies, given that the national and international policy frameworks remain uncertain (e.g. carbon tax and measures to support CCS). Moreover public confidence in the safety and reliability of CO_2 transportation and storage will be necessary for overall success (this might be particularly important for landlocked nations with no access to deep sea aquifers).

2.4 Technological Challenges of Oxy-fuel Combustion

Oxy-fuel combustion has long been a common process in the glass, cement and steel industries. However, oxy-fuel technology with FGR for fossil fuel plants was first proposed by Abraham *et al*. (1982), with the aim of producing CO_2 for Enhanced Oil Recovery (EOR). Since then a number of small and medium scale experiments have been conducted and, together with several demonstration projects, have significantly contributed to our current understanding of the process. Although the individual components of the process are all commercially available, they have never been integrated together on a large scale. There was, therefore, a requirement for full scale plant experience to assess the plant's availability and load following capability when using high pressure steam cycles, viable with unit sizes of typically above 250 MW_e (Davidson and Santos, 2010).

A number of large scale oxy-fuel plants are currently at the planning and development stages (MIT, 2014). These include:

- 426 MW coal fired CCS plant at Selby, UK, a partnership between ALSTOM and Drax Power Ltd.,
- a 200 MW retrofit project to Amerden's coal fired plant, in Illinois, USA – as part the FutureGen 2.0 initiative,

- a 350 MW power plant in China, a partnership between Alstom and China Datang Corporation,
- one possible option for the Korea-CCS2 project promoted by the Korea Carbon Capture and Sequestration R&D Center the building of 500 MW oxy-fuel power plant,
- and CIUDEN is pursuing a 323 MW circulating fluidised bed oxy-fuel plant at El Bierzo, Spain.

A number of demonstration projects have been successfully implemented in order to provide information for scaling up, which include:

- Doosan Babcock's 40 MW OxyCoal^{TM} system at Renfrew, UK,
- Vattenfall's 30 MW plant at Schwärze Pumpe, Germany,
- CS Energy's Callide 'A', a 30 MW retrofit plant in Queensland, Australia,
- CIUDEN 20 MW plant (along with a 30 MW CFB unit) in Spain,
- Total's 35 MW gas fired Lacq project in France,
- Babcock & Wilcox Group's 15 MW_{th} facility in Indiana, USA,
- and also their 30 MW_{th} Clean Environment Development Facility (CEDF) in Ohio, USA (Davidson and Santos 2010; MIT 2014)

These demo plants all contribute to important advancements in our technical understanding of oxy-fuel technology.

2.5 CFD Modelling as a Development Tool

Oxy-fuel technology is still in development and to facilitate Research & Development Computational Fluid Dynamics (CFD) can be used.

In short, a CFD software package is used to model the real life combustion application on a computer. It uses an array of mathematical models (so called submodels) to describe the numerous thermo-physical phenomena taking place during combustion (e.g. devolatilisation, char combustion, radiation etc.), and their interaction with one another.

The first commercial CFD packages became available more than 25 years ago and, due to the state of the computational park (especially limited power and processing speed), simplified models were used to make predictions (Schmidt *et al*., 2004). But simplifications require assumptions that introduce errors in the predictions, and, as combustion modelling incorporates numerous submodels, these errors can compound and distort the results significantly.

Due to significant advances in computational power, CFD can now be used to model the complex physical and chemical processes taking place during combustion more accurately. Therefore CFD has become a useful tool aiding burner and furnace design and development. Even though computer modelling cannot (yet) replace physical testing of a new design, it can, for example, be used for pre-screening of alternate designs, thereby reducing the physical simulations required and offering significant cost and time savings (Smith *et al*., 2003). The use of CFD is recognized to be able to provide reliable qualitative solutions (i.e. correctly predict trends) (Williams *et al*., 2002), of, for example, in-furnace temperature profiles, heat flux distribution, flame characteristics, pollutant formation trends, etc. In certain aspects predictions can match experimental results within 10%, e.g. NO_x emission from single burners (160 kW & 40 MW) and in full scale 500 MW furnaces at Didcot and Ratcliff power stations both equipped with 48 low NO_x burners (Stopford, 2002).

CFD may also be used to model furnace performance changes due to the usage of different coal blends, which is common practice nowadays to counter price fluctuations of coals used. Thus, there are increasing requirements for CFD codes to provide not only qualitative trends, but quantitative results as well (Williams *et al*., 2002).

Currently, however, the submodels are not yet refined enough to produce quantitative results for conventional combustion applications. In the case of Oxy-fuel combustion, modelling is further complicated by the fact that the submodels were developed (and validated) for air fired coal combustion.

Detailed knowledge and understanding of the underlying elementary physics is required in order to successfully describe them by mathematical models, which when incorporated into the overall model, should in theory, be more general and accurate, and also retain this accuracy throughout a range of different problems.

Although Magnussen and Hjertager (1977) noted that one must be cautious with model selection, as they may mask important effects with less important ones.

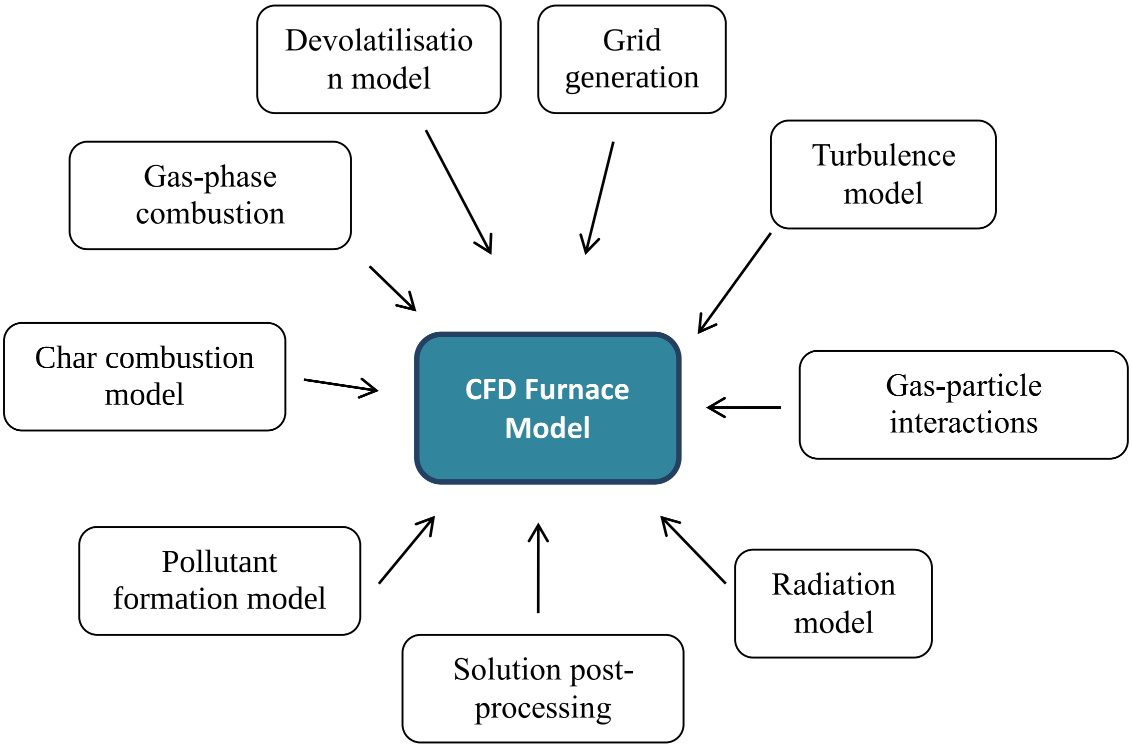

Figure 2.4. Illustration of different submodels and components of a CFD model.

Each mathematical submodel of combustion requires numerous inputs. These include physical properties related to the materials whose behaviour they describe (e.g. in the case of char combustion the porosity and chemical structure of the char particles), which require empirical data, often specific to that particular material, and also physical conditions (e.g. the heat transfer to the particle, concentration species surrounding the particle), which is calculated by the CFD code during modelling of the fluid flow.

The modelling process begins firstly with defining the computational domain and discretizing it into a finite number of cells. Within these cells partial differential equations of mass, momentum, species concentration and energy are solved by integrating them over the domain, converting the integrals to algebraic equations and solving them via iterative methods. This, in essence, is the finite (or control) volume method.

The following sections detail the physical combustion phenomena as well the approach for modelling them using CFD.

In order to maximise the chance that the large scale plants will succeed (and thus demonstrate the technological and economic feasibility of the process) the fundamentals of oxy-fuel combustion technology have to be understood (for recent reviews of the technological developments and overall status of the field see Chen *et al.* (2012), Scheffknecht *et al*. (2011), Davidson and Santos (2010), Toftegaard *et al*. (2010), Wall *et al*. (2009)).

It is clear that replacing N_2 with CO_2 changes the fundamentals of the combustion process. This is due to the fact that the thermophysical properties of CO_2 differ significantly from N_2. The differences are listed below (and are illustrated graphically in Figure 2.5):

- CO_2, being a tri-atomic gas, actively participates in thermal radiation thus impacting the in furnace heat transfer profiles,
- CO_2 (57.83 kJ/mol at 1127°C) has a higher heat capacity than N_2 (34.18 kJ/mol at 1127°C), which can impact on the adiabatic flame temperature,
- CO_2 has a higher molecular weight (44 g/mol) than N_2 (28 g/mol), which will increase the density of the mixture,
- the thermal conductivity of the O_2/CO_2 mixture differs from O_2/CO_2, and may have an impact on the heating up rate of the coal articles, and consequently flame characteristics.
- the increased CO_2 concentration in oxy-fuel combustion results in a lower O_2 diffusion rate than in conventional cases, hindering O_2 diffusion to the char particle and may also increase the importance of the Boudouard gasification reaction, influencing char burnout.

The presence of the flue gas recycle and the additional process plants (O_2 production and CO_2 processing units) further complicates the process and, as a result, oxy-coal combustion differs from conventional air fired combustion in a number of ways:

- Flame characteristics
- Coal reactivity
- Heat transfer
- Emissions characteristics
- Corrosion
- Process control

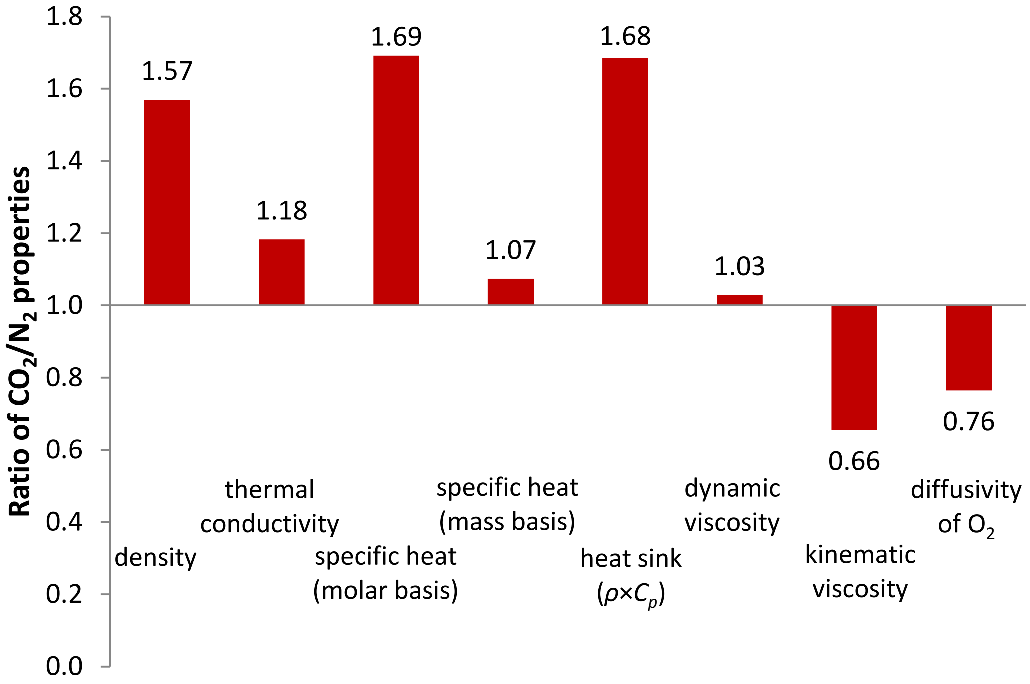

Figure 2.5. Comparison of thermophysical property differences between CO_2 and N_2 - determined at 1127°C and 1 atm. Data taken from Toftegaard *et al*. (2010).

2.5.1 Flame Temperature

In pulverised fuel flames, the flame temperature is considered to be the most important factor influencing particle heat up, ignition and burnout (Dhungel, 2010). At the same O_2 concentrations, the adiabatic flame temperature (ATF) of an oxy-fuel flame is lower than an air fired one. This is due to differences in the thermal property of the mixture, which is characterised by the product of density and specific heat and is referred to as the heat sink (Shaddix and Molina, 2009). However, by increasing the O_2 concentration, and as a result reducing the CO_2 concentration and thus the heat sink, the AFT of the air firing application can be matched. This is typically achieved at 30% O_2 concentration, which is, at a fixed oxygen to fuel ratio, controlled by varying the amount of the recycled flue gas, requiring approximately 60% recycled (Wall, 2007).

2.5.2 Particle Heat Up, Ignition and Flame Propagation

Increasing the O_2 concentration also enhances reaction and heat release rates and consequently increases the rate of devolatilisation, lowers the time required for ignition, and increases the flame propagation speed (all of which is retarded by substituting N_2 with CO_2). Thus by proper O_2/CO_2 ratio selection, it is possible to match ignition times and volatile flames of oxy-fuel furnaces to conventional flames (Shaddix and Molina, 2009). Ignition studies carried out by Man and Gibbins (2011) on thirteen coals from a wide range of coal ranks, confirmed these findings. The optimal recycle ratio was found to be 30-35% percent.

Smart and Riley (2011) carried out tests firing South African bituminous and Russian semi-anthracite coals, fired with a 0.5 MW burner operated in RWE npower's Combustion Test Facility (CTF). They found that by reducing the recycle ratio (thus increasing the O_2 enhancement and flame temperature) the flame stability and luminosity may both be increased, and demonstrated that oxy-fuel combustion allows for a wider range of coals to be burned in a conventional utility boiler (potentially including semi-anthracites).

2.5.3 Burnout

Toftegaard (2010) notes that char combustion is typically controlled by both kinetics and diffusion (Zone II), and as the diffusivity of O_2 in CO_2 is 0.8 times that of its diffusivity of N_2 (at 1127°C), at the same O_2 partial pressures, the lower diffusivity is expected to lower the rate of char combustion. Similarly, as the diffusivity of small hydrocarbon is also lower in CO_2 atmospheres, the rate of volatile combustion is also negatively affected by the increased presence of CO_2. However, when the AFT is matched, the increase in O_2 concentration results in an overall enhanced burnout of char and volatiles.

The enhanced burnout may also be explained by the increased importance of the Boudouard reaction at a high CO_2 partial pressure:

$$C + CO_2 \rightarrow 2CO$$

However, as at high O_2 partial pressures, the CO_2 has to compete with the O_2 for the char, the influence of this reaction is not yet clear, and requires further investigation (Wall *et al*., 2009).

2.5.4 Heat Transfer

In pulverised fuel furnaces, radiation is the principal mode of heat transfer, which is dependent on the flame temperature and the radiative properties of the gas mixture and the particles. Furthermore, as the emissivity of the CO_2 and H_2O is higher than that of N_2, oxy-fuel combustion results in higher radiation fluxes, and therefore for retrofit applications lower AFT is required to match the HT to the radiative section. The increased heat transfer in the radiative section will, though, result in lower gas temperatures in the convective section. This heat transfer between the two sections will have to be optimised for retrofit applications.

Smart *et al*. (2009), Smart *et al*. (2010b) and Smart and Riley (2011) investigated the effect of the recycle ratio on the furnace radiation profiles and found that overall the radiative heat transfer matched air firing cases at 72-74% recycle ratios. Even when semi-anthracite was used, the radiation profile away from the burner region (axial distance >0.75 m) could be matched to profiles produced by bituminous coals under air fired conditions (Smart and Riley, 2011). Although near the flame region (axial distance <0.75 m) the radiation flux was significantly lower for the semi-anthracite (due to low volatile content of semi-anthracites).

2.5.5 Emissions

Numerous studies have been conducted on the impact of oxy-firing on the pollutant formation (see for example Shaddix and Molina, 2011, Smart *et al*., 2010b). The consensus view is that oxy-fuel combustion results in significantly lower NO_x and SO_x emissions per unit of energy produced than conventional air firing. The concentration of pollutant species in the flue is, though, significantly increased due to the accumulating effect of the recycle. The reduction of NO_x may be attributed to a number of reasons, including: decreasing thermal NO_x formation by the low nitrogen concentration and lower AFT, limiting the fuel-N conversion by the high NO concentration, the reduction of the recycled NO (Davidson and Santos, 2010). Toftegaard *et al*. (2010) list the following methods resulting in lower NO_x emissions: oxidant staging, wet flue gas recycling (thus increasing the H_2O concentration), increasing the partial pressure of NO_x in the oxidant, increasing oxygen purity and limiting air ingress. The decrease of SO_x emissions is attributed to higher retention rates of S in the fly ash particles due to the higher in-boiler SO_x concentrations.

2.5.6 Corrosion

Jordal (2004) notes that the high concentration of CO_2, sulphur and chlorine species increases the corrosive nature of flue gases. Also Fleig *et al*. (2009) found that as the partial pressure of SO_2 increases, the percentage of SO_3 conversion also increases compared to conventional air-blown combustion. Therefore as the dew point is a function of the partial pressure of the gases, the increase in SO_3 (and H_2O) concentration may result in operational problems due to low temperature corrosion. The increased partial pressure of CO_2 may also exacerbate issues associated with carburization of Cr containing steel tubes (Toftegaard *et al.*, 2010).

2.6 Coal Combustion Processes and Modelling Strategies

Coal is supplied to conventional utility boilers in a pulverised form. The coal is milled directly before it is combusted in ball mills, to a typical diameter range of 4-500 µm and it is transported to the burners via the primary air stream. In the combustion chamber the coal is heated rapidly (typically at the rates of 10^5 °C/s (Williams *et al.*, 2007)) and first its moisture and then is volatile content is released leaving behind the porous char, which is then oxidised to CO and CO_2 leaving the inert ash, which in case of incomplete combustion, contains some unburned carbon.

Coal combustion is generally divided into the following three parts:

- particle heat up and dehydration,
- volatile release and combustion,
- char combustion.

In reality these steps can overlap with each other. The late stage devolatilisation and onset of char combustion, for example, have been found to overlap, particularly for lower rank coals (due to the higher reactivity of lignite chars). For high rank coals, on the other hand, the lower volatile flux can allow sufficient O_2 to diffuse to the particle and reach high enough concentration to initiate heterogeneous combustion before all the volatiles are released (Fletcher and Hardesty, 1992). However, for simplicity, these steps are modelled in succession (while the successive steps are not allowed to commence before the previous step is completed).

2.6.1 Coal Analysis

Many of the models used for coal combustion modelling require parameters which depend on the type of coal. Therefore experimental analysis of the coal used is required.

The different types of coals are classified based on coal rank, where a higher rank represents a further stage in the process of the evolution of coal. The proximate and ultimate analyses are used commonly to assess the rank of the different types of coals.

Coal originates from biomass that over millions of years has been "physically compacted and chemically carbonised" (Abbas *et al.*, 1996) forming a diverse range of coals with variable chemical as well as physical properties. These depend on the type of biomass materials from which the coal is formed, as well as the geological, geographical and climatic conditions during the process. Coal is made up of organic compounds, so called macerals (vitrinite, liptinite and inertinite), and inorganic mineral matter. The properties of different maceral vary (especially in their swelling behaviour and the structure of char produced). However, due to their relatively small unit size (typically 2-5 µm in diameter), the pulverised fuel particles can be considered as pseudohomogeneous when modelling their combustion (Williams *et al.*, 2000).

Mineral matter originates either from the biomass or mineral matter from the surroundings of the coalification site and thus the composition may vary significantly, and can influence slagging and fouling in boilers (Abbas *et al.*, 1996). This effect has to be considered (especially when firing blends of different coals) as slagging and fouling reduces the heat transfer to the steam banks because of the added thermal resistance of the deposits, and thus can require more frequent maintenance shutdowns of the furnace.

Coal also contains S, N, and trace amounts of Cl, Hg, K, etc., from which during combustion various pollutant and corrosive gases and vapours can form, which have to be dealt with accordingly in order to minimise the environmental impact of the combustion plant and adhere to emissions regulations.

2.6.2 Particle Heating and Dehydration

As the pulverised coal enters the combustion domain, its temperature rises due to convective and radiative heat transfer to the particle:

$$m_p c_p \frac{dT_p}{dt} = \hslash A_p \left(T_\infty - T_p\right) + \epsilon_p A_p \sigma \left(\Theta_R^4 - T_p^4\right)$$

The film heat transfer coefficient is evaluated using the correlation of Ranz and Marshall (1952a, 1952b). The rate at which the particle is heated is proportional to the temperature gradient and the surface area of the particle. The surface area is dependent on the particle diameter, which is modelled by discretising the complete size range into an adequate number of size intervals, each representative of an average diameter. This is based on sieving data fitted to the Rosin-Rammler distribution (ANSYS Inc., 2013).

Another assumption during modelling is that the internal resistance to heat transfer is negligible compared to the boundary layer resistance (ANSYS Inc., 2013), i.e. for typical pulverised coal particle diameters, the Biot number is low, and internal temperature profile of the particle can be assumed as uniform (Williams *et al.*, 2000).

The moisture content of particle is evaporated between a specified onset temperature 11°C and 100°C. Below 100°C the vaporisation is assumed to be governed by diffusion, driven by the water vapour concentration gradient between the surface of the particle and the bulk of the gas:

$$Ni = k_c\left(C_{i,s} - C_{i,\infty}\right)$$

where k_c is the film mass transfer coefficient, and it is evaluated using the Ranz and Marshall (1952a, 1952b) correlation.

When the particle reaches a temperature of 100°C, the droplet boiling law is activated. During this process the particle temperature is assumed to remain constant and the rate of moisture release is driven by the convective and radiative heat transfer to the particle:

$$-\frac{dm_p}{dt}\hbar_{fg} = \hbar A_p\left(T_\infty - T_p\right) + \epsilon_p A_p \sigma\left(\Theta_R^4 - T_p^4\right)$$

After all the moisture is evaporated, the particle temperature begins to increase again, initiating the evolution of volatile products.

2.6.3 Devolatilisation

Devolatilisation governs the major characteristics of the flame, including flame shape, size, stability, etc. (Williams *et al.*, 2007). Therefore correct predictions are necessary for accurate modelling of pulverised fuel combustion.

Devolatilisation is an endothermic process (Baum and Street (1971) estimated that devolatilisation becomes significant at 327°C), and it depends on a number of structural parameters of the parent coal matrix (Williams *et al.*, 2000). At the heating rates encountered in typical pulverised fuel applications (~10^5 °C/s), and considering the small size of the pulverised fuel particles, devolatilisation is a rapid process and it is measured in milliseconds (for Pittsburgh coal at 1427°C devolatilisation times were measured as 6 to 12 ms in a range O_2/N_2 mixtures (Shaddix and Molina, 2009), in contrast with char combustion which may require several seconds to complete).

The volatile matter content of coal is routinely measured by the proximate analysis at 950°C (which is comparable to pulverised fuel conditions), but at relatively low heating rates. As the volatile release depends significantly on the encountered heating rates (Fletcher and Hardesty, 1992), specification of the dimensionless 'high temperature volatile yield' is necessary for CFD modelling. The coal characterisation experiments conducted by the IFRF found that for most high volatile coals, the high temperature volatile yield exceeds the value obtained during proximate analysis by up to 60% to 70% (Peters and Weber, 1997), but low and medium volatile coals do not exceed the proximate yield. Ideally high temperature volatile yield should be determined experimentally for each coal (Fletcher and Hardesty, 1992, Peters and Weber, 1997).

Volatile release is typically estimated based on Arrhenius rate expressions fitted to empirical devolatilisation data or by the use of network pyrolysis codes. The models available are as follows.

2.6.3.1 Constant Rate Model

This model assumes a single rate for devolatilisation, which remains constant from the onset of the devolatilisation until all the volatiles are evolved. Pillai (1981) recommends the appropriate value of 12 1/s for coal combustion. However, as the rate of devolatilisation increases with the particle temperature (Fletcher and Hardesty, 1992), the use of more complex models is necessary to obtain realistic results.

2.6.3.2 Single Rate Model

This model assumes that the volatile release is first order dependent on the amount of volatiles left in the particle:

$$\frac{dV}{dt} = k(v^* - v)$$

The rate of devolatilisation is related to the particle temperature and it is expressed in the form of Arrhenius expressions:

$$k = Ae^{-E/RT}$$

The pre-exponential factor and the activation energy are determined by best fit approach (plotting the log of empirically obtained reaction rates against $1/RT$).

A limitation of this model is that these constants are specific to the type of coal and also to the combustion conditions, and thus have to be determined empirically at heating rates relevant to pulverised fuel combustion (typically at 10^5°C/s).

2.6.3.3 Two Competing Rates

The volatile release is described by two reactions with different rates, both of which compete for the coal available:

$$Coal \overset{k_1}{\rightarrow} Volatile_1 + Residue_1$$

$$Coal \overset{k_2}{\rightarrow} Volatile_2 + Residue_2$$

where the rates are expressed as:

$$k_1 = A_1 e^{-E_1/RT}$$

$$k_2 = A_2 e^{-E_2/RT}$$

Kobayashi *et al*. (1977) recommended setting the yield of the first (slow) reaction, y_1, to the proximate volatile content of the coal, and the second (fast) reaction, y_2, to 1.

The low yield reaction is favoured at low temperatures and high yield at higher temperatures. Therefore this model takes the effect of increasing the heating rate into consideration on predicting the ultimate volatile yield. However a comparison of one and two step devolatilisation models by Fletcher and Hardesty (1992) found that using the coefficients of Kobayashi resulted in poor predictions compared against experimental data, but coefficients proposed by Ubhayakar *et al*. (1976) agreed more closely with the data. However the constants in these models are still dependent on the coal type, thus experimental measurements are still necessary, and limit its application by the availability of such data.

2.6.3.4 Network Pyrolysis Models

Alternatively these rates can be estimated using network codes, such as FG-DVC (Functional-Group Depolymerization, Vaporization, Crosslinking), FLASHCHAIN or CPD (Chemical Percolation Devolatilisation). They are based on the description of the structural network of coal, and if measurements of these properties are available then these network codes can be used as pre-processor to estimate the constants required by singe and two competing rate models (Williams, 2002). For a detailed description of the former two models, see Smith *et al*., 1993; Solomon and Fletcher, 1994; and Niksa, 1996. The CPD model is available in FLUENT.

2.6.3.5 CPD Model

This model was developed at Sandia National Laboratories and describes the devolatilisation rates based on the chemical and physical transformations of the coal structure. It considers the parent coal as a network of chemical bridges, which connect the aromatic clusters. As a result of pyrolysis, these bridges are cleaved to form light gases, which having low vapour pressures, escape the particle at the early stages of devolatilisation, and heavier tar precursors which remain in the lattice for longer and vaporise at later stages to form tars. The CPD code models this process by assigning Arrhenius type rates to these processes. These rates are shown to be independent of coal type and thus do not require measurements (which would have to be carried out at temperatures, heating rates and oxidising atmospheres appropriate to the modelled conditions). A number of structural parameters still have to be determined empirically using ^{13}C NMR spectroscopy (ANSYS Inc., 2013, and Fletcher & Hardesty, 1992). This is an expensive technique, but a collection of results for thirteen typically utilised coals is listed by ANSYS Inc. (2013). Alternatively the correlation of Genetti *et al*. (1999) can be used to estimate NMR data from the ultimate and proximate analysis of the coal.

Williams *et al*. (2007) found that the choice between the above models influences the predicted location of the flame front slightly.

2.6.3.6 Swelling

Swelling is an important phenomenon as it increases the diameter of the particle (thus the reactive surface available for the subsequent char combustion). It takes place during the devolatilisation process and its progress was found to be related to the extent of volatile evolution (Street *et al*., 1969):

$$\frac{d}{d_0} = 1 + (C_{sw} - 1)\frac{v}{v^*}$$

where C_{sw} is the swelling coefficient and it is determined experimentally.

Swelling ceases at the end of devolatilisation and the char particles burn approximately at a constant diameter, forming hollow spheres (so called cenospheres) in the process (Anson *et al.*, 1971).

2.6.4 Char Combustion

Towards the end of devolatilisation, when the particle temperature is sufficiently high and diffusion flux of volatiles away from the particle has decreased (allowing O_2 diffusion towards the particle to intensify) the combustion of char particles begins. This is a heterogeneous process, thus resulting in mass transfer between the two phases (solid char and gaseous mixture). Char combustion occurs on the surface, and thus first requires the absorption of the oxidant onto the char surface, where recombination takes place, forming CO and CO_2. The products of combustion then diffuse away from the char surface.

When char oxidation is considered, it is generally modelled as a two step reaction, assuming that the carbon oxidises to form CO on the particle surface and this CO is added to the gas phases through source terms:

$$C_{(S)} + \frac{1}{2}O_2 \rightarrow CO \quad \Delta\widehat{H}_c = -110.52\, kJ/mol$$

$$C_{(S)} + O_2 \rightarrow CO_2 \quad \Delta\widehat{H}_c = -393.51\, kJ/mol$$

The heat of formation of CO is assumed to be liberated entirely onto the particle, where the heat of combustion of CO is added to the gas phase enthalpy. This is based on Baum and Street’s (1971) calculation, which predicted that a 50 μm particle burning at 1000°C at O_2 concentrations between 10-21%, less than 6% of the CO is burnt within a distance of two diameters away from the particle. Although Peters and Weber (1997) suggest that at higher temperatures the fraction of carbon reacting in the close vicinity of the particle is increased.

The rate at which the chemical processes take place (oxidiser absorption to the surface, recombination, and diffusion of products away from the particle) is a function of the particle temperature, due to the dependence of the surface reaction on the Arrhenius term. Whereas the diffusion of the oxidiser to and products away from the surface is only weakly dependent on temperature (Griffiths and Barnard, 1995).

Thus at low temperatures, the rate of combustion is limited by chemical kinetics. This temperature region is called Zone I (illustrated in Figure 2.6). At higher temperatures, the chemical reaction rate is increased, and the diffusion rate of O_2 towards the particle surface becomes significant (Zone II). Whilst at very high temperature the chemical rate is sufficiently high that the combustion is limited only by the rate at which the O_2 diffuses towards the particle (Zone III).

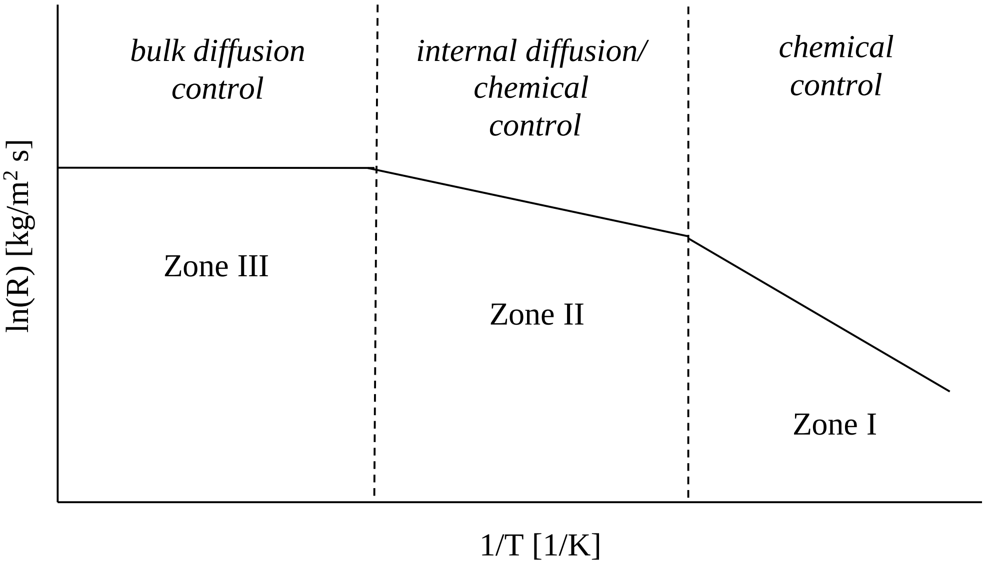

Figure 2.6. Schematic of the combustion regimes.

The transition temperature between these zones is a function of coal char reactivity, as well as the particle size. Typically very small particles never burn under diffusion control alone, whereas combustion rates of particles > 10 mm are limited by diffusion alone.

The reactivity of coal chars is a function of the parent coal, thus reactive brown coal chars burn at Zone I conditions up to approximately 377°C, whereas less reactive anthracite chars may burn under chemical control up to about 527°C (Griffiths and Barnard, 1995). However, Baum and Street (1971) concluded that in the majority of pulverised fuel applications char particles burn under Zone II conditions.

For modelling purposes the onset of char combustion is only initiated after completion of the devolatilisation process. A number of different approaches exist for char combustion modelling, which are discussed below.

Until the 1970s, mathematical modelling considered the char particles as spheres of constant density, the diameter of which reduced as a function of the carbon burnout.

However, as illustrated by Figure 2.7, char particles burn approximately at a constant diameter, forming hollow spheres (so called cenospheres) in the process (Anson *et al*., 1971). Thus, Baum and Street (1971) developed their model, which took this into account.

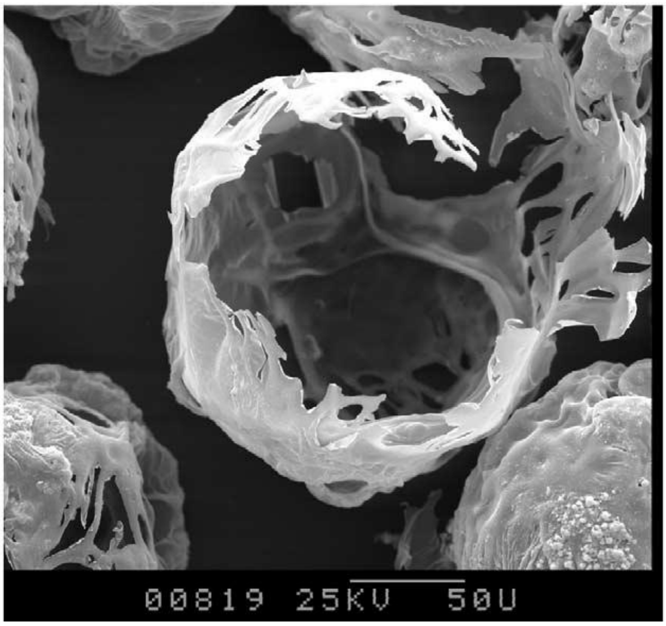

Figure 2.7. SEM of Thosby char produced in a drop tube furnace (DTF) at 1377°C and 250 ms at 5% O_2 (Williams *et al*., 2002).

2.6.4.1 Diffusion Limited Model

A simplified version of their approach is the diffusion limited model, which assumes that the rate of char combustion depends only of the diffusion of O_2 onto the particle surface. The particles are assumed to burn at a constant diameter with decreasing bulk density (thus increasing the porosity). The rate of mass release is governed by:

$$\frac{dm_p}{dt} = -4\pi d_p D_{i,m} \frac{Y_{OX} T_\infty \rho}{S_b (T_p + T_\infty)}$$

This approach assumes that the diffusion of the oxidant is the rate determining step (Zone III), and thus there is no need for experimental determination for the Arrhenius rates of surface combustion. However, neglecting these rates means that the effect of chemical control is neglected as well, and as Zone II conditions are dominant in pulverised fuel combustion, the effects of chemical kinetics have to be included.

2.6.4.2 Kinetics/Diffusion Limited Model

The char combustion model of Baum and Street (1971) determines the rate of char combustion based on both bulk diffusion and chemical kinetics rates, according to:

$$\frac{dm_p}{dt} = -A_p p_{Ox} \frac{D_0 \mathscr{R}}{D_0 + \mathscr{R}}$$

where A_p is the surface area of the particle, p_{OX} is the partial pressure of the oxidant in the surrounding mixture, D_0 is the diffusion limited rate and $\mathscr{R}$ is the chemical kinetics rate, which are evaluated as:

$$D_0 = C_1 \frac{\left[(T_p + T_\infty)/2\right]^{0.75}}{d_p}$$

$$\mathscr{R} = C_2 e^{-(E/RT_P)}$$

where C_1 and C_2 are the binary diffusion coefficient of O_2 in the air and are the Arrhenius pre-exponential factor, respectively.

The weighting built into the rate equation means that it will be applicable to Zone I and III conditions as well, since when either D_0 or $\mathscr{R}$ assumes a large value its effect its negated on the overall rate of mass loss.

The disadvantage of this approach is that the Arrhenius constants of the chemical reaction have to be determined experimentally, in order for each coal to be modelled. However, this also means that the effect of the internal surface area and pore diffusion are also included in this rate. This is because C_1 incorporates the surface factor, ψ, defined as the area of the reacting surface over the external surface area of the particle, which is adjusted to match the experimental measurements.

However, Williams *et al*. (2000) noted that this model still neglects a number of important characteristics that influence the char combustion, namely (i) changes in the pore structure during combustion, (ii) Stefan flow, (iii) particle fragmentation, (iv) effect of char petrographic structure and impurities on the reactivity, and (v) continued change in the char surface area.

2.6.4.3 Intrinsic Model

Schmidt's Intrinsic (1982) model is similar to the previous model in assuming the importance of both the bulk diffusion and chemical kinetics rates. It also incorporates the effects of the pore structure (porosity and pore radius) on the internal diffusion rate of the O_2 into the latter:

$$\mathcal{R} = \eta \frac{d_p}{6} \rho_p A_g k_i$$

where η is the effectiveness factor (the ratio of actual combustion rate if no pore diffusion resistance existed), A_g is the specific internal surface area, and k_i is the intrinsic reactivity expressed in Arrhenius terms. The effectiveness factor incorporates the effect of Knudsen diffusion, thus taking the internal pore structure into account.

The continued change of particle size and density, are also expressed considered by this model (as a function of burnout).

Backreedy *et al*. (2006) noted that the specific internal surface area, A_g, increases during char combusting. This is due to the swelling of vitrinite compounds (whereas inertinite does not contribute to swelling). Therefore they proposed to express the changes in the original A_g as a function of carbon burnout (using a quadratic equation fitted to DTF experimental data).

In order to make their empirical equation applicable to different types of coals, a maceral correction factor, f_{mac}, was defined in terms of the inertinite and vitrinite content of the parent coal.

Another important process influencing the char burnout is the thermal annealing of the particle during char combustion, which decreases the reactivity as a function of temperature and time (Hurt, 1998). Therefore Backreedy *et al*. (2006) introduced a simple annealing factor, f_{ann}, into the overall rate equation, which is described as a function of particle temperature, carbon burnout and particle diameter. The overall char burnout rate thus takes the form:

$$\frac{dm_p}{dt} = f_{ann} f_{mac} \left(\alpha A_g\right) \frac{\rho_p R T_\infty Y_{Ox}}{M_{W,Ox}} \frac{D_0 \mathcal{R}}{D_0 + \mathcal{R}}$$

where D_0 is evaluated based on the correlation used by Baum and Street's (1971) kinetics/diffusion limited model, and $\mathcal{R}$ is based on Smith's (1982) intrinsic reactivity rate equation.

Thus the intrinsic model with the above modification has been an accepted method for modelling char combustion by the ETII group for both conventional air-blown combustion (Backreedy *et al.*, 2006, Ma *et al.*, 2009, Pallarés *et al.*, 2007) and oxy-fuel combustion (Edge *et al.*, 2011b).

Another recent method for char combustion predictions is the carbon burnout kinetics (cbk) model, which is a variation of the intrinsic model and was designed to predict the carbon burnout and resulting carbon content of the flash based on temperature and O_2 concentration histories. Modifications to the original cbk model have been proposed to include the effects of morphological changes in char structure, maceral composition, char annealing and the effect of char gasification (Edge *et al.*, 2011a).

Due to the complexity of coal combustion, quantitative predictions of burnout is shown to be inaccurate, when the reaction of char with species other than O_2 is not included in the models, e.g. H_2O, CO_2 (Stopford, 2002), which is especially important in the case of oxy-fuel combustion where the partial pressure of these is significantly increased due to the recycle and the elimination of N_2. Blending, applied routinely nowadays, increases the uncertainties about char burnout predictions further.

2.6.5 Volatile Combustion

As the products of devolatilisation (tars and lighter volatile gases), diffuse away from the particle, they react with the oxidiser species and break to form lighter hydrocarbons and intermediate species (CO, H_2, and also radical fractions (e.g. OH-, H-, CH_x-)). In subsequent steps, these oxidise to form CO_2 and water vapour. At high temperatures, a significant amount of CO is present in the flue gases (even if there is adequate amount of O_2 available), as CO is an equilibrium product of combustion. Whereas at lower temperatures, the exit CO concentration is negligible (provided there is enough oxidiser present). Besides C, H and O, coal contains a wide range of other compounds (S, N, Cl, K etc.), many of which react during combustion to form pollutant and corrosive species, including SO_x and NO_x, HCl, KOH and KCl.

Combustion is an exothermic process, which increases the temperature of the gas mixture and consequently heats the particles, thus enhancing char combustion and shaping the in-furnace heat flux profiles. This heat release rate is dictated by the rate at which the volatiles are consumed, therefore modelling of volatile combustion is also crucial to the success of combustion models.

As noted by Magnussen and Hjertager (1977) in turbulent non-premixed flames, the chemical reactions may assumed to be very fast, and therefore the rate of homogeneous combustion is determined by the rate of mixing between the oxidiser and reactant species on the molecular scale (eliminating the need to calculate complex and often ambiguous chemical rates). In diffusion flames, the fuel and oxidiser occur in separate eddies, and their intermixing is determined by the rate of dissipation of these eddies. The fuel and the oxidiser are both fluctuating quantities, with a relationship between their mean concentration and their fluctuations. Magnussen and Hjertager (1977) proposed that their mean concentration is adequate to express the rate of dissipation. Therefore the reaction rate is taken as the lower value of the following equations:

$$R_{i,r} = \nu'_{i,r} M_{w,i} A \rho \frac{\varepsilon}{k} min_{\mathcal{R}} \left(\frac{Y_{\mathcal{R}}}{\nu'_{\mathcal{R},r} M_{w,\mathcal{R}}} \right)$$

$$R_{i,r} = \nu'_{i,r} M_{w,i} A B \rho \frac{\varepsilon}{k} \frac{\sum_R Y_P}{\sum_j^N \nu''_{j,r} M_{w,j}}$$

where $R_{i,r}$ is net rate of production of *i* due to reaction *r*, Y_P is mass fraction of product species, Y_R is mass fraction of reactant species, v' and v'' are the stoichiometric coefficients of reactants and products, respectively, and *A* and *B* are constants 4 and 0.5, respectively.

The reaction rate will depend on the local concentration of the reactants and will be proportional to the inverse of the large eddy mixing time scale, k/ε. Therefore, volatile combustion rates depend on performance of the turbulence model. Consequently the accuracy of the above models can be increased by the use of more advanced turbulence models. Therefore the use of LES modelling is recommended.

The second equation is significant during premixed combustions, where fuel and O_2 occur in the same eddies but separated by eddies containing the hot product species. In cases when the concentration of the hot product gases are low the effect of their dissipation on the combustion rate is taken into account by the second equation (Magnussen and Hjertager, 1977).

This means that the combustion rate is independent of the temperature (as infinitely fast kinetics is assumed), but also when combustible gases are present the combustion does not require an ignition source. Therefore the EDM is not suitable for premixed combustion when the burner annuli are included into the geometry, as the EDM would initiate combustion as soon as the reactants enter the domain (for this situations the finite rate/eddy-dissipation model is recommended).

In most combustion situations, the assumption of infinitely fast chemistry is justifiable, with the exception of situations when flame ignition and extinction is investigated via unsteady simulation, and also when intermediate species do need to be taken into account. For example, when predictions on pollutant formation are required, as these may involve complex intermediate steps.

The Eddy-Dissipation Concept (EDC) is a modified version of the EDM, and also introduced by Magnussen (1989), considering non equilibrium chemistry (i.e. includes the effect of chemical kinetics). It assumes that the reaction takes place over a small time scale, in small turbulent structures, called fine scales, and the rate is dictated by an Arrhenius expression. This model is suitable for assessing formation and destruction of pollutants in modern combustors (Schmidt *et al*., 2004).

A distinct type of homogeneous combustion modelling is the use of statistical averaging techniques, using probability density functions (PDF), with an assumed shape of the probability curve derived from experimental data. The system is modelled as two streams of fuel and oxidiser, the PDF table is pre-processed, and used as a 'look up' reference during the simulation to determine the rate of the combustion based on the mixture fraction. With the assumption of equilibrium conditions the species fractions, temperature and density are uniquely related to the mixture fraction (ANSYS Inc., 2013).

2.7 Pollutant Formation

Emissions for electricity generation from coal fired power plants are covered under the Large Combustion Plant Directive (LCPD) 2001/80/EC, setting emissions limits for NO_x, SO_x, CO and particulate matter, due to their detrimental effect on the environment. Therefore emissions predictions of these compounds are vital in combustion modelling applications.

2.7.1 Nitrogen Oxides

Nitrogen monoxide (NO) is a major pollutant generated during pulverised coal combustion, a small proportions of this is converted to nitrogen dioxide (NO_2) in the flue gases and together they are referred to as NO_x. Eventually all the NO is converted to NO_2 in the atmosphere, where it may cause acid rain, which is dangerous to plant life, water systems, the built environment and human health. The formation of N_2O is favoured at low temperatures and may be significant in fertilizer production, but it is a negligible pollutant when pulverised fuel combustion is considered.

In pulverised coal applications the most important methods of NO_x formation are the oxidation of molecular nitrogen (thermal NO) and oxidation of nitrogen containing compounds present in the char (fuel NO). The latter accounts for approximately 70-80% of the total NO_x formation, and the letter to around 20% (Edge *et al.*, 2011a).

Thermal NO formation is due to the oxidation of N_2 molecules in air. At high temperatures, O_2 molecules dissociate to O radicals, which in turn attack the N_2 molecules to form NO and N radicals (this reaction is the rate controlling step). The N radicals than reacts with an O_2 molecule to form more NO and an O radical (de Nevers, 2000). The rate of this process is exponentially related to temperature.

$$\mathrm{N_2 + O \xleftrightarrow{k_{1f}, k_{1b}} NO + N}$$

$$\mathrm{N + O_2 \xleftrightarrow{k_{2f}, k_{2b}} NO + O}$$

These above two reactions are usually referred to as the Zeldovich mechanism. In fuel rich and near stoichiometric air-fuel mixtures the presence of the OH radicals also becomes important.

$$\mathrm{N + OH \xleftrightarrow{k_{3f}, k_{3b}} NO + H}$$

Prompt NO is formed in fuel rich regions of the flame, where N_2 is attacked by hydrocarbon radicals to form cyanide and hydrogen cyanide, according to the equations:

$$\mathrm{CH + N_2 \rightarrow HCN + N}$$

$$\mathrm{C + N_2 \rightarrow CN + N}$$

The cyanides are then oxidised to NO after the fuel rich zone (de Nevers, 2000). The contribution of prompt NO to total NO_x formation is small (~5%) (Edge *et al.*, 2011a).

Fuel NO is a result of the chemically bound nitrogen in the pulverised fuel. Part of this nitrogen is released during devolatilisation (volatile-N) to the gaseous phases in the form of hydrogen cyanide (HCN) and ammonia (NH_3), which after subsequent oxidisation steps can be converted to NO. The remaining fraction of the nitrogen in the char (char-N) is released via heterogeneous reactions to the cyanide/amine pool, where they can be oxidised forming NO. However if the N containing intermediate species evolve in reducing atmospheres the conversion of the reduction of these species to molecular N_2 is promoted (Figure 2.8). This mechanism is used for NO_x reduction in burner or fuel staging applications, where fuel rich zones with very low O_2 concentration are produced near the burner where devolatilisation is taking place.

Another form of NO reduction technique takes advantage of the reburn mechanism, by recycling NO formed downstream of the flame to the root region via internal recirculation patterns. This NO then can be reduced to N_2 by other volatiles or recycled back to intermediate volatile-N products through heterogeneous char surface reactions (Hill and Smoot, 2000).

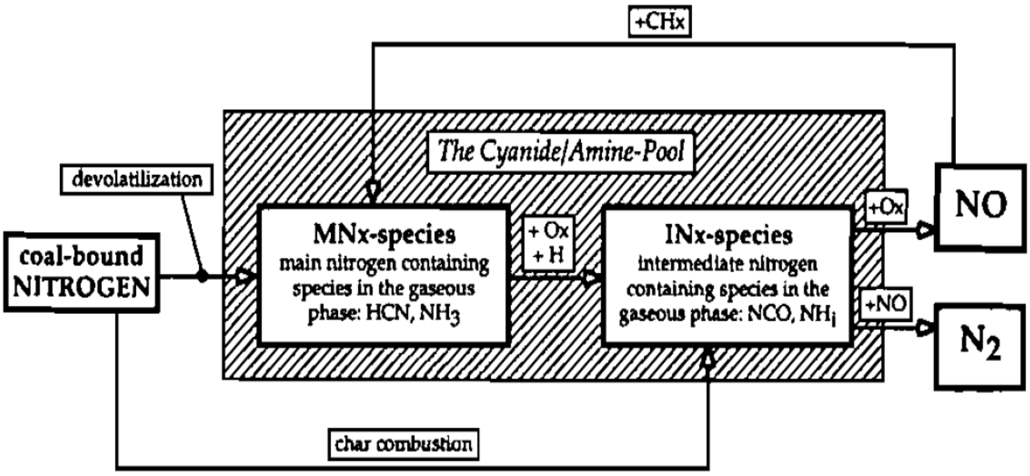

Figure 2.8. The simplified fuel-NO formation and reduction mechanisms – MN_x refer to the main and IN_x to the intermediate nitrogen containing species (Peters and Weber, 1997).

Predicting accurately the distribution of fuel N between the char and volatiles is important, as they release nitrogen species at different regions of the flame. This distribution depends on the particle temperature, heating rate, coal type and particle size. Network codes, such as FG-DVC or CPD models, may be used as pre-processors to determine the N partitioning between volatiles and char.

The rate of fuel NO formation and destruction depends on the concentrations of the nitrogen containing species and on the temperature. Where formation reaction is also dependent on the concentration of the oxidiser, and the reduction reaction on the amount of NO present (Backreedy *et al*., 2006).

As the amount of NO is negligible compared to the total gas phases, its modelling may be considered in a post-processing step, where temperature contours and concentrations of major species had been calculated beforehand.

NO_x is controlled primarily by the application of low NO_x burners, or application of over-fire air to create controlled rich and lean zones, both of which are characterised by lower than stoichiometric temperatures and thus lowering thermal NO_x formation which is dependent exponentially of temperature. However it must be noted that this comes with a loss of efficiency in the form increasing the amount of unburned carbon in ash. As the lower flame temperature zones decrease the radiative heat flux to the particles, the carbon burnout is reduced (Williams *et al*., 2000). This results in decreased combustion efficiency and reduced sale value of ash.

Other control methods are the use of auxiliary fuel (e.g. pulverised tyres, biomass, natural gas) as reburning agents or the injection of ammonia or urea with selective non-catalytic reduction (SNCR) or selective non-catalytic reduction (SCR) techniques.

2.7.2 Sulphur Oxides

The sulphur oxides (SO_x) emitted from pulverised fuel plants may cause acid rain. SO_x is a function of the sulphur content of the coal and this is released as H_2S during devolatilisation and subsequently oxidised to SO_2. A small proportion of this is then converted to SO_3 in the lower temperature zones of the flue ducts, where it can combine with H_2O to form H_2SO_4. SO_x may be controlled by using low sulphur content coals or the application of flue gas desulphurisation (FGD).

2.7.3 Soot

Radiative heat transfer is greatly enhanced by the presence of soot in pulverised coal flames, and it is also determining factor of flame luminosity. This is due to the strong radiative properties of soot, and its large surface area compared to coal particles. Its formation is controlled by the local temperatures and air-fuel ratios. The main precursors to soot formation are the polyaromatic hydrocarbons (PAH) (contained in coal tars) and acetylene (C_2H_2). Surface growth on these, and their subsequent coagulation results in the formation of the spherical soot particles.

2.8 Heat Transfer Modelling

In pulverised fuel boilers, radiation is the major method of heat transfer due to the high in-furnace temperatures (caused by the fourth power dependence of radiation on the absolute temperature), and the high concentration of agents with strong radiative properties. These include the coal particles, char, ash, soot, and the tri-atomic combustion products of CO_2 and H_2O. Therefore the accurate modelling of the radiative processes from each of these is key for successful furnace models.

The radiative transfer equation (RTE) is solved using the Discrete Ordinates (DO) model (Murthy *et al*., 1998) and the radiative properties of the gases were calculated using the Weighted Sum of Gray Gases (WSGG) approach (Hottel *et al*., 1967; Smith *et al*., 1982). The correlation proposed by Smith *et al*. (1982) has been successfully applied in numerous CFD studies involving the combustion of coal and biomass in air (see, for example, Ma *et al*., 2007; Ma *et al*., 2009).

In oxy-fuel combustion, the increased presence of strongly absorbing CO_2 and H_2O (if a wet recycle is used), adds further complications. This is because the radiative properties of the overall gaseous mixture is increased significantly, and the models developed for combustion in air are shown to be inaccurate (Wall *et al*., 2009).

The full spectrum correlated k-distributions (FSCK) model, developed by Porter *et al*. (2010), has been shown to provide more accurate results for a typical oxy-fuel FGR environment compared to the WSGG model. However, a major limitation in implementing the FSCK model is the level of computational resources required. Therefore a number of studies have proposed new correlations for the WSGG model under oxy-fuel conditions (Johansson *et al*., 2010; Johansson *et al*., 2011; Kangwanpongpan *et al*., 2012; Krishnamoorthy *et al*., 2010).

2.9 Turbulence Modelling

In turbulent regimes, the large recirculating eddies induce finer and finer ones and these fine recirculating structures enhance the intermixing of reactants and therefore their rates of combustion. Thus turbulence will influence local species concentrations, temperature gradients, and so the heat fluxes to the steam banks, carbon burnout as well as pollutant formation inside the furnace (Tian *et al.*, 2009). Therefore for accurate modelling of combustion, it is imperative to predict the turbulence inside the computational domain.

The transport equations discussed previously describe the combustion phenomena explicitly in coal combustion problems. However, they cannot be solved analytically, and therefore the use of numerical methods is required, namely Reynolds Averaged Nervier-Stokes (RANS), Large Eddie Simulations (LES) and Direct Numerical Simulations (DNS). In the order listed, they resolve the turbulent flow to smaller and smaller scales and thus provide more and more accurate solutions. However each step drastically increases the requirement for computational resources. Thus a trade-off between accuracy of solution and requirement of computational recourses has to be made, and the choice of technique will depend on the type of the problem and level of accuracy required from the solution.

2.9.1 Reynolds Averaged Navier-Stokes (RANS)

Due to limitations in computational power, RANS is the preferred choice in most commercial problems, and it produces a solution with a sufficient degree of accuracy to be suitable in most engineering applications. The fluctuating properties of the flow are broken up into mean and fluctuating terms:

$$f = \bar{f} + f'$$

where $\bar{f}$ and f' are the mean and fluctuating parts of f, respectively, and $\bar{f}$ is defined as:

$$\bar{f} = \frac{1}{\mathrm{\delta t}} \int_0^{\delta t} f(t) dt$$

The mean of the fluctuating part, f', is defined as zero and when considering a large enough time interval the relative value of these fluctuations becomes very small. When they are substituted into the Navier-Stokes equation, many of the additional terms become zero, except one term which is a product of the fluctuating velocities (called the Reynolds Stresses). This produces the time averaged Navier-Stokes equation. The product of the fluctuating velocities is nonlinear by nature and cannot be solved analytically and therefore it has to be modelled.

There is a wide range of turbulence models developed to solve this problem of closure, from which the most widely used is the k–ε model.

This model solves two transport equations, one for the turbulent kinetic energy, k, and one for its dissipation, ε. The turbulent kinetic energy of the flow is dissipated in the fine eddies due to the viscous stresses between boundary layers and it is converted to heat. The coefficients were derived empirically, and are valid for fully turbulent flows only. This is true for most combustion environments, which are characterised by high Reynolds numbers (typically above 10^5).

The standard k–ε model is well established and the most widely validated turbulence model. It is proven to be robust, computationally inexpensive and it is regarded as easy to converge.

However a major disadvantage of this mode is that it assumes isotropic shear stresses, which, in reality, is not correct, and can lead to erroneous resolution of flow patterns, especially when the flow is characterised by:

- strong swirls, or curved boundary layers,
- rotating flows,
- or flows in fully developed non circular ducts.

Another problem associated with the model is that it over predicts the spread of jet flames (Versteeg and Malalasekera, 2007).

The RNG k–ε model is a modification of the standard model, based on extensive mathematical derivation, and it is found to be more suitable for strongly swirling flows and regions near separation (ANSYS Inc., 2013, and Versteeg & Malalasekera, 2007). Thus, as most burners used in the furnaces of power station inject swirled combustion air, the use of the RNG model is recommended even though it requires 10-20% more CPU time than the standard k–ε turbulence model. Also the RNG method is less diffuse than the standard k–ε turbulence model, and when steady state modelling is applied it is more prone to instabilities. In such cases, switching to the standard $k - \varepsilon$ models may be necessary, as numerical diffusion has a stabilising effect on the solution process (as experienced during the 2D modelling work on the IFRF Furnace no. 1 confirmed the existence of this problem).

The $k - \omega$ model replaces the equation for ε by modelling the turbulent frequency, ω, instead. It does not require the use of damping functions and offers better near wall predictions in low *Re* applications. However, it requires a fine resolution of the grid near the walls (which requires more computational power), and the application of this model is still limited by the isotropic assumption of shear stresses.

The Reynolds Stress Equation Model (RSM) overcomes the limitation of the isotropic assumption by modelling the directional effect of the Reynolds stresses. It solves six independent transport equations for the dynamic Reynolds stresses and an additional one for the dissipation of this scalar (as dissipation takes place in the small eddies, the assumption of isotropy of dissipation can be justified, requiring only one transport equation). It is regarded as the most general of the classical turbulence models, and therefore applicable to many different types of flow regimes (without requiring adjustments for each case). Thus it is suitable for flows with strong swirls, curved boundary layers, non-circular ducts, asymmetric channels, etc.

However the main disadvantage of this model is that it requires seven transport equations to be solved, thus increasing the requirements for computation resources. Furthermore, on average, it requires 50-60% more CPU time and 10-20% more memory compared to the standard k–ε and k–ω models. Thus the application of RSM requires lengthier solution processing time. Thus it is recommended to approximate the solution with a 2 equation model first and only then switching to the RSM because in this way the stability of the solution can be improved as well.

2.9.2 Large Eddie Simulations (LES)

The main shortcoming of all of the RANS models is that they describe all scales of the turbulent eddies by the same model. This is challenging as eddies of different scales behave differently. The large eddies, which extract energy from the mean flow and transfer it to smaller ones are highly anisotropic in nature and are influenced profoundly by the geometry of the confinement, the boundary conditions and the body forces. Whereas fully turbulent small eddies are isotropic in nature and behave uniformly. In LES, time dependent resolution of the large eddies is used, whilst small eddies are filtered out, and their effect on the large eddies is considered by applying sub-grid scale models. This method allows for better representation of the turbulence field and therefore suitable for studying the effect of large fuel rich eddies on the local pollutant formation. Therefore its use is recommended for oxy-fuel studies where pollutant formation is assessed. Also, the effect of higher CO_2 partial pressures on flame stability can also be examined, as LES is a time resolved approach. LES is also found to better predict radiation profiles emitted from the flame surface. Edge *et al*. (2011b) found that RANS modelling results in a smooth temperature profile along the flame edge, whereas LES produced much hotter local temperatures, due to resolution of large eddies convecting hot gases from the centre of the flame. This resulted in increased radiation profiles approaching the experimental results better than the RANS results. However, LES modelling requires significantly more computational resources (due to the time resolution approach) and therefore its use may be limited by the available computational resources.

2.9.3 Direct Numerical Simulations (DNS)

DNS solves the instantaneous NS equations without any modelling, solving the mean as well fluctuating flow properties, and thus obtaining exact time dependent solutions resolving every scale of the solution. However this requires very fine grids (to resolve the Kolmogorov length scales) and very small time steps (to resolve the fastest fluctuations). Therefore, in general, the demand on computational resources limits its use to fundamental research conducted on simple, one- or two-dimensional problems, and in commercial applications the use of DNS is prohibited by the limitations in the current computer technology.

Having outlined some of the major questions surrounding the principles of oxy-fuel combustion, the dissertation now sets out the experimental investigations that were performed.

Chapter 3

Experimental Facilities

3.1 Chapter Outline

This chapter focuses on the experimental facilities used to obtain the data that is presented and analysed in Chapters 4 and 5. First, it describes the experimental furnace, burner and other major sections of the rig. It then outlines the measurement techniques that were utilised during the experimental programme. The chapter concludes with a summary of the operating philosophy, presents the results of the fuel analysis and details the experimental parameters.

3.2 250 kW Combustion Test Facility

The 250 kW Combustion Test Facility (CTF) is part of the UKCCSRC PACT facilities. It is located near Sheffield in South Yorkshire. The CTF consists of a 250 kW down fired cylindrical furnace, capable of burning pulverised coal and biomass, under both air and oxy-firing conditions. It can also be operated on natural gas, which is used for preheating the furnace. The plant has a dedicated fuel feeding system, interchangeable coal/biomass burners; dedicated air and O_2/CO_2 metering skids; a temperature and flow monitored cooling water system for the furnace, flue jackets and a dedicated heat exchanger, a high temperature candle filter, an exhaust fan and a chimney. The plant is operated and monitored using a local Human-Machine Interface (HMI), which is connected to an industry standard SCADA system located in the control room. The monitoring interface was developed from P&I drawings of the system and it is shown in Figure 3.1.

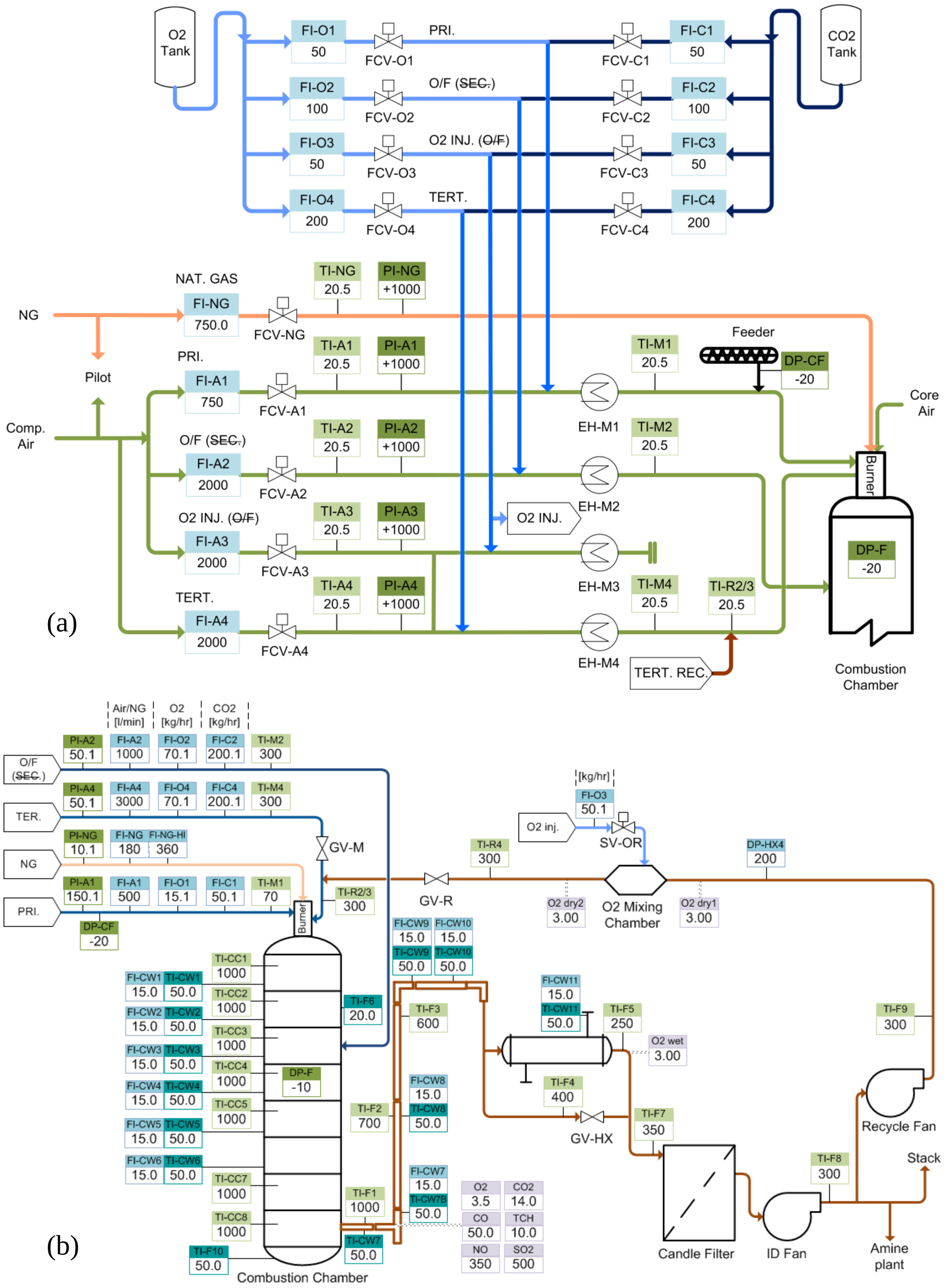

Figure 3.1. Schematic P&I Diagram used as screens on the HMI for online process monitoring, (a) oxidiser supply to the furnace, (b) main screen with all instruments on the furnace and flue sections, plus the major parameters from the oxidiser supply (values in boxes are for illustrative purposes only).

3.2.1 Furnace

The furnace body is 4 m long and it is made up of eight 500 mm long sections. The 8 furnace sections are lined with a 100 mm thick, lightweight alumina silicate refractory, which allows rapid heating, and thus steady state conditions to be reached sooner than in furnaces lined with refractory bricks. The outer and inner diameter of the sections are 1100 mm and 900 mm, respectively. The top section and burner quarl are cast from high density concrete, for its heat retentive properties which enhance flame stability. Viewing ports are installed in the top 3 sections of the furnace to allow for visual inspection of the flame.

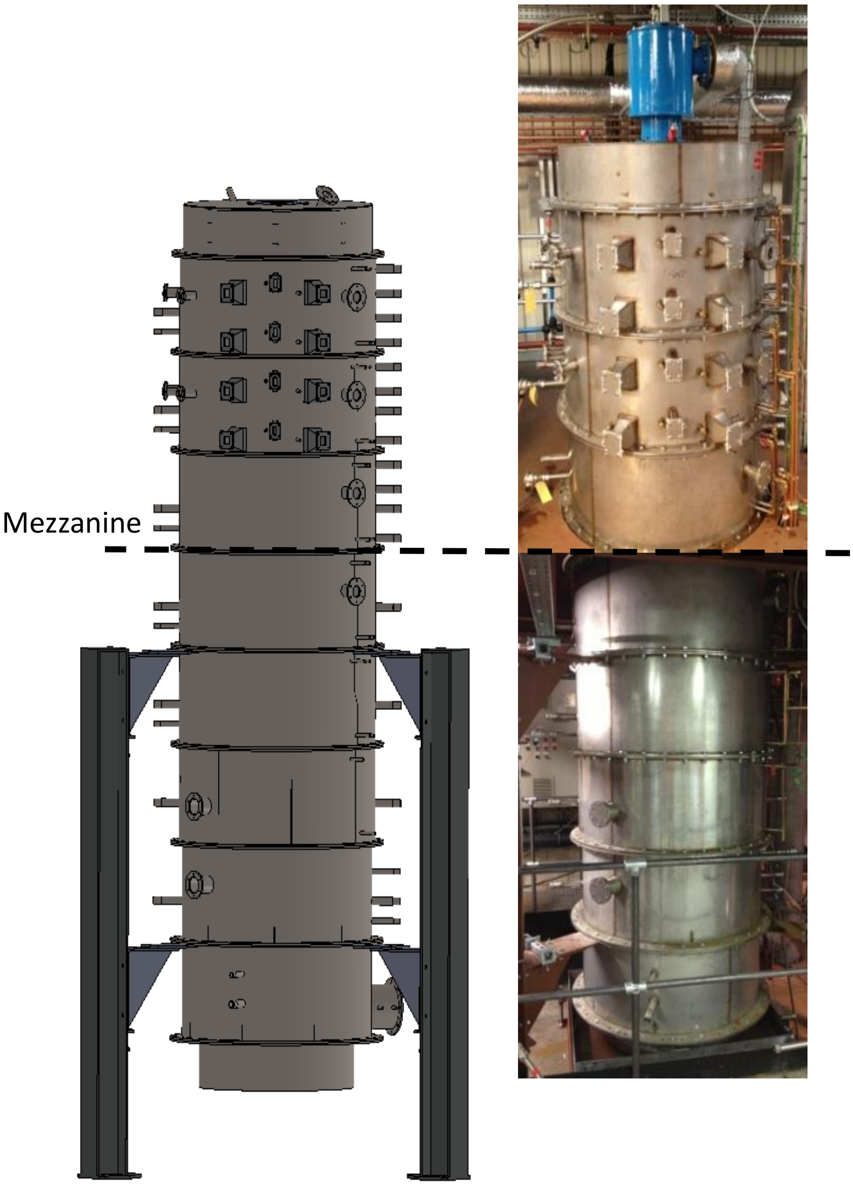

Figure 3.2. CAD drawing and photographs of the mezzanine and ground level sections of the furnace. All images are showing the front side of the furnace.

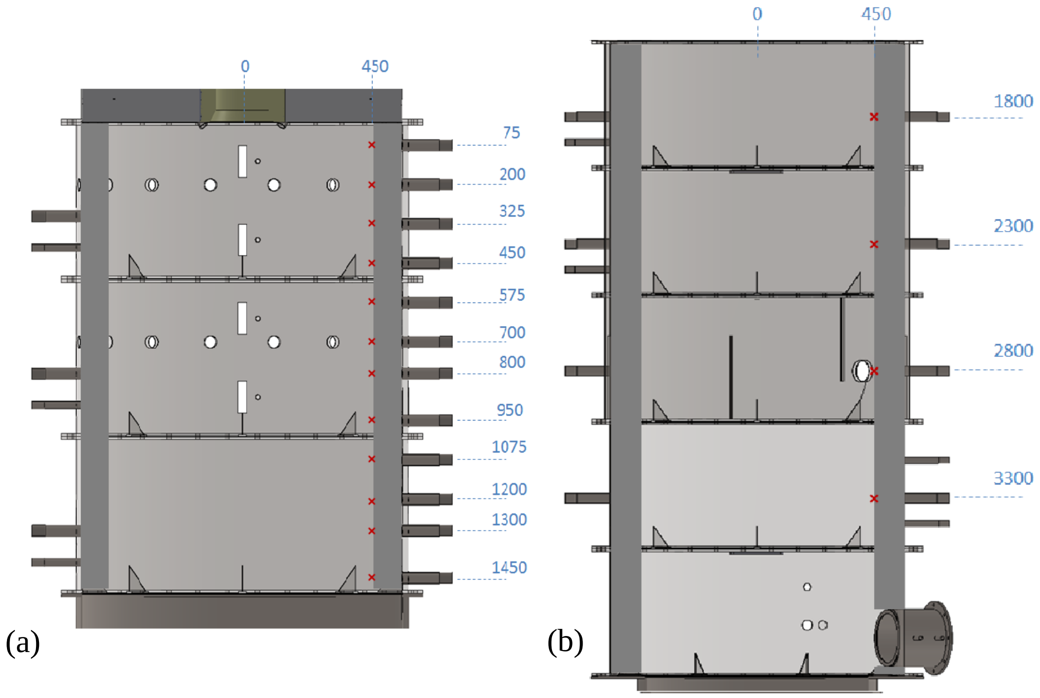

Figure 3.3. Measurement port locations along, (a) the mezzanine, and (b) ground level sections of the furnace.

Ports for in-furnace measurements are installed along the furnace. The first 3 sections along the flame are fitted with 4x38.1 mm (1.5”) ports each (RHS of Figure 3.3(a)), and the lower sections have one of these ports each (RHS of Figure 3.3(b)). Process thermocouples are installed at the 25.4 mm (1”) ports on the opposite side (LHS of Figure 3.3a&b).

The first 6 of the furnace sections are water cooled. The water temperatures out of these are measured individually, which allows heat transfer through the different sections of the chamber to be monitored. The bottom of the rig is sealed with a water tray which serves a number of purposes; to prevent the escape of combustion gasses whilst providing a means of pressure release and as a trap/quench for slag deposits and bottom ash. The flue gas is drawn from the bottom section of the furnace, approximately 4 m from the burner throat. The furnace pressure is balanced by the exhaust fan, maintaining the furnace below atmospheric pressure at -1 mbar to ensure safe operation. The extraction system can be operated in automatic mode to a set-point pressure measured directly from a tapping point in the furnace or in manual mode to a fixed exhaust fan speed.

3.2.2 Burner

The burner is a scaled version of a commercially available low-NO_x Doosan Babcock burner. It is mounted at the top of the furnace in a down firing arrangement. The primary annulus is used for introducing the pulverised coal and carrier gas, and the swirled secondary and tertiary annuli that delivers the rest of the oxidiser.

The burner has an internal air splitting system that provides both secondary and tertiary air feeds from a single air supply. The disadvantage of the inner air split system is that the amount of air entering through the secondary and tertiary annuli is not individually metered. However, this design was necessary due to the compactness of the burner. The determination of individual flows is possible using detailed CFD analysis using the geometry shown in Figure 3.4.

When the damper is fully pushed in (split position 0), the wedge shaped end of the slide pushes into the tertiary annuli, sealing it from the combustion air, which then enters the furnace only thought the secondary annuli. As the split slide is pulled outwards, the oxidiser is allowed to enter the tertiary annulus though increasing cross sectional area (due to the wedge shaped tip). Furthermore, as the slide is pulled outwards it also obstructs the triangular ports through which the air enters the secondary annulus, and therefore sending more of the combustion air through the tertiary annuli. Figure 3.4 shows the split slide fully pulled out, with the wedge shaped end completely blocking the triangular openings to the secondary, thus producing an extreme setting of all the combustion air entering through the tertiary.

The gas flame is ignited using a premixed torch igniter. Once lit, a flame safeguard control system provides supervision for the natural gas flame, monitored by a UV sensor.

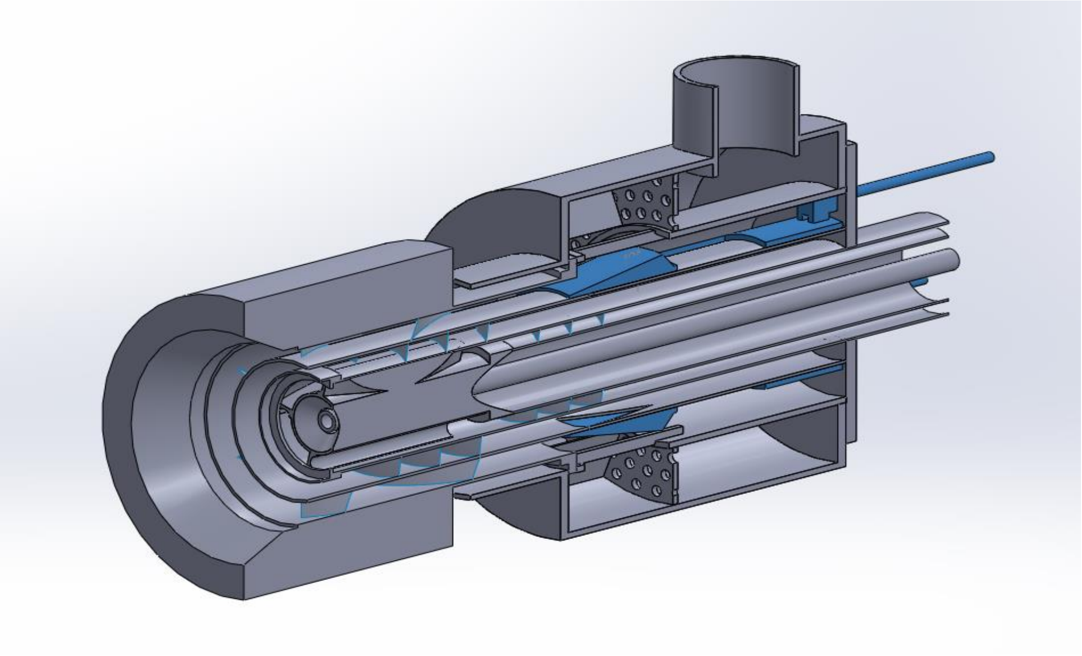

Figure 3.4. CAD drawing of the burner, with the Secondary/Tertiary split slide highlighted.

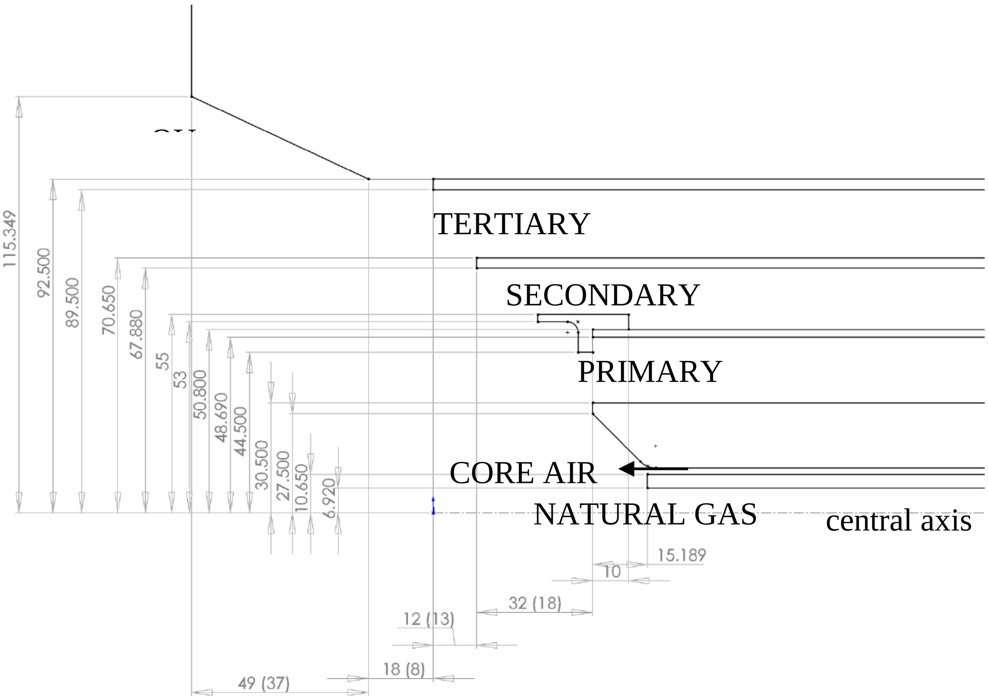

Figure 3.5 Burner annuli and quarl dimensions used.

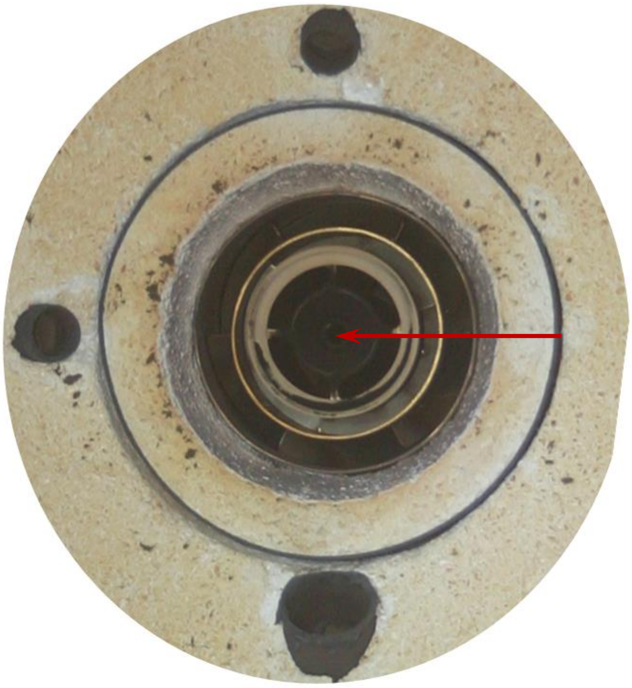

Figure 3.6. Photograph of the burner throat and quarl taken before the experimental trials. The red arrow denotes the access side for the in-furnace measurements of suction pyrometry and heat flux. This is in line with two of the four coal concentrators in the primary annulus.

3.2.3 Oxidiser Supply

The combustion air is supplied by a compressor at 6-7 bar pressure. The supply line is fitted with a cooler, 2 coalescing filters and a carbon filter, which removes both the oil contamination and moisture from the air supply. The primary and combined air stream of the Secondary and Tertiary air are provided by separate lines fitted with thermal mass flow meters linked to flow control valves. This provides precision control of the air streams. Also the mass flow meters are linked to the PLC which enables the flow set-points to be set and individual air flows to be recorded on the SCADA system.

The primary air line is connected to a coal/biomass feeding system to pick up the solid fuel and then the primary oxidiser and fuel are fed directly to the burner. The secondary/tertiary line provides the rest of the combustion air. It is fed to the burner through the wind box and the feed is split into separate secondary and tertiary streams internally within the burner. The ratio of the split can be controlled via a movable slide, and can be positioned to offer optimum NO reduction for acceptable carbon in the ash (CIA).

For oxy-fuel operation, the O_2 and CO_2 are supplied from liquid storage tanks at a stable pressure of 5 bar. The O_2 and CO_2 mixtures are provided to the furnace by a dedicated O_2/CO_2 mixing skid (oxy-skid) fitted with Coriolis mass flow meters and pneumatically actuated flow control valves. The Primary and secondary/tertiary oxidiser delivery lines of the air- and oxy-skids are joined (Figure 3.7), which allows a controlled, gradual switchover from air to oxy-fuel operation.

To verify the mixed gas O_2 content, the lines are fitted with Hitech Instruments G610 series O_2 analysers, which use galvanic cell technology and can measure O_2 concentrations from 0.01 to 100%.

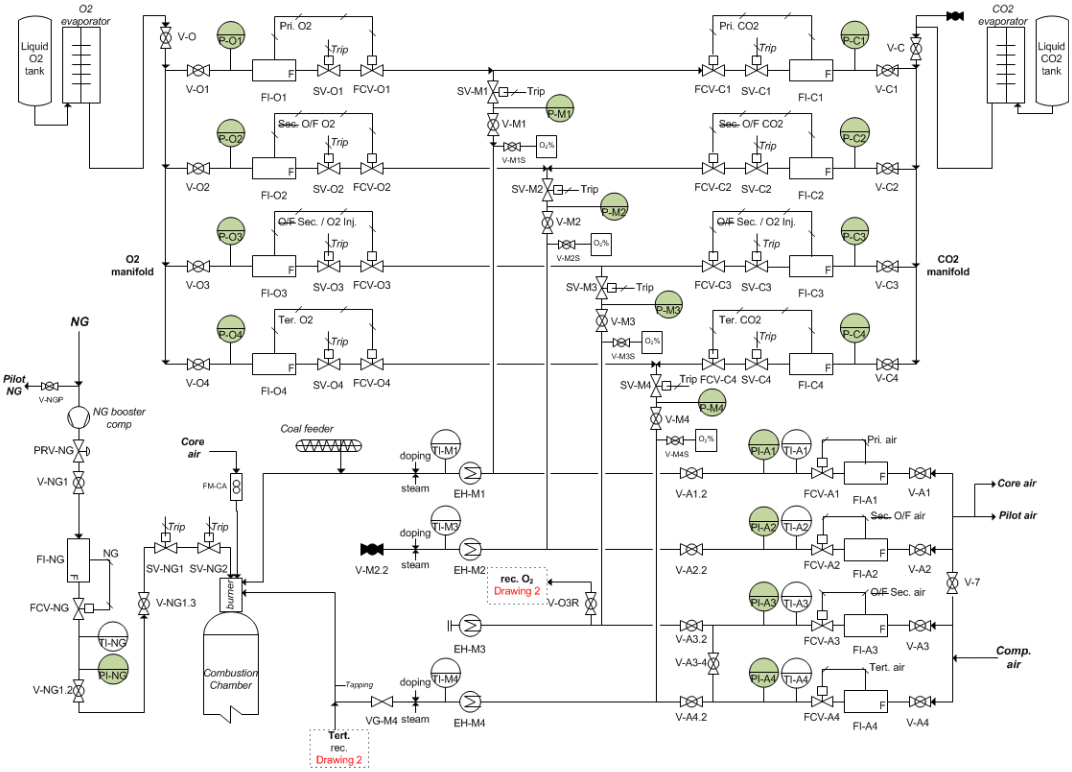

Figure 3.7. P&I diagram of the air and O_2/CO_2 supply to the rig.

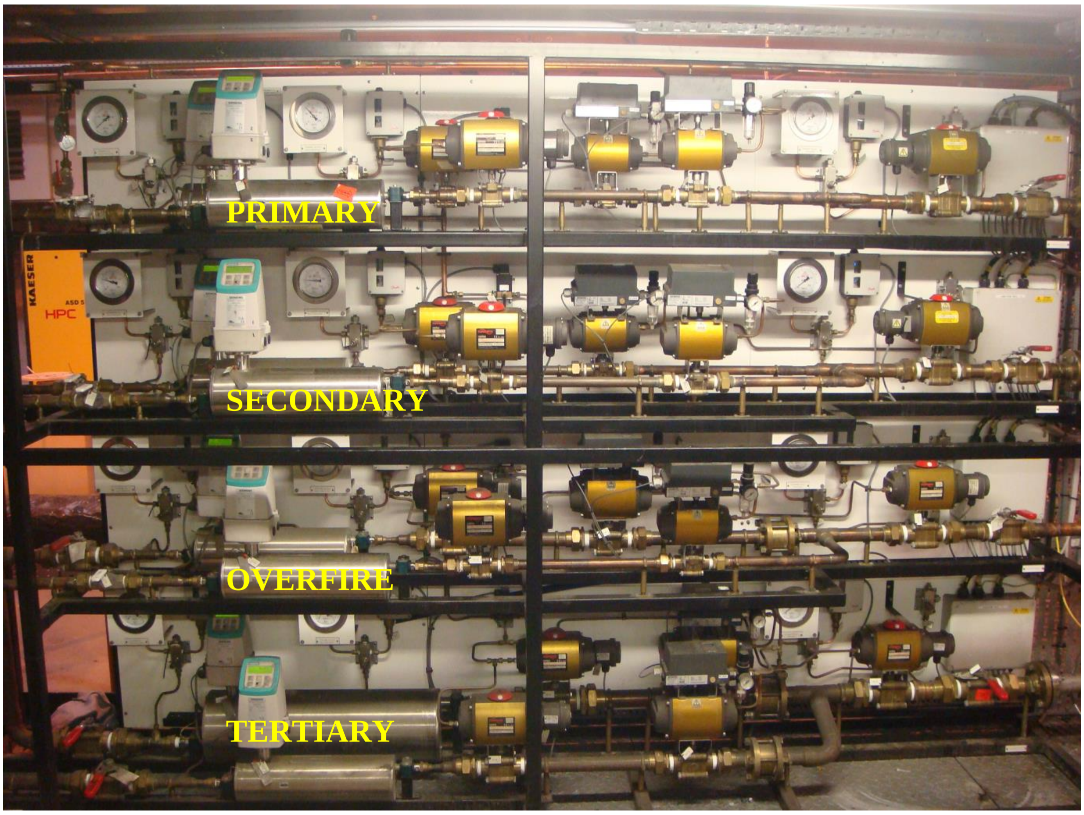

Figure 3.8. O_2/CO_2 mixing skid. Instruments on the O_2 line are at the front and CO_2 ones at the back.

The oxidiser supply is preheated using electrical heaters to achieve a burner inlet temperatures of 250 °C, similar to those at power stations. The temperature exiting these heaters are monitored with sheathed Type-K thermocouples fitted downstream of the preheaters.

Due to fire safety concerns, the Primary line is not enriched with O_2 and is not preheated either. Instead, air at ambient temperature is used to carry the coal to the furnace or for the oxy-fired cases a synthetic CO_2/O_2 mix can be used, but limiting O_2 to slightly less than 21% by volume in order to avoid O_2 levels greater than 21% during operation due to flow variations induced by the PID loop.

3.2.4 Fuel Feeder

The fuel feeder is shown in Figure 3.9. The coal feed metering system is of a screw feeder type. The coal is loaded into a day storage hopper at the beginning of the test, which is located on the mezzanine level. This feeds a lower hopper via a rotary valve, from which the coal is conveyed by a screw feeder. The coal is continuously agitated within the lower hopper in order to keep the supply at the same density and eliminate the risk of bridging.

The amount of coal delivered is regulated by adjusting the rotation rate of the screw. The coal is dropped onto a vibrating plate (spreader) to produce a more uniform coal feed, and it is dropped into the primary line through a Venturi type feeder. The coal is then carried to the burner pneumatically by the primary air.

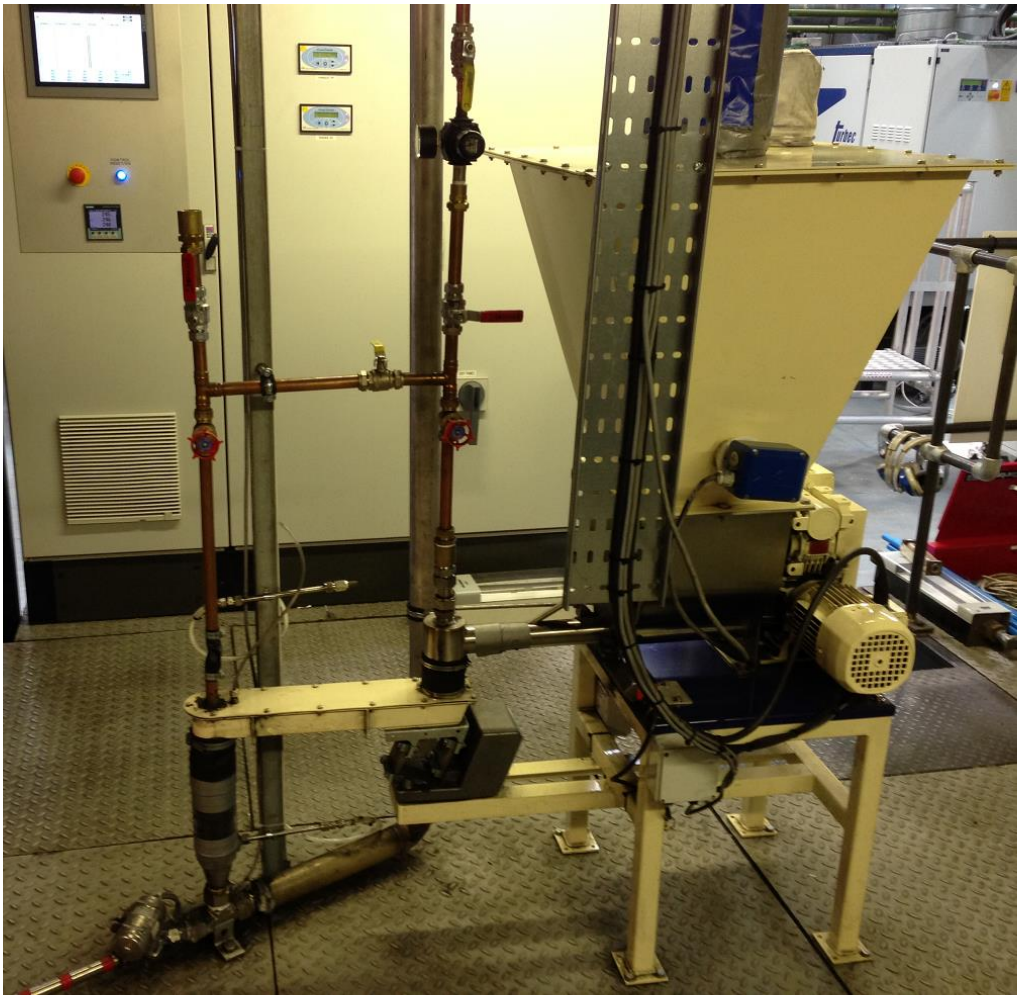

Figure 3.9. Fuel feeder, with feed storage hopper, screw feeder, vibrating tray, venturi feeder as well as the primary bypass line used to eliminate air ingress.

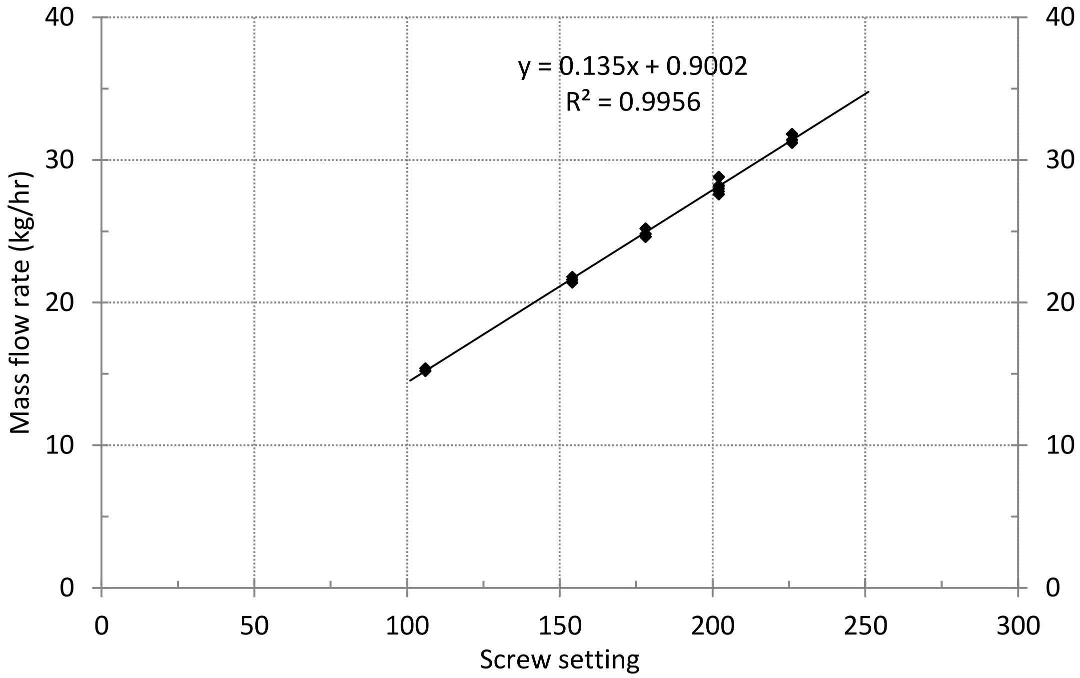

Figure 3.10. Coal feeder calibration curve used to calculate the rate setting of the screw feeder.

The coal feeder was calibrated volumetrically by measuring its output at different screw settings for short, 3 min periods, four times per setting. This was only performed after a uniform bed of coal was established on the spreader plate. The calibration curve (Figure 3.10) was used to set the feeder control to the required coal feed rate to achieve the desired thermal input.

Normally, a Venturi feeder is open to air so that it is able to generate suction, thereby allowing air ingress, requiring an estimation of the additional air input. This feeder was modified so that a part of the metered primary oxidiser can be diverted and fed through the suction end of the Venturi, thereby eliminating the air ingress. The suction within the feeder tray is monitored using a differential pressure cell and the amount of air diverted is adjusted to maintain negative pressure within the suction side of the Venturi feeder.

3.2.5 Cooling Water System

The water cooled jackets of the furnace, flue sections, and the shell and tube heat exchanger are supplied from the site cooling water loop. This consist of a pump set circulating CW around the site in the main cooling water loop, which is cooled by a 500 kW atmospheric cooler located outside the building.

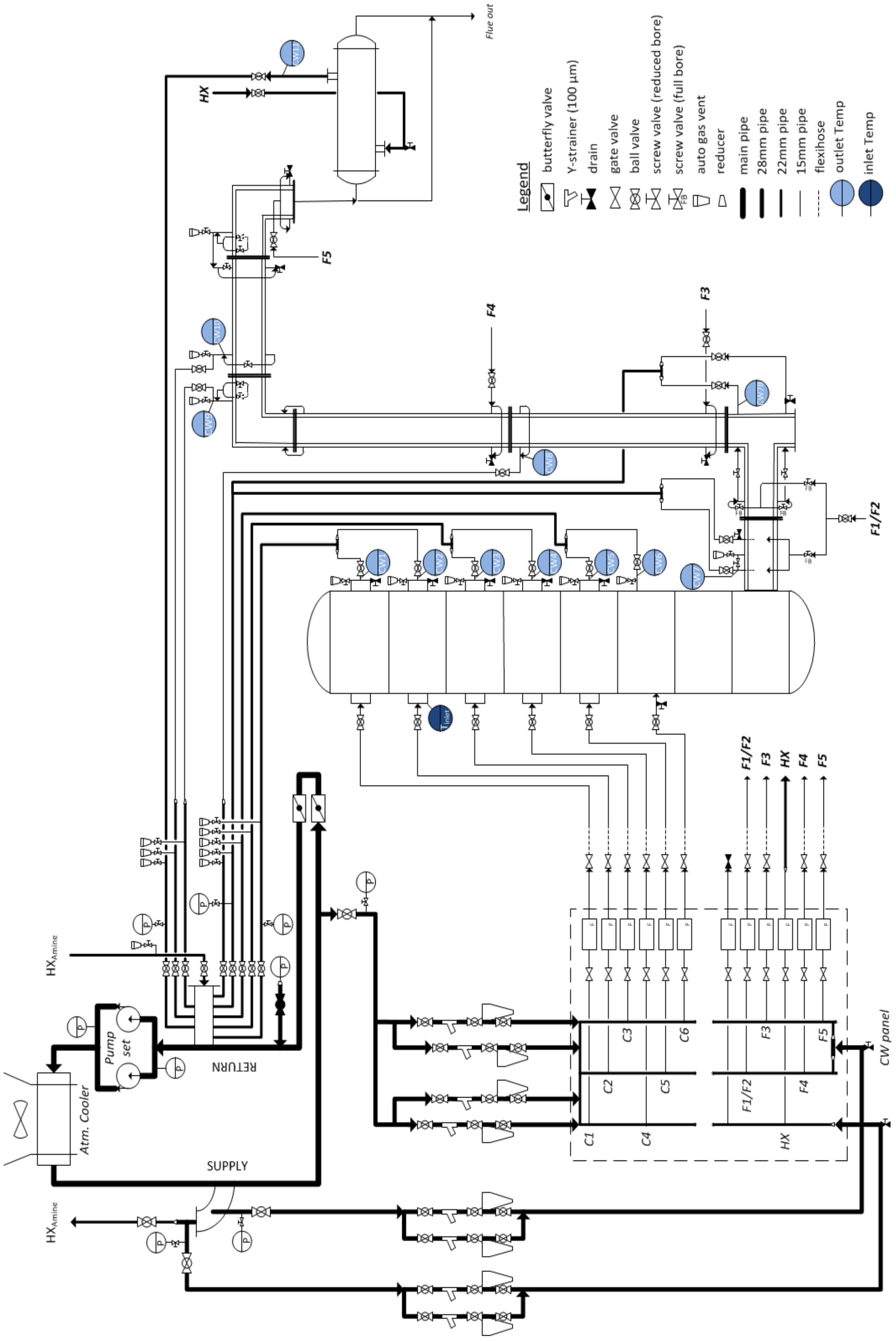

Figure 3.11. The as built P&I Diagram of the water cooling system after modifications to provide, the increased flow of water to the water jackets.

The return temperature from the cooling battery, and hence the inlet temperature to the cooling system was 32°C. Flows were metered using external magnetic sensors on paddle type flow meters with pulse detection and converted to signals that were interpreted by the central PLC for display on the HMI and recording on the SCADA system. The P&I Diagram of the water cooling system is shown in Figure 3.11.

3.3 Analytical Systems

The furnace was designed with detailed measurement and characterisation capabilities, and a range of techniques were used to obtain a detailed assessment of the oxy-fuel combustion process. The location of the ports for in-furnace sampling of the gas species, temperature and heat flux are shown in Figure 3.3, on the right hand side of each furnace section. These ports are 38.1 mm (1.5”) in diameter and 25.4 mm (1”) compression fittings were used to enable the use of probes up to 25.4 mm (1”) in diameter. These fittings also allowed easy and quick adjustment to the probe positions, whilst providing a good seal around the probe, thus eliminating air ingress during measurements. Process thermocouples are located on the opposite side of the sections, and within the flue gas duct. The flue gas composition is measured at the furnace outlet.

3.3.1 Flame Imaging Capabilities

Smart *et al.* (2010a) have noted the importance of the flame imaging techniques for assessing the impact of oxy-fuel combustion for retrofit applications. Project collaborators from the University of Kent used a two-dimensional (2D) imaging technique (Sun *et al.*, 2011) to determine the flame temperature, luminous intensity, point of ignition as well as shape and size under different operating conditions.

The top 2 sections of the furnace are also equipped with ports designed for a three-dimensional (3-D) flame imaging system (Hossain *et al.*, 2011), also developed by the University of Kent. This uses a computational tomography technique to reconstruct the temperature distribution of the flame sections based on eight 2-D images captured, using two digital cameras incorporated with eight imaging fibre bundles. This 3-D imaging system also provides the possibility for non-intrusive in-flame soot concentration measurements.

3.3.2 Gas Sampling

Flue gas concentrations of O_2, CO_2, CO, NO_x and SO_2 were measured at different regions within the furnace and in the flue gas. A schematic and photographs of the system is shown in Figure 3.12.

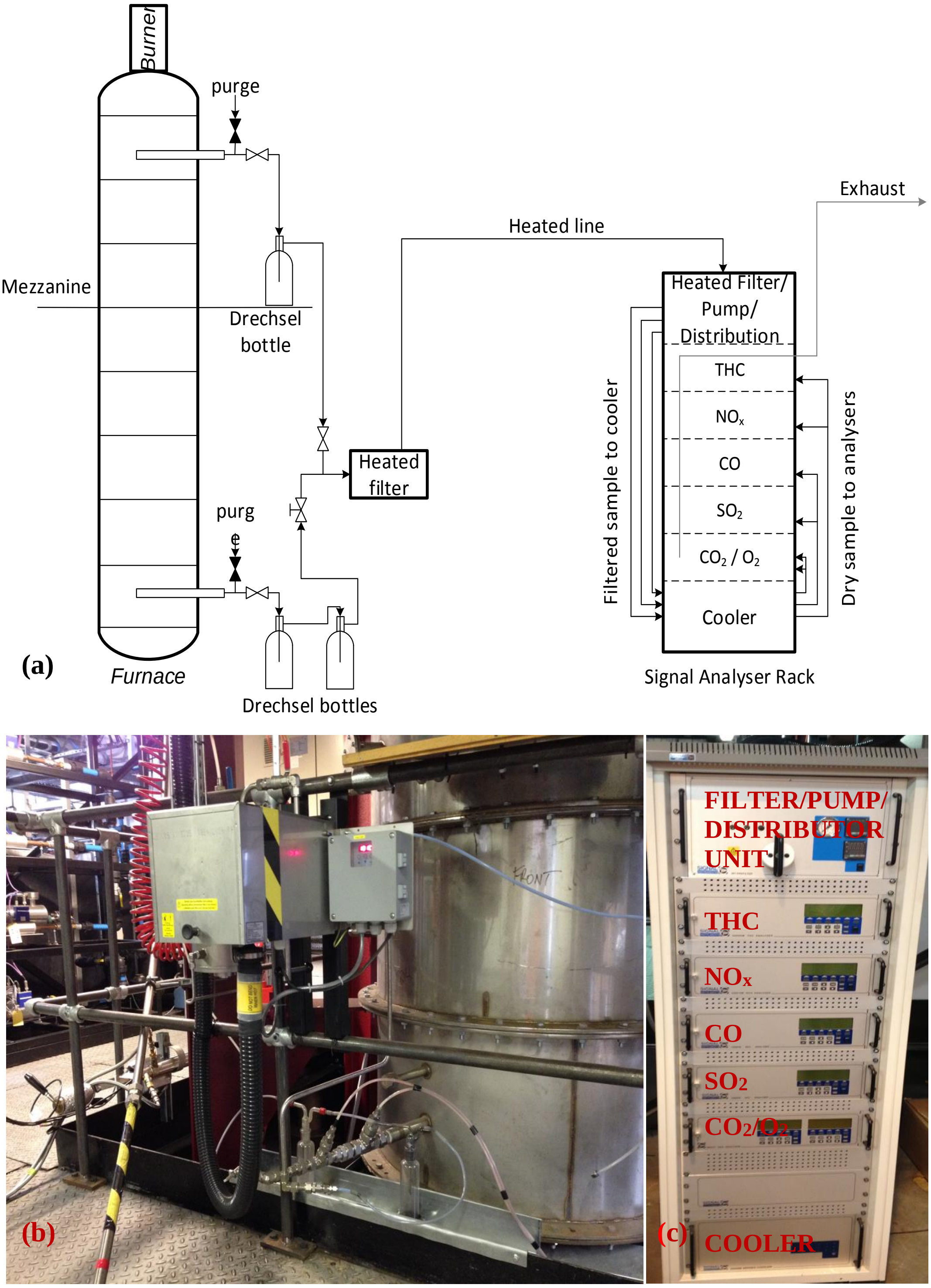

Figure 3.12. Gas sampling. (a) schematic arrangement, (b) gas sampling probe, and (c) Signal gas analyser rack.

Two custom made water cooled gas extraction probes were used for this purpose. One was fixed permanently for sampling from within the furnace exhaust, and the other, used for in-furnace sampling in a range of locations, was inserted when required. Both probe outlets were connected to the compressed air line, thus allowing them to be periodically purged during sampling to prevent blockages.

The probe outlets opened into Drechsel bottles to capture the condensate forming within the water cooled probes. This also removed a portion of the largest particles present in the sample. Only one probe was used at any given time and ball valves were used to switch between the sample paths. Furthermore the remaining section of the sample train was heated to prevent condensation. The sample is introduced into a heated particle filter, kept at 180°C, for fine particle removal and piped to the gas analyser rack (Signal MAXSYS 900 Series) through a heated sample line, maintained at 191°C. The suction, drawing the sample, was provided by the analyser rack's inbuilt pump. The sample was then sent to the cooler unit, thus removing any significant amount of moisture remaining, by cooling it to 5°C. The dried sample was then distributed to the different analysers, which were heated to 191°C, thus eliminating condensation of any remaining moisture on the instruments. The flows were balanced by pressure regulators to achieve optimal sample gas flows to each of the analysers (~1 L/min) and the remaining portion of the sample drawn was expelled, together with the exhaust from the analysers.

3.3.2.1 O_2 Analysers

A 7208MG Signal Multi Gas analyser, fitted with a paramagnetic analyser, was used for measuring the dry O_2 concentrations. A paramagnetic type of O_2 analyser was chosen over thermo-magnetic types since the latter are known to be influenced by the CO_2 content (Pickard, 2013). High levels of CO_2 are measured during oxy combustion and significantly affects the heat capacity of the flue gas. If the O_2 calibration of the instrument is significantly different to the actual measurement then significant errors in the O_2 measurements will occur. This is due to the thermal detection component in the thermo-magnetic technique.

The analyser is fitted with a dumb-bell filled with N_2, arranged in rotational symmetry in a magnetic field, and with a mirror fitted on its axis. O_2 has a strong magnetic susceptibility and the O_2 atoms are drawn to the magnetic field, acting to displace the dumbbell. A light beam is shone onto the mirror on the dumbbell and its rotation is detected by a pair of photo cells. The resulting potential difference generates an electrical current, which is amplified and conducted to the dumb-bell, varying the magnetic field to move the dumb-bell back to its original position. This current is proportional to the O_2 concentration within the sample (Signal Group, 2013).

A Servomex 2700 Zirconia O_2 sensor was also fitted within the flue gas duct for process monitoring checks offering wet O_2 monitoring capability. However, due to the strong vacuum generated by the exhaust fan, this unit was often starved of sample gas and often proved to be unreliable. Therefore modifications were made to the method of gas withdrawal from the flue to improve the reliability by overcoming the negative pressure in the flue duct. To achieve this, a higher pressure was set on the air driven educator system.

3.3.2.2 CO_2, CO and SO_2 Analysers

The 7208MG Signal Multi Gas analyser is also fitted with a Gas Filter Correlation (GFC) Non-dispersive Infrared (NDIR) analyser to measure the CO_2 concentrations. CO and SO_2 are also measured with the same technique using a Signal 7100FM and a 7800FM analyser, respectively.

These gases absorb infrared radiation at specific wavelengths and this phenomenon can be used to measure their concentrations. The analysers have an IR light source, which is shone through a single sample cell of specific length. A solid state detector is located at the other end of the cell and it measures the intensity of radiation passing through the cell. The Beer-Lambert law is used to correlate the infrared intensity reaching the detector and the concentration of the absorbing species:

$$I = I_0 e^{-KCL} \tag{3.1}$$

where, I is the intensity of radiation reaching the detector, I_0 is the radiation source intensity, C is the molar concentration of the gas, L is the optical path length and K is a system dependent absorption coefficient (Lodge, 1988).

To eliminate interference between different species absorbing in the IR region (e.g. CO, CO_2, H_2O), the GFC technique is used. A spinning filter wheel, containing two cells, is fitted between the radiation source and the measurement cell. One cell is filled with the sample, absorbing virtually all the IR radiation specific to the sample gas, and the other a nonspecific gas, N_2, which transmits all the IR radiation. This produces a changing signal at the detector, with the amplitude of oscillation proportional to the concentration of sample gas. The interference from other IR absorbing gases with uncorrelated absorption spectrums produce both a positive and negative effect, thus eliminating most of the interference from these species. The residual interference is reduced further by a band filter fitted between the cell and the IR detector, thus restricting the IR radiation to the narrow region where the gas strongly absorbs (Jernigan, J.R. 2007).

3.3.2.3 NO_x Analyser

NO concentrations are determined with a Signal 4000VMA chemiluminescence analyser. The method is based on the chemiluminescent reaction between NO and O_3, producing NO_2 and O_2:

$$NO + O_3 \rightarrow NO_2 + {NO_2}^* + O_2 \qquad 3.2$$

Approximately 10% of the NO_2 produced is in an electrically excited state ${NO_2}^*$and as the molecules return to normal state they emit a photon, with wavelengths between 0.6 and 0.3 µm. The intensity of the emitted light is proportional to the amount of NO entering the chamber and is measured by a photomultiplier tube. If measurement of total NO_x is desired, the sample is first passed through a catalytic converter, which is kept at ~440°C, reducing NO_2 to NO in the presence of carbon (Signal Group, 2008) followed by the process in equation 3.2.

3.3.2.4 Analyser Operating and Calibration Procedure

The analysers were calibrated daily in order to make sure that the gas composition measurements are representative and as accurate as possible.

To minimise drift during measurements, the analysers were left in standby mode overnight, which kept the internal electronics at the operating temperature. The pump and cooler units were turned on first thing in the morning and the analysers were switched to sample mode (drawing air only) to allow the analyser rack to reach steady state temperature as the furnace was heating up on natural gas.

Every morning the gas tightness of the sample path, leading from the sampling probe to the analyser pump, was checked utilising the pumps inbuilt vacuum safety switch.

The probe outlet was isolated with the analyser pump running and if the pump cut out due to the vacuum generated, it demonstrated that the sample train was gas tight.

An additional gas tightness check was also performed when the system was set up. The span gas was introduced after the sample probe bypass was fitted at the calibration gas inlet. The bypass was opened to the atmosphere, and the calibration bottle pressure regulator was set to produce a slight flow from this bypass, assumed to correspond to ~1 L/min. This calibration gas flow allowed the sample train to be under the vacuum generated by the analyser pump, and therefore conditions close to sampling from the furnace were replicated.

Before the measurements started, the analysers were calibrated manually. The calibration gases were permanently piped up to the analyser rack, thus allowing calibration checks whenever desired throughout and at the end of the experiments. Zero grade N_2 was used for calibrating the zero point of the analysers, and the span points were calibrated with Beta Standard calibration gases (with ±2% accuracy). The Span gases used were 15.37% CO_2, 2.95% O_2, 151 ppm CO in a balance of N_2, 760 ppm SO_2 in a balance of N_2 and 414 ppm NO in a balance of N_2. These concentrations were chosen according to the expected measurements.

3.3.2.5 Experimental Error Estimation

The total error given in the Chapters 4 and 5 are calculated from the statistical and experimental uncertainties using (Palmer, 2014):

$$E_{Total} = \sqrt{{E_x}^2 + \cdots + {E_Y}^2} \tag{3.3}$$

where x and y denote random and independent errors, which are associated with quantities which are added or subtracted when calculating the measured quantity.

The statistical uncertainty was determined as ±1 standard deviations from the mean measurement value. Furthermore the experimental uncertainties were determined from manuals and calibration certificates. The sources of experimental errors are summarised in Table 3.1, values in red were considered as significant errors which could not be eliminated by good experimental practices and so were included in the calculation of the total experimental uncertainties.

Table 3.1. Summary of experimental error sources for the gas analyser units. Values in red were considered as significant error which could not be eliminated by good experimental practices and so were included in the calculation of the total experimental uncertainties. Values in italic are collected from the general manuals of the analysers, and values in bold are from the factory calibration certificates. FSD (Full Scale Deflection) corresponds to the analyser range used during a measurement, pk pk (peak to peak) corresponds to the error between the minimum and maximum signals during the factory error assessment, corresponding to the zero and the maximum ranges of the analysers, respectively.

Error Source	**NO$_x$**	**O$_2$**	**CO$_2$**	**CO**	**SO$_2$**
Calibration gas	**≤2% of certified value**				
Repeatability	*≤1% FSD*	*≤0.02% FSD*	*≤1% FSD*	*≤1% FSD*	
Bypass flow sensitivity	*≤1% in reading for 1-3 l/min*	*≤1% in reading when flow changing from 0.2-2 l/min*			
Detector noise:					
Zero	**≤0.04ppm pk pk**	**≤0.005% pk pk**	**≤300ppm pk pk**	**≤5ppm pk pk**	**≤10ppm pk pk**
Span	**≤0.5% FSD**				
Linearity	**≤0.5% FSD**				
Response time	**rise 2.4 s / fall 3.2 s**	**r5 s / f5.8 s**	**r1.2 s / f1.5 s**	**Cell1: r1 s / f0.9 s** **Cell2: r1.4 s / f3.4 s**	**r6.8 s / f6.1 s**
Drift :					
Zero	**≤0.02ppm /day**	**≤0.008% /day**	**≤1584ppm /day**	**≤2.5ppm /day**	**≤10ppm /day**
Span	**≤0.5% FSD /hr**	**≤0.5% FSD /hr**	**≤0.5% FSD /hr**	**≤0.5% FSD /hr**	**≤0% FSD /hr**
Ambient P effect	n/a	*output is directly proportional to the absolute barometric pressure (measured at the exhaust port)*			
Ambient Temp effect:					
Zero	**≤0.027ppm /°C**	**≤0.008% /°C**	**≤250ppm /°C**	**≤2ppm /°C**	**≤5ppm /°C**
Span	*≤1% of range/3°C*	*≤0.1% form 5-40°C*	*≤0.2%/°C of the highest range*		
Chart recorder output	*≤0.02% of range/°C*				
Converter efficiency	**96%**	n/a			

The total experimental uncertainty, calculated using Equation 3.3, is shown in Table 3.2. The CO$_2$ measurement errors significantly increase for the oxy cases, which is due to the repeatability as well as the span and linearity errors being a percentage of the range used (25% for the air cases and 100% for the oxy cases).

Table 3.2. Total experimental uncertainty calculated for air- and oxy-fired gas measurements.

Experimental error	**O_2 (%)**	**CO_2 (%)**	**NO_x (ppm)**	**CO (ppm)**	**SO_2 (ppm)**
Air	**0.1**	**0.4**	**15**	**8**	**22**
Oxy	**0.1**	**1.3**	**15**	**8**	**22**

Sources of errors excluded from the estimation of the total error:

- Errors under an order of magnitude smaller than the reported precision, e.g. *Zero noise for the O_2 and NO analysers*.
- *Bypass flow sensitivity*: as the zero and span gases were introduced to the analyser with the same flow rate as the sample (at 1 L/min). A visual check of the flow rate using the digital flow meters on each analyser display was made before each calibration.
- *Drift (Zero and Span)*: calibration checks were made, both before and after the experiments as well as throughout the sampling period ~every 2 hrs. If a drift was identified then the analyser was recalibrated and a note was made that the data will have to be corrected during the data analysis.
- *Ambient temperature effect (Zero, Span and Chart recorder output)*: as noted in the previous point, the time was allowed for the analyser rack to reach a steady state temperature. Furthermore the calibration checks during the sampling period listed above also identified drift due to temperature changes.
- *Ambient pressure effect:* the analyser output was directly proportional to the absolute barometric pressure (measured at the exhaust port). The sample gases were filtered (1-10µm) before they were admitted to each analyser and the exhaust gases were collected into and vented through a 25.4 mm (1”) exhaust pipe. Due to the initial filtering, and the wide pipe diameter, no blockages were expected, which could lead to an increased pressure within the exhaust port downstream of each analyser. Also daily variations in the ambient pressure during a typical afternoon were assumed to be negligible.

- *Converter efficiency:* due to the low NO_2 emissions in the flue gases, the converter efficiency of 96% was assumed not to influence any total NO_x measurements.

When correcting for a Zero drift, the offset was simply added to the measurements, for a Calibration drift (when the Zero reading was correct) the calibration offset was interpolated to the measurement value and this value was added to the measurement, i.e. if during the SO_2 calibration check (using 760 ppm calibration gas), the analyser read 700 ppm, and the sample reading was 260 ppm, the calibration drift of 60 ppm was interpolated from 760 to 260 ppm, giving 21 ppm, then adding this to 260 yielded the corrected measurement of 281 ppm.

It should also be noted that the presence of larger chambers, e.g. the Dreshcel bottles, heated filter near the rig and inside the analyser rack all produce averaging effects during sampling. This, for example, may reduce the measured magnitude of the temporary spikes.

The response time in Table 3.1 shows that there is a significant time lag between each analyser, with the O_2 and SO_2 analysers being the slowest, and therefore when correcting the measurements to 6% O_2 content, the correction was made against the average O_2 value, instead of correcting each measurement against the O_2 measurement recorded at the same time.

3.3.3 Temperature Measurements

Process temperature measurements were made using ceramic sheathed Type R thermocouples installed within the furnace and Type K thermocouples within the flue gas ducts and cooling water pipes. These measurements were available online during the operation to aid monitoring and the control of the combustion facility.

However these thermocouples cannot be used to obtain the true gas temperatures since they are susceptible to error due to radiation exchange between the thermocouple and its surroundings, and the measurements require correction to obtain the gas temperature. Given the level of detailed information needed (e.g. estimating the convective heat transfer coefficient around sheathed thermocouple), this is not practical.

3.3.3.1 Suction Pyrometry

To determine the in-furnace gas temperatures, without the need for corrections, a suction pyrometer (Figure 3.13) was used. A Type B Pt-30% Rh/Pt-6% Rh thermocouple is located at the tip of the probe, within the inner alumina sheath, protecting it from deposits and chemical attack. This inner sheath is surrounded by an outer radiation shield, thus reducing the radiative heat exchange. At high velocities (> 150 m/s) the effect of convection is significantly augmented compared to the radiative heat exchange, thus ensuring that the equilibrium thermocouple temperature is close to that of the gas sampled. The suction velocity was provided by a Venturi ejector fitted downstream of the suction line outlet, which was driven by compressed air. It should be noted that, due to the high velocity suction applied, the temperature measured is a volume average value surrounding the probe tip. However, since the gas at the tip is being replaced at a faster rate than extraction then a good representation is being obtained of the gas temperature in the immediate vicinity of the tip.

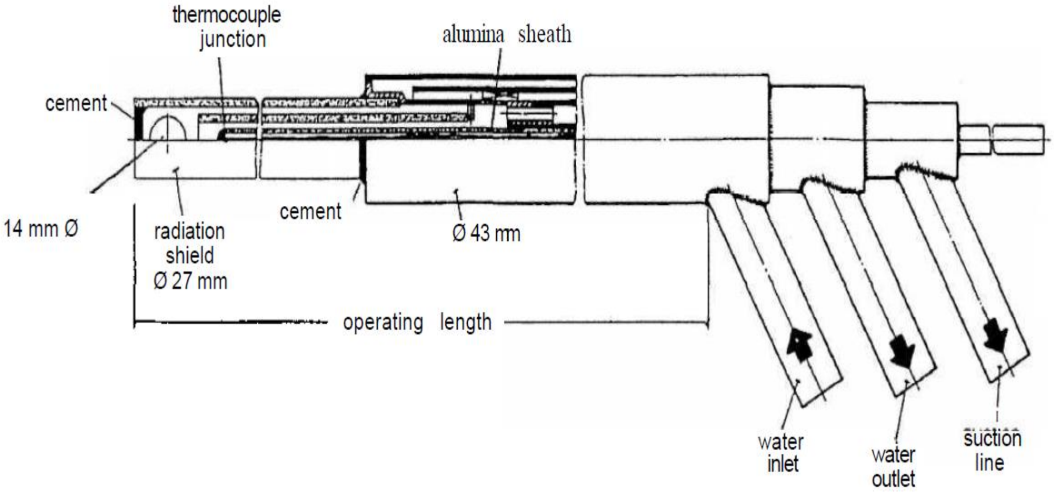

Figure 3.13. Schematic of the suction pyrometer (Rooijmans, 2012).

The probe can be fitted to any of the 38.1 mm (1.5”) ports along the furnace (shown on the RHS in Figure 3.3 (a)&(b)), and traversed to the required measurement depth within the furnace. The manufacturer’s recommendations stated that the probe required 3 min for the thermocouple to reach steady state temperature when placed within the furnace, and a further 1 min was needed for each 100°C temperature change. However in practice this time was observed to be less and the readings stabilised within 0.5-1 min and the sample period was considered to commence.

Sampling was performed for 3 min at each locations, except for the locations directly under the coal collectors which clogged up the probe within a couple of minutes. Sampling at these locations were conducted for just over a minute.

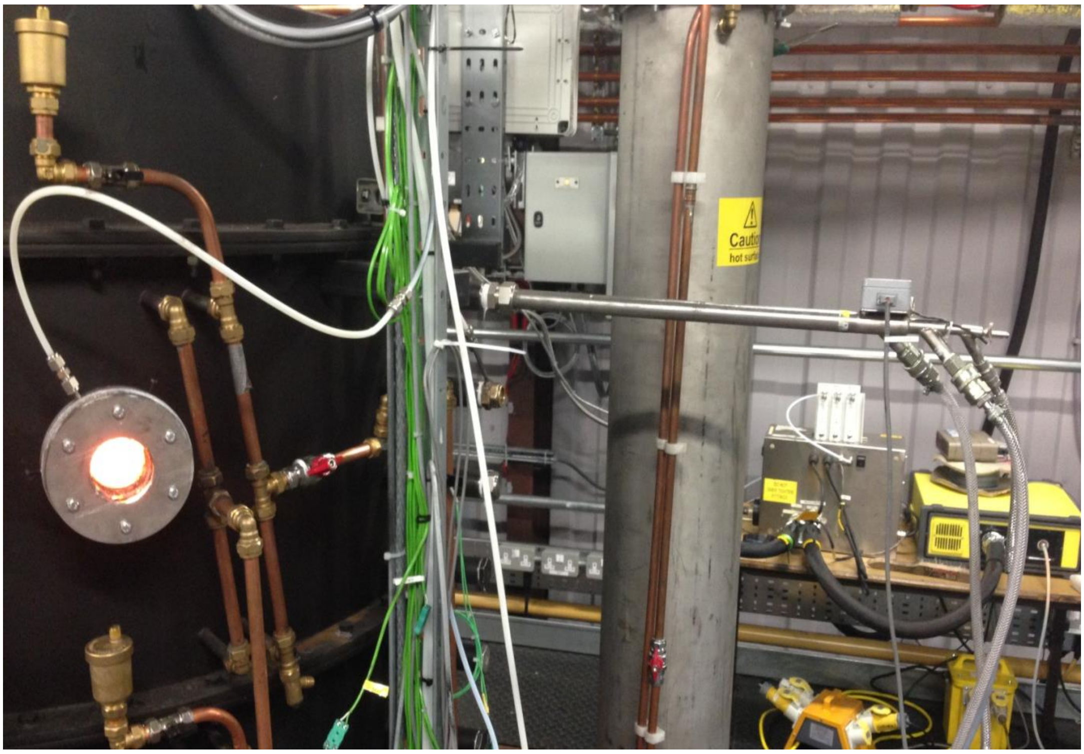

Figure 3.14. Suction pyrometer positioned in the first 38.1 mm (1.5”) measurement port during an air-fired experiment.

The required positioning of the probes were calculated from the CAD drawings of the furnace. It was also confirmed visually by opening up the front port, which is in alignment with the rear port, circled on Figure 3.15(c), and inserting the probe to the calculated distance to reach the centre of the furnace. There was a ~1cm error observed, compared to the calculated depth from the CAD drawings, and the positioning depth was adjusted accordingly to yield the exact position when using the probes.

Also to make sure that the probe is inserted within the furnace accurately the distance was counted not from the end of the compression fitting but from the end of the ports welded to the furnace (black pipe end on Figure 3.16). The position of the compression fitting was dependent on how much the fitting was tightened and also could vary from port to port depending on how deep each fitting could be screwed into the port.

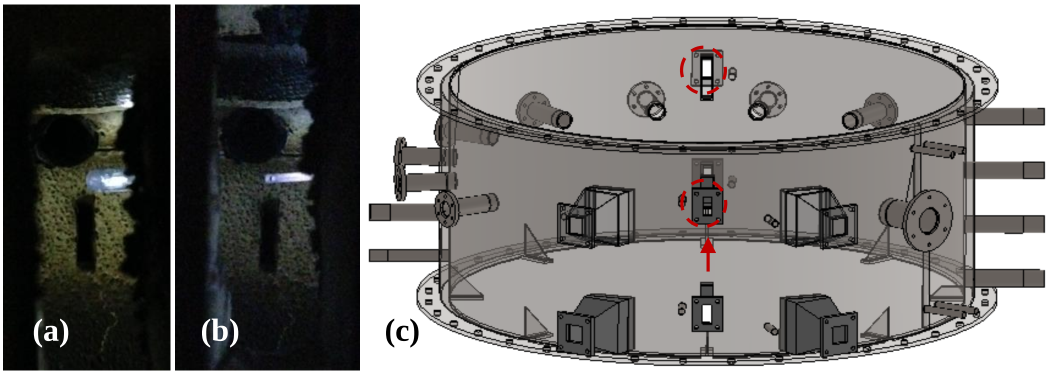

Figure 3.15. Positioning checks of probes pushed 450 mm into the furnace, (c) as viewed from the front, to ensure that the suction holes are positioned at the centre of the furnace for (a) gas sampling probe (opening at the tip), and (b) suction pyrometer (opening on side, ~1cm from the tip).

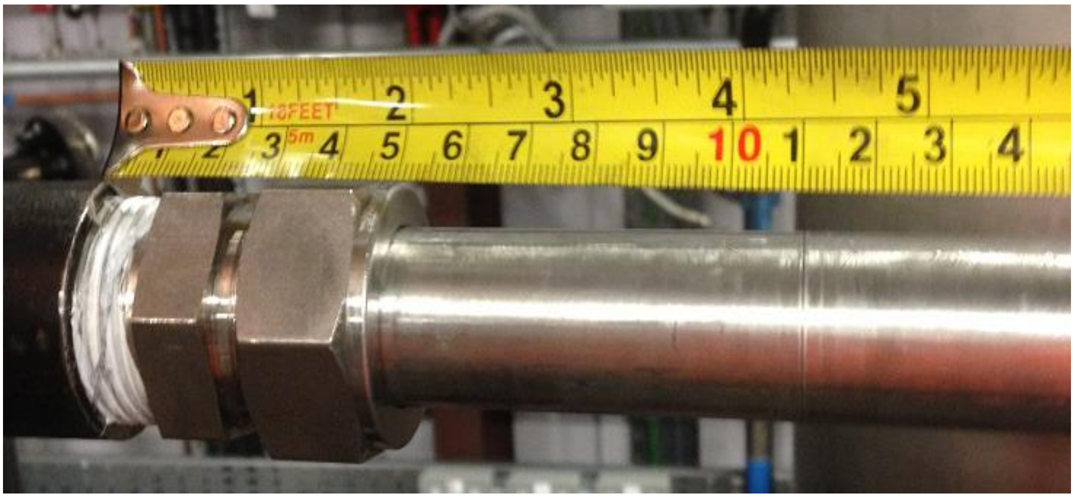

Figure 3.16. Positioning of the sampling probe; position counted 6cm from the end of the black furnace port (shown on the left).

3.3.4 Heat Flux Measurements

The heat transfer was measured using a Medtherm heat flux transducer, which is convertible between total and radiative heat flux measurements. The sensor is of the Schmidt-Bolter type, with a thermopile fitted at the probe tip. The heat flux is absorbed at the sensor surface and is transferred normal to that surface to the inner, cooled end of the sensor. A thermopile with junctions at both surfaces generates an emf signal corresponding to the temperature difference between the two surfaces. The sensor provides a linear output directly proportional to the heat transfer rate reaching the sensor tip.

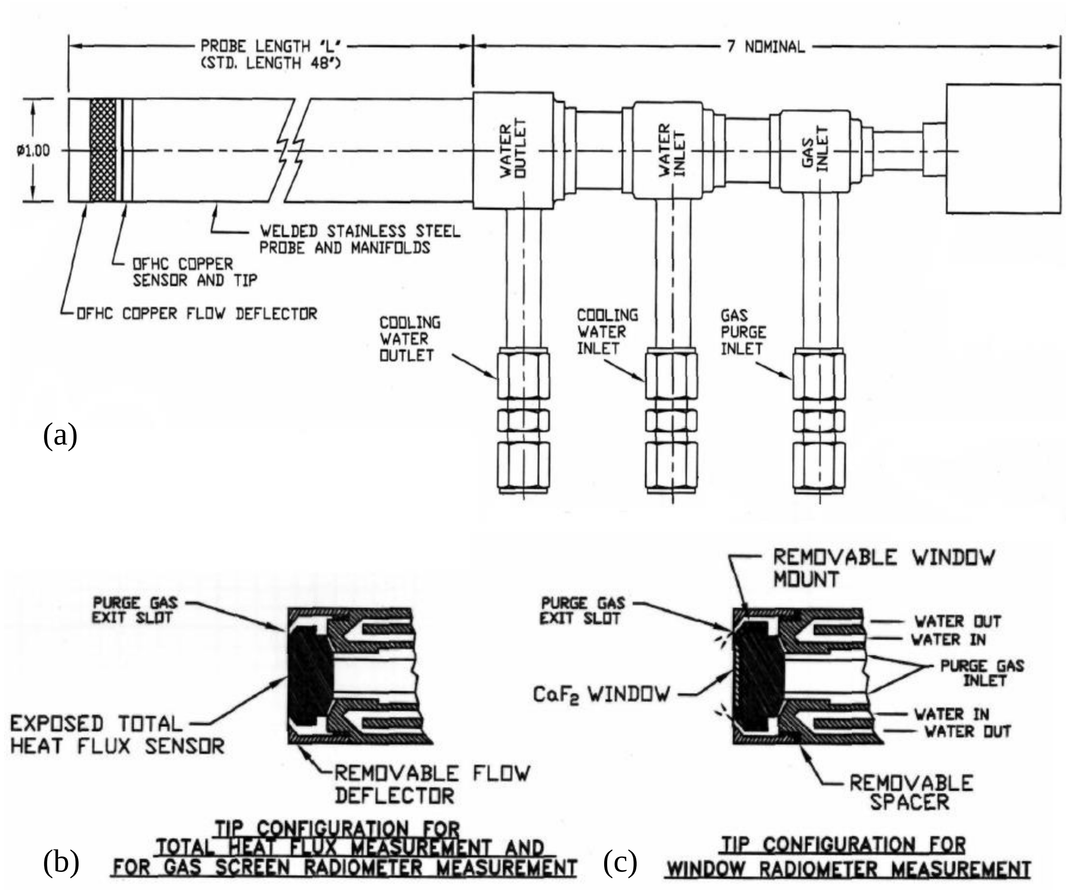

Figure 3.17. Schematics of the Medtherm heat flux probe (a), and the different tip configurations (b) and (c) (Medtherm, 2012).

The total heat transfer measurement is done using the configuration shown in Figure 3.17(b). With the sensor tip exposed to the combustion gases, the probe is exposed to convective heat transfer, next to the incident radiative heat flux.

The radiative heat flux measurements require the use of a gas purge to shield the probe tip from convection as well as from the build up of soot and ash on the surface. O_2 free N_2 was chosen for this purpose, which is preferable to air or CO_2 – air would introduce O_2 at the probe tip, potentially altering the combustion environment close to the sensor, and CO_2 with its higher heat capacity would cool the surroundings of the probe and the flame more than N_2.

An optional accessory for radiative measurements is a CaF_2 window attachment (Figure 3.17(c)). It shields the sensor from direct contact with the combustion gases, but it was prone to cracking, condensation and sooting even with the gas purge applied. Therefore the radiative measurements were taken without the window attachment using the configuration shown in Figure 3.17(b).

As with the gas sampling probe described above, this probe can also be fitted to any of the 38.1 mm (1.5”) ports (shown on the RHS on Figure 3.3 (a)&(b)). When taking readings at each port location, first the radiative and then the total heat flux measurements were taken. The N_2 purge was switched on before introducing the probe to the furnace, which minimised the chance of any ash, settled within the port, from depositing on the probe tip whilst it was inserted. Radiative flux readings were taken after the tip was aligned with the inner wall, and then the purge was turned off in order to enable total heat flux measurements to be collected. This also allowed for the calculation of the convective heat flux, which was the difference between the total and radiative measurements.

3.3.4.1 Experimental Error Estimation

The experimental error associated with the measurements was determined by the manufacturer as ±3%.

An additional influence on the measurements was whether the probe was used with or without the window attachment. Due to the restricted view angle, 150°, associated with the window attachment, compared to the full hemispherical view angle of the probe with a bare tip. The measurements with the window attachment were also more susceptible to deposition on the probe tip, producing sharp dips in adjacent measurements (see Chapter 4).

Although the probe was only pushed in up until the surface of the inner wall, the radiative heat flux measurements were still considered intrusive due to the use of the gas purge. Its effect was considered to be the strongest for the near flame measurements when the gas screen is directed at the flame, and reducing in influence downstream of the flame.

3.3.5 Burnout

The combustion efficiency was assessed by determining the Loss on Ignition (LOI) of the ash and the burnout using the ash tracer method. It was assumed that the volatile portion of the coal is released and the mineral matter is conserved during combustion. Ash samples were collected from the candle filter after each test and the ash content of the char was determined in line with the British Standard 1013-104.4:1998.

The LOI was calculated using:

$$LOI = \frac{W - A_i}{W} \qquad 3.4$$

where W is the dry weight of the ash sample and A_i is the dry ash content of the ash sample remaining after the BS burnout determination.

The burnout is calculated using:

$$B = 1 - \frac{A_0}{1 - A_0} \times \frac{1 - A_i}{A_i} \qquad 3.5$$

where B is the burnout, and A_0 and A_i are the dry ash content of the coal and ash, respectively (Li *et al.*, 2013).

3.4 Fuel

The coal used for the project is a subbituminous coal from the El Cerrejon region in Columbia. It was premilled in the UK prior to the experimental campaign and stored on site in 25kg bags. The fuel analysis results are presented in Table 3.3 and Figure 3.18 & Figure 3.19.

Table 3.3. Ultimate and Proximate analysis and calorific value data.

Ultimate	ar	dry	daf
C	73.57	78.11	79.31
H	5.04	5.35	5.43
O (by diff.)	11.31	12.01	12.19
N	2.47	2.63	2.67
S	0.37	0.40	0.40
GCV	30.79	32.69	33.19
NCV	29.57	31.39	31.88

Proximate	ar	dry	daf
FC	54.92	58.31	59.21
VM	37.84	40.17	40.79
Ash	1.43	1.52	---
Moisture	5.81	---	---

The Proximate analysis was performed following the procedures listed in the British Standard - BS ISO 17246:2010, for determination of the moisture (BS 1016-104.1:1999), ash (BS 1016-104.4:1998) and volatile matter (BS 1016-104.3:1998), and the carbon content was calculated by difference. The analysis was performed on duplicate samples and repeatability limits set out in the standards were observed when accepting a pair of measurements. The averages of the results obtained are shown in Table 3.3.

The Ultimate analysis was performed using the high temperature combustion method, using a Scientific Flash 2000 CHNS analyser. This burned the samples in pure O_2 at 1350°C in a tube impervious to the ambient gases, and measured the evolving H_2O, CO_2, SO_2 and NO_x to establish the H, C, S, and N content of the coal. The test was performed on an as received basis, and the H within the moisture was subtracted from the results according to BS ISO 17247:2013. A moisture content analysis on the sample batch was repeated on the sample day to eliminate errors between moisture content determinations performed weeks apart, due to differences in ambient moisture contents in the laboratory or doubts over the sample drying in the tubs over time. The O content was calculated by difference according to the BS ISO 1170:2013 standard. The samples were analysed in duplicate and the average value is shown in Table 3.3.

The gross calorific value of the coal was measured according to the standard: BS 1016-105:1992. A Parr 6200 O_2 bomb calorimeter was used for the analysis and titrations were performed on the washings to correct the results for the heat of formation of sulphuric acid and nitric acid. The heat release from the firing wire was also subtracted from the results. Duplicate results were performed and observing the repeatability limit set out in the standard. The net CV was then calculated according to the ISO 1928:1976 standard, and the average of the results is shown in Table 3.3.

Particle size distribution was measured by the sieve method, using sieves with aperture sizes of 53, 150, 212, 355, 600µm. To ensure a representative measurement, samples were collected from 2 bags, each selected from a different pallet. Each bag was rolled around 10 times to mix the compacted coal, the bags then were opened and samples were scooped from 5 different regions of the bags, scooping from the bottom to collect from the full height of the sample. The same method was used when ~100 gram samples were drawn for each sieve analysis. The results are shown in Figure 3.18.

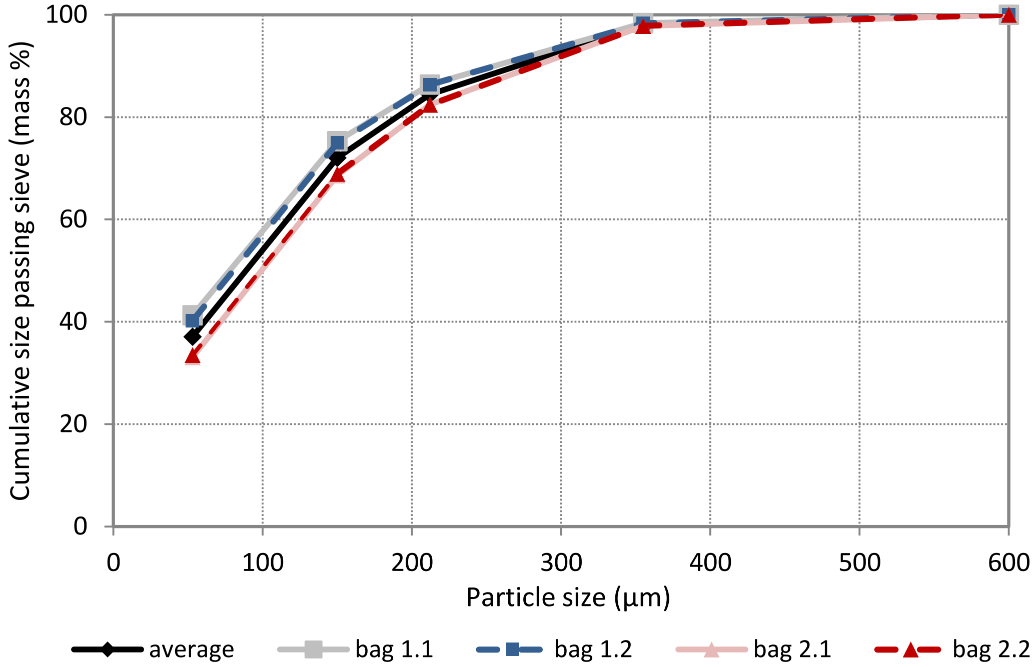

Figure 3.18. Cumulative particle size distribution of the tested coal.

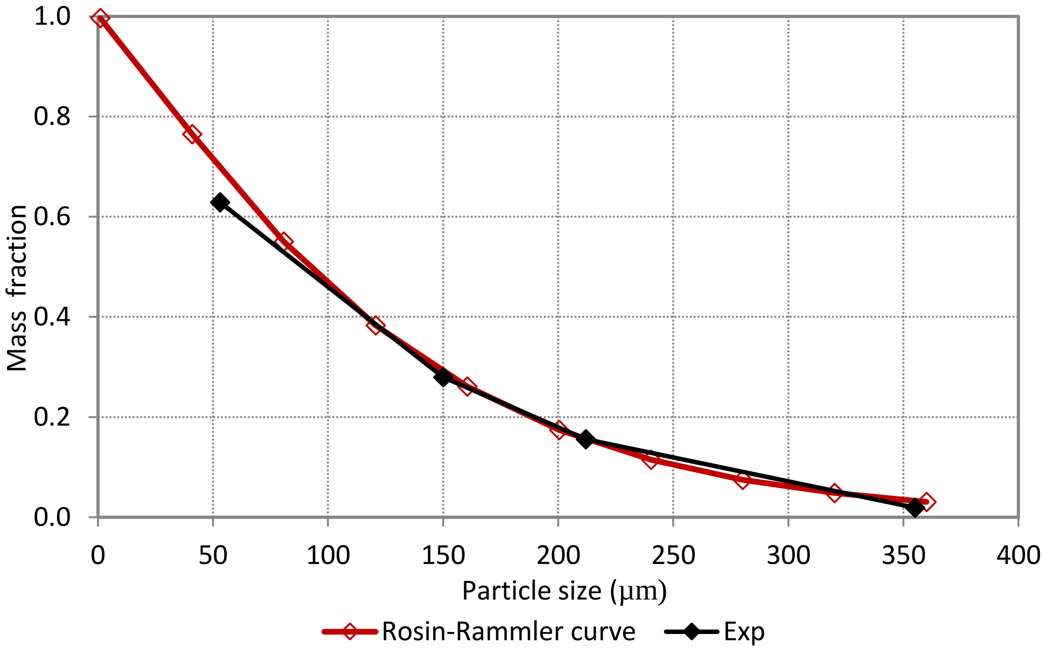

Figure 3.19. Rosin-Rammler curve and the experimental particle size distribution for the coal used.

The mean diameter and corresponding spread parameter was chosen to be 125 and 1.179, respectively, in order to obtain a close fit with the experimental results. For the CFD analysis, the minimum and maximum particle sizes were chosen as 1 and 360µm, distributed over 10 bin sizes (Figure 3.19).

3.5 Data Logging

The output from the air/O_2/CO_2 flow meters, thermocouples, analysers, measurement probes etc. are each connected to the Siemens PLC controlling the rig. The data coming from the instruments (typically on a 4-20 mA, or 0-10 mV bases) was converted by the Siemens PLC to its own scaling system of 0-27648, shown in the RAW column on Figure 3.20. These limits represent 0 and 100% of the instrument ranges, respectively, which were then converted to the engineering units (SCALED column) of the instrument by scaling it according to the measurement range of each instrument (LOW and HIGH columns). Real time data can be viewed online (Figure 3.1), and it is also transmitted to the Siemens SCADA data logging system, which records the output of each channel at 5 second intervals.

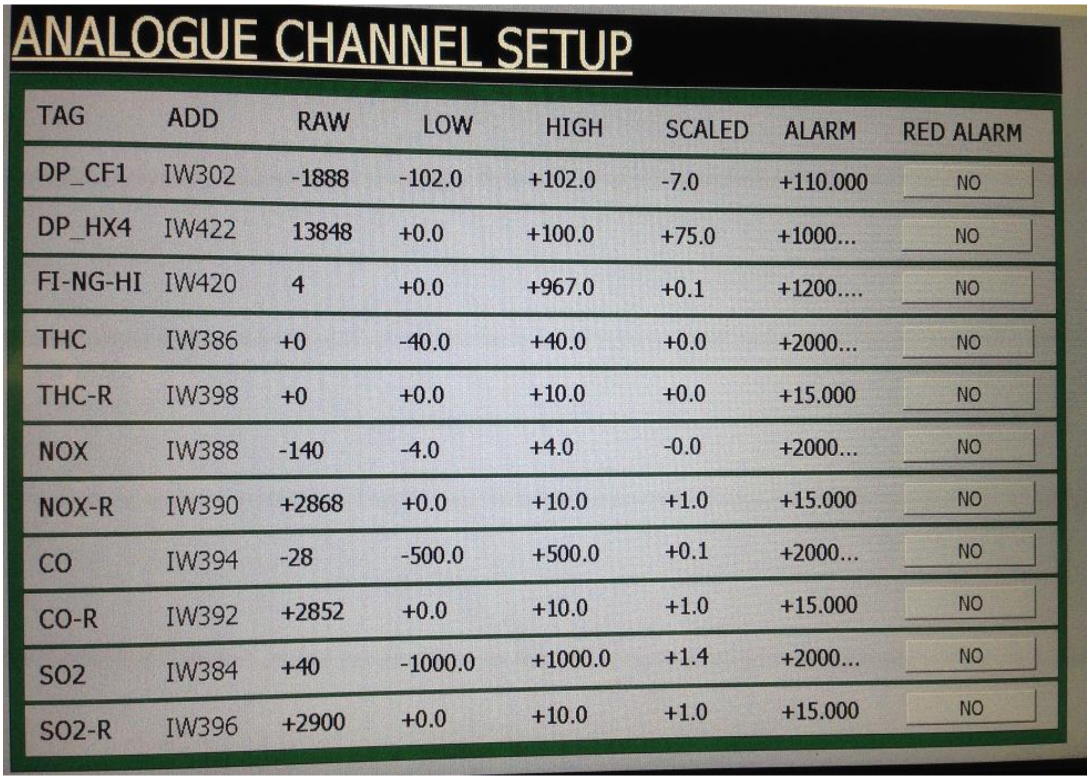

ANALOGUE CHANNEL SETUP

TAG	ADD	RAW	LOW	HIGH	SCALED	ALARM	RED ALARM
DP_CF1	IW302	-1888	-102.0	+102.0	-7.0	+110.000	NO
DP_HX4	IW422	13848	+0.0	+100.0	+75.0	+1000...	NO
FI-NG-HI	IW420	4	+0.0	+967.0	+0.1	+1200....	NO
THC	IW386	+0	-40.0	+40.0	+0.0	+2000...	NO
THC-R	IW398	+0	+0.0	+10.0	+0.0	+15.000	NO
NOX	IW388	-140	-4.0	+4.0	-0.0	+2000...	NO
NOX-R	IW390	+2868	+0.0	+10.0	+1.0	+15.000	NO
CO	IW394	-28	-500.0	+500.0	+0.1	+2000...	NO
CO-R	IW392	+2852	+0.0	+10.0	+1.0	+15.000	NO
SO2	IW384	+40	-1000.0	+1000.0	+1.4	+2000...	NO
SO2-R	IW396	+2900	+0.0	+10.0	+1.0	+15.000	NO

Figure 3.20. I/O (input/output) channel setup page.

3.6 Operating Philosophy

During the start up, the furnace is initially operated with an air-fired gas burner, to raise the furnace temperature to approximately to 1000°C at a central point in the furnace. At this temperature, the coal can be introduced to the burner, and the natural gas shut off. Then, both the coal and air feeds are increased to the required thermal input of 200 kW, and the furnace is allowed to reach thermal equilibrium. This is deduced from in-furnace temperature measurements. When these variables reach a stable value, baseline measurements can be taken, after which switching to oxy-fuel firing can be initiated.

During the start up, the primary and secondary streams are both ambient air. During oxy-fuel operation, however, a synthetic mixture of O_2/CO_2 is used as the primary carrier and the secondary stream can be operated on either once through (synthetic) or wet flue gas recycle. Consequently the flue gases can either be cooled and rejected entirely or partially recycled back to the system, with the latter option representing typical large scale oxy-fuel processes.

The oxy-fuel mode can be operated either with a wet flue gas recycle or by using a synthetic dry recycle.

This is achieved by initially replacing the primary carrier stream with the synthetic mixture of O_2/CO_2. Recycled flue gas was not used for the primary stream in order to avoid any problems associated with the high moisture content of the recycle. This is because the pulverised coal would absorb significant amounts of moisture, possibly leading to coagulation (altering the originally measured particle size distribution) and sticking to the pipe and burner internal surfaces. Also due to safety issues, the primary is only enriched to 18% O_2, thus allowing for a safety margin to ensure the O_2 content in the primary does not exceed 21% during incidental spikes (the control PLC allows up to 10% deviations from the flow rate on a temporary bases). In the next stage, the O_2 enrichment of the secondary stream and the addition of the recycle is initiated gradually, with the subsequent reduction in the air flow rate. During this it is necessary to maintain similar mass flow rates in order to avoid blow off of the flame. When the air is completely switched off and the desired overall ratio of O_2/CO_2 is reached, the furnace is allowed to reach steady state operation before the oxy-fuel testing is commenced.

Under the recycled flue gas mode of operation, the air is incrementally reduced but at each step following an increase in the flue gas recycle and O_2 top-up. The flow rate of recycle flue gas is monitored by a differential pressure (DP) cell and the stoichiometry is monitored by O_2 metering at flue and recycle flue gas after the O_2 injection. Using this method incremental steps in the increase of recycle flue gas are made while maintaining the correct burner stoichiometry and flue gas dry O_2 concentration at a minimum of 3.5% throughout the process.

3.7 Experimental Parameters

The experimental parameters for air- and oxy-fired cases, are shown in Table 3.4. These flow rates were calculated using mass balance equations, assuming complete combustion of the fuel (the composition of which was taken from the ultimate and proximate analysis). Dry air with a 20.9% O_2 concentration was used in the calculations and the dry exit O_2 composition of 3.5% was targeted. For more details on the technique, see section 9.B, Theoretical Air Requirements, in Harker and Backhurst (1981).

For the oxy-fired trials, flow rates corresponding to different techniques in splitting the combustion air were calculated; one maintaining the volumetric flow, and therefore the velocity, constant within the Primary, whereas the other keeping the split between the Primary and Secondary/Tertiary registers constant.

Smart *et al*. (2010a) and Zang et.al. (2011) both fixed the primary volume flow when moving from air to oxy-firing, and also as the amount of the total O_2 concentration was increased (corresponding to decreasing the recycle ratios). This scenario represents an ideal condition in terms of operational control as the flow of the primary air stream carrying the pulverised fuel is not changed. It also maintains the velocity in the primary annulus, and therefore the momentum of the coal particles leaving the burner throat. This approach corresponds to Oxy Opt1 shown in Table 3.4.

However, Fry (2011) found that the above approach decreased the flame stability and this resulted in a lifted unstable oxy-flame. Furthermore, reducing the primary volume flow resulted in a stable oxy-flame, with a visibly similar intensity as that of the air fired base flame.

At EON’s test facility, where a 1 MW version of the 250 kW Doosan burner used here, was tested under oxy-firing, the primary to the total oxidiser volume ratio was maintained approximately constant, resulting in reduced primary volume flows at increasing total O_2 concentrations (Gharebaghi, 2011). This corresponds with Oxy Opt2 shown in Table 3.4.

Table 3.4. Experimental parameters for the non-preheated and preheated air-firing cases, together with the oxy-coal combustion programme. Different options for the oxy-fuel oxidiser split were considered, shown in Opt1 and Opt2. Theoretically calculated values are shown in Italic and actual flow measurments during the cases investigated are shown in bold and

	Air		**Oxy-fuel Opt1– Constant Primary velocity**			**Oxy-fuel Opt2– Constant Burner Split**		
	Non-Preheat	Preheat	Preheat			Preheat		
Total O_2 (vol%)	20.95		21	27	30	21	27	30
Total O_2 (wt%)	23.15		16.2	21.2	23.8	16.2	21.2	23.8
Primary								
Flow (kg/hr)	**60.1**	**60.1**	*83.4*			*88.3*	**64.6**	**57**
sd (kg/hr)	**0.1**	**0.2**	*n/a*			n/a		
O_2 (vol%)	**20.95**		*18*			**18**		
O_2 (wt%)	**23.15**		*13.8*			**13.8**		
O_2 (kg/hr)	n/a	n/a	*11.5*			*12.2*	**8.9**	**7.9**
sd (kg/hr)	n/a	n/a	n/a			n/a	**0.4**	**0.4**
sd (% of total O_2)	n/a	n/a	n/a			n/a	**0.5**	**0.6**
CO_2 (kg/hr)	n/a	n/a	*71.9*			*76.1*	**55.8**	**49.2**
sd (kg/hr)	n/a	n/a	*n/a*			*n/a*	**0.6**	**1.0**
Temp (°C)	**18**	**21**	*n/a*			*n/a*	**21**	**28**
sd (°C)	**0.1**	**0.2**	*n/a*			*n/a*	**0.3**	**1.1**
Sec/Tertiary								
Flow (kg/hr)	**244.3**	**244.3**	*354.3*	*231.7*	*192.1*	*349.4*	**250.4**	**222.8**
sd (kg/hr)	**1.1**	**1.0**	n/a			n/a		
O_2 (vol%)	**20.95**		*21.7*	*30.1*	*34.8*	*21.8*	**29.3**	**33.0**
O_2 (wt%)	**23.15**		*16.8*	*23.9*	*28*	*16.8*	**23.1**	**26.4**
O_2 (kg/hr)	n/a	n/a	*59.4*	*55.3*	*54*	*58.7*	**57.7**	**57.6**
sd (kg/hr)	n/a	n/a	n/a			n/a	**0.9**	**1.0**
sd (% of total O_2)	n/a	n/a	n/a			n/a	**1.3%**	**1.5%**
CO_2 (kg/hr)	n/a	n/a	*294.9*	*176.4*	*138.1*	*290.7*	**192.1**	**160.2**
sd (kg/hr)	n/a	n/a	n/a			n/a	**0.3**	**3.3**
Temp (°C)	**20**	**258**	***~250***			n/a	**244**	**253**
sd (°C)	**0.0**	**0.2**	n/a			n/a	**0.2**	**0.4**
Purge air								
Flow (kg/hr)	**7.8**	**3.1**	*3.1*			**3.1**		
Temp (°C)	**18**	**21**	*~20*			**20**		
Fuel								
Coal (kg/hr)	**24.4**		*24.4*			**24.4**		
Coal (kW)	**200**		*200*			**200**		

It is found that the second method appears to offer greater flame stability and, following informal consultations with industrial experts, was selected.

A 21% by volume O_2 concentration case, similar to that of air, has not been studied here due to the expectation that this case would produce significantly lower furnace temperatures and heat flux results than that of the air-firing case, and therefore rendering this setup not feasible for retrofit applications. This assumption is based both on the findings in the literature (e.g. Liu *et al*., 2004) and on the measurements conducted for this thesis which show that the temperature and heat flux values for the oxy27 case are lower than those for the air-firing case.

3.8 Commercial 500 MW boiler

Chapter 6 presents CFD modelling work undertaken on a commercial 500 MW boiler, which draws on the validation data provided by RWE npower. A brief description of the modelled part of the boiler, the fuel used and experimental conditions are outlined below.

Didcot A is a 500 MW_e sub-critical coal-fired power plant based in the UK. The CAD illustration of the furnace volume used for the CFD modelling is shown in Figure 3.21.

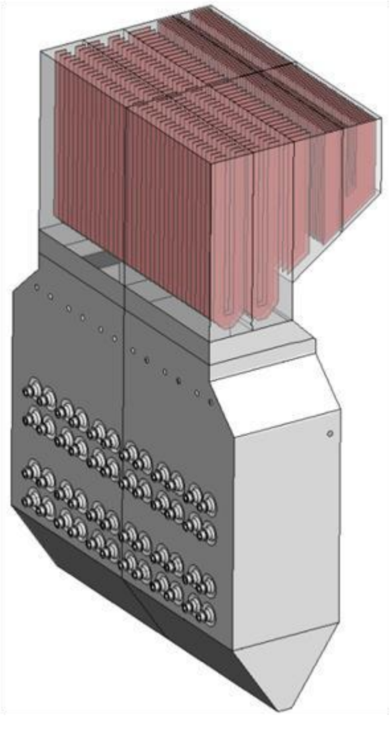

Figure 3.21. CAD drawing of the 500 MW Didcot A boiler (Edge, 2011).

The furnace measures 30m(w) x 10m (d) x 20m (h), and the burners, arranged in 4 rows of 12, are mounted on the front wall. The ash hopper is located at the bottom of the furnace. The arrangements of the radiative superheaters are shown in Figure 3.22.

The geometry and initial mesh was taken from Edge (2011), where more detailed geometrical data can be found.

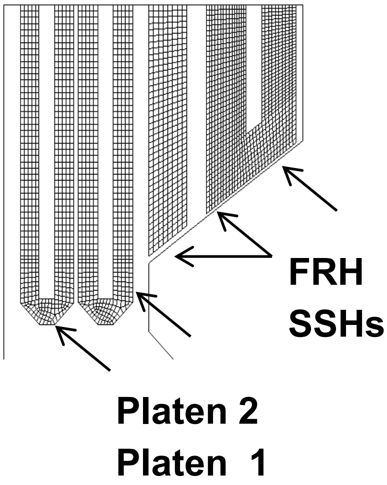

Figure 3.22. Arrangement of the heat exchangers on the radiative boiler section.

3.8.1 Burner Description

The furnace is fitted with 48 Doosan Babcock MK-III Low-NO_x burners, each with three co-axial inlets (Figure 3.23). The coal is delivered through the primary annulus by the carrier air, and the rest of the combustion air is delivered through the swirled secondary and tertiary annuli. The inner and outer diameter of the primary annulus is 32.4 and 53.6 cm, respectively, the secondary 53.6 and 73 cm and the tertiary is 73 to 94.9 cm.

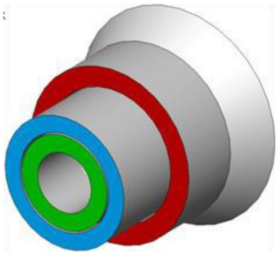

Figure 3.23. Primary (green), secondary (blue), tertiary (red) burner registers (Edge, 2011).

3.8.2 Test Fuel Used

The coal fired in the modelled case, was Pittsburgh 8. The fuel analysis was provided by RWE and is shown in Table 3.5, together with the properties of the milled wood modelled. The size distribution of the coal given by RWE is shown in Table 3.6, which was measured for a similar coal used at Didcot A. Calculated Rosin-Rammler parameters and mean shape factor of the fuels are shown in Table 3.7. The calculation procedure is described in more detail in Section 3.4.

Table 3.5. As received fuel analysis for Pittsburgh 8 provided by RWE (Edge, 2011) and milled wood.

Ultimate	Coal (mass%)	Biomass (mass%)
C	67.5	52.3
H	4.5	6.4
O (by diff.)	5.6	41.1
N	1.3	0.2
S	2.1	trace
NCV (MJ/kg)	27.3	17.4

Proximate	Coal (mass%)	Biomass (mass%)
FC	50.1	18.9
VM	30.9	72.6
Ash	10.6	2.8
Moisture	8.4	5.7

Table 3.6. Coal particle size analysis (Edge, 2011).

Sieve size (µm)	% remaining
300	0.03
150	4.1
75	24.15

Table 3.7. Calculated Rosin-Rammler parameters and mean shape factor of the fuels.

	Pittsburgh No. 8 (µm)	White wood (µm)
Minimum dimension	1 (sphere)	90 (cylinder)
Maximum dimension	300 (sphere)	3000 (cylinder)
Mean diameter	70 (sphere)	330 (spherical equiv.)
Spread	1.19	1.35
Mean shape factor	1	0.83

3.8.3 Boundary Conditions

The overall heat transfer coefficient through the walls, taking account of the slag layer, was approximated as 0.2 kW/m^{2}K, with a likely range of 0.1-0.35 kW/m^{2}K (Edge, 2011). Outer wall temperatures for the boundary were assumed to be determined by the temperature of the water/steam flowing within the tubes. The temperature of the water wall was taken as 350°C, and the temperature of the superheaters were taken as the mean of the inlet and outlet steam temperatures, shown in Table 3.8.

Table 3.8. Approximate steam inlet and outlet temperatures within the superheaters (Edge, 2011).

	Steam in (°C)	Steam out (°C)
Superheater platen 1	390	471
Superheater platen 2	403	489
Secondary superheater	489	568
Final reheater	494	570

The air and fuel flow rates for 1 of the burners are shown in Table 3.9. From the 48 burners 36 were firing during this test, and it is assumed that the total flows were split equally between the burners. The swirl angles within the annuli and swirl pattern within the boiler are shown in Table 3.10 and Table 3.11, respectively.

Table 3.9. Fuel and air flow rates, and temperatures for the modelled test case (Edge, 2011).

Settings	
Coal (kg/s)	46.7
Total air (kg/s)	529
PA temperature (°C)	90
SA, TA temperature (°C)	250

Table 3.10. Swirl angle of burner registers (Edge, 2011).

Annulus	Flow (%)	Swirl angle (°)
Primary	20	0
Secondary	15	50
Tertiary	65	25

Table 3.11. Pattern of swirl direction for the burners (Edge, 2011).

Swirl direction (X = clockwise)		
OXOX	OXOX	OXOX
XOXO	XOXO	XOXO
OXOX	OXOX	OXOX
XOXO	XOXO	XOXO

3.8.4 Test Results

A limited amount of experimental measurements were provided by RWE (Table 3.12). Further results were provided by RWE's in-house MOPEDS model (see Mobsby, 1984), developed empirically at Didcot. A full list of boiler data provided by this code for the modelled case can be found in Edge (2011). The rate of heat transfer to the heat exchangers modelled here is shown in Table 3.13.

Table 3.12. RWE test results (Edge, 2011).

O_2 (%, dry)	CO (ppm at 6% O_2)	NO (ppm at 6% O_2)	CIA (%)	Furnace exit temperature (°C)
7.5	64	306	11.6	1043

Table 3.13. Heat absorbed by the modelled heat exchangers (Edge, 2011).

	Heat distribution (MW)
Plat 1	106
Plat 2	110
Secondary superheater	110
Final reheater	79

3.8.5 Modelled Cases

Table 3.14 shows the boundary conditions investigated for the modelled oxy-fired and biomass co-firing cases.

Table 3.14. Operating conditions for all test cases, where V corresponds to the validation conditions

	Fuel	Oxidising atmosphere		
		Air	Oxy25	Oxy30
Fuel feed rate (kg/s)	coal	46.7^{V}	46.7	46.7
	blend (coal/biom.)	37.4/14.7	37.4/14.7	37.4/14.7
	biomass	73.2	73.2	73.2
Oxidiser feed rate (kg/s)	coal	529^{V}	500	402
	blend	530	490	395
	biomass	535	461	375
Recycle Ratio (%, wet)	coal	n/a	71	65
	blend	n/a	69	63
	biomass	n/a	65	58
Exit O_2 (vol%, dry)	for all fuels	5^{V}	5	5
Thermal input (MW_{th})	for all fuels	1275^{V}	1275	1275
Leakage (air)	for all fuels	$3\%^{V}$	3%	3%
Operating burners	for all fuels	36^{V}	36	36

The results of the air and oxy-fired cases obtained in the 250 kW Oxy-fuel Combustion Test Facility are discussed in the Chapters 4, and the CFD modelling results obtained on the 500 MW commercial scale boiler decried here are discussed in Chapter 5.

Chapter 4

Experimental Results and Analysis

This chapter first presents results for the air-firing of coal using non-preheated and preheated air. Comparison of the cases is drawn against flue gas emissions, char burnout, in-furnace process temperature measurements and radiative heat flux.

The effect of using the low NO_x burner's capability to modify burner staging is examined. Staging is achieved by adjusting the split of combustion air through the secondary and tertiary registers and its effect on NO and CO emissions are compared between the cases.

Flame temperatures, measured by suction pyrometry are compared for the different axial positions. The results of total and radiative heat flux characterisation are presented and discussed, along with the calculated convective heat flux data.

Next, results for oxy-firing of coal at the total O_2 concentration of 27% (oxy27) and 30% (oxy30) by volume are presented. Comparison of the cases is drawn against flue gas emissions, in-furnace temperatures and heat flux measurements.

Given the reliance on existing coal-fired power stations, it is essential that oxy-fuel technologies have a retrofit capability. Therefore the focus is on assessing the possibility of matching air-fired temperature profiles and heat transfer characteristics during oxy-firing, which are especially important when retrofitting existing boilers that were designed for air-firing. By matching these, it may be possible to achieve similar flame stabilities, burnout, amount and quality of steam raised and also similar slagging and fouling tendencies (Chen *et al*., 2012). Another important aspect is the effect of oxy-firing on flue gas emissions, which is also investigated below.

The results presented in this chapter, which are based on experiments using a high volatile bituminous coal, add to those from oxy-coal experiments undertaken at other facilities. Also, they assist in the building of a data base for oxy-fuel specific CFD submodel development and validation work.

4.1 Air-fired Results and Analysis

The results for air-firing of coal are presented below. The effect of using non-preheated and preheated air, as well as the low NO_x burner's capability to modify burner staging, is examined. Furthermore, flame temperatures and radiative heat flux characterisation are presented and discussed, along with calculated convective heat flux data.

4.1.1 Effect of Preheating the Combustion Air

As part of the development of the furnace, the burner was commissioned with non-preheated air. This also provided an opportunity to compare the effect of preheating the combustion air on the combustion performance of the burner.

4.1.1.1 Emissions

Table 4.1 presents the flue gas emission measurements for the two cases. Values for both the actual measurements, and those corrected for 6% O_2, are shown.

The actual measurements show a reduced O_2 and increased CO_2 concentration when moving to the pre-heated case. Theoretical calculations showed that the effect of improved burnout for the preheated case (Table 4.3) is less significant and only expected to reduce the O_2 and increase the CO_2 at the exit by ~0.1%. Flow rates of coal and air supply to the burner were kept the same for both cases but the purge air to the observation windows were different due to higher flow rate being used after commissioning and optimising the window purge (for the non-preheated measurements), 100 L/min as opposed to 43 l/min during the subsequent runs. Theoretical calculations show ~0.2% decrease in O_2 and increase in CO_2 concentration, when the purge in reduced. Therefore, the difference is mainly due to the amount of the window purge, partially to the differences in burnout, but partially may also be due to the experimental uncertainty having an influence.

The SO_2 emissions were not affected by preheating (variation observed was within the total uncertainty). However, NO emissions were significantly increased, producing 36% higher emissions for the preheated case, whereas CO emissions decreased. Preheating the combustion air increases the temperature of the shear combustion layer between the oxygen-lean primary and the staged-secondary streams, thus increasing the thermal NO_x formation.

Table 4.1. Flue gas emissions for the preheated and non preheated cases.

	Non-Preheat		**Preheat**	
Flue, dry	**Value**	**Error**	**Value**	**Error**
O_2 (%)	3.8	± 0.2	3.3	± 0.2
CO_2 (%)	15.3	± 0.5	15.7	± 0.4
SO_2 (ppm)	291	± 22	284	± 23
NO (ppm)	276	± 17	374	± 17
CO (ppm)	29	± 9	4	± 8
Flue, dry at 6% O_2				
CO_2 (%)	13.4	± 0.5	13.3	± 0.4
SO_2 (ppm)	254	± 22	240	± 23
NO (ppm)	241	± 17	316	± 17
CO (ppm)	25	± 9	3	± 8

The previous 6% O_2 correction table is suitable for comparing emissions performance between similar technologies, e.g. different commercial air-fired boilers burning pulverised coal. However, emission indices reported on a unit heat input allow for the comparison of emissions between different power generation technologies, which may use different oxidisers, which can radically change the flue gas volume flow and concentration of pollutant species. Emission indices on this basis are shown in Table 4.2.

In comparison, NO emissions measured by researchers at a number of other experimental facilities are: 340 mg/MJ (University of Leeds' 20 kW combustor), 255 (RWTH Aachen University's 100 kW CTF), 161 (Chalmers University's 100 kW CTF), 97 (at EON's 1 MW CTF) (Chen *et al.*, 2011). These results show a wide range of variations, which is reasonable when considering the variables between these facilities influencing the NO emissions. These include the N content of the coal, the burner configuration and the resulting aerodynamics which is also influenced by the shape and dimensions of the furnace enclosing the flame. The NO results obtained in this PhD thesis fit within the emissions measurements at these facilities.

Table 4.2. Emissions indices for the preheated and non preheated air fired cases.

	non-preheat	**preheat**
CO_2 (g/MJ)	103	106
SO_2 (mg/MJ)	287	287
NO (mg/MJ)	128	173
CO (mg/MJ)	13	2

4.1.1.2 Burnout

Burnout, which is a measure of combustion efficiency, is shown in Table 4.3. It shows significant carbon content in the ash for the non-preheated case (LOI of 25.5%). Under current legislation, this ash would not be permitted to be sold on (e.g. for use as an aggregate in the construction industry) since the maximum acceptable carbon content is 6-7%. Instead, it would have to be landfilled and, rather than generating income, would incur charges due to landfill tax and other associated costs.

In a commercial application, modifications would be necessary to improve burnout and in this case, preheating was applied to the combustion air supplies. This achieved a threefold reduction in the carbon content of the ash (producing an LOI of 7.2%). This just falls above the permitted target. However, it should be noted that the ash content of the coal fired in these cases is very low (1.5%), as opposed to a typical bituminous coal. The uncertainty associated with burnout measurements increases significantly when the ash content of the coal is low. The accuracy of the measurements of the fuel ash content could be increased. This can be achieved by blending the coal with a higher ash content fuel, or inert additives, such as perlite could be used to artificially increase the total ash content of the blend, such as used by Ballantyne (2005). However for the results obtained for the low ash content coal, it can be seen that even a low remaining char constitutes a larger fraction of the ash. For comparative purposes, Table 4.3 shows LOI values calculated for a typical 8% ash content coal. Assuming that the change in ash content does not alter the total amount of char remaining in the ash, the preheated case would produce an LOI of 1.5%, which is well within the target; thus suggesting good burnout. This is confirmed by the ash tracer results, which show burnout as a percentage of original dry ash free coal. For the preheated case, the burnout was 99.9%.

To meet the 6% target for carbon content in ash, the coal used here could be blended with a higher ash-content coal.

Table 4.3. Burnout determinations made for the non-preheated and preheated air cases. For comparison purposes LOI and burnout were also calculated for a typical 8% ash content coal.

	Non-Preheat		**Preheat**	
at dry ash % of	**1.5**	**8***	**1.5**	**8***
LOI (%)	25.5	6.1	7.2	1.5
ash tracer (%)	99.5		99.9	

4.1.1.3 Process Temperature Measurements

The effect of preheating the air is also shown in the readings of the sheathed Type R thermocouples. These are located at different axial positions along the furnace. However, all of them are at the same radial position, 200 mm from the inner wall of the furnace and 250 mm from the centre line. As can be seen in Figure 4.1, the temperature difference is largest close to the burner. It then decreases progressively due to the heat being extracted through the refractory sections, as higher gas temperatures increase the heat transfer through the light density refractory wall. The temperature increase that is limited to the flame section is beneficial for burnout, even though it reduces the residence time due to the increased volume flow rate (Su *et al.*, 2001).

However it must be noted, that the sheathed process thermocouples are subject to radiative losses as they are exchanging heat with the relatively cooler walls, which results in them measuring temperatures that are lower than the true gas temperatures. Therefore the results presented in Figure 4.1 should be considered as qualitative only, and also specific to the location of the thermocouples rather than along the whole of the furnace cross section at each axial position shown. For quantitative results with detailed spatial resolution suction pyrometry was used, and these results are detailed in Section 4.1.3.

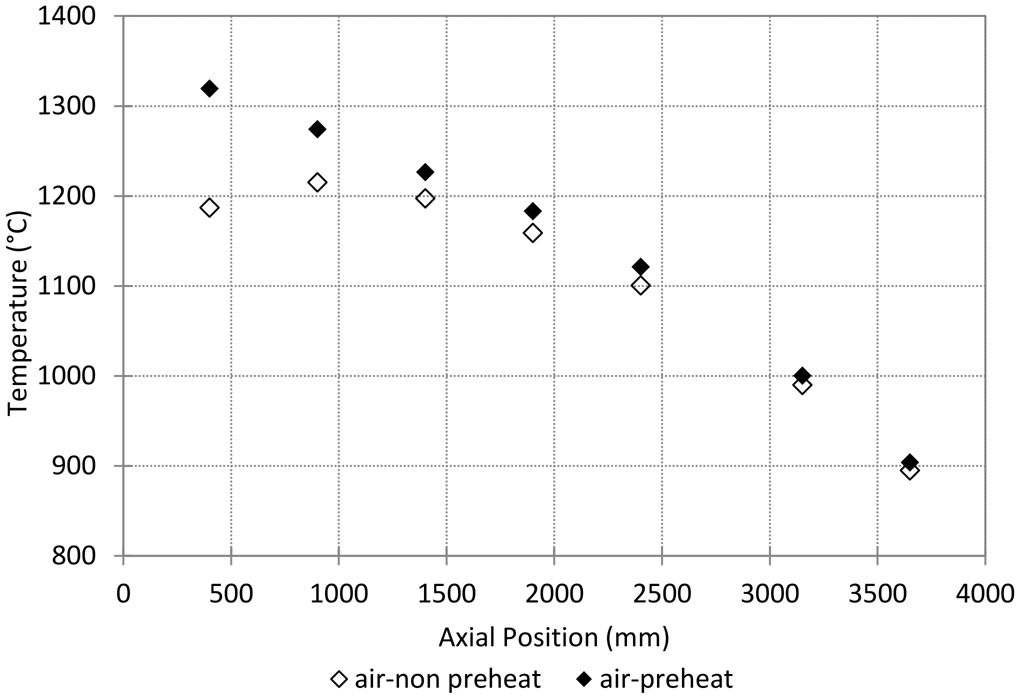

Figure 4.1. In-furnace process temperature measurements, recoded using sheathed Type R thermocouples positioned 200 mm from the inner wall.

4.1.1.4 Radiative Heat Flux

Results of radiative heat flux measurements using the Medtherm heat flux probe fitted with the CaF_2 window attachment (described in Section 3.3.4) are shown in Figure 4.2. Pronounced dips, deviating from the general trend, were observed in both cases. This is likely to be due to increased levels of deposition on the probe window that were observed at these locations during the tests. Although the probe is equipped with a N_2 screen to shield the front window attachment from the convective heat flux, and also to protect it from particulates and soot deposition, at certain positions this gas screen appeared less effective even when it was increased to the maximum recommended purge pressure (4.5 bar at the supply). Since measurements from these locations were affected by deposition and clearly erroneous, they were removed from the data sets used for comparison (see Figure 4.3).

It should be noted, however, that the dips due to deposition occurred at different axial positions from the burner in the two cases. This indicates changes in the aerodynamics between the cases. The higher inlet velocity of the preheated secondary and tertiary air streams increases the shear between the primary and combustion air streams and this increases their mixing. This may shorten the flame and shift the impingement point shown in Figure 4.14, resulting in the shift in the location of the high particle/soot load near the furnace wall.

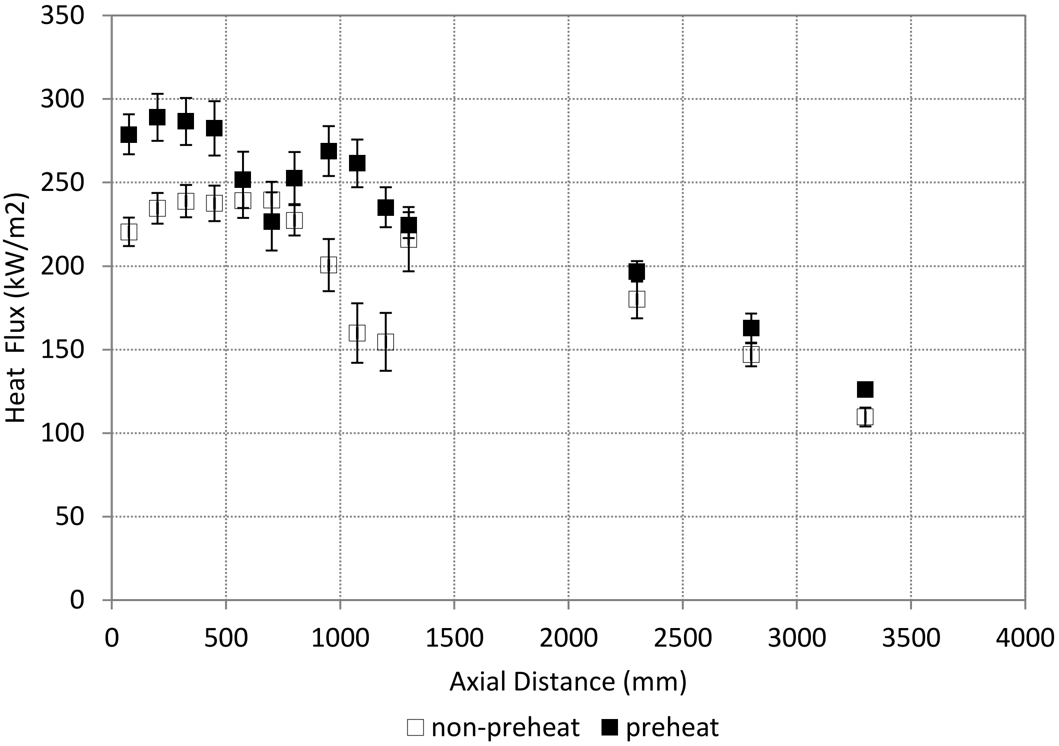

Figure 4.2. Radiative heat flux measurements for the non-preheated and preheated cases using the CaF_2 window attachment and N_2 screen.

Radiative heat flux increases for the pre-heated case. The difference is at its largest near the burner throat, and then reduces towards the furnace exit (a similar trend to that observed with the thermocouples, see Figure 4.1). Since radiative heat transfer is proportional to the temperature to the power of 4, this result is to be expected. For greater clarity, the ratio of the radiative heat flux between the preheated and non-preheated cases is shown in Figure 4.4. The increases near the flame region would result in increased radiative feedback between adjacent burners in commercial multi burner boilers, further increasing the radiative heat available to heat the fuel particles and having a beneficial effect on flame stability.

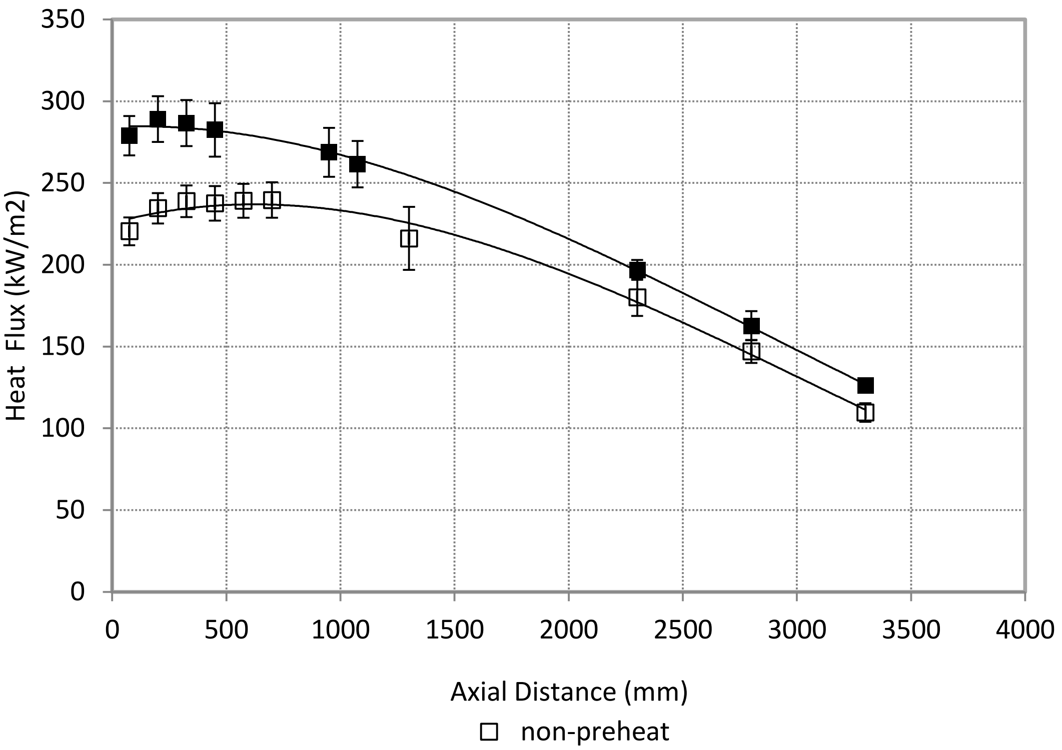

Figure 4.3. Radiative heat flux measurements for the non-preheated and preheated cases using the CaF_2 window attachment and N_2 screen. Measurements below the trend line (more than their respective error bars) were removed on the assumption that they were affected by the sooting of the probe window attachment.

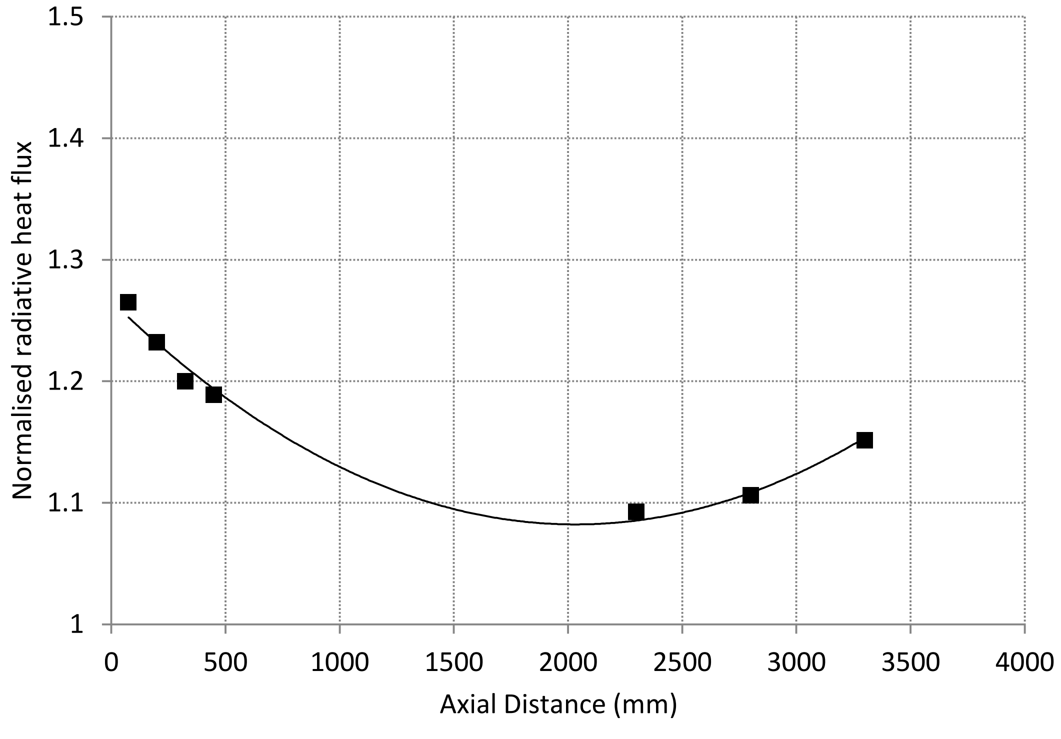

Figure 4.4. Normalised radiative heat flux measurement. Calculated as preheated over the non-preheated heat flux value.

4.1.1.5 Summary of Findings

Preheating the combustion air has significant advantages. It increases the efficiency of the power generation process by enabling low-grade sensible heat recovery from the flue gas, recycling it into the boiler. This increases the heat input to the burner, facilitating ignition and therefore stabilising the flame. The additional heat also enhances the devolatilisation and improves burnout, further enhancing the efficiency of the process. The radiative heat transfer from the flame also increases, which is significant because it is the main and most important form of heat transfer within the furnace (Chedaille and Braud, 1972). However, the disadvantage of preheating combustion air is that it also increases the temperature of the shear combustion layer between the O_2-lean primary and the staged-secondary streams, thus increasing thermal NO_x formation.

4.1.2 Effect of Varying Burner Staging on Emissions

The theory and mechanics of NO_x reduction by burner staging was discussed in Chapter 2. This test campaign was performed in order to investigate the effect of burner staging on NO_x and CO emissions and also to establish the optimal emissions performance of the burner for the non-preheated and preheated cases.

The total amount of air and the ratio of the primary air were maintained the same throughout the tests and the investigation was performed by modifying the ratio of secondary to tertiary combustion air streams. This was achieved by altering the position of the internal secondary/tertiary split slide (Figure 3.4).

Flue gas emissions for the non-preheated and preheated cases are shown in Figure 4.5 and Figure 4.6, respectively, showing the results at the different secondary/tertiary split settings. Each split position shown refer to ~10 mm adjustments of the position of the internal slide (the operation of the slide is described in more detail in Section 3.2.2). The secondary x-axis shows the resulting of the secondary/tertiary splits calculated using CFD modelling (Black, 2014).

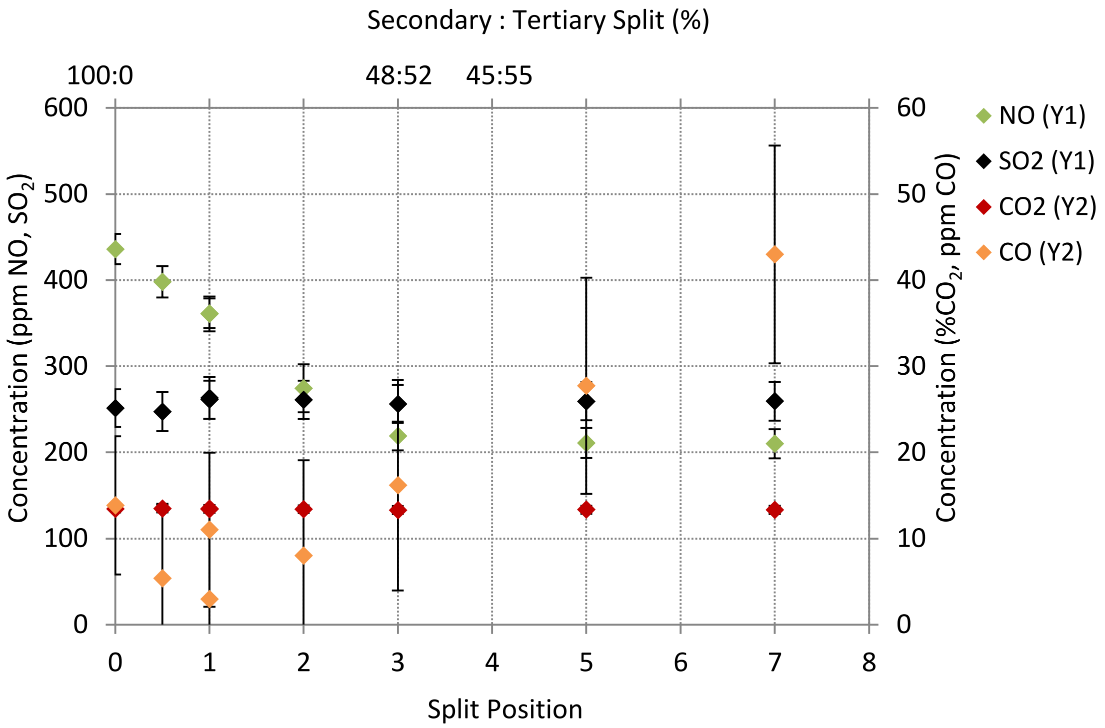

Figure 4.5. Emissions measurements of NO, SO_2, CO_2 and CO for the non-preheated air-fired case at different Secondary/Tertiary split settings, corrected to 6% exit O_2.

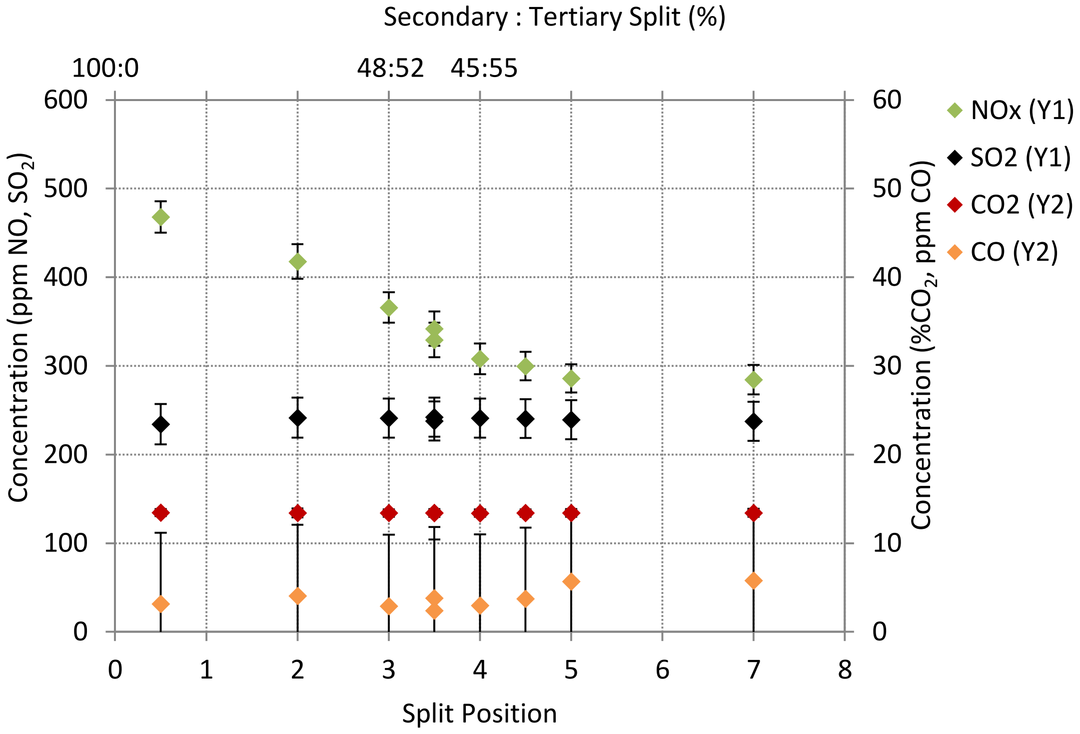

Figure 4.6. Emissions measurements of NO, SO_2, CO_2 and CO for the preheated air-fired case at different Secondary/Tertiary split settings, corrected to 6% exit O_2.

CO_2 and SO_2 emissions remained stable as the split positions were adjusted, which suggests that there were no major problems with the flame. The effect of staging on NO and CO emissions is compared across the cases.

The highest NO emissions correspond to a split position 0 for both cases (Figure 4.7 and Figure 4.9). This is where the tertiary annulus is blocked off, and all of the combustion air is supplied through the secondary stream (for more details see Section 3.2.2). As the split slide is adjusted, NO emissions decrease steadily, before stabilising at split positions 3 and 4, for the non-preheated and preheated cases, respectively.

For the non-preheated case, there are no further reductions in NO emissions after split position 3. The CO emissions follow an opposite trend, remaining relatively stable, with slight changes within the range of 3-16 ppm, up until split point 3. Thereafter, CO emissions increase dramatically, reaching 43 ppm by split position 7. For the non-preheated case, based on these results, the split position 3 was adopted as the optimal mode of operation for the burner. Figure 4.8 shows a repeat of these measurements taken during the 2D/3D flame imaging studies conducted in collaboration with the University of Kent. The measurements shown here do not replicate those of the original experiments. Indeed, the aerodynamics within the flame region were changed considerably due to air purges introduced through the 7 imaging probes (130 l/min in total) pointed towards the flame at 200 mm axial distance from the burner quarl. At split 0, NO emissions are matched for both cases, but as the split is adjusted during the Kent trial, NO emissions showed higher levels, which is probably due to the purging jets enhancing the mixing between the internal recirculation zone and the staged combustion air swirling around it. Nevertheless, the general downward trend previously observed for the non-preheated case is confirmed.

For the preheated case, NO emissions continued to reduce beyond split position 3, but CO emissions remained low at every split ratio trialled (Figure 4.9) and for this case split position 4 was identified as the optimal mode of operation.

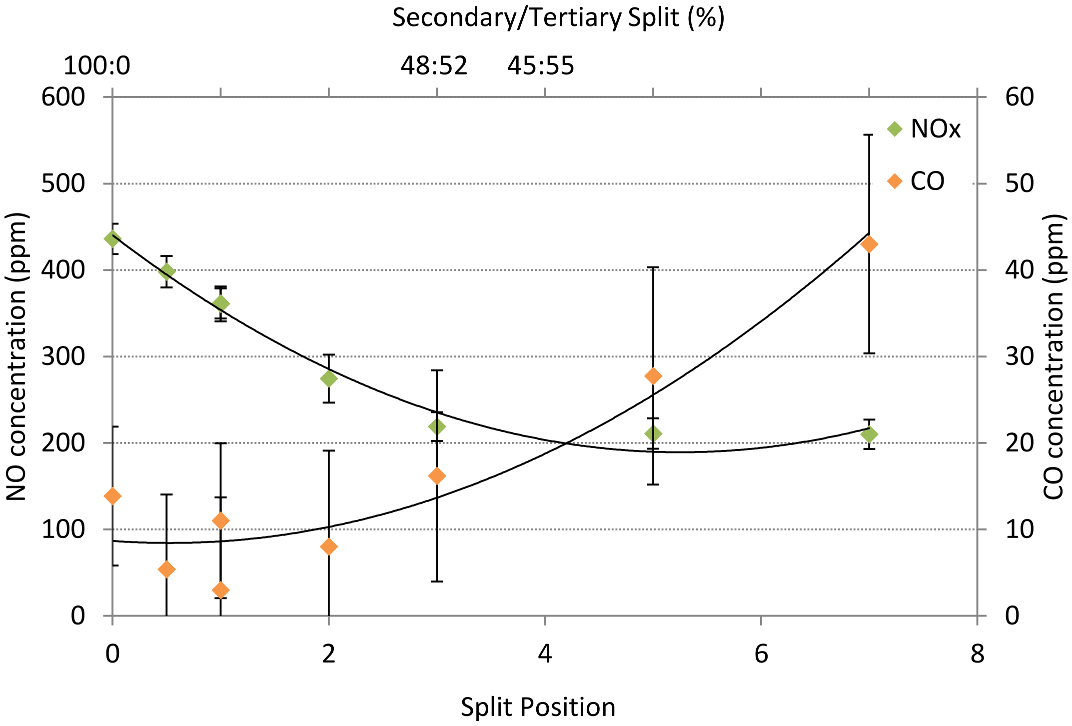

Figure 4.7. NO and CO emissions for the non-preheated air-fired case at different Secondary/ Tertiary split settings, corrected to 6% exit O_2.

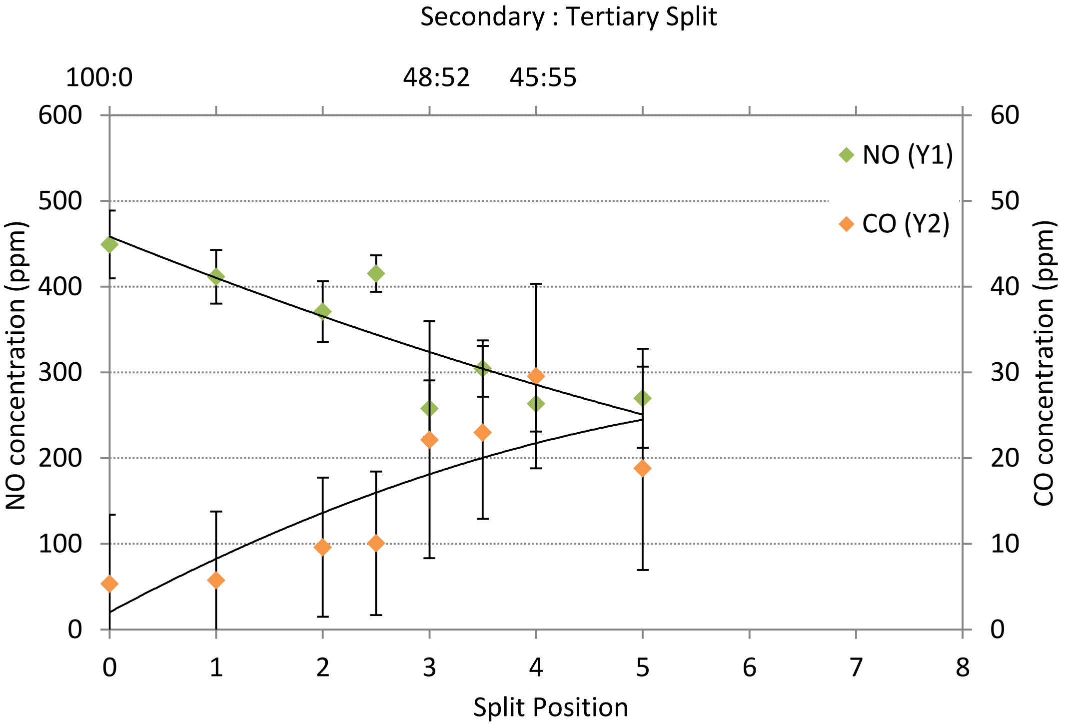

Figure 4.8. NO and CO emissions for the non-preheated air-fired case at different Secondary/ Tertiary split settings, corrected to 6% exit O_2. Results were recorded through the 2D/3D flame imaging study (with a total of 130 l/min purge air streams directed towards the flame from the imaging probe fitted at 200 mm axial distance from the quarl).

NO emissions are higher at every split setting compared with the non-preheated case (Figure 4.10). This effect was expected as the preheated air increases in furnace temperatures within the flame zone and most importantly within the quasi stoichiometric layer between the fuel rich primary zone and secondary combustion air stream, where most of the thermal NO formation takes place, due to the high temperatures associated with stoichiometric regions. However, the difference between the results at each split setting differ significantly, ranging from 11 to 67%. This difference points to the effect of changes in the aerodynamics within the flame, which is caused by the significant increase in the secondary and tertiary velocity whilst the primary inlet velocity remained constant. This changes the interaction between the primary and staging jets, increasing the shear and therefore the mixing between them. The increased mixing results in an increase in fuel NO formation as the residence time of the coal particles and the evolved volatile N species is decreased within the fuel rich reducing zone, which increases NO formation.

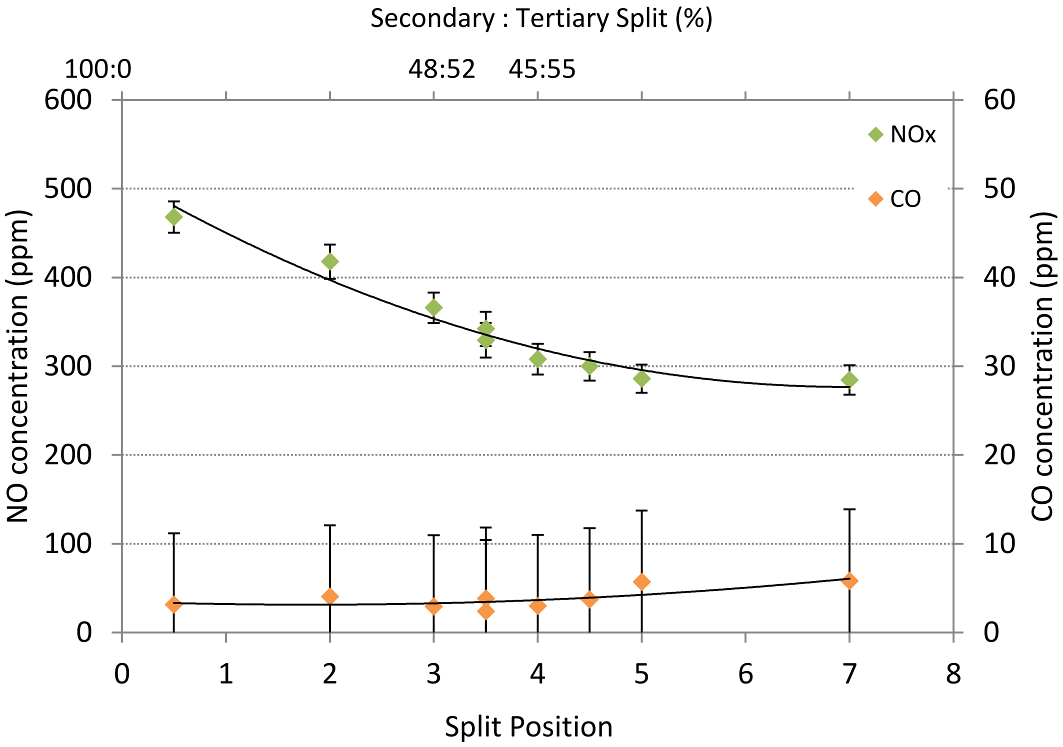

Figure 4.9. NO and CO emissions for the preheated air-fired case at different Secondary/ Tertiary split settings, corrected to 6% exit O_2.

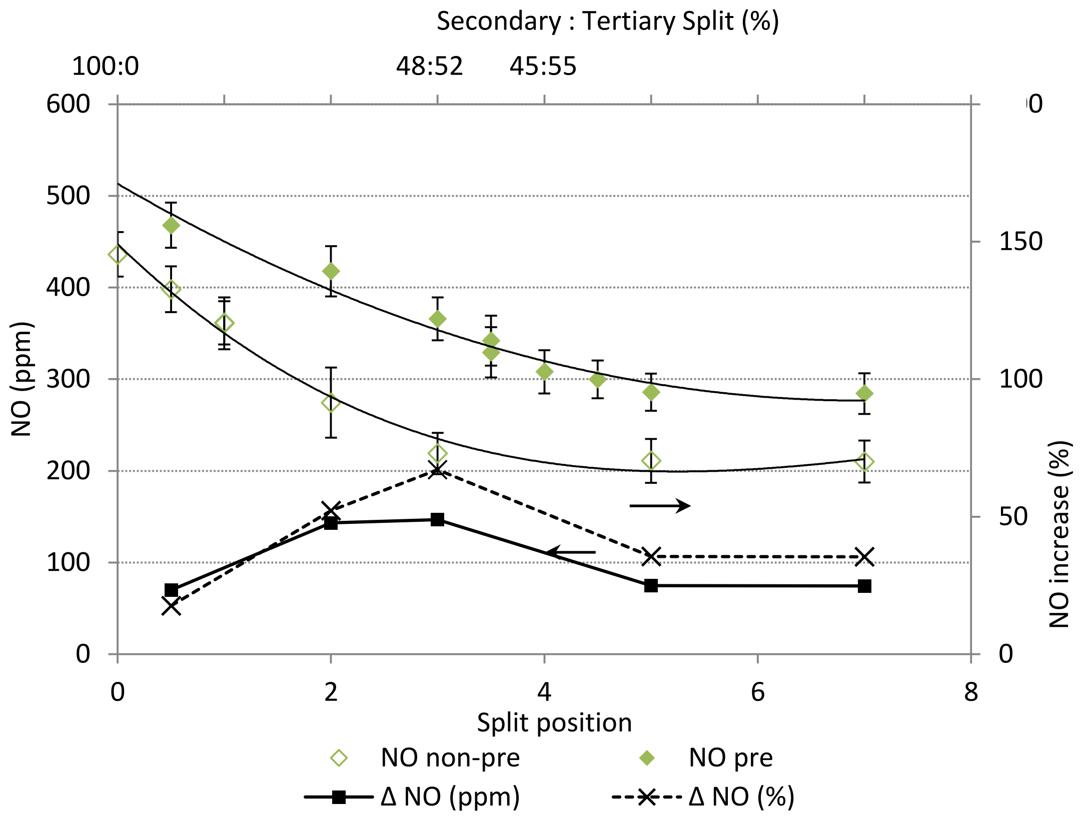

Figure 4.10. Comparison of NO emissions for the non-preheated and preheated cases.

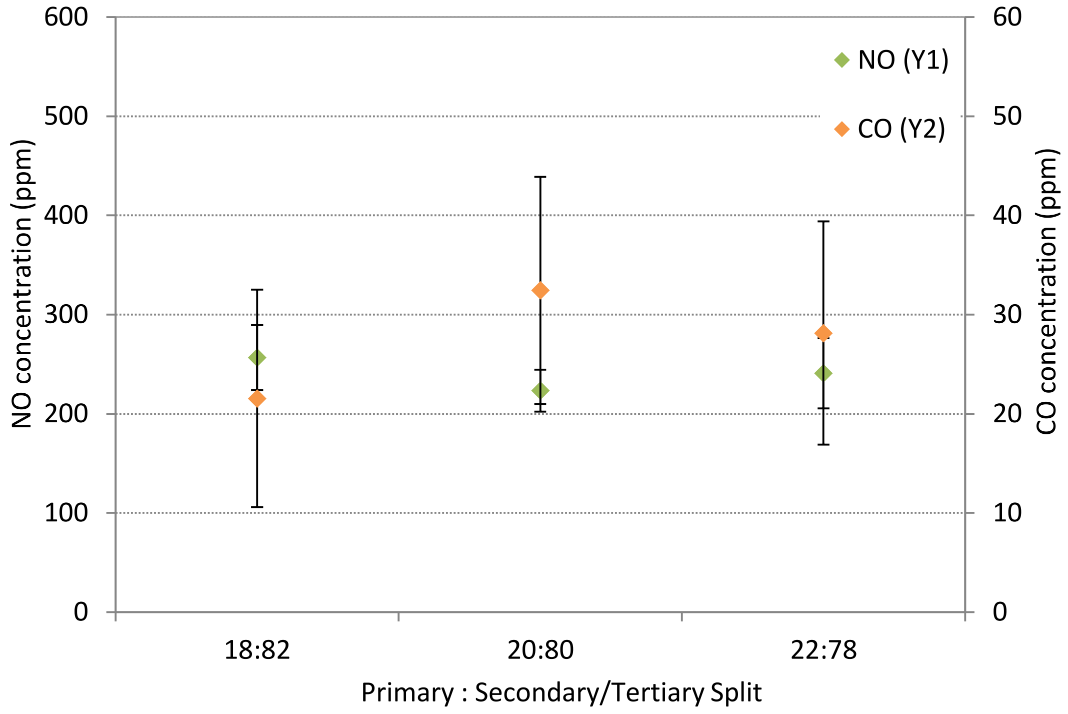

Figure 4.11. NO and CO emissions for the preheated air-fired case at different Primary ratios, corrected to 6% exit O_2, during 2D-3D flame imaging studies.

The primary to the total combustion air ratio was also investigated. The 20:80 primary to secondary/tertiary ratio was previously adopted based on the experience gained during the modelling work performed with the commercial 40 MW version of this burner (Szuhánszki *et al.*, 2013; Black *et al.*, 2013), on which the design of the 250 kW test burner was based. Figure 4.11 shows the test results when the secondary:tertiary ratio was maintained constant at 48:52 (split position 3), whilst the ratio of the primary was modified. Flue gas emissions showed a slight increase in the NO levels for both the reduced (18%) and increased (22%) primary cases, as well as a slight drop in the average CO emissions. However, the major impact of these changes was on flame stability. Figure 4.12 shows selected instantaneous images from the videos recorded by the 2D camera probe. It must be noted that during the imaging work 6 other probes were fitted in a half circular pattern opposite the 2D probe taking these images. The 2D probe had a 30 l/min purge stream directed towards the centre of the furnace, and the other 6 probes a total of 100 l/min. The effect of this is evident on the images as well as on the videos where a sustained deflection of the flame to one side is apparent.

The images (a1), (b1) and (c1) in Figure 4.12 show typical appearances of the flames. Individual jets are clearly visible in all cases near the burner throat, which are produced by the 4 coal concentrators fitted in the primary line. These are fitted for NO reduction purposes and cause the coal to devolatilise in highly concentrated jets, thus ensuring that the volatile N species evolve in regions of very low O_2 concentration (Paul and Datta, 2008). These jets remain separate within the quarl but start to spread out and merge within less than a burner diameter.

Important stability issues are highlighted on images (a2), (b2) and (c2) in Figure 4.12. The 20% primary case, (b2), shows 1 or 2 of the coal jets to detach from the burner and lift out of the quarl. This may have a significant effect on the NO emissions as the heating up and devolatilisation of the coal jets entering above these lifted jets will be affected, and possibly both reduced. Flame stability was observed to worsen for the 22% primary case where 3 or all 4 of the coal jets detach from the burner on a more regular basis. This is due to the increased primary velocity, 12% higher than for the 20% primary case.

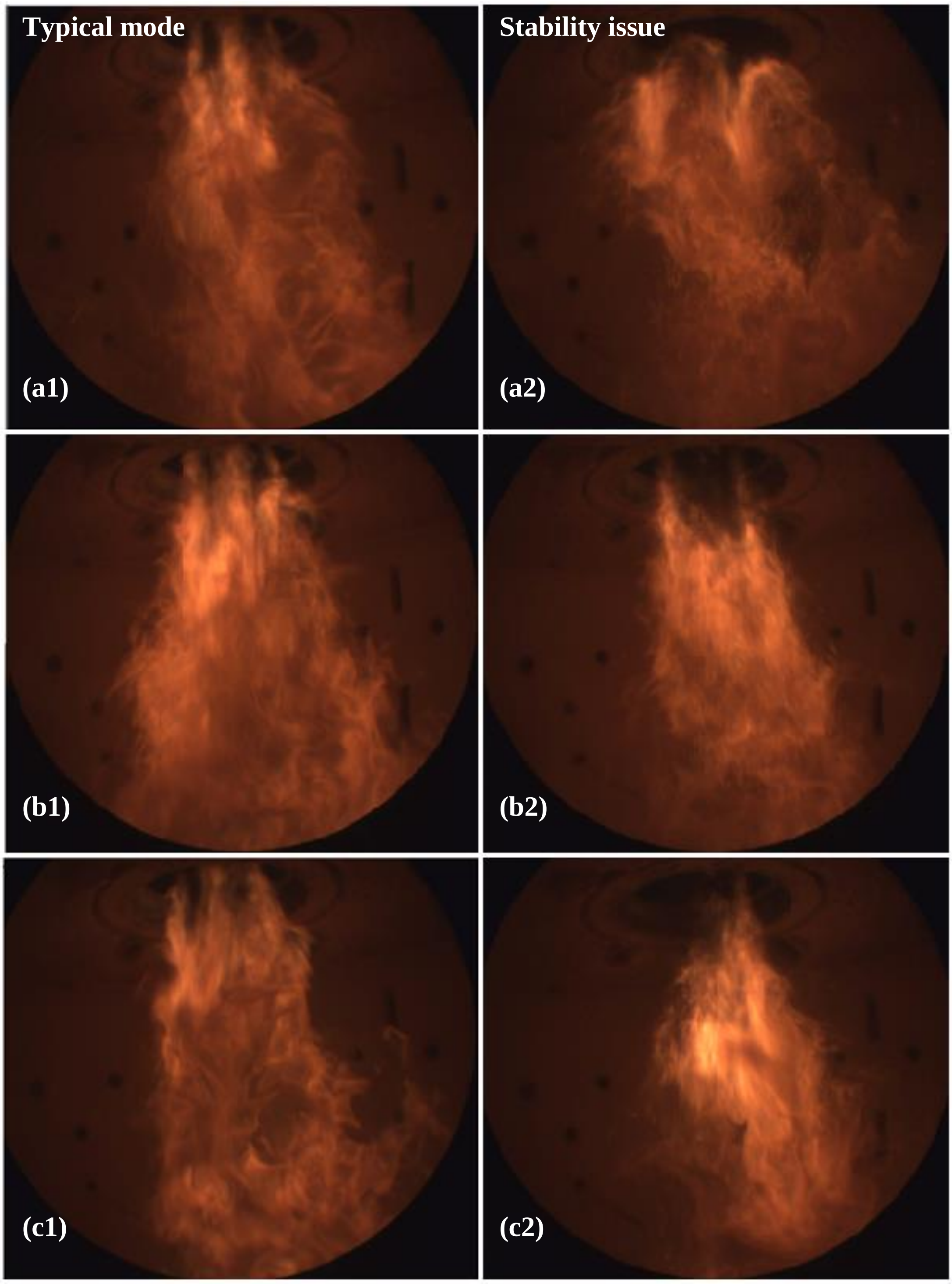

Figure 4.12. Instantaneous flame images taken for non-preheated air cases with the Secondary/Tertiary split position set at mark 3. The Primary to Secondary/Tertiary ratio was varied as: (a) 18-82%, (b) 20-80% and (c) 22-78%. The 1st image for each case shows the typical operating mode observed, whereas the second image show the main stability issue observed during the run. *These images in collaboration with Dr Moinul Hossain, Dr Duo Sun, Dr Gang Lu and Prof Yong Yan and the University of Kent*.

For the 18% primary case, the primary velocity is reduced by 10%, decreasing both the primary air and coal particle inlet velocities. This increases the residence time in the quarl zone, thus improving the heating up of the particles and therefore the stability of the flame, which is in general less prone to detachment of any of the 4 coal jets than for the other cases. However, periodically this flame was observed to completely detach from the burner, and, as a result, the 20% primary case was accepted as the optimal mode of operation.

Also, although there are no preheated images available at the time of writing, it is expected that flame stability improves for the preheated case. Preheating of the secondary and tertiary streams allow a higher quarl temperature to be sustained. This is due to the tendency of these jets to attach to the quarl, due to the swirling motion induced by the secondary and tertiary swirl blades, and therefore cooling it due to the good thermal contact, especially for the non-preheated case when the air is supplied at ~20°C. The quarl surface is an important source of radiative heat for the coal particles entering the furnace. Therefore it is expected that for the preheated case, the quarl surface temperature increases and the stability of the 20% primary case improves.

4.1.3 In-furnace Suction Pyrometry

Suction pyrometry enables measurement of local gas temperatures within the furnace. Knowledge of these is important when considering pollutant formation, especially thermal NO_x, as well as flame radiation, reaction kinetics, and soot formation. These measurements also provide detailed data from within the flame region close to the burner throat, which are important for CFD validation.

Figure 4.13 shows in-furnace temperature measurements at the axial distance (AD) of 75 mm from the quarl exit for the pre-heated air-fired case. The radial temperature distribution varies significantly across the furnace. There is an asymmetry that is not unexpected with this type of burner. All the air streams are swirling and the coal is collected into 4 concentrated primary air/coal streams which are well defined at close proximity to the burner outlet, lesser so further downstream.

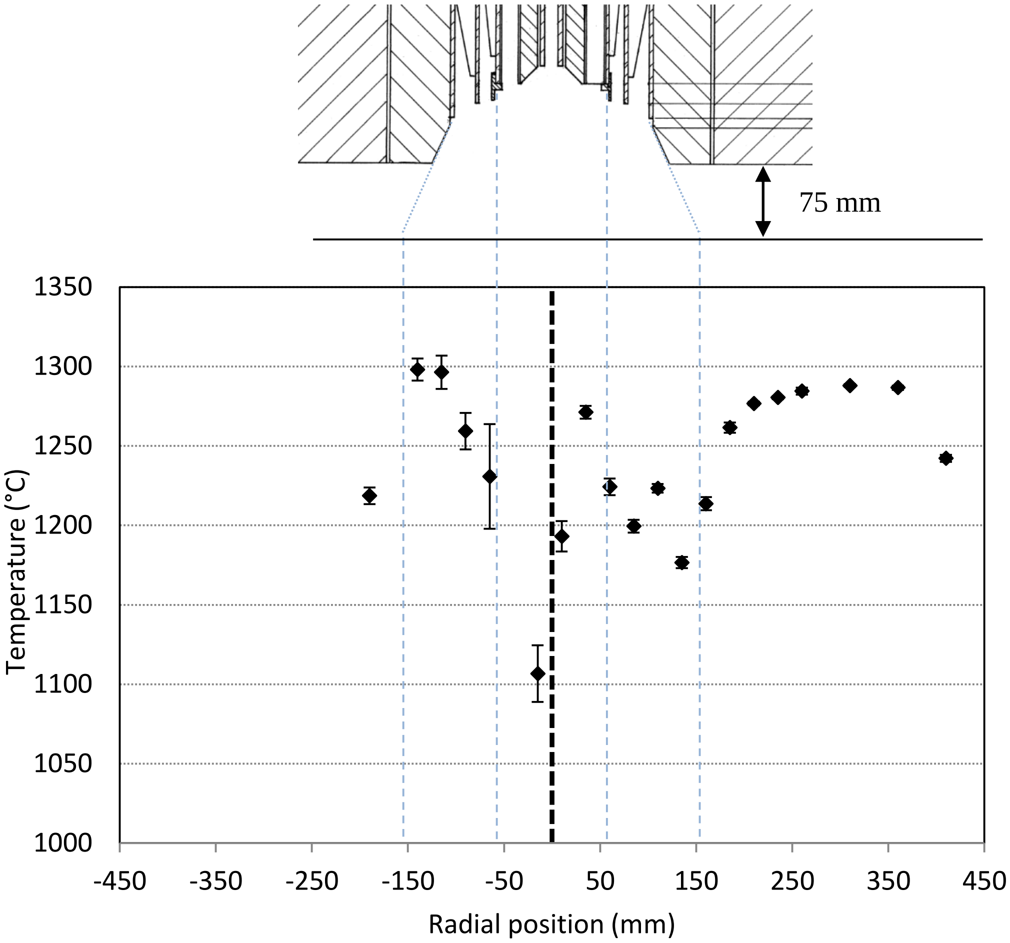

Figure 4.13. In-furnace temperature measurements using suction pyrometry at the axial position of 75 mm from the quarl exit. The black dashed line show the burner axis. The blue dashed lines indicate the location of the primary annulus and the straight line extension of burner quarl reaching to the distance of the measurement port. Error bars shown represent the statistical error of 1 standard deviation.

Moving from the near wall measurement at 410 mm to 360 mm, the temperature increases sharply, which is attributed to the cooling effect of the wall, which is made of light density refractory and enclosed in a water cooled jacket. On the other hand the effect of air in leakage at the probe inlet port to the furnace may also cause a detectable cooling in the measurements and this effect would be the largest at the measurement port close to the wall. However, care was taken during the measurements to tighten the compression fitting at the port inlet to eliminate this source of error.

Moving towards the centre, a uniform profile was observed between the 360 and 260 mm radial positions. After this, however, a slight downward trend is set up, for the locations of 235 and 210 mm, which then continue in a sharp dip until the 135 mm radial position. This is a result of the penetration of the secondary and tertiary combustion air streams, which are supplied to the burner at 260°C. The swirling combustion air stream leaving the burner attaches to the quarl and therefore the quarl angle is important in determining the trajectory of the swirling jet within the furnace. This is confirmed when comparing the dip observed at 135 mm to the straight line extension of burner quarl reaching to the distance of the measurement port at 75 mm AD.

The combustion air stream leaving the quarl entrains gas from its surroundings, which, in case of enclosed flames, is entrained from the combustion air/products stream downstream. This is responsible for setting up the external recirculation zone (ERZ), which has an important flame stabilising effect as the ERZ recycles heat into the root of the flame (Smart and Morgan, 1992). A schematic of the ERZ is shown in Figure 4.14, though it should be noted that the shape and dimensions of the ERZ are dependent on several parameters, including: the quarl exit to furnace diameter ratio, the quarl angle, swirl strength.

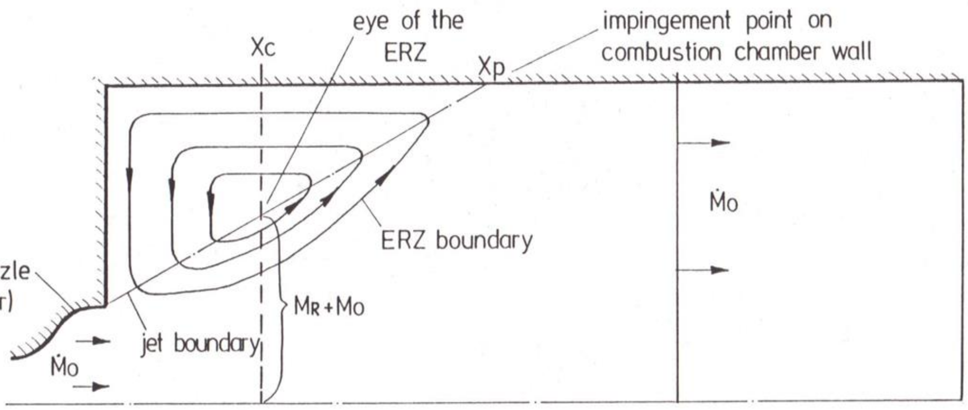

Figure 4.14. External recirculation zone within a confined furnace geometry (Smart and Morgan, 1992).

Lower temperature measurements were recorded moving from the 160 to 60 mm radial positions. However, it must be noted that the spatial resolution through the measurements was 25 mm, and it is possible that local peaks were not captured.

A sharp increase in the temperature measurements were recorded at the 35 mm radial position. This position was directly under one of the four coal collectors located within the primary annulus (Figure 3.6), which produce four concentrated streams of coal. The temperature increase suggests that the coal jet is already ignited at this axial distance. However, measurements taken from around the centreline show significantly lower temperatures. This suggests that either the O_2 content is reduced, or the majority of coal is not penetrating this central region and it is likely that both are true. Lockwood and Parodi (1998) noted that next to an ERZ an internal recirculation zone (IRZ) is also set up for confined flames. The bottom half of Figure 4.15 shows an internal recirculation pattern set up for a similar staged burner (though secondary only) where the primary annulus also surrounds a bluff body (gas injector). As with the schematic of the ERZ (Figure 4.14), it must be noted that the shape and dimensions of the IRZ differ between cases and is dependent on several parameters, e.g. velocity and swirl of the different streams, the furnace and quarl geometry and in particular the quarl angle.

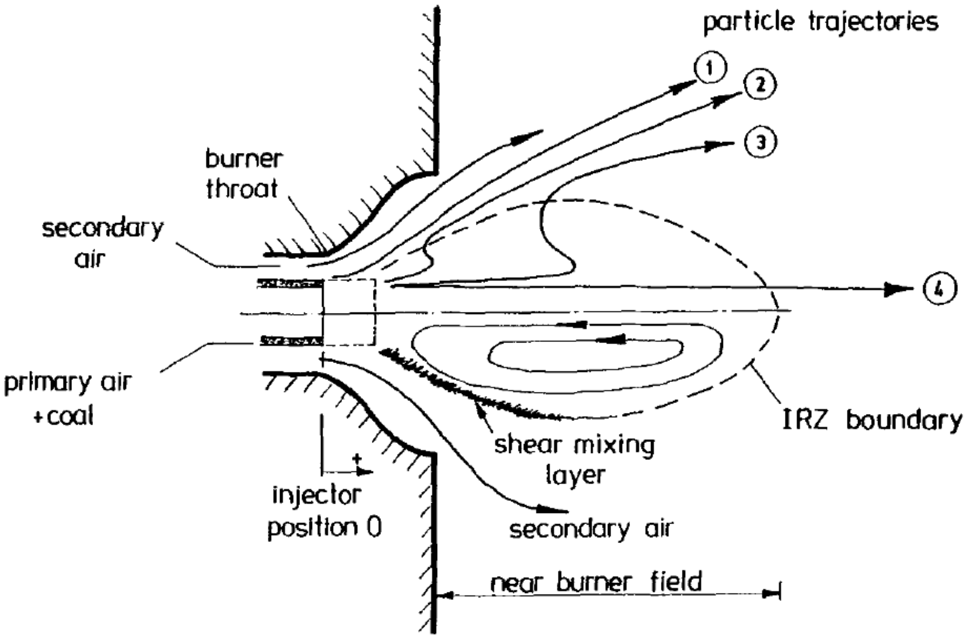

Figure 4.15. Coal particle dispersion in the near burner field and recirculation patter of the IRZ for IFRF Type I (trajectories 1 and 2) and II (trajectories 3 and 4) flames (Smart and Morgan, 1992).

As the ERZ the IRZ also carries heat back towards the root of the flame, thus facilitating the heat up and devolatilisation of the particles and therefore the stabilising of the flame. Furthermore the recirculating stream is low in O_2 and produces a reducing atmosphere, thus playing an important role in reducing fuel NO_X. As the coal particles devolatilise under reducing conditions, the conversion path of the released volatile-N to N_2 will be favoured and therefore the presence of the IRZ can significantly reduce the fuel NO formation. Also, Lockwood and Parodi (1998) noted that in practical pulverised coal burners the recirculating products are shown to contain small amounts of hydrocarbons and N-based radicals (NH_i) as well as CO, which all contribute to the gas phase destruction of NO (Nimmo and Liu, 2010). As the IRZ carries combustion products back towards the burner it also carries some of the NO already formed back to the root of the flame which is rich in hydrocarbon radicals, thus allowing for NO_x reduction through the reburn mechanism.

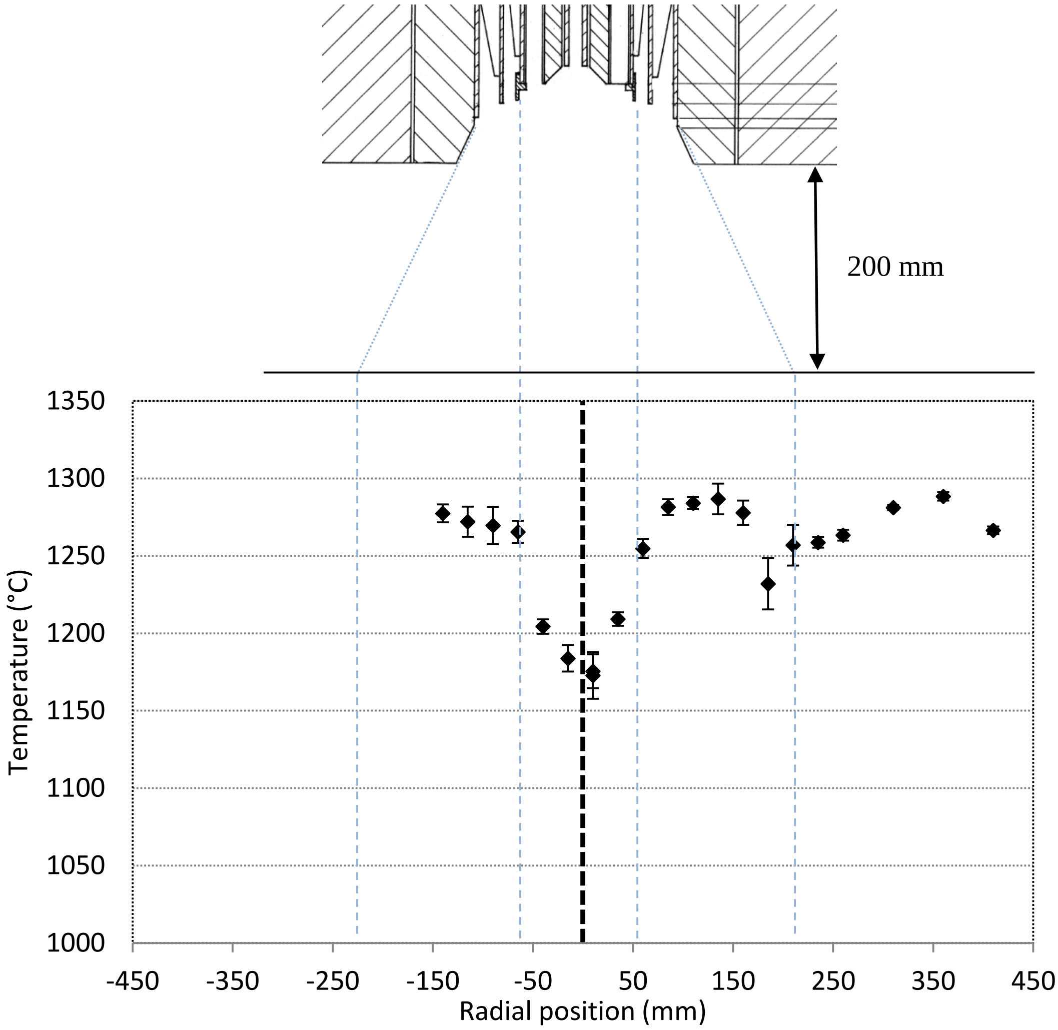

Figure 4.16 In-furnace temperature measurements using suction pyrometry at the axial position of 200 mm from the quarl exit. The black dashed line show the burner axis. The blue dashed lines indicate the location of the primary annulus and the straight line extension of the burner quarl reaching to the distance of the measurement port. Error bars shown represent the statistical error of 1 standard deviation.

Figure 4.16 shows in-furnace temperature measurements at the axial position of 200 mm from the quarl exit. The width of the ERZ shrank, compared to the 75 mm axial distance (AD), which confirms the suggestion made earlier that the swirling combustion air stream leaving the quarl at an outward expanding angle tends to follow this trajectory. The drop in temperatures measured at positions 210 and 260 mm compared to measurements at 310 and 360 mm, indicates the cooling effect of the combustion air supplied mixing into the ERZ.

The dip in temperature near the furnace wall, between locations 360 and 410 mm, is still present as at the 75 mm AD, although the difference is lower, 21°C instead of 45°C. This could be due to a lower wall temperature at this AD, or due to changes in the velocity of the recirculation streams within the ERZ. However, it is likely to be due to the fact that this measurement port is closer to the tip of the ERZ and points to the continued cooling as the recirculating gas flows upstream near the wall from the 200 mm to the 75 mm AD location.

The penetration of the staged combustion air stream is clearly visible at this AD as well, near the radial position of 185 mm, where the temperature drops sharply. As previously stated, absolute peaks are difficult to capture with the spatial resolution of 25 mm and, based on the sharp temperature changes observed between points at 160, 185 and 210 mm, it is likely that only the trend rather than the absolute peaks were captured. Moreover the readings become more unstable in this region, which can be observed from the larger error bars as opposed to the measurements collected from the ERZ. This is expected and it is due to the turbulent nature of the shear layer between the IRZ and the staged combustion air streams.

There is a sharp temperature rise between the measurements at 185 and 160 mm, and this higher temperature trend continues until the 85 mm position. This suggests that at these positions, the coal particles and the evolving volatiles penetrated and mixed with the secondary/tertiary combustion air streams supplying the O_2 for the combustion of the volatile products.

The coolest temperatures were measured within the IRZ around the centre of the furnace, and this corresponds to the combustion products recirculating from the lower regions back towards the burner.

At positions 30 and 65 mm, the temperature changes sharply, suggesting the location where the flow pattern changes within the IRZ; between the upstream flow region at the centre of the IRZ, at -15 to 10 mm, and the downstream flowing region, at 85 to 160 mm.

Figure 4.13 and Figure 4.16 show that the difference between the lowest and highest temperature measured along the same AD decreases moving away from the burner.

This corresponds to the air heating upon leaving the burner and the fuel burning out along the flame. A continuation of this trend can be seen in Figure 4.17, where the difference between the measurements along the AD of 575 mm reduced significantly. However, the presence of this gradient suggests that burnout is still taking place at this location. However at the AD of 800 mm, the temperature profile is flattened out, suggesting that burnout of the majority of the fuel finished between these two measurement traverses.

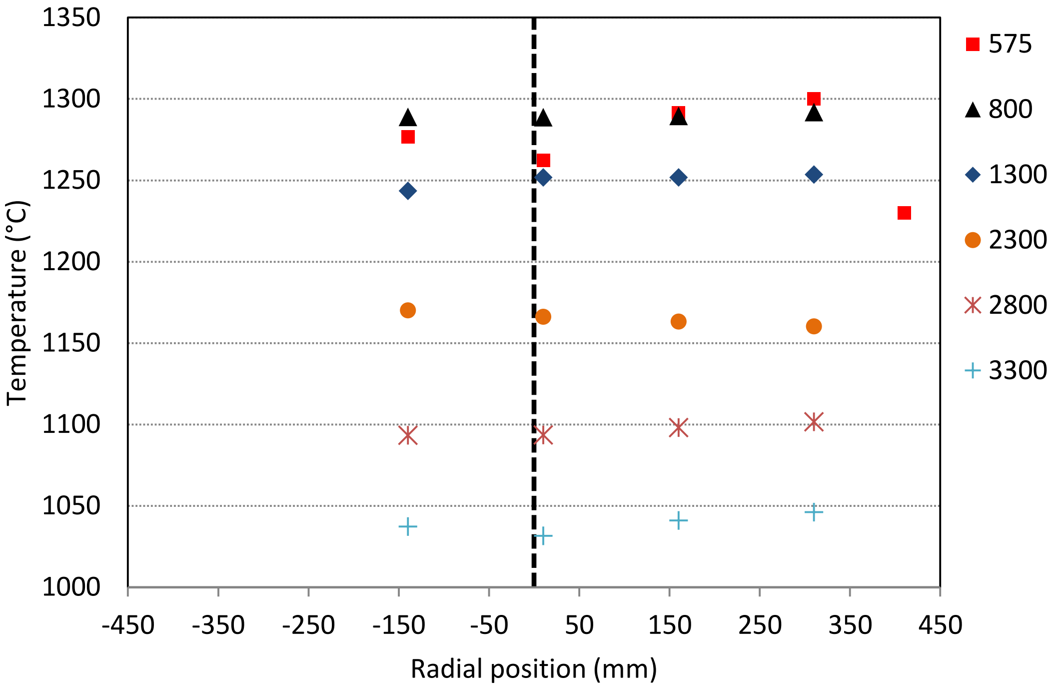

Figure 4.17. In-furnace temperature measurements using suction pyrometry at the axial positions of 575, 800, 1300, 2300, 2800 and 3300 mm from the quarl exit.

The flat temperature profiles allows for the reduction in the spatial resolution of the measurements past the flame, and also for more time to be spent on the AD of 75 and 200 mm to better resolve these important zones.

Figure 4.18 shows temperatures recorded along the central axis of the furnace. Centreline measurements were actually made 10 mm from the furnace axis due to difference between locations calculated form the CAD drawings from the manufacturers of the furnace shell and actual positions. These were identified subsequently (Figure 3.15) and measurement point locations adjusted accordingly.

The centreline temperatures increase progressively up until the 800 mm position. As discussed above, the end of the volatile flame is considered to be situated between the 575 and 800 mm points. Downstream of this, there is a steady decline in gas temperatures and this corresponds to heat removal through the refractory walls of the furnace.

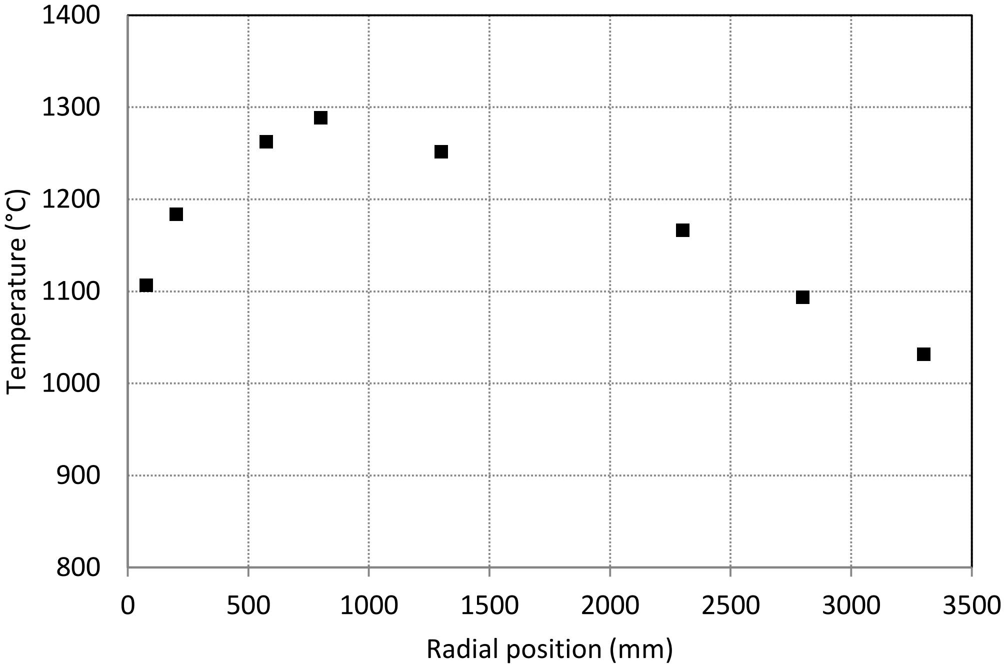

Figure 4.18. Centreline gas temperature measurements using suction pyrometry during the 200 kW air-preheated case. Centreline measurements were actually made 10 mm from the furnace axis.

4.1.3.1 Comparison of Suction Pyrometry and Process Thermocouple Measurements

The inherent issue with temperature measurements using thermocouples is the underreporting of the temperature due to radiation losses (Shaddix *et al*., 1999), which is a consideration in this furnace as well. The refractory wall of the furnace is heated by the flame and there are hot gases on one side but cooled by a water jacket on the other side, thus lowering the inside wall temperature. As the sheathed thermocouple is heated by convection and radiation from the gases and radiating particles, it loses heat by radiative heat exchange with the cooler walls. Roberts *et al*. (2011) noted that this may produce significant errors in the measurement of gas temperatures.

The thermocouples are fixed at 200 mm from the inner wall, at the 250 mm radial distance from the furnace axis. Figure 4.19 shows a comparison of the temperature measurements by these sheathed thermocouples with the gas temperatures measured by suction pyrometry at the radial location of 310mm.

It is observed that the first process thermocouple recorded a higher temperature than any of the suction pyrometry measurements. As discussed in the previous section, due to the spatial resolution of the suction pyrometry measurements, absolute peaks are likely to be difficult to measure. However, a more likely explanation is the constant deposition and burnout of the particles with significant carbon content on the surface of the thermocouple. It should be noted that the sheathed type R thermocouples are important only for process observation and control purposes.

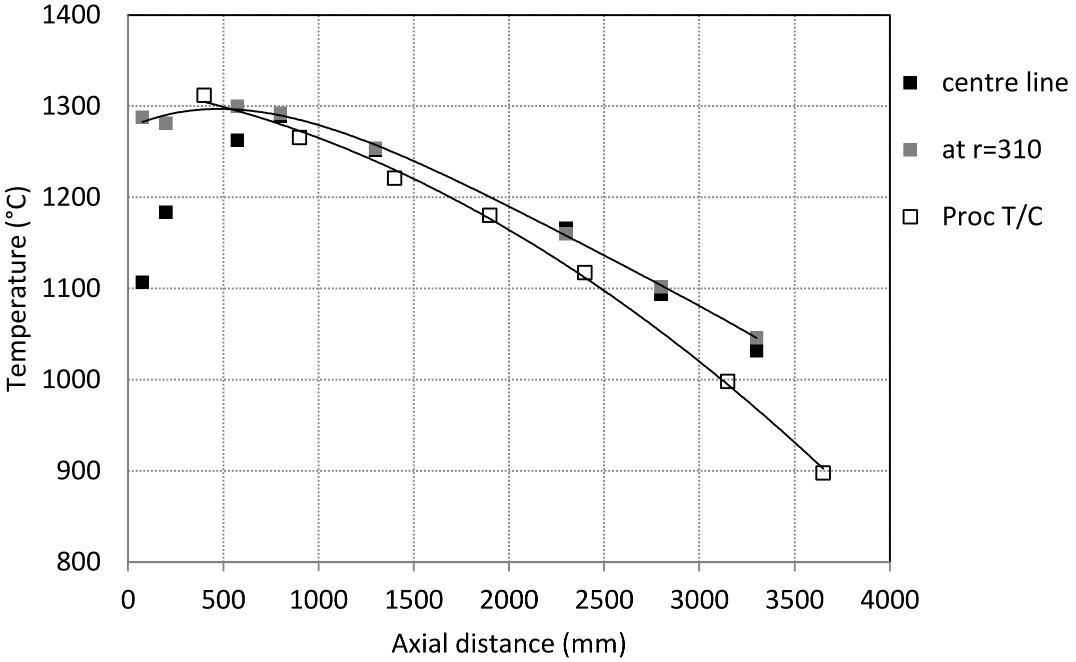

Figure 4.19. Comparison of gas temperature measurements using suction pyrometry against the readings recorded by the sheathed process thermocouples (fixed at r=250 mm), at the 200 kW air-preheated case. Full markers are for suction pyrometry measurements and hollow ones for process thermocouple recordings.

As seen before, there are considerable variations in gas temperatures in the radial direction up until the 800mm AD measurement port. This means that the 60mm difference between the sheathed thermocouple and suction pyrometry measurement points (located at the radial positions of 250 and 310 mm, respectively) as well as the asymmetries of the flame can be significant. However, from the 800mm AD port the radial profiles were observed to flatten out and comparison of measurements at 60mm distance and at different sides of the flame become reasonable. Figure 4.19 shows an increasing difference between sheathed thermocouple and suction pyrometry measurements downstream in the furnace. A major factor in this is the increasing proximity of the water tray, located at the bottom of the furnace, which constitutes the coolest boundary of the furnace with the temperature maintained at ~50-60°C. As observed by Roberts *et al*. (2011), a larger temperature gradient between the thermocouple and the furnace boundary results in a larger temperature difference between the measured and the true gas temperature.

4.1.4 Heat Flux Characterisation Measurements

4.1.4.1 Evaluation of Heat Flux Measurement Methods for Validation Data

The comparison of radiative heat flux measurements was discussed in Section 4.1.1.4. Measurements for that comparison study were taken with the CaF_2 window attachment of the heat flux probe. However, as discussed in Section 4.1.1.4, the window attachment was prone to condensation and deposition, particularly near the flame region, and representative measurements at these regions could not be obtained. Issues with the window attachments cracking were also encountered during both tests.

After discussions with the manufacturer of the probe, it was decided to deploy the probe without the window attachment, a method which is less susceptible to the effects of deposition. The added benefit of this was that without the window attachment the probe can measure the full hemispherical radiative heat flux as opposed to the 150° reduced view angle of the probe with the window attachment.

At the 75 and 200 mm locations, the difference was significantly lower, at 7 and 8%, respectively. This difference is attributed to the increased view angle, as no sooting was observed on the probe tip during these measurements. Indeed, this location is shielded from the particles as the ERZ is formed from the outer edge of the tertiary stream. This region is effectively shielded from particles by the swirling secondary/tertiary stream, which carries the entrained coal particles and partially combusted combustion products further downstream.

The largest discrepancy was obtained at the 575 mm location, where a 29% increase was recorded, but similar large measurement differences were maintained up until the 1300 mm location. The dip in the trend for the measurements with the CaF_2 window corresponds to the locations of largest degree of sooting observed. Discrepancies in this region are attributed to the combined effect of sooting and increased view angle.

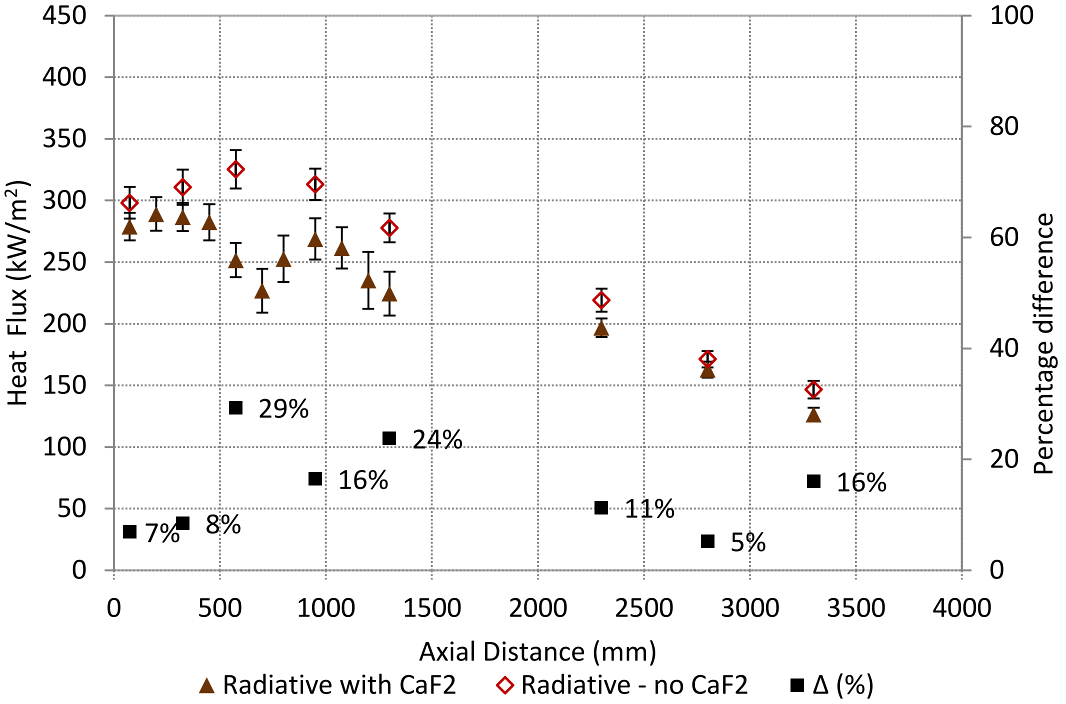

Figure 4.20. Effect of sooting, condensation and reduced view angle on the radiative heat flux measurements when using the CaF_2 window attachment as compared to measurement without the window attachment where condensation was eliminated and sooting was observed to be greatly reduced.

Downstream of the flame, in the lower sections of the furnace, the difference between the measurements significantly decreases and compares in magnitude to those seen near the ERZ (the magnitude of the difference is 19 and 24 kW/m^2 at 75 and 200 mm, respectively, and 22, 9 and 20 kW/m^2 at the 2300, 2800 and 3300 locations, respectively).

The measurements with the bare probe tip yielded higher measured values at every location, it was possible to retain measurement at locations which previously had to be discarded due to the soot deposition, and as a consequence the shape of the trend line was also changed. It was decided that for future measurements for the basis of CFD validation studies, the bare tip method should be employed. This also made measurements more suitable for modelling validation, as hemispherical radiation on a surface is predefined in the ANSYS Fluent analysis package as ‘incident surface radiation’.

4.1.4.2 Heat Flux Characterisation Study

Figure 4.21 presents the radiative and total heat flux measurements collected without the CaF_2 window attachment over 2 measurement days. Day 1 was intended as a scoping day, whereas on day 2 more detailed radiation measurements were performed. The air and fuel supply was kept at the same level for both days and time was allowed for the furnace to reach steady state operation. There is an overall good agreement between the repeated measurements, which are within each other's associated error bars.

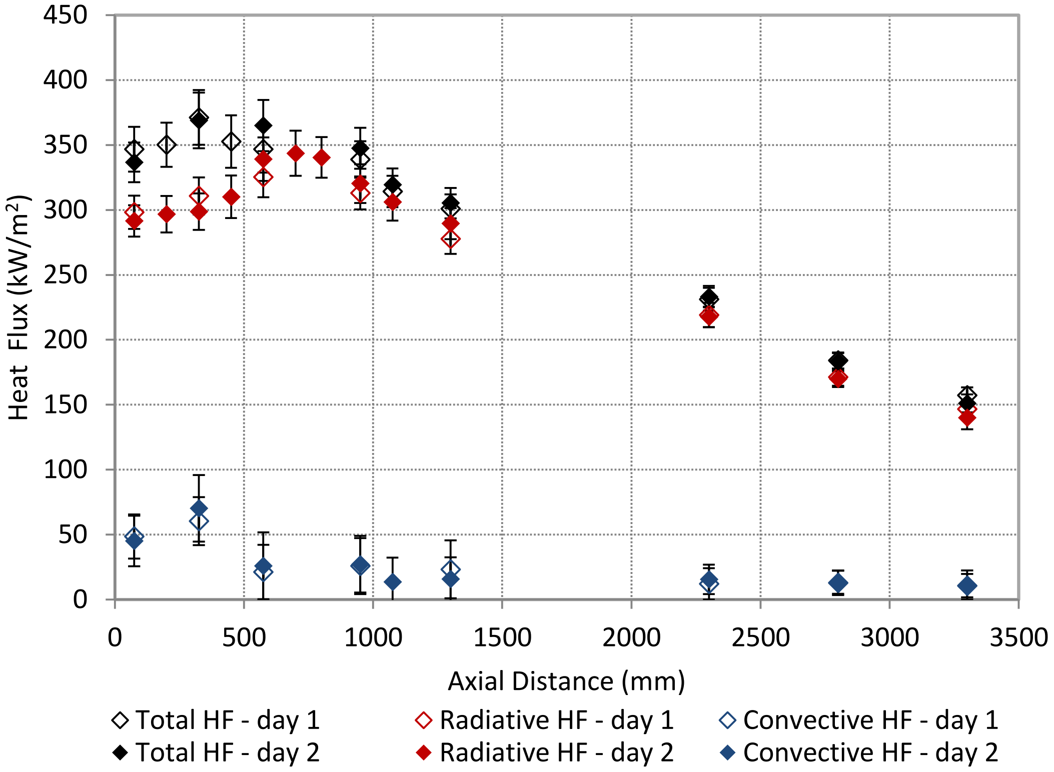

Figure 4.21. Repeated radiative and total heat flux measurements on the preheated case. Convective measurements were calculated as the difference of these two measurements.

The difference between the radiative and convective heat flux, equating to the convective portion of heat flux, along the furnace produces two separate trends, thus identifying two distinctive regions. The first region is characterised by a relatively large convective heat flux with 47 and 65 kW/m^2 values obtained being at the 75 and 325 mm locations, respectively. This is followed by a sharp reduction to 24 kW/m^2 at 575 mm, marking the beginning of a second region where similarly lower convective heat fluxes are observed downstream of this point, ranging from 11 to 27 kW/m^2.

The sharp divide between these two regions is likely to be associated with the impingement point shown in

Figure 4.14. The first region with the high convective heat flux corresponds to the location of the ERZ and likely incorporates the impingement point where the swirling stream, set up by the swirling combustion air, hits the wall and it is forced to change direction flowing downstream along the furnace. Also, it pulled away from the wall, towards the centre of the furnace by the pressure gradient, reducing towards the centre of the furnace, thus setting up the IRZ recycling combustion products to the centre of the flame. The intensity of the flow along the wall is weakened as the flow is distributed across the cross section of the furnace and the convective part of the heat transfer reduces for the rest of the furnace accordingly. Another reason for the observed downward trend in the convection is the cooling of the combustion products downstream of the flame (Figure 4.17 and Figure 4.18), losing heat to the refractory wall, reducing the temperature gradient near the wall as well, which is a driver of the convective heat flux.

However, radiative heat transfer follows the trend observed during the centreline temperatures measured with suction pyrometry. This can be attributed to the dependence of thermal radiation to the temperature of the power of 4. The radiative heat flux increases from the first measurement port at 75 mm near the root of the flame and peaks between the 575 and 800 mm measurement ports, corresponding to the centreline temperature trends recorded in Figure 4.18, as well as to the widening of the flame and the high temperature zone across each cross section at 75, 200, 575 and 800 mm (Figure 4.13, Figure 4.16 and Figure 4.17). After the 800 mm location, as the gases within the combustion chamber cool, the radiative heat flux progressively decreases as well, with the lowest reading recorded at the last measurement location before the flue outlet.

The location of the peak in the total heat transfer is shifted from the radiative peak at the end of the flame, closer to the root of the flame. However, it is important to understand that this is due to the effect of the ERZ on the heat transfer to the wall, and it is also unique to the confined environment of the enclosed single burner furnace. In a commercial power station fitted with multiple rows of burners, the ERZ would increase the burner-burner interactions, which in a typical boiler is reduced by changing the direction of the swirl for adjacent burner pairs, arranging them in a checkerboard arrangement (Lockwood and Parodi, 1998). The trends observed suggest that the total heat transfer, which is the sum of the convective and radiative terms, is manly influenced by the thermal radiation in the furnaces firing pulverised coal. This conclusion is consistent with the literature (Chedaille and Braud, 1972). Therefore the radiative heat flux data is of great importance the validation of the newly developed CFD submodels on this furnace.

Another use of radiative heat flux measurements is the burner development when trying to understand and predict the radiative heat transfer interactions between neighbouring burners. This radiative heat feedback is especially important in stabilising the open flames in commercial boilers where there is no hot refractory wall providing this heat near the flames, but instead the radiative heat exchange between the neighbouring flames.

However, single burner test furnaces also differ from commercial boilers in the level of confinement surrounding the flame. The relatively large hot refractory wall, with a large thermal inertia, increases flame stability during the frequent transitions to different experimental conditions and the cooling and disturbing effect of different sample and measurement techniques. But it also increases radiative heat exchange.

4.2 Oxy-fired Results and Analysis

Results for oxy-firing of coal at the total O_2 concentration of 27% (oxy27) and 30% (oxy30) by volume are presented below. Comparison of the cases is drawn against flue gas emissions, in-furnace temperatures and heat flux measurements. The focus was kept on assessing the possibility of matching air-fired temperature profiles and heat transfer characteristics during oxy-firing. These are especially important when retrofitting existing boilers that were designed for air-firing.

4.2.1 Flue Gas Emissions

Flue gas emission for the investigated oxy-fuel cases are shown in Figure 4.22 and Figure 4.23 compared to the air fired base line. Atmospheric $N_{2,}$ which constitutes the majority of the oxidiser in air-firing applications, is replaced by CO_2 during oxy-firing, and thus the concentration of CO_2 is significantly increased in the flue gas.

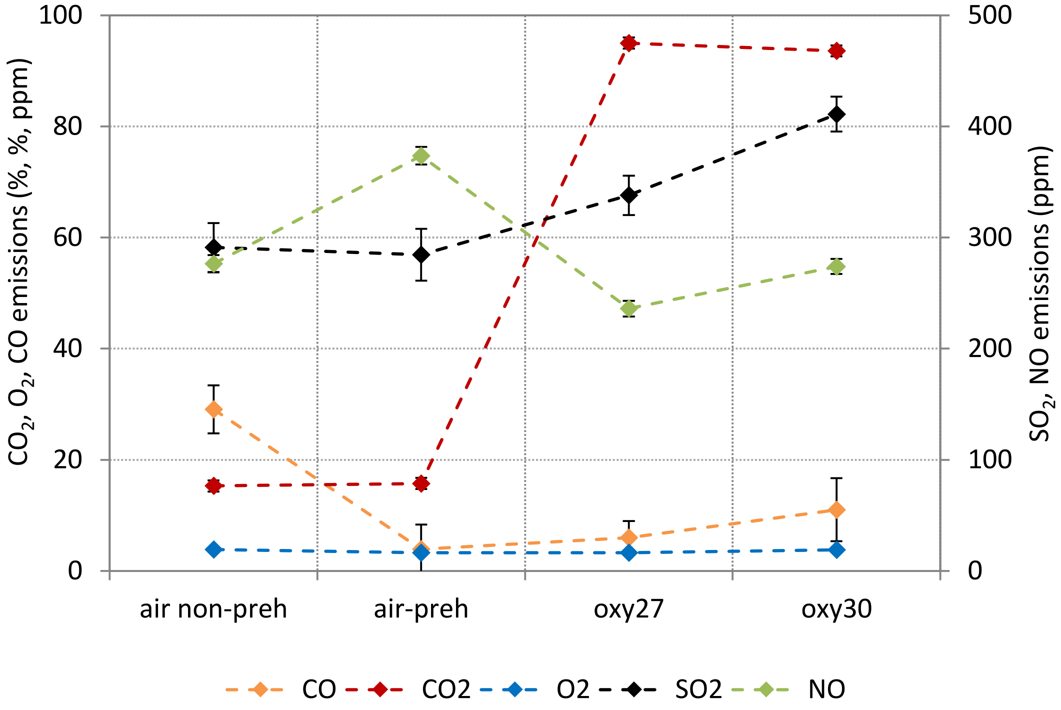

Figure 4.22 Flue gas emissions for the investigated experimental cases.

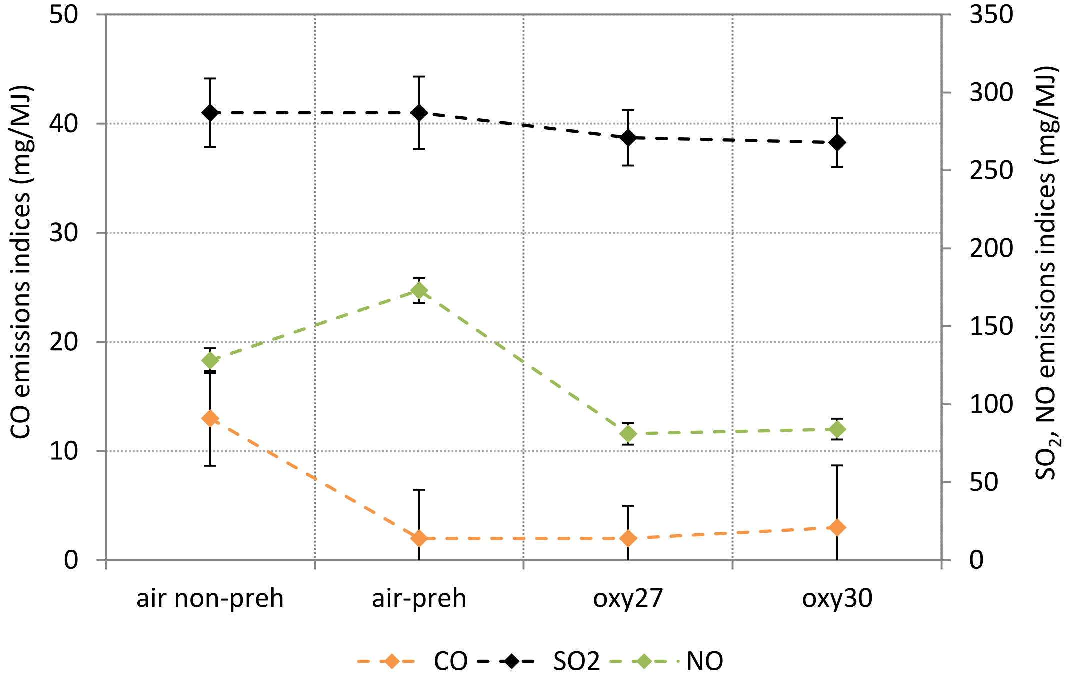

Figure 4.23 Emissions Indices for the investigated experimental cases.

However, it must be noted that the experiments were performed using a once through system and during real Flue Gas Recycle (FGR) applications the CO_2 concentration produced might decrease due to the in-leakage of air though the flue gas system. The sum of O_2 and CO_2 concentrations was 98.3 and 97.4% for the oxy27 and oxy30 cases, respectively.

In addition, the calculated amount of N_2 introduced by the window purge stream and fuel-N not converted to NO, was 1.4 and 1.6%, respectively. This takes the sums to 99.7 and 99.0%, respectively. The remaining percentages are well within the margins of errors of the O_2 and CO_2 measurements, but also there were slight fluctuations in the flows during the oxy30 case, which caused a difference in O_2 and CO_2 concentrations between the two cases. These flows are reported together with their standard deviations in Table 3.4.

4.2.1.1 NO Emissions

Since NO is the primary NO_x species produced in turbulent pulverised fuel flames, the research undertaken in these tests was focused on the NO emission. The exit concentration of NO increased with the total O_2 concentration for the oxy-fuel cases - rising by 16% between the oxy27 and oxy30 cases, see Figure 4.22. However, the emission indices showed only a much lower increase of 6% between these cases, see Figure 4.23. Therefore, the majority of the volumetric concentration increase in the measured NO concentrations between the oxy27 and oxy30 cases is due to the reduction in the simulated recycle ratio, achieved by the lower CO_2 input, which resulted in a decrease in the dilution of the flue gas, and therefore trace emission concentrations.

Furthermore, both the oxy cases produced a lower NO concentration than the preheated air-firing case, and the emissions indices show a 53% and 51% decrease in the NO produced on a thermal input basis for the oxy27 and oxy30 cases, respectively (see Table 4.1 and Figure 4.22).

To put the NO emission of the oxy27 and oxy30 cases in to context, NO emissions measured at other experimental facilities are listed in Table 4.4. It should be noted that the Leeds and the RWHT facilities were operated in a once through mode, as in the present investigation, whereas the other facilities using FGR.

Table 4.4. NO emissions measurements of the investigated cases together with measurements from a number of other oxy-fuel research facilities (Chen *et al.*, 2012).

Research group	**Thermal load**	**NO (mg/MJ)**	
		Air-fired	**Oxy-fired**
Leeds University (present work)	*200 kW*	*128-173*	*81-84*
Leeds University	20 kW	340	278
RWHT Aachen University	100 kW	255	136-218
Chalmers University	100 kW	161	41-48
EON	1 MW	97	25

In the following sections the contributions of different mechanisms important in NO formation and destruction are examined.

4.2.1.1.1 Contribution of Thermal NO

Thermal NO formation is exponentially dependent on the temperature, as discussed in Section 2.7.1.

Although the sheathed thermocouples did not record any temperatures above ~1500°C, the point at which thermal NO formation becomes significant (Chen *et al.*, 2012), it should be noted that temperature measurements with these thermocouples at fixed locations are not representative of the radial temperature profiles recorded within the flame zone (see Figure 4.13, Figure 4.16 and Figure 4.17). In addition, the sheathed thermocouples are susceptible to radiative losses underreporting the gas temperature (Section 4.1.3). Therefore local peaks, significantly above the recorded measurements, are expected within the flame, especially in stoichiometric flame pockets around the shear combustion layer between the Primary and Secondary oxidiser streams, where most of the thermal NO formation is thought to take place. Therefore the increased temperatures recorded between the oxy27 and oxy30 cases may correspond to increased temperatures in the shear combustion layers, and therefore, may contribute to the 6% increase in the NO emissions indices.

However, the contribution of thermal NO to the total NO formation is reduced under oxy-firing conditions as the N_2 in the oxidiser is replaced by CO_2 (Toftegaard *et al.*, 2010). Toftegaard *et al.* (2010) concluded that the reduction of the partial pressure of N_2 to very low levels causes oversaturation of the furnace atmosphere with NO, which reverses the Zeldovich mechanisms reducing the NO already formed to N and N_2. These findings were in line with the theoretical predictions of Normann *et al*. (2009) showing that NO formation is significantly reduced when the concentrations of N_2 in the oxidiser is reduced from 10% to 1% and 0%.

The reduction in thermal NO formation is likely to have contributed to the lower than air NO emissions indices for the oxy-fired case. However, as explained in Section 2.7.1 the contribution of the thermal NO to the total NO formation is only ~20% under air-fired conditions, so the reduction in thermal NO formation on its own does not explain the over 50% reduction in NO indices.

As shown above, in order to reduce thermal NO formation, the air in-leakage must be kept to a minimum. Shah (2006) calculated that an increase in the air in-leak from 1% to 3%, 5% and 10% decreased the dry exit CO_2 concentrations by 8%, 14% and 28%, respectively, due to the recycling of N_2 by the FGR, thus a small air ingress results in a considerable increase in the amount of N_2 in the oxidiser.

4.2.1.1.2 Contribution of Prompt NO

The effect of prompt NO formation, which is estimated to contribute only ~5% of the total NO in air-firing, see Section 2.7.1, is also reduced by the very low N_2 partial pressures, making this route of NO formation even less important for oxy-fuel combustion (Toftegaard *et al*., 2010) when only low levels of air in-leakage are present. Although to a small degree this may also have contributed to the lower than air NO emissions indices.

4.2.1.1.3 Contribution of Fuel NO

During devolatilisation the fuel-N is split between the volatile-N released and char-N remaining. The combustion atmosphere in which the release of N containing intermediate species takes place influences the fate of the fuel-N, where conversion to N_2 is favoured in reducing condition and oxidation to NO is promoted under oxidising conditions, see Figure 2.8.

O and OH radicals are important in fuel NO formation via the oxidising reactions with the N containing intermediate species. The concentration of OH radicals was shown to be higher in high CO_2 atmospheres, via the reversible reaction between CO_2 and H forming CO and OH (Normann *et al.*, 2009). This alters the radical pool and could promote the formation of NO from volatile-N.

However, to make up for the over 50% reduction in NO levels seen in the oxy-fired cases, the fuel NO formation had to be significantly reduced, as fuel NO contributes to ~80% of the total NO formation in air-fired combustion (Section 2.7.1). Fuel NO formation is also affected by the fluid dynamics, via its effect on burner staging and mixing between the fuel rich primary and staged secondary and tertiary streams. Compared to the air-firing cases the volumetric flows are reduced for the oxy-fired cases, which cause a reduction in the burner velocities. This may then result in decreased mixing between the fuel rich flame root and the staged combustion air streams, allowing more residence time for the volatile-N in the reducing zones of the flame, significantly lowering fuel NO formation.

Snape (2014) conducted a series of drop tube furnace (DTF) experiments on the El Cerrejon coal used in the cases investigated in this thesis. It was found that when replacing the 100% N_2 atmosphere with 100% CO_2 the volatile release was increased, at temperatures of 1150°C and above. The increase was 6%, 9%, 14% and 25% at temperatures of 1150°C, 1200°C, 1300°C and 1450°C, respectively. This pointed towards the increased importance of the CO_2 gasification reaction where CO_2 and carbon from the char react to form CO. The increased volatile release corresponded to a -5%, 4%, 11% and 15% change in volatile-N release for the above cases, respectively.

When Low-NO_x burners are used, such as the one used in this investigation, increased volatile-N release may reduce fuel-NO formation due to more fuel-N being released in the staged fuel rich zones promoting volatile-N conversion to N_2.

4.2.1.1.4 Contribution of the Reburn Mechanism

The reburn mechanism is important in the fuel rich regions of the flame, where the concentration of hydrocarbon radials is high. Here the NO already formed is attacked by these radicals and converted back to intermediate nitrogenous species. These then may be converted to NO or N_2 depending on the combustion environment.

The NO emission indices are expected to decrease when FGR is used as the NO already formed is recycled back into the furnace with the flue gas. The recycled NO passes through the fuel rich regions of the flame rich in hydrocarbons and low in O_2 (Wall *et al.*, 2009). Indeed, Table 4.4 shows a significant reduction in NO emissions when moving from once through set ups (as used for the Leeds and RWHT experiments) to FGR (as used at the Aachen and EON facilities).

Okazaki and Ando (1997) concluded that the NO reburn by CH_x radicals contributes to 50-80% of the recycled NO reduction when RFG is used. Other NO mechanisms which attack the recycled NO are reactions with intermediate N containing species released during coal devolatilisation, which were estimated to contribute 10-50% to the total NO reduction. Finally the reduction of NO via heterogeneous reactions with char was found to be only of minor importance.

4.2.1.2 SO_2 Emissions

Moving from the oxy27 to the oxy30 case shows an increase in exit concentrations of SO_2, even though the amount of sulphur introduced with the coal remained the same between the two cases. This is attributed to the reduction in the simulated recycle ratio for the oxy-fuel cases, thus resulting in reduced dilution of the flue gas by the CO_2 supplied (as discussed in Section 4.2.1.1).

Emission indices are shown in Figure 4.23. As the coal input was kept the same for both cases, the emissions indices did not change with the total O_2 concentration. This corresponds to the findings of Croiset *et al*. (2000). Furthermore, the SO_2 emissions indices are also similar to the values measured during the air-fired test case (Table 4.2). This suggests that SO_2 emissions are independent of the combustion atmosphere used, and depend on the amount of sulphur supplied with the coal. Therefore the SO_2 emissions can be altered by the choice of coal used.

However, it must be noted that the experiments were conducted in a once through system, and SO_2 emissions are expected to increase significantly when flue gas recirculation (FGR) is employed (e.g. Buhre *et al*., 2005, Davidson and Santos, 2010). This is due to the SO_2, which is produced during combustion, being recycled back into the furnace. Fleig *et al*. (2009) recorded an up to 4 fold increase in SO_2 concentration using FGR. As described in Section 2.5.6, this results in the increase of SO_3 concentrations as well, and this is due to the thermodynamic equilibrium between the species, which also increases with increasing O_2 concentrations in the flue gas (Toftegaard *et al*., 2010). This poses additional challenges for controlling corrosion (Wall *et al*., 2011), especially in the low temperature regions of the furnace, e.g. the primary stream where the temperatures, below that of the acid due point, are present.

To avoid these issues, the Primary stream is only supplied from the liquid O_2 and CO_2 tanks, and the Secondary/Tertiary recycle stream is kept above 250°C, well above the acid dew point of the flue gas.

On the other hand, it is also suggested that the capture of sulphur by the ash increases during oxy-fuel combustion. However, Folgueras *et al*. (2004) reported that this effect is not likely to be observed within the radiative sections of the furnaces, and this is due to the unstable nature of the sulphates above 1000°C and therefore this effect is only likely to be observed downstream of the furnace when FGR is used.

4.2.1.3 CO Emissions

CO emissions were found to drop significantly in air-firing when preheating was applied to the Secondary and Tertiary streams (Tables 4.1 & 4.2). Both the oxy-fuel cases investigated here involved the preheating of the above streams, and low CO emissions were measured for both of these cases.

The results indicate that there are no significant issues in the control of CO emissions when moving to oxy-fuel combustion.

4.2.2 Temperature Measurements and Residence Time

Figure 4.24 shows temperature measurements recorded with the sheathed Type R thermocouples. For the oxy27 case, lower temperatures were recorded than for the preheated air and oxy30 cases, especially within the first part of the furnace, i.e. near to the flame zone. This shows the cooling effect of replacing atmospheric N_2 with CO_2 in the oxidiser streams, due to the higher heat capacity of CO_2. Lower temperatures and the lower diffusivity of O_2 within CO_2 atmospheres may lead to a reduction in the reaction rates. However, it must be noted that the measurements were made at a fixed point location (as explained previously in Sections 4.1.1.3) and therefore the change in the temperatures recorded may also be due to changes in the fluid dynamics that result in changes in flame shape. This is because reduced burner velocities may lead to reduced mixing between the Primary and the staging secondary and Tertiary streams.

The oxy30 case produced overall higher temperatures within the furnace, with the measured temperature difference reducing along the furnace as the extra heat was removed through the successive furnace wall sections.

However, for both the oxy cases investigated, the shape of the trend changed slightly, with the measured peak temperature shifting from the first to the second measurement position compared to the preheated air-firing results. This could be due to either of the phenomenon described above (the fire-retardant properties of CO_2 or changes in fluid dynamics), and it is likely that both had an influence.

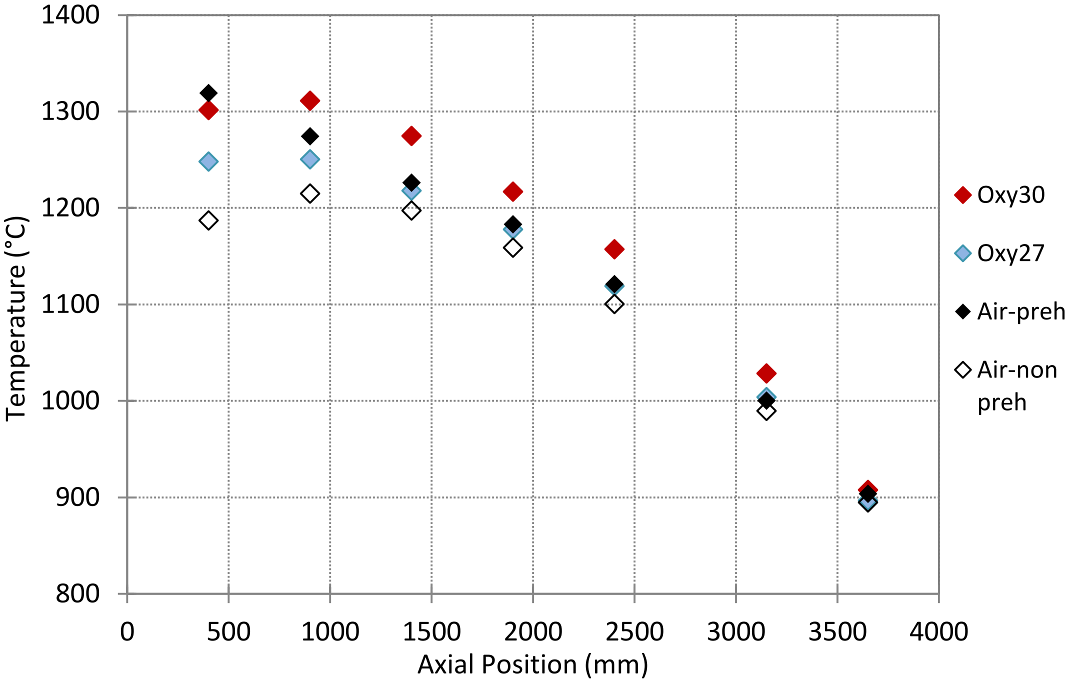

Figure 4.24 In-furnace temperature measurements, recoded using sheathed Type R thermocouples positioned 200 mm from the inner wall of the furnace.

Based on these temperature measurements, it can be concluded that it is possible to match the air-firing temperatures within the furnace with the optimal O_2 concentration lying between the two investigated cases.

Furnace residence times are shown in Figure 4.25. They were calculated assuming plug flow and using the section temperature profiles shown in Figure 4.24. The air-fired cases have a very similar residence time, with a slight decrease when moving to the preheated condition due to the increased in-furnace temperatures. However, there is a marked difference when moving to the oxy-fuel cases, where the residence time increases with the total O_2 concentration. This trend is consistent with the results of Smart *et al*. (2010b), obtained for a 0.5 MW experimental furnace designed to replicate the flue gas path of a commercial scale boiler. The reason for this trend is the significant reduction in the oxidiser flow, when moving to higher total O_2 concentration cases. Compared to the preheated air-fired case, the oxy27 and oxy30 cases had a 26% and 34%

increase in residence time, respectively, due to the reduced CO_2 flow in the oxidiser streams.

It should be noted that an increase in the total firing rate to the full thermal output of the burner at 250 kW, from the present 200 kW conditions will reduce residence times by an estimated 20% due to the increased volume flows of the oxidisers alone, and additional reduction will be due to increased furnace temperatures and therefore the increase in volume flows.

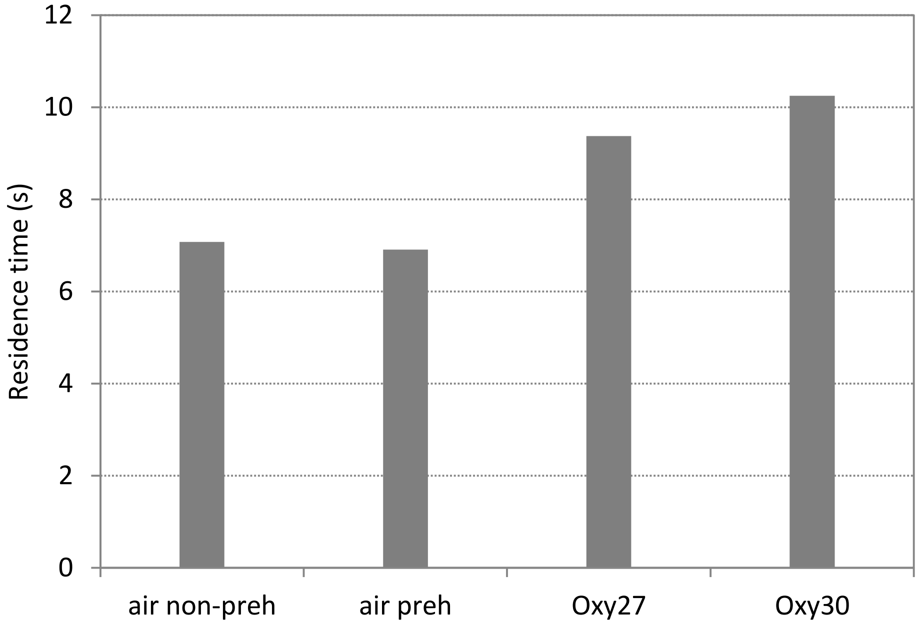

Figure 4.25 Residence times within the furnace for the investigated cases, calculated using plug flow assumptions for the furnace sections.

Smart *et al*. (2010b) found that the increase in residence times coupled with the higher in-furnace temperatures improve burnout as the total O_2 concentration was increased. Both of these trends were observed here (Figure 4.25 and Figure 4.24, respectively), and thus the burnout is expected to improve between the cases.

An additional factor, which is expected to improve burnout for oxy-fuel combustion, is the char gasification, which becomes more important in the later stages of combustion when the O_2 concentrations are low and the gas temperatures are still high. This is due to these reactions being slower than the char-O_2 reaction, and thus are being kinetically controlled (Chen *et al*., 2012).

4.2.3 Heat flux Characterisation

Figure 4.26 shows the radiative heat flux measurements for the oxy27 and oxy30 cases compared against the air-firing result. The peak values of the air and oxy30 cases correspond to the typical range predicted on a coal-fired boiler using the FURDEC heat transfer code, which was 340-500 kW/m^2 (Smart *et al.*, 2010b).

When compared against the air-fired results, a 9% lower peak radiative heat flux was measured for the oxy27 case, and the oxy30 case produced higher radiative heat flux, especially near the flame zone, with a 27% increase in the peak value. Therefore, the peak radiative heat flux was found to significantly increase with the total O_2 concentration, which is consistent with the findings of Smart *et al.* (2010b).

A downstream shift of the peaks for the oxy-fuel cases was observed when compared to the air-firing result, suggesting a longer flame, but the location of the peaks did not change with the recycle ratio. This is in contrast to results obtained by Smart *et al.* (2010b), where the peaks moved upstream, towards the burner, with increasing total O_2 concentration, although the degree of shift in the peaks were considerably different for the two coals investigated. This suggests that the resulting flame and corresponding distribution of radiative heat transfer is dependent on the fuel properties for cases with the same recycle ratio. Other factors which may be of importance are significant differences in the geometry, and aerodynamics of the burners used. The most significant difference between the burners is the presence of coal concentrators in the primary annulus of the Doosan Babcock burner used for this study (see Section 3.2.2). This shows the need for research using different commercial burners for oxy-fuel combustion, and also to investigate further modifications in burner configurations (e.g. direct O_2 injection (Fry *et al.*, 2011)); just like there is a need to investigate the performance of different coals (Dhungel, 2010).

Smart and Riley (2011) found that when using oxy-fuel technology a wider range of coals may be used in typical power stations, which were designed for air-firing of high volatile bituminous coals. This can increase fuel flexibility and consequently may decrease operational costs. They compared the combustion performance of a semi-anthracite and a bituminous coal under oxy-firing conditions, and found that by the appropriate choice of total O_2 concentration the flame ignition, stability and luminosity as well as the radiative heat transfer performance of the low volatile semi-anthracite could be significantly improved.

These may be further improved by optimised burner configuration (e.g. direct O_2 injection) or blending with high volatile fuels such as biomass.

The downstream shift in the location of the peaks in the present study corresponds with the trends observed for the temperature profiles shown in Figure 4.24, which again demonstrates the 4th order power dependence of the radiative heat flux on the temperature.

In the second half of the furnace where similar temperature measurements were recorded within the furnace sections for the air and oxy27 cases (Figure 4.24), the radiative heat flux was seen to be 10-21% higher for the oxy27 case (Figure 4.26). A significant difference between the cases is the increase in the partial pressure of the CO_2, and as CO_2 is a tri-atomic molecule, it actively participates in radiation and increases the overall gas emissivity. Indeed, Anderson *et al.* (2011) found that the proportion of the gas radiation increased significantly when moving from air- to oxy-firing due to the effect of increased CO_2 partial pressures.

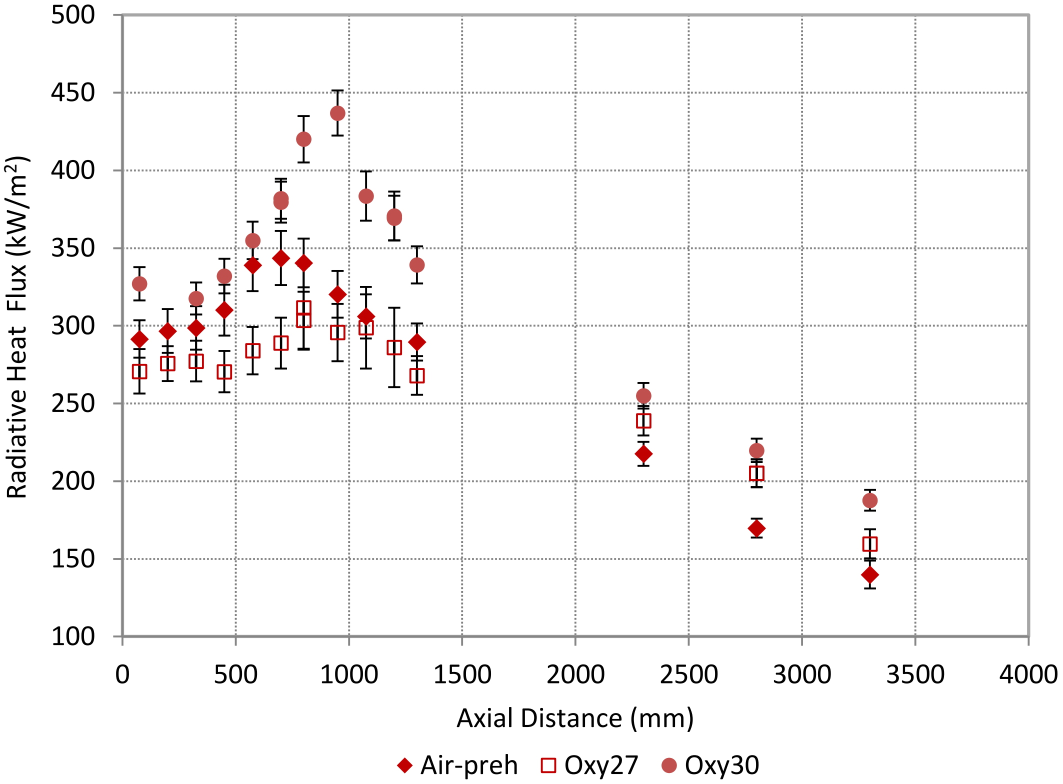

Figure 4.26 Radiative heat flux measurements for the oxy27 and oxy30 cases, taken without the CaF2 window attachment, compared against the preheated air-fired results.

Next to matching the radiative heat transfer for oxy-fuel retrofits, it is also important to closely approximate the heat transfer in the convective sections of boilers. Smart *et al*. (2010b) found that heat transfer in the convective furnace section of their 0.5 MW facility was inversely proportional to the total O_2 concentration. They attributed the reduction in the convective heat transfer to the reduction in the flue gas mass flow. This indicated that both radiative and convective heat transfer profiles cannot be matched exactly, but a balance may to be found with an acceptable operational range existing, where both radiative and convective that heat transfer closely approximates the air-fired values. Smart *et al*. (2010b) found this recycle ratio to lie between 70-75% for retrofit applications. Recycle ratios of above 75% were not recommended for any applications whereas recycles below 70% can be suitable for the newly built applications.

4.2.3.1 Investigation into the Heat Flux Measurement Method

For the oxy30 case the radiative heat flux measurements using N_2 as the purge gas were repeated using a CO_2 as the purge. The flows were kept constant, by setting the same supply pressure and using the equivalent length and diameter purge gas tube. Both of these gases are inert and offer a better alternative to air, where the additional O_2 would alter the combustion environment.

This investigation was done to examine the effect the purge gas has on the measurements. After the radiative measurements, the total heat flux measurements were also repeated to increase confidence in the repeatability of the measurements.

The radiative heat flux measurements, shown in Figure 4.27, show a notable difference between the results, especially in the vicinity of the flame. The difference between the measurements is 4% on average across all the measurements, 8% at the peak and with the maximum value of 10% at the 575 mm location. In comparison, the total error in the N_2 purged measurements was ±11% on average, ±15% at the peak and took the maximum of ±16% at the 1075 mm and 1200 mm locations.

The overall lower heat flux measurements using the CO_2 purge method may be due to the increased cooling effect on the probe tip as a result of switching N_2 to the higher heat capacity CO_2 purge. As the purge gas exits the probe tip, it expands and some may be recirculated to the probe tip. Because the CO_2 has a higher heat capacity it may cool the surface of the probe more. Moreover, the increased cooling effect near the flame zone may be due to increased disturbance and cooling of the flame when using the CO_2 as the purge gas. Again this is due to the thermophysical differences between these gases and especially the higher heat capacity of CO_2 compared to N_2.

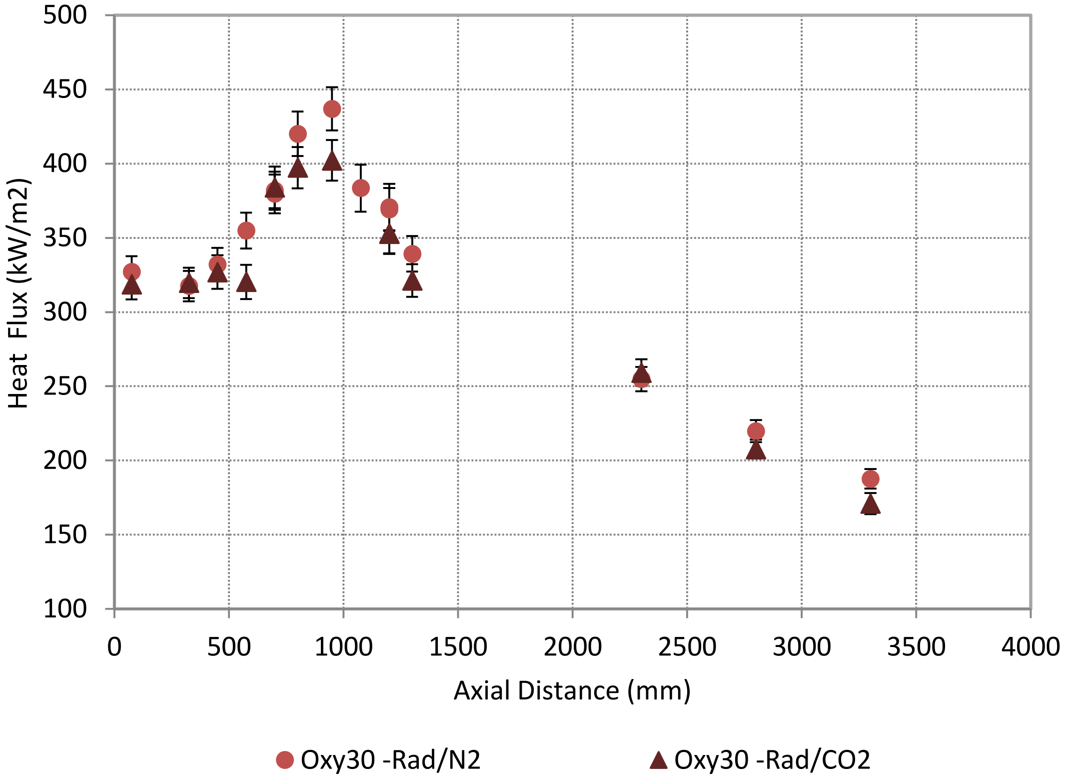

Figure 4.27 Radiative heat flux measurements for the oxy27 and oxy30 cases, taken without the CaF2 window attachment, using N_2 and CO_2 as purge gases.

Using any purge gas constitutes an intrusive measurement, but the N_2 purged method, which is in line with the manufacturer’s recommendation, appears to be a less intrusive alternative and this method was adapted for future measurements. However, as an alternative Argon (Ar) might offer improvements in the accuracy of future measurements as Ar has a lower molar heat capacity than CO_2 or N_2. The additional benefit of using Ar over N_2 is when FGR is used. Because Ar does not affect NO chemistry, and this way NO emission measurements can be conducted in-between heat flux measurements or sooner after them, even with trace amounts of the purge gas remaining in the oxidiser due to the effect of the recycle.

There was a reduction observed in the total heat flux measurements compared to the radiative heat flux results, especially near the peak of the trends. This reduction was not observed during the oxy27 measurements, but may be due to the increased deposition on the probe for the oxy30 case, where higher particle concentrations may exist due to the reduction in oxidiser flow. This may result in increased deposition, forming a substantial thermal barrier on the sensor surface reducing the results.

However, the total heat flux measurements, shown in Figure 4.28, indicate good repeatability, reproducing the same trend and with all measurement pairs located within each other's margin of error.

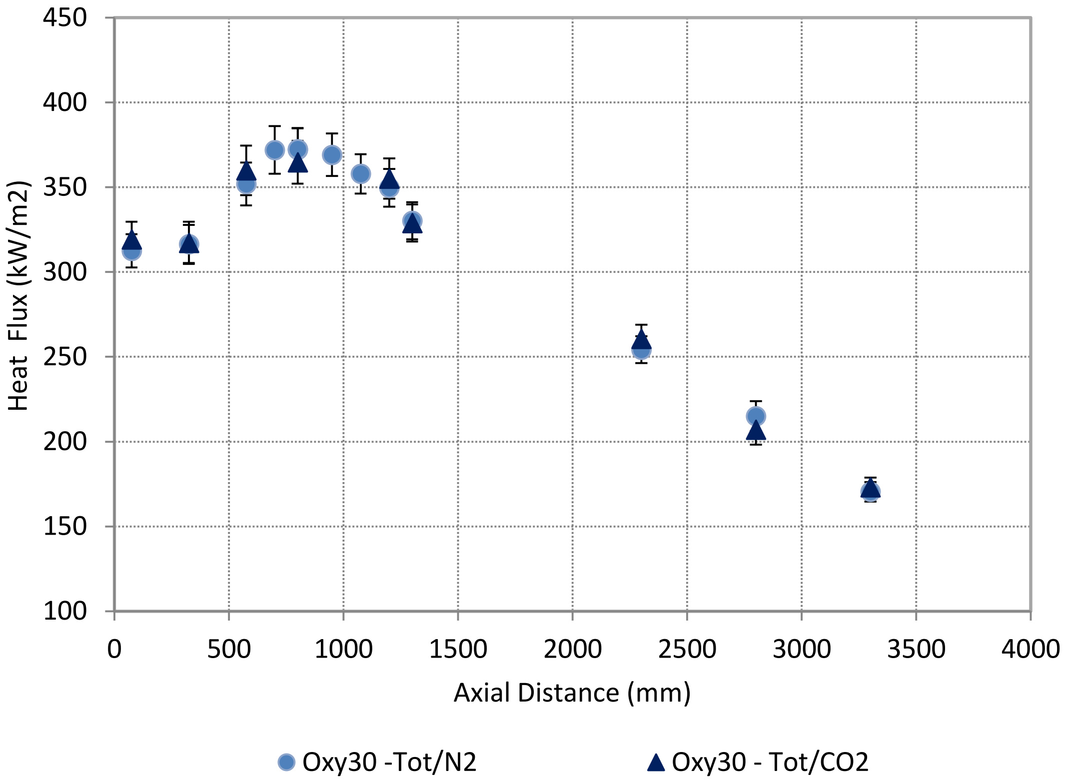

Figure 4.28 Total heat flux measurements for the oxy27 and oxy30 cases, without the CaF2 window attachment, taken after the radiative heat flux measurement using N_2 and CO_2 as purge gases.

Nonetheless, as shown in Section 4.1.4.2, the heat flux to the furnace walls is dominated by radiation, which is consistent with the findings in literature and therefore the focus for the oxy-fuel experiments was on investigating the radiative heat transfer presented in Section 4.2.3.

4.3 Summary of the Experimental Conclusions

4.3.1 Air-fired Experiments

Coal was fired in air under both non-preheated and preheated conditions and a range of detailed measurements were taken to investigate the impact of these on the combustion performance of the burner. The following conclusions can be drawn:

- Preheating the combustion air increases the heat input to the burner, facilitating ignition and therefore stabilising the flame.
- Preheating the Secondary and Tertiary streams increases the velocity of these streams and therefore changes the aerodynamics of the burner, enhancing the mixing between these streams and the primary stream.
- The additional heat also enhances devolatilisation and improves burnout, enhancing the efficiency of the process.
- The radiative heat transfer from the flame also increases, which is significant because it is the main and most important form of heat transfer within furnaces. The largest increases are observed near the flame region, which would result in increased radiative feedback between adjacent burners in commercial multi burner boilers, further increasing the radiative heat available to heat the fuel particles and having a beneficial effect on flame stability.
- Furthermore, preheating increases the efficiency of the power generation process by enabling low-grade sensible heat recovery from the flue gas, recycling it into the boiler.

A test campaign was performed in order to investigate the effect of burner staging on NO and CO emissions with both non-preheated and preheated combustion air, and also to establish the optimal emissions performance of the burner for the non-preheated and preheated cases:

- CO_2 and SO_2 emissions are not affected by burner staging.
- CO emissions decreased with preheating the combustion air, and also with increasing burner staging for both the non-preheated and preheated cases.
- The disadvantage of preheating combustion air was found to be that it increased thermal NO_x formation due to increasing the temperature of the shear combustion layer between the O_2-lean primary and the staged-secondary/tertiary streams.
- Evidence for increased fuel NO_x formation was also found based on the significant differences between the NO emissions at each split setting.
- However a decreasing trend in NO emissions was observed in both preheated and non-preheated cases when the burner staging was increased. Split positions 3 and 4 were identified as optimal setup parameters for the non-

preheated and preheated cases, respectively, with the lowest NO emissions. Further increasing burner staging does not result in a significant further reduction in NO emissions. Subsequent CFD calculations revealed that these settings corresponded to 48:52 and 45:55 ratios between the secondary and tertiary streams.

- The effect of the primary air ratio was only found to influence the emissions slightly with the 20% primary ratio, corresponding to the operating setting of a 40 MW scaled version of this burner, resulting in the lowest NO emissions.
- The primary air ratio was found to have a significant effect on flame stability. Stability was observed to worsen for the 22% primary air case, corresponding to an increased primary air velocity and reduced residence time. Whereas the overall the flame stability improved for the 18% primary case, which resulted in a reduced momentum of the primary jet and coal particles.

Conclusions from detailed measurement of in-furnace suction pyrometry and heat flux results for the preheated combustion air case included:

- Evidence for the presence of the ERZ was seen in both the suction pyrometry results as well as in the heat flux measurements. The location of the ERZ corresponded to an increase in convective heat transfer measurements. The suction pyrometry results revealed a level temperature profile at the ERZ, which corresponds to the theory that the ERZ consists of recirculated combustion products.
- The penetration of the combustion air supplied is evident on the suction pyrometry results obtained close to the burner at 75 and 200 mm axial distances, resulting in significant dips in the radial temperature profile.
- The combustion air stream was found to follow the trajectory of the quarl angle as it enters the furnace. This is seen from the radial shift in the location of the temperature dips corresponding to the penetration of the combustion air. This is due to the swirling combustion air attaching to the quarl before it enters the furnace.
- Gradual mixing between the combustion air streams and the ERZ is seen from the steady change in radial temperature profiles between these regions.

- The IRZ associated with staged burners with a stabilising bluff body region at the centre was also identified. The importance of the IRZ and ERZ on stabilising the flame was emphasised due to the recycling of heat to the root of the flame, increasing particle heat up and devolatilisation.
- The effect of IRZ on NO_x reduction was also argued, as the volatile-N species evolving from coal, devolatilising in the reducing IRZ, tend to form N_2 instead of NO. Also as the IRZ recirculates NO already formed downstream of the flame, to the root rich in hydrocarbon radicals, this zone has an important NO_x destruction effect.
- The relatively high temperatures measured at the centre of the furnace at the 75 mm axial distance, confirmed early ignition of the flame, which corresponded to visual observations from 2D imaging.
- The end of the burnout zone was estimated to be between the 575 and 800 mm axial distances, as the temperature profiles flatten put at this zone and downstream of which a gradual cooling of the flue gas is measured, corresponding to heat transfer to the furnace walls and heat removal by the cooling water jackets.
- When contrasting the suction pyrometry results with the measurements of the sheathed thermocouples, errors associated with radiative losses of typical sheathed thermocouples were also confirmed. A larger temperature gradient between the thermocouple and the furnace boundary results in a larger temperature difference between the measured and the true gas temperature. Evidence for erroneous measurements due to the effect of deposition and burning of slag on the first sheathed thermocouple placed within the flame was also argued and the use of suction pyrometry in gas temperature measurements was justified.
- Radiative heat transfer follows the trend observed during the centreline temperatures measured with suction pyrometry, peaking between the 575 and 800 mm measurement ports. After the 800 mm location, as the gases within the combustion chamber cool, the radiative heat flux progressively decreased as well, with the lowest reading recorded at the last measurement location before the flue outlet.

  - The location of the peak in total heat transfer is shifted from the radiative peak at the end of the flame, closer to the root of the flame.
  - The trends observed suggest that the total heat transfer, which is the sum of the convective and radiative terms, is manly influenced by the thermal radiation in furnaces firing pulverised coal. Therefore the radiative heat flux data is of great importance to the validation of the newly developed CFD submodels on this furnace.

4.3.2 Oxy-fired Experiments

Coal-fired experiments were performed under oxy-fuel conditions at the total O_2 concentrations of 27% (oxy27) and 30% (oxy30) by volume. The cases investigated involved simulated recycle, using a once-though approach.

Relating to the emissions performance, the following conclusions can be drawn:

- Oxy-fuel combustion is a viable technology to produce flue gas high in CO_2 concentration, which is required to enable carbon capture without chemical scrubbing processes. Dry CO_2 concentrations of 95% and 93.6% were achieved for the cases investigated.

NO emissions:

- As the recycle rate reduced, corresponding to higher O_2 concentration cases, the exit concentrations of NO increased by 16%. This was largely due to the reduced oxidiser flow and the resulting reduction in dilution by CO_2.
- The above was confirmed by the much smaller increase in NO emissions (6%), on a mg/MJ basis, when moving from the oxy27 to the oxy30 case. It was reasoned that the higher temperatures measured by the process thermocouples corresponded to higher temperatures all over the flame and therefore may increase the production of thermal NO.
- Both NO concentrations and emissions indices showed a significant reduction in the amount of NO produced when moving to the oxy-firing cases. Compared to the preheater air base case, the oxy27 and oxy30 cases resulted in a 53% and 51% reduction in NO emissions, respectively.
- Reduced thermal NO formation may be important in the reduction of NO due to low levels of atmospheric N_2 in the oxidiser, which may produce

oversaturation of NO in the combustion atmosphere reversing the Zeldovich mechanism.

- To keep thermal NO formation suppressed it is important to keep the level of air ingress to a minimum, especially as low levels of air ingress can result in significant accumulation of atmospheric N_2 in the oxidiser due to continuous recycling of the flue gas produced.
- The reduced atmospheric N_2 in the oxidiser also reduces prompt NO formation. Therefore the importance of prompt NO, which was low in air-firing applications, is thought to decrease further in oxy-fuel combustion.
- O and OH radicals are important in fuel NO formation via the oxidising reactions with the N containing intermediate species. The concentration of OH radicals increase in high CO_2 atmospheres, via the reversible reaction between CO_2 and H forming CO and OH. This alters the radical pool and could promote the formation of NO from volatile-N.
- However, fuel N formation, which is regarded as the major mechanism for NO formation, producing ~80% of the total NO in pulverised coal flames, was reasoned to have significantly reduced when moving from air- to oxy-firing using preheated combustion oxidiser.
- Fuel NO formation is affected by the fluid dynamics, via its effect on burner staging and mixing between the fuel rich primary and staged secondary and tertiary streams. Compared to the air-firing cases the burner velocities decreased significantly. This may then result in decreased mixing between the fuel rich flame root and the staged combustion air streams, allowing more residence time for the volatile-N in the reducing zones of the flame, significantly lowering fuel NO formation.
- Evidence of higher volatile formation in oxy-fuel combustion was found in the literature, which was attributed to the heterogeneous gasification reaction of CO_2 with the char, which also affected N partitioning producing an increased volatile-N release. When Low-NO_x burners are used, such as the one used in this investigation, increased volatile-N release may reduce fuel-NO formation due to more fuel-N being released in the staged fuel rich zones promoting volatile-N conversion to N_2.

- Based on finding in the literature, the reburn mechanism is expected to increase in importance when flue gas recycle is used. The NO, recycled back into the furnace, reacts with hydrocarbons in the root region of the flame and also with intermediate volatile-N species released during devolatilisation. This reduces the recycled NO to intermediate volatile-N, which then may be converted to NO or N_2 depending on the combustion environment.

SO_2 emissions:

- As the recycle rate reduced, corresponding to higher O_2 concentration cases, the exit concentrations of SO_2 increased. As the amount of sulphur introduced with the coal remained the same between the two cases, the increase in exit SO_2 concentrations was attributed to the reduced oxidiser flow and the resulting reduction in dilution by CO_2.
- The above was confirmed by emissions indices, which showed no significant difference between SO_2 emissions between the oxy-fired cases (calculated on a mg/MJ basis). This emission indices (on a mg/MJ basis), showed a significant reduction in the amount of NO produced and similar SO_2 emissions as measured during air firing.
- Comparison of air and oxy-fired emissions indices suggested that SO_2 emissions are independent of the combustion atmosphere used, and depend on the amount of sulphur supplied with the coal. Therefore the SO_2 emissions can be altered by the choice of coal used.
- Based on findings published in earlier studies, when moving to real flue gas recycle the concentration of the trace pollutants, such as SO_2, is expected to increase further, due to recycling of SO_2 produced back into the furnace, with this the concentration of SO_3 is also expected to increase, raising additional challenges for controlling corrosion. On the other hand, capture of sulphur by the ash increases during oxy-fuel combustion.

CO emissions:

- The results indicate that there are no significant issues in the control of CO emissions when moving to oxy-fuel combustion.

The effect of oxy-firing on the temperature profiles and on the heat flux characteristic of the flame was also investigated, and the following conclusions were drawn:

- The peak radiative heat transfer values of the air and oxy30 cases correspond to the typical range predicted on a coal-fired boiler using the FURDEC heat transfer code, which was 340-500 kW/m^2.
- The results indicate that it is possible to match the air-fired temperature profiles when retrofitting for oxy-fuel combustion by modifying the recycle ratio. The optimal recycle ratio lies between the investigated cases of 27% and 30% total O_2 concentrations (when dry recycle is used).
- Similarly, the radiative heat flux profiles can also be adjusted, due to the dependence of thermal radiation on the temperature.
- For the oxy-cases, in furnace temperatures and heat flux increased with increasing total O_2 concentration.
- The temperature and heat flux measurements trends showed significant differences in the first furnace section between the air- and oxy-fired cases. This pointed to delayed combustion due to the higher heat capacity of CO_2; and delayed mixing between the Primary and Secondary/Tertiary streams, which may produce longer flames for the oxy-fired cases where the same burner is used for both firing modes.
- The increased gas emissivity was found to increase the radiative heat transfer. Gas emissivity increases when replacing atmospheric N_2 with the tri-atomic CO_2, which actively participates in gas radiation and has a higher emissivity than N_2. Evidence for this was found in the second half of the furnace, where similar temperatures were measured for the preheated air and oxy27 cases, but these corresponded to significantly higher radiative heat transfer measurements for the oxy27 case than for the air case.
- Comparing the findings with the literature showed that flame properties at the same recycle ratios may vary significantly with the type of coal used, and also depend on geometry and aerodynamics of the burners used. This confirmed the need for experimental trials using a range of coals with scaled versions of the burners to be used at commercial oxy-fired power stations.
- The residence time within the furnace is higher for the oxy-fired cases, where the residence time increases with the total O_2 concentration. This is due to the

reduction in recycle rate and therefore in the total oxidiser flow. Compared to the preheated air-fired cases, the oxy27 and oxy30 cases had a 26% and 34% increase in residence time, respectively.

- The burnout is expected to improve with the reduction of recycle rate, which corresponds to higher volumetric O_2 concentrations, higher in furnace temperatures and higher residence times.
- The use of Argon purge was recommended instead of N_2 in future heat transfer measurement trials. This may offer improvements in the accuracy of the measurements due to the lower heat capacity of Ar.

Chapter 5

Combustion Modelling on Coal Fired Test Furnaces

The performance of large scale pulverised fuel burners may be assessed by experiments carried out on small scale test facilities using scaled burners typical to the commercial facilities. Furthermore, the use of CFD is increasingly used to complement the experimental work.

In this section a description of the development of the modelling approach with recommended techniques from the literature is presented. First these techniques are applied to the 250 kW oxy-fuel facility fitted with a theoretical scaled version of an IFRF burner. Then this approach is applied and validated on the IFRF furnace equipped with a 2.4 MW pulverised coal burner operated under air-firing conditions.

Building on this work, the modelling of a 500 MWe utility boiler was undertaken, in relation to furnace temperatures, heat transfer and burnout. Coal, a 20% biomass blend, and 100% biomass fired in air and oxy-fuel environments for a wet-recycle with the same thermal input were studied.

5.1 Modelling Work on the Proposed 250 kW Test Facility

5.1.1 Geometry and Burner Scaling

Although the design of the 250 kW furnace and burner had not been finalised at the start of my PhD, I based my simulations on the 250 kW, but it was fitted with a scaled version of a 2.5 MW IFRF burner.

The furnace body is described in detail in Section 3.2, however the description of the burner dimensions used during this study are given below.

The dimensions of the burner were obtained by scaling the 2.5 MW IFRF Aerodynamically Air Staged Burner (AASB) to the required output.

As the majority of the NOx formation takes place in the near burner zone, the effect of scaling on the aerodynamics of the region has to be considered, and the mixing between the air, fuel and recirculating combustion products controlled, thus creating controlled chemistry zones and maintaining low NOx emissions for the scaled burner as well (Smart *et al.*, 1989). Ideally, the scaling should produce a complete similarity of all the mixing, heat transfer and combustion processes, but as all physical and chemical phenomenon do not scale the same way, some of the similarity criteria has to be relaxed (Smart *et al.*, 1992). Beér and Chigier (1972) noted that if the Reynolds number is large enough, there is no need to maintain the same value of Re in the scaled version. This is true in the typical pulverised coal applications with typically Re > 10^5. Also, as the combustion process is controlled by turbulent mixing, molecular transport processes can be neglected, thus the scale dependency of the Prandt and Schmidt numbers need not be considered. The Froude number is another similarity criteria, which can be neglected when inertial forces dominate over the buoyancy effects, which is valid in most combustion applications, with the exception when low burner velocities are used. Smart and Morgan (1992) list two traditionally used scaling methods as the constant velocity and constant residence time scaling. Both of these methods maintain geometric similarity, constant co-axial momentum ratios as well as constant swirl number. The former method also results in constant co-axial velocities, whilst the latter scales the velocities with the burner diameter (which is a function of the thermal throughput). However, as constant residence time scaling results in excessively low wind box pressures for small scale burners (Weber, 1996), the use of constant residence time scaling was adopted. Detailed description of this method can be found in Smart and Morgan (1992), the schematic of the scaled burner is shown in Figure 5.1, and its dimensions are listed in Table 5.1.

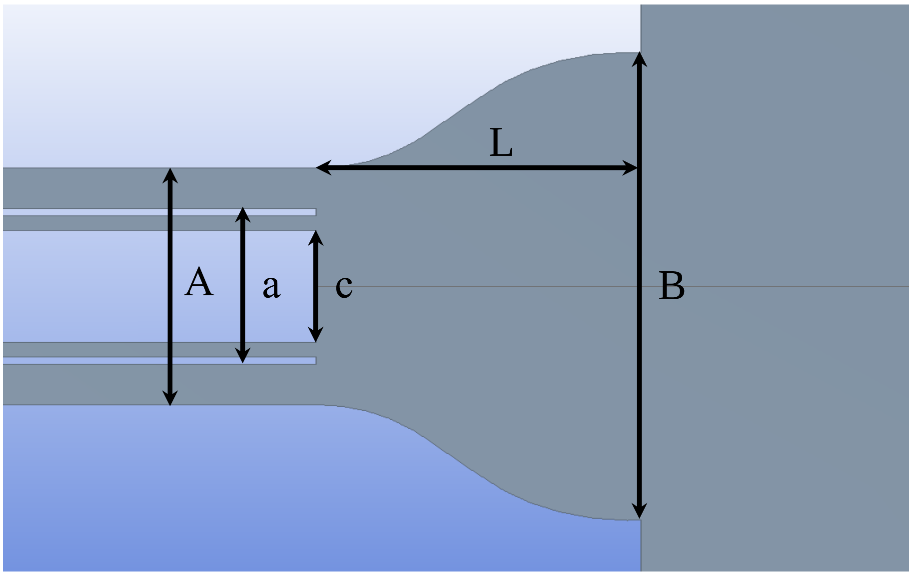

Figure 5.1. Schematic of the modelled 250 kW burner.

Table 5.1. Dimensions of the 2.5 MW AASB (c is not specified by the authors, but given as a correlation: c/a=0.7 (Smart and Morgan, 1992)) and the scaled 250 kW burner.

Dimensions (mm)	2.5 MW (base)	250 kW (scaled)
a	140	49
A	234	82
c	98	34
B	468	163
L	234	82

The inner annulus is used to introduce the primary flow of the transport air and coal, and the secondary (outer) annulus is for the balance of the combustion air and the secondary flow is swirled by movable swirl vanes. Their effect was taken into account by modelling the axial and tangential components of the swirled secondary flow. Thus modelling the geometry of the swirl vanes was not necessary, and the computational domain was truncated at the burner inlet pipe upstream of the swirl vanes.

The shape of the quarl is based on the standard IFRF quarl equation (a case specific version of this can be found in the literature: Peters and Weber (1997)). This equation was not available at the beginning of the work, and so initially a number of alternative quarl designs were assessed (see the results section) and finally a shape similar to the schematic drawing shown by Weber *et al*. (1992) was employed.

5.1.2 Grid Generation

In order to model the combustion process in furnaces, a computational domain (corresponding to the furnace geometry) has to be created. This is then decomposed into a finite number of cells, in order to create the computational grid (or mesh). Within these cells, the transport equations describing the system are solved, including the mass and momentum conservation, species concentration, temperature, radiation as well as the turbulence. The calculated values are assumed to be constant within each of these cells, and therefore the choice of grid resolution influences the accuracy of solution. Confidence in the grid independency of the solution can be gained by comparing the results obtained on different grid resolutions. For this purpose, five grids were created. The number of cells in order of increasing fineness were 5700, 9000, 13600, 19000 and 24000 (to 3 significant figures) with the 19000 cell size grid adopted for further studies (see Section 5.1.8).

In general, the accuracy of the solution increases with the increase in the mesh resolution. However, this increase in the number of computational cells corresponds to an increased demand for computational resources. Therefore it is the job of the CFD engineer to design the computational grid based on the type of the problem, the accuracy of the solution required and considering the computational power available.

In combustion applications, the area of prime interest is the burner inlet and flame region where the flow changes significantly spatially, and also most of the chemical reactions take place. The combustion process strongly depends on the turbulence chemistry interactions. Thus, given the importance of the region, it is common practice to use finer cells within this zone in order to resolve the special gradients of the transported properties with the desired accuracy. Also, the shape of the cells can influence the accuracy of resolving the flow patterns. If the geometry permits, the use of hexahedral cells is recommended as they can be aligned with the flow. Although the x, y and z components of the flow are calculated by most CFD codes, the use of tetrahedral cells are regarded to over predict the numerical diffusivity, which results in reduced accuracy of the solutions.

The computational grid can be either structured or unstructured. For combustion applications, the use of structured grids is recommended (due to the regular hexahedral cells associated with this approach). However the use of fully structured grids can be prohibitive due to the complex geometries (e.g. modelling of the combustion air flow over a complex system of swirl veins), and require an unstructured grid. Although, in these cases, the latter should only be used in the zone of the problematic region, and the rest should still be structured. A disadvantage of the structured grids is the considerable time required for their creation, in contrast to unstructured ones (which can even be generated fully automatically). Nonetheless, as structured meshes require a reduced number of cells to obtain similar accuracy, and thus accelerating the computational solution process, their use was adopted in this thesis.

For the grid generation, ANSYS ICEM was used and initially the modelling was performed on 2D geometries. Although the whole of the furnace is not axi-symmetric, as the outlet at the bottom is situated on the side of the shell, its influence on the flow pattern within the flame is assumed to be negligible (it is situated approximately 4 meters downstream of the burner throat), and the use of 2D axi-symmetric simulations was justified.

The 2D grid is shown in Figure 5.4 with the denser mesh in the burner region. This region is sown in higher resolution in Figure 5.5.

5.1.3 Boundary Conditions

5.1.3.1 Inlet

The primary and secondary inlets were modelled as mass flow inlets of air (modelled as 23.15wt% O_2 and 76.58wt% N_2) and the conditions of these streams entering the domain are shown in Table 5.2.

Table 5.2. Modelled inlet conditions.

	Primary	**Secondary**
coal mass flow (kg/s)	0.0077	---
air mass flow (kg/s)	0.0138	0.0705
temperature (K)	298	573
axial velocity component (dimensionless)	1	0.68
tangential velocity component (dimensionless)	0	0.32
turbulent intensity (%)	4	8

The intensity of the swirl generated is described by the swirl number. During the simulations, the swirl intensity analogous to a swirl settings of 0.6 was considered, and the corresponding ratios between the axial and tangential velocities were determined based on the IFRF’s 2nd equation for the swirl number (Weber and Dugué, 1992).

Swirls are very important in combustion applications, since they enhance the turbulent mixing of the reactants (thus improving the combustion and burnout), and in this type of geometry it also generates an adverse pressure gradient, which plays an important role in shaping the internal recirculation zone (IRZ). By manipulating the shape of the IRZ, the residence time of the coal particles in this rich zone can be increased, thus achieving substantial NO_x reductions (Smart *et al.*, 1989).

The amount of air was calculated based on assuming 15% excess supply in addition to the stoichiometric requirement for the coal chosen for the simulation. The stoichiometric A/F ratio was calculated to be 9.21, and the actual 10.71. The distribution between the primary and secondary air streams was based on the distribution for the original 2.5 MW IFRF burner (Smart and Morgan, 1992), resulting in an primary A/F ratio of 2. The mass balance calculations were compared to the predictions obtained using FLAME (an equilibrium combustion software), with the mass fractions matching the calculated values to 4 decimal places.

5.1.3.2 Outlet

The outlet was modelled as a pressure outlet, and initially its location was chosen at 3 m distance from the quarl, assuming that the flame does not extend to this length and the conditions downstream of this point does not affect significantly the main characteristics of the flame. Thus the diameter of the outlet was the same as the furnace diameter.

However, this produced an excessively low mean outlet velocity, which resulted in significant backflow being induced. Although there is a capability to set the temperature and composition of this backflow, these settings are not applicable to this simulation as the back flow induced here is essentially a recirculation zone (with s non-uniform composition and temperature). This backflow was due to the very low mean outlet velocity (0.8 m/s), and its uneven distribution over the outlet, combined with the fact that the domain after the outlet is unknown to the solver. The large volume of backflow distorted the results and did not allow for a converged solution to be reached. Thus after the 3 m furnace section, a 1 m long convergent section was included, gradually constricting the diameter to 0.3 m. This approach resulted in a significantly increased outlet velocity (8.4 m/s), with similarly high velocities over the whole of the outlet which eliminated the backflow entirely, thus the subsequent simulations were performed on the grids with this convergent section included.

5.1.3.3 Walls

In addition to the inlets and outlet, the domain is bounded by the walls of the chamber (and of the burner pipe). The application of correct boundary conditions are required in order to obtain an accurate solution. However, likely sources of uncertainties are the temperature profile and the emissivity along the wall. This is due to a combination of reasons, since the emissivity is not only a function of the material but of the surface properties as well. Furnace walls typically do not have regular properties due to ash deposition, slagging and fouling (especially for non axi-symmetrical flames or horizontally fired furnaces) and also change with the progress of the deposition. In this case, the wall emissivity was expected to be approximately 0.8 (characteristic of a typical refractory lined furnace (RWE Power, 2008)), and thus a uniform emissivity of 0.8 was assumed.

Wall temperatures on the other hand were expected to differ significantly, not only between different walls, but over the length of the sidewalls as well, peaking next to the flame region and decreasing gradually towards the outlet. As there were no experimental results available, the wall boundaries were modelled by assuming an overall resistance and assuming a temperature at the outside wall (the steel shell touching the water jacket). This method allows the calculation of the resulting furnace wall temperature profile by FLUENT based on the specified resistance and net wall heat transfer.

The wall temperature at the water jacket was assumed to be 60°C, and the resistance was calculated as 0.2098 K/W, by summing the resistances of the individual layers (3 mm steel shell, 100 mm refractory and also 2 mm of ash deposition, see Figure 5.2). The quarl resistivity was set to 0.6 K/W, due to the stronger heat retarding nature of the quarl refractory material used to achieve a close to ambient outside wall temperature without water cooling. The inlet pipes were modelled with fixed wall temperatures equal to the temperatures of the transported air streams and with the emissivity as 0.6, which is appropriate for the metallic burner annuli (Peters and Weber, 1997). The wall temperature of the bluff body at the burner core was set as 573 °C, based on the assumption of Peters and Weber (1997) for a scaled version of this burner with 2.4 MW output.

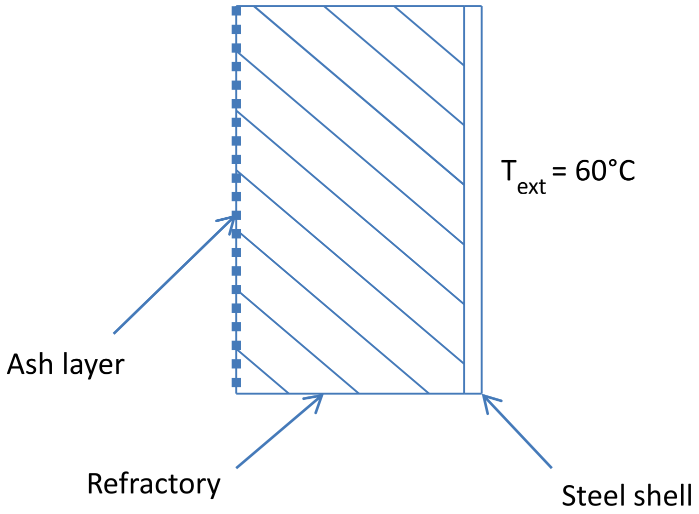

Figure 5.2. Schematic of the wall structure.

Table 5.3. Wall boundary conditions employed.

wall	**temperature (K)**	**emissivity**
primary annulus	298	0.6
secondary annulus	573	0.6
burner core	800	0.8
wall	**resistance (K/W)**	**emissivity**
quarl	0.6	0.8
furnace top section	0. 2098	0.8
furnace body	0. 2098	0.8

5.1.4 Coal Properties

Pittsburgh 8 was chosen for the simulations, based on the availability of comprehensive data (Fletcher and Hardesty, 1992). The ultimate and proximate analysis of this coal is shown in Table 5.4, and its gross calorific value was set as 30.17 MJ/kg on an as received basis. However, it should be noted that, volatile matter content listed is not representative of the evolution of the actual amount. This is due to the high heating rates encountered in pulverised fuel furnaces (typically 10^5 K/s) and the amount of volatiles evolved is considerably higher than at the low heating rates conditions applied during conventional proximate analysis. Therefore a high temperature volatile yield of 1.5 was specified (increasing the volatile mass fraction from 33.56 to 50.34 and reducing the fixed carbon content accordingly).

Table 5.4. Coal analysis data from the Penn State Coal Bank of Pittsburgh 8 (Fletcher and Hardesty, 1992).

Ultimate	wt% (daf)
C	83.26
H	5.41
O	8.1
N	1.58
S	1.58

Proximate	wt% (ar)
Fixed Carbon	50.58
Volatile Matter	33.56
Ash	13.32
Moisture	2.54

The size distribution of the coal particles was assumed to be represented by the Rosin-Rammler curve (ANSYS Inc., 2013), with the minimum and maximum particle size assumed to be 15 and 350 μm, respectively, with a mean size of 75 μm. Assuming that the particles are very small, their trajectories were tracked in the domain by the Lagrangian approach, with dispersion accounted for by using stochastic tracking to evaluate the effect of random fluctuations on the dispersion of particles. The mass, heat and momentum exchange between the solid and gas phases were accounted for by the source/sink terms in the appropriate equations. The density of the coal particle was taken to be 1400 kg/m^3.

5.1.5 Combustion Modelling

The coal particle temperature was calculated as governed by convective and radiative heat transfer, cooled by the latent heat of droplet evaporation and heated by the combustion of char. The particles were assumed to be represented by spheres, which swell to 1.4 times the original diameter during devolatilisation and then burn at constant diameter during char combustion when the density is decreased as a function of burnout. Uniform internal particle temperature was assumed, appropriate for pulverised coal particles in the given size range (the Biot number is <1 for typical particle diameters of <250 μm (Ma *et al.*, 2009)).

The devolatilisation was modelled using the single rate model with the Arrhenius constants for Pittsburgh 8 given by Fletcher and Hardesty (1992): 2.3×10^{14} 1/s and 230 kJ/mol as the pre exponential factor and activation energy, respectively; and the onset of devolatilisation was set to 327 °C, as suggested by Baum and Street (1971).

The volatiles evolve as either light gases or heavier aromatic compounds, but as pollutant formation was not investigated during this stage then they were modelled as a single species, with the molecular weight set to 50 g/mol according to the assumptions of Peters and Webber (1997) for another high volatile bituminous coal.

Volatile combustion was modelled by the eddy dissipation model proposed by Magnussen and Hjertager (1977), assuming that the reaction rate depends on the local concentration of the reactants, which is determined by the intermixing of the fuel and oxidiser containing eddies. This in turn is controlled by the dissipation of these eddies, and is proportional to the inverse of the large eddy mixing time scale, k/ε. The combustion of this volatile gas was assumed to proceed in a single step reaction:

$$\mathrm{C_{3.11}H_{4.48}O_{0.42}N_{0.0942}} + 2.46\ O_2 \rightarrow 3.11\ CO + 2.42\ H_2O + 0.0471\ N_2$$

Volatile combustion was assumed to take place entirely in the gas phase according to experimental observations of Baum and Street (1971), indicating that "spurts of volatiles could be ejected into the gas stream to distances up to 500 diameters away from the particle and would mix rapidly with the gas". Therefore the heat of combustion of the above reaction is added entirely to the gas phase enthalpy, thus raising its temperature.

The char combustion step was modelled by the diffusion limited model based on the work of Baum and Street (1971), where the rate of combustion is assumed to be limited by the rate of O_2 diffusing to the particle surface. This model was chosen as the Arrhenius constants for the chemical control were not available for Pittsburgh 8. Although this model neglects the influence of chemical control (the combination of O_2 with the carbon surface and the diffusion of combustion products away from the particle), which may be significant in regimes such as the one modelled, and thus could result in higher burnout predictions. Furthermore, in the further work (Section 5.3), char combustion modelling using the intrinsic model is adopted where the Arrhenius rates are independent of the coal used (Fletcher *et al.*, 1992), and structural properties of a number of coal are summarised by ANSYS Inc. (2013).

The combustible fraction of the char was assumed to be pure carbon and two step combustion was assumed, with the carbon oxidising to CO on the surface of the particle and as the CO diffuses away from the particle it is further oxidised to CO_2:

$$C_{(S)} + \frac{1}{2}O_2 \rightarrow CO \qquad \Delta\hat{H}°_c = -110.52\,kJ/mol$$

$$CO + \frac{1}{2}O_2 \rightarrow CO_2 \qquad \Delta\hat{H}°_c = -282.99\,kJ/mol$$

The heat of combustion evolved by the former reaction on the char surface is assumed to be absorbed by the char particle to increase its temperature and the heat of combustion of CO diffusing away from the char particle is added to the gas phase enthalpy as source term to raise the gas temperature (as assumed by Baum and Street (1971) and Peters and Weber (1997)).

5.1.6 Turbulence Modelling

Swirled diffusion flames are turbulent in nature. As discussed in the Chapter 2, the resolution of the turbulent flow field via DNS modelling is impractical for furnace modelling due to the prohibitively large requirement for computational power and memory. LES modelling is more affordable than DNS. Here the large eddies, which extract energy from the bulk flow and are non isotopic in nature, are computed directly. LES uses special filtering to exclude the smaller eddies from direct simulation, as these are isotropic in nature and can be modelled as such via RANS methods. This method allows for the resolution of fluctuations in space and time and thus is better suited for the modelling of pollutant formations and is also shown to better predict the radiation profiles in the near burner region (Edge *et al*., 2011b).

However, due to the large increase in computational memory and time (due to the time dependent resolution) LES modelling is not attempted within this thesis, and the use of the RANS techniques was chosen. A range of RANS models are available for turbulence modelling. From these the standard *k–ε* model is the most widely validated one. It is regarded as robust, computationally inexpensive and it is regarded as easy to converge. However, it is shown to be inaccurate in predicting the flow in the presence of swirl, due to the isotropic eddy viscosity assumption (Versteeg and Malalasekera, 2007).

The realisable k-ε model, is shown to produce good results in oxy-fuel modelling work on turbulent coal combustion with a swirl stabilised burner (Hjärtstam, 2012).

5.1.7 Heat Transfer Modelling

Since radiation dominates the heat transfer process in pulverised fuel boilers, its accurate prediction is essential. It must be noted that, although radiation is not influenced directly by the turbulent flow field, the effect of the latter on the temperature and species concentration profiles results in the strong indirect dependence of radiation on the turbulent flow resolution. For this case, the use of the Discrete Ordinates (DO) model was adopted with theta and phi pixels of 2.

5.1.8 Results

Figure 5.3 shows the assessment of the quarl shape on the IRZ. The straight quarl produces a significantly wider and longer IRZ, with lower velocities which increases the residence time of the particles. However, as the IRZ widens, the flame front moves closer to the furnace walls. This may result in the flame impinging on the refractory material, which can produce surface temperatures significantly above the maximum 1400°C recommended for the refractory to be used. Also, as the volume of the IRZ widens, the mean temperature decreases significantly, which reduces the radiation heat transfer (due to radiations the 4th power dependence on the temperature), thus decreasing the heat transfer to the particles. This may retard the ignition, char combustion and affect the burnout of the particles. Thus IFRF’s curved quarl shape was justified. Two of these were drawn (according to schematic drawings of Smart and Morgan (1992)), the one shown in Figure 5.3(b) and another with a stronger curvature in the middle of the quarl line, but the curvature at the quarl exit was not modified. This resulted in a similar shaped IRZs, which indicates the importance of the exit curvature.

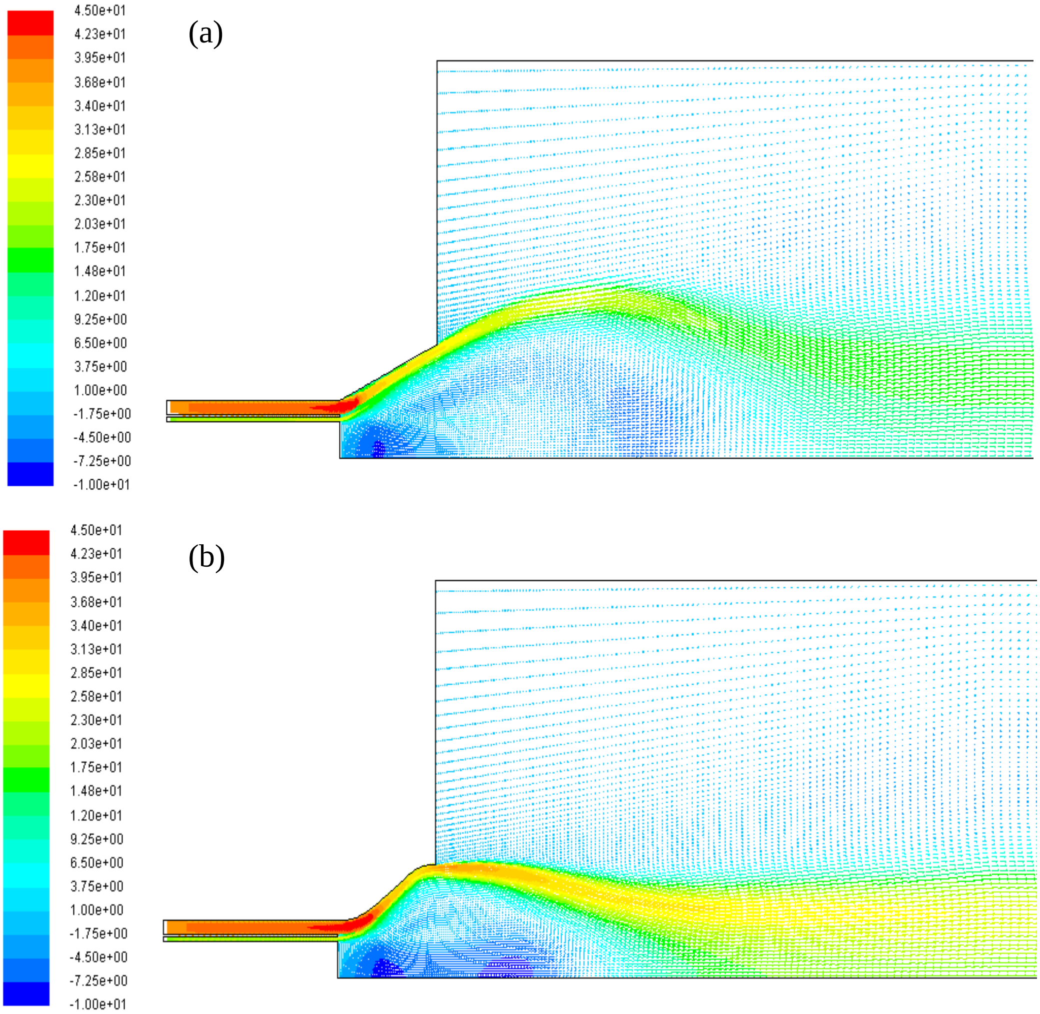

Figure 5.3. Velocity vectors for the (a) straight and (b) curved quarl shapes coloured by the magnitude of the axial velocity in m/s (combustion results).

5.1.9 Grid Independence Study

In general the accuracy of the solution increases with the mesh resolution, until a point is reached when the solution no longer depends on the grid resolution and is thus considered to be grid independent. Therefore establishing grid independence is mandatory in every CFD simulation in order to minimise the errors resulting from the grid resolution.

For this purposes, five grids were created see Table 5.5. The course (C_1) and fine (C_5) meshes are shown in Figure 5.4. As the experimental result were not available for validation then the final (finest) mesh was adopted as the base case (C_B).

Table 5.5. Cases examined during the grid independence study, listed in order of refinement, with C_B corresponding the very fine mesh adopted as a base case.

Case	Total no of cells in 2D	no. Cells,$_i$ / no. Cells,$_B$	Cell savings in 2D	Total no of cells in 3D (Quarter)	no. Cells,$_i$ / no. Cells,$_B$	Cell savings in 3D
C_1	5,772	0.24	76%	not calculated	---	---
C_2	8,984	0.38	62%	not calculated	---	---
C_3	13,644	0.57	43%	294,749	0.51	49%
C_4	16,278	0.68	32%	363,233	0.63	37%
C_B	23,934	1	---	580,966	1	

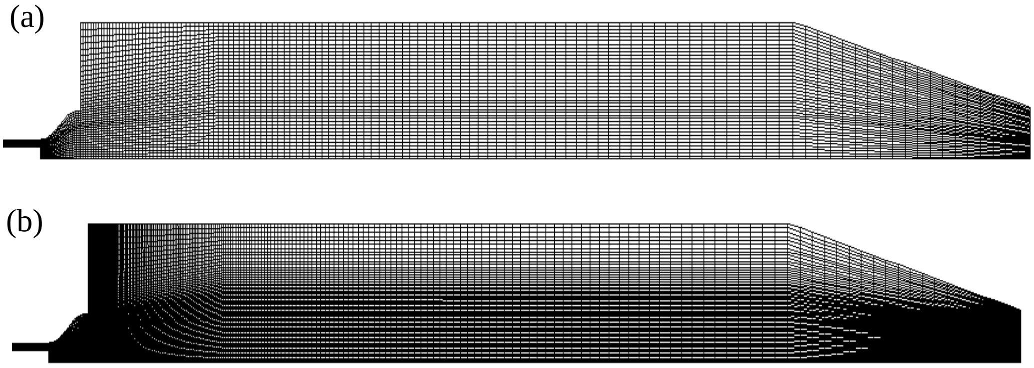

Figure 5.4. Outline of the (a) course mesh, C_1 and (b) the fine mesh adopted as the base case, C_B.

The majority of the refinements of the grid were concentrated in the flame region, given that in combustion applications this is the region of prime interest, as the most of the chemical reactions take place here. Also the flow patterns change significantly in this region and the combustion process strongly depends on the turbulence chemistry interactions. The mesh refinement in the near burner regions is illustrated by Figure 5.5 between the coarse and base meshes. The width of the cells close to the primary and secondary annuli are kept low, even for the coarse mesh (which overall contains 75% less cells than the fine mesh shown in Figure 5.5), in order to produce regular square shaped cells to capture the separation region as accurately as possible (where the primary and secondary streams separate from the burner walls and their intermixing begins). For the finer cases, the cells are expanded further down in the quarl with a much lower expansion ratio in order to further reduce the numerical diffusivity further.

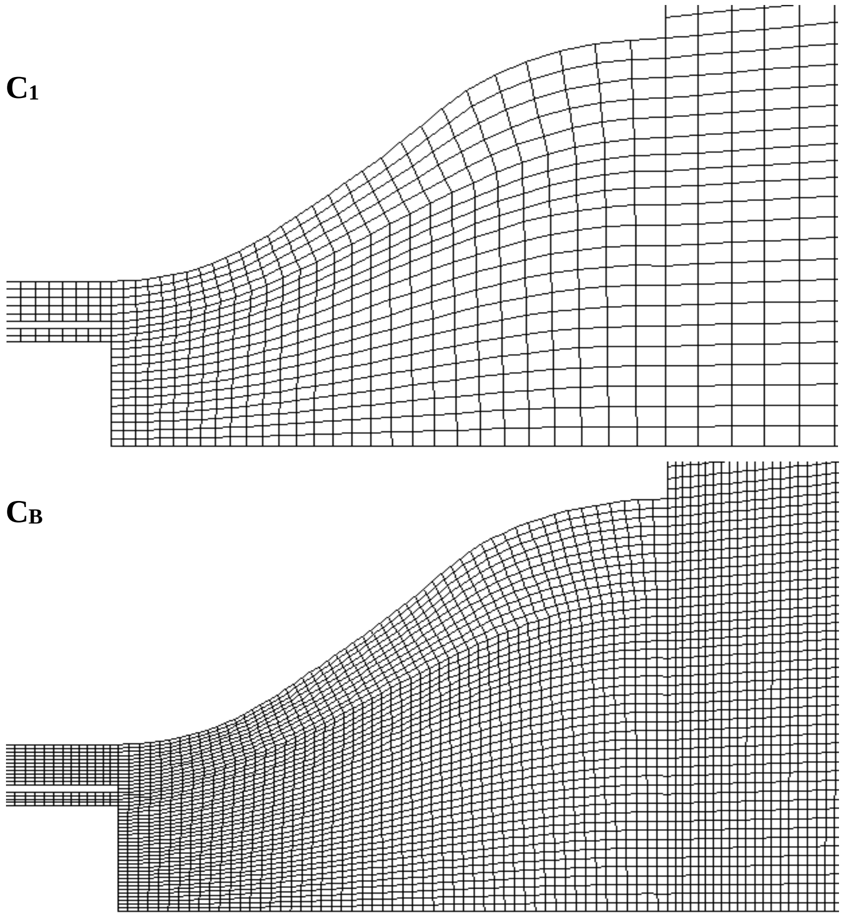

Figure 5.5. Mesh refinement of the near burner zone illustrated by the course mesh C_1 and the final mesh C_B.

Due to the strong coupling between the turbulent flow field and the chemical reactions of the combustion process, the correct resolution of the turbulent flow field in the flame region is essential. Therefore, first a comparison assesses the shape and strength of the IRZs produced for the five cases (Figure 5.6).

Each arrow represents a velocity vector predicted for each cell of the mesh, coloured by the magnitude of the axial velocity. The different arrow density is due to the different cell densities used between the cases. The magnitude and direction of the velocity vectors predicted and the location of the vortices were found to be very similar between all the cases investigated. This resulted in the conclusion that the overall flow patterns are only weakly influenced by the grid resolutions employed.

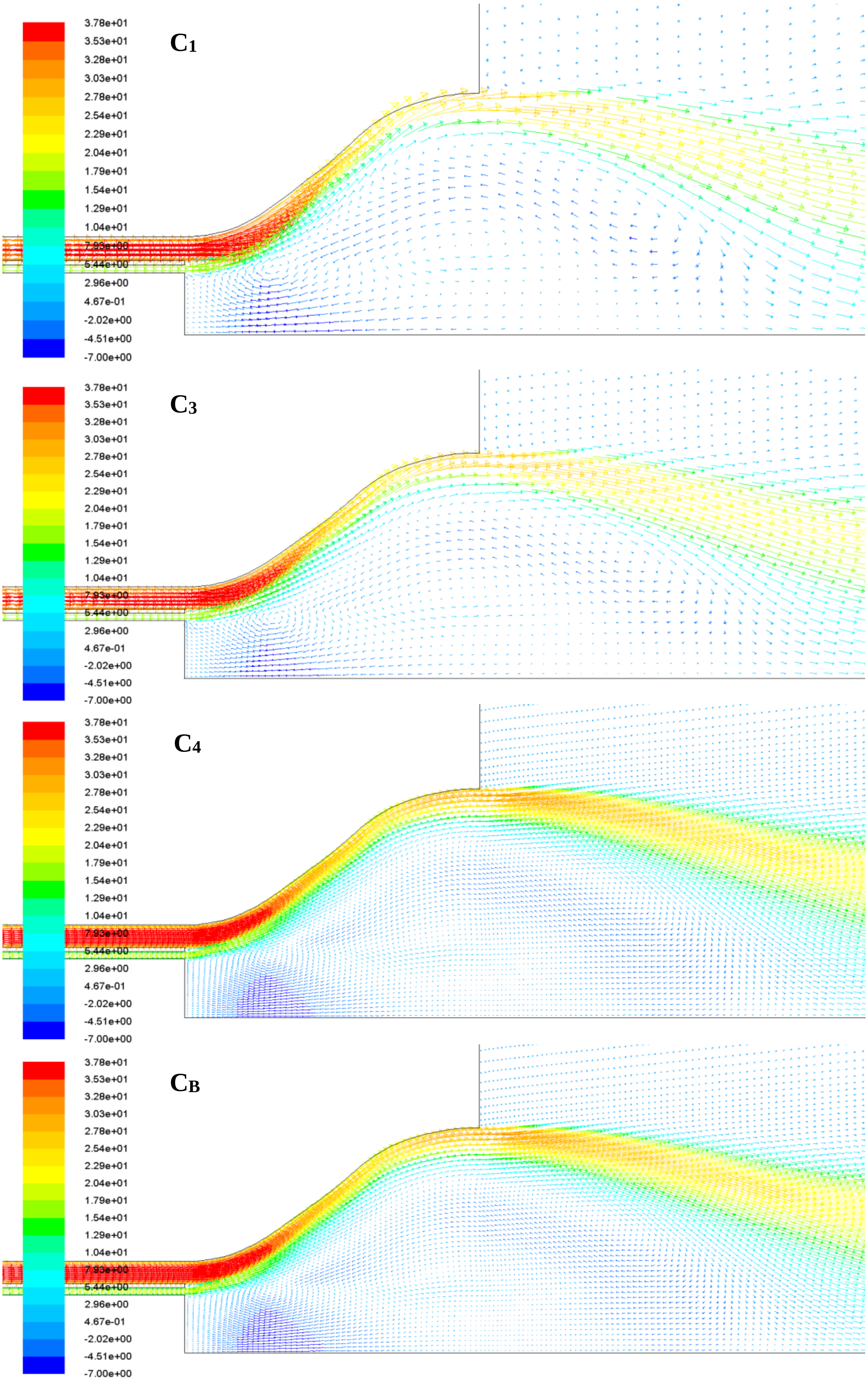

Figure 5.6. Comparison of the predicted velocity vectors between the cases investigated, coloured by magnitude of the axial velocity in m/s.

However when the radiation profiles were examined, significant differences were observed between the cases (Figure 5.7). Radiation is a major source of heat transfer in pulverised fuel combustion (and its importance is augmented in the oxy-fuel combustion). Its correct estimation is imperative in CFD modelling of pulverised fuel combustion, in order to correctly predict the heat transfer to the radiative section of the boiler tube banks.

Therefore, by examining the results presented in Figure 5.7, C_1 and C_2 could be eliminated, based on the notably lower radiation intensities predicted in the flame zone and as a consequence of this the lower radiation intensities produced near the walls next to these flame zones. The use of these cases would result in distorted predictions of the radiative heat transfer to the walls.

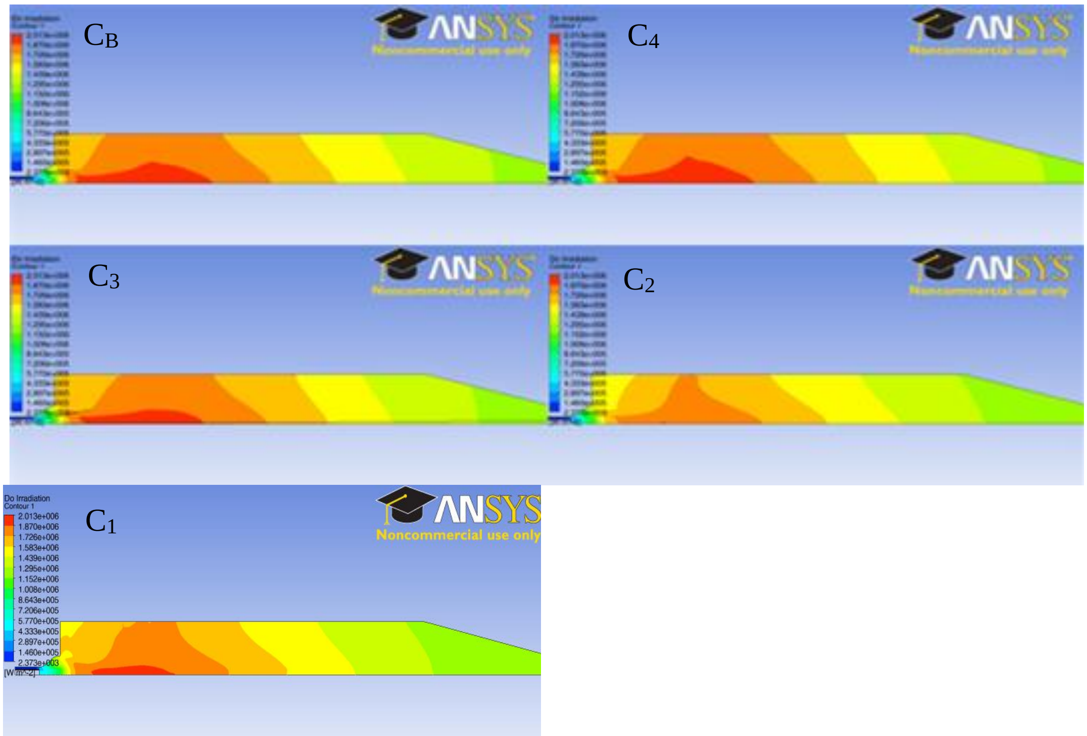

Figure 5.7. Radiation profiles predicted for the five different cases.

These differences in the radiation fields were attributed to discrepancies in the predicted temperatures (for the gas phase and therefore also the particles), which resulted in the reduction in radiation intensity (due to the radiation’s 4th power dependence on the temperature). For a better visualisation of the temperature profiles, ANSYS CFD-Post was used, for its capability to display the absolute difference in the examined variables between cases. Thus Figure 5.8 was produced by subtracting the temperature profiles calculated for the lower resolution meshes from the temperature profile calculated for the base case.

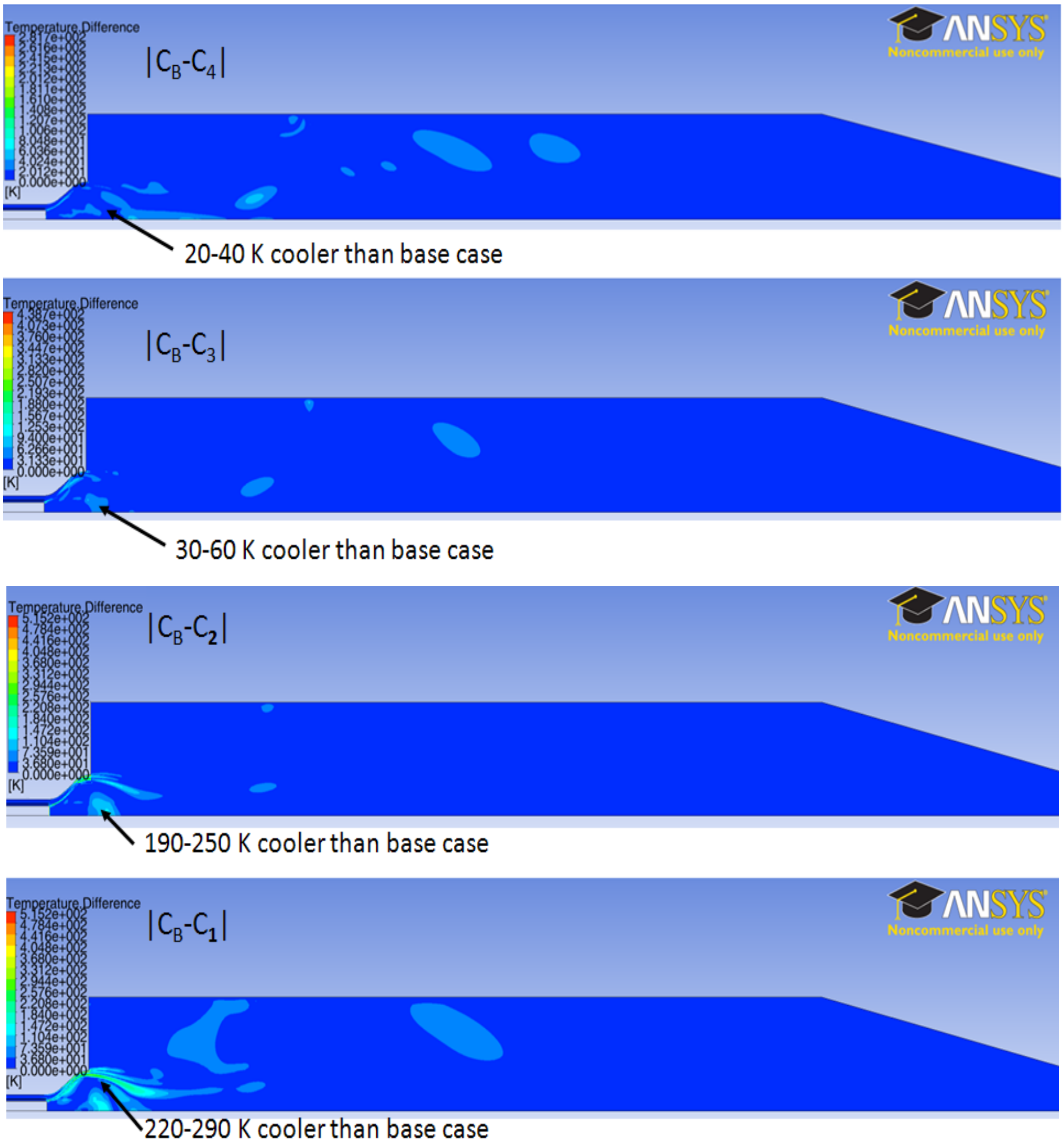

Figure 5.8. The magnitude of temperature differences between the base case and the lower resolution meshes (colour scales are bounded by the minimum and maximum values for each case, therefore the magnitude of difference is indicated by the arrows).

Figure 5.8 proves that the lower radiation profile predictions were a result of lower temperature predictions inside the quarl zone, which correspond to the gas phase temperature. This in turn influences the temperature and thus the combustion of the discrete phase particles as well. It was also argued that the source of this difference has to originate from the gas phase, as the particle combustion models were not varied, and due to the Lagrangian particle tracking approach, the discrete phase combustion rates are not directly dependent on the mesh resolution.

Gas phase temperatures are significantly influenced by homogeneous volatile combustion, which is modelled by the eddy dissipation model of Magnussen and Hjertager (1977), where the reaction rate is first-order dependent on the inverse of the large-eddy mixing time scales, *k/ε*. Indeed, Figure 5.9 confirms that the difference in the predictions of *k/ε* compared to the base case is approximately an order of magnitude higher for cases C_1 and C_2 compared to case C_4, which corresponds to an order of magnitude difference in the temperature differences predicted for the cases C_1 and C_2 compared to case C_4, see Figure 5.8.

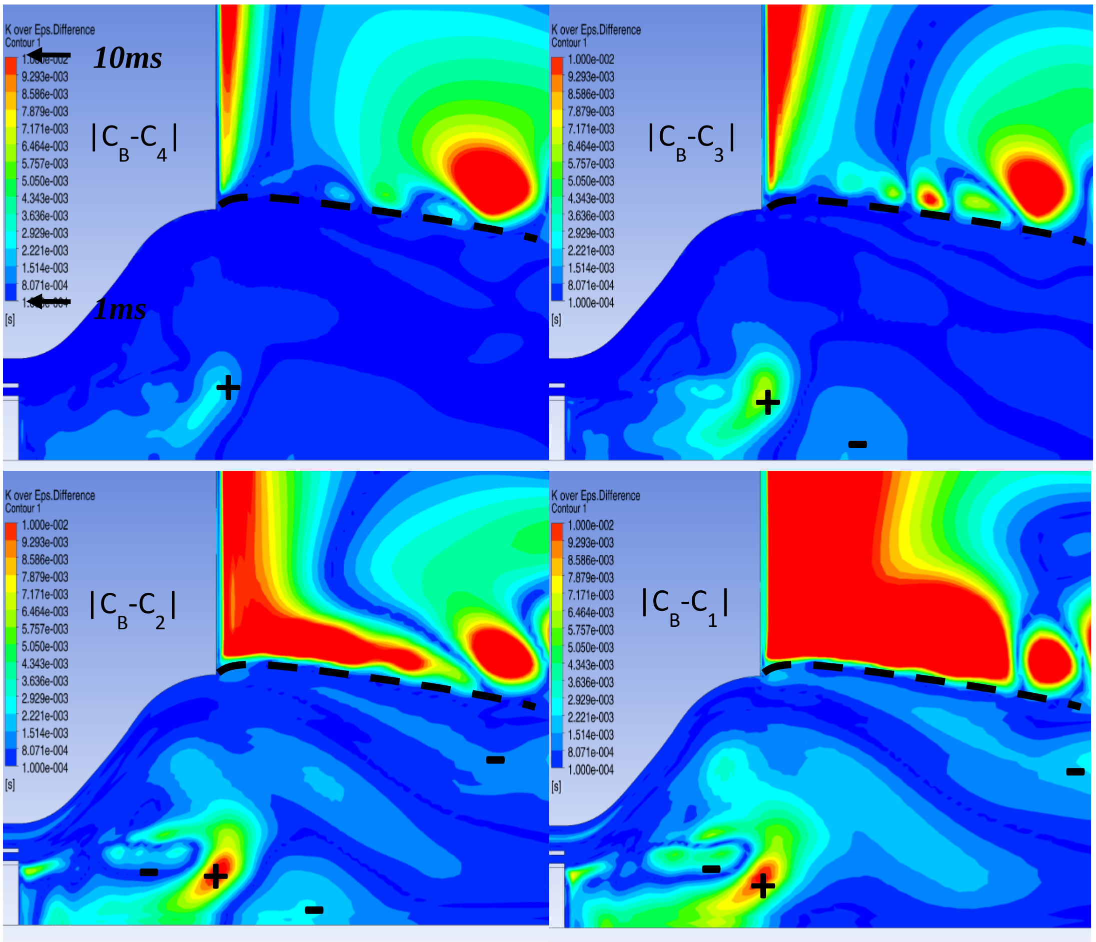

Figure 5.9. Absolute difference in the predicted large-eddy mixing time scale, *k/ε*, compared to the base case (C_B). The red zones corresponds to values ≥10 ms and the dark blue to values ≤1 ms (with the + signs indicate larger and the - signs smaller values than for the predicted for the base case).

It should be noted that the region above the dashed lines is not relevent to the homogeneous combustion rate, as the devolatilisation and volatile combustion takes place in the internal recirculation zone and in the mixing region between the primary and the secondary flows separating from the quarl. Above these lines, the external recirculation zone is situated, where there is no combustion, and thus even though large differences exist in the values of *k/ε*, these do not influence the temperatures in the region. This is confirmed by Figure 5.8.

Table 5.6 compares important heat transfer parameters between all the cases investigated (outlet temperature and heat transfer through the furnace walls), and it is observed that the maximum error is less than 2.5% for all the cases. This is well below the 5% limit considered acceptable for most engineering applications (the errors are relative to the base case, defined as Error = $|C_B - C_i| / C_B$ i=1, 2, 3 and 4).

Table 5.6. Comparison of the calculated outlet temperature, the maximum local wall temperature, and furnace wall heat transfer rate.

Case	Cell savings (% of C_B)	T_{Outlet} (°C)	Error	Furnace wall heat transfer (kW)	Error
C_1	76%	1247	1.39%	115.5	2.04%
C_2	62%	1249	1.25%	115.3	2.21%
C_3	43%	1266	0.15%	117.5	0.34%
C_4	32%	1267	0.05%	117.7	0.17%
C_B	---	1269	---	117.9	---

However, in a furnace, in addition to the magnitude of the overall heat flux, its distribution is also very important, influencing the heat duties to the radiative and the convective sections. Also the local wall temperatures, which are relevant to the longevity of the material through, for example, high temperature corrosion. Thus the radiation profiles near the flame are examined over a 1.5 m long section (Table 5.7). It is observed that the heat transfer is predicted with over 5% errors for cases C_1 and C_2. Thus the choice is reduced to cases C_3 and C_4 and in order to maintain the error to be below 1%, C_4 was adopted as the grid independent mesh, which still offered a 32% cell reduction over the base case and thus considerable savings in computational resources.

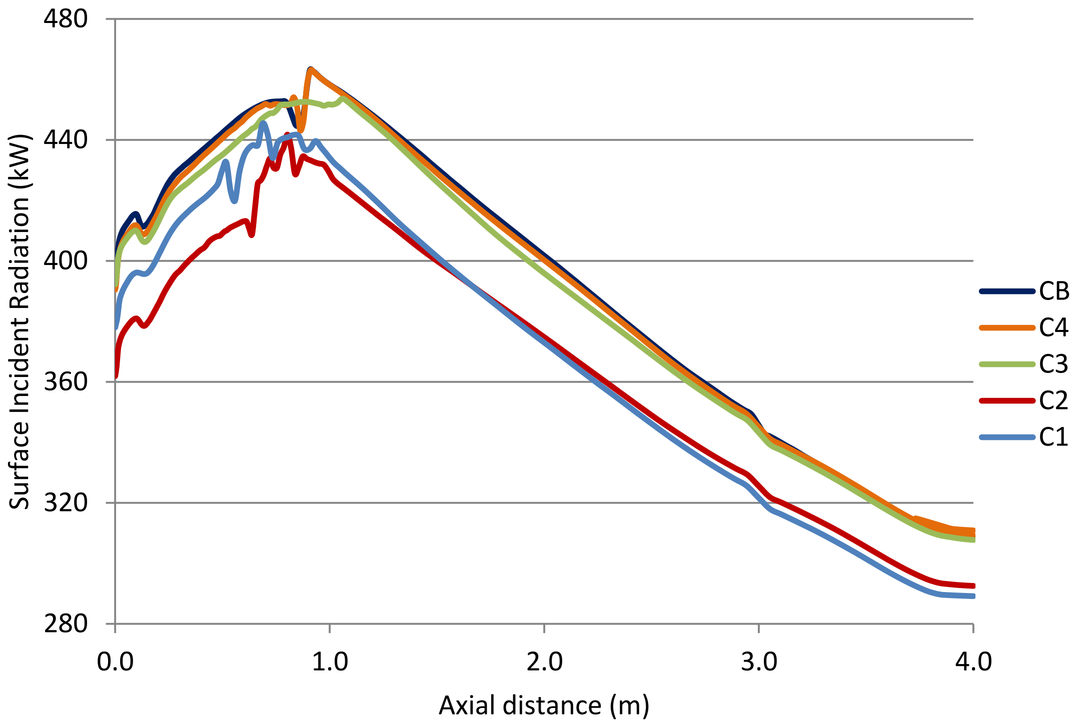

Figure 5.10. Surface incident radiation profiles along the cylindrical furnace wall for all the 5 cases investigated.

Table 5.7. Comparison of the total and surface incident radiation results over a 1.5 m long wall section next to the flame (between 0.5 and 2 m axial distance from the quarl exit).

Total incident radiation (MW)	Error	Surface incident radiation (kW)	Error	Wall T_{MAX} (°C)	Error
1.630	5.51%	413.7	5.44%	1389	0.83%
1.611	6.61%	409.0	6.51%	1382	1.23%
1.708	0.99%	433.3	0.96%	1392	0.60%
1.721	0.23%	436.6	0.21%	1401	0.08%
1.725	---	437.5	---	1403	---

5.2 Validation Case

Validation work was performed against the experimental results obtained by Weber *et al*. (1992), performed with an IFRF 2.4 MW burner fired in the horizontally fired IFRF Furnace No. 1.

5.2.1 Geometry and Simulation Conditions

This furnace is rectangular in shape (2 × 2 × 6.25 m), with a slightly arched top wall. No information could be found of the dimensions of this arch, but the influence of this arch on the fluid dynamics of the flame was assumed to be small, and it was not considered during the modelling. Also, the flame is assumed to be axi-symmetrical by Peters and Weber (1997) and therefore is appropriate for 2D modelling. The reasons behind this assumption are due to the cylindrical shape of the burner and quarl, the high inlet momentum (due to the constant velocity scaling of the burner used), and the expansion of the flame towards the walls is restricted by the curvature of the quarl and the strongly swirled secondary air.

The diameter of the 2D cylindrical furnace was determined as 2.26 m so that its cross sectional area equals the modelled rectangular furnace. The seven cooling loops were modelled as cylindrical bodies with 2.26 m outer diameter, length 0.16 m and thickness 0.04 m, so that the their surface area equals the area of the real cooling loops. The swirl was modelled by defining the tangential and axial velocity components, thus the computational domain was truncated upstream of the swirl vanes. The outlet of the domain was modelled as a pressure outlet, and only the first section of the exhaust duct was modelled (0.83 m) in order to conserve computational cells. Previously, in Section 5.1.9, it was highlighted that a grid independence study should always be performed for every case modelled, but due to the time constraints the mesh resolutions used was based on the findings of the gird independence study described in Section 5.1.9. The resulting grid is show in Figure 5.11 and is composed of ~68000 cells, with the highest grid resolution used in the flame zone.

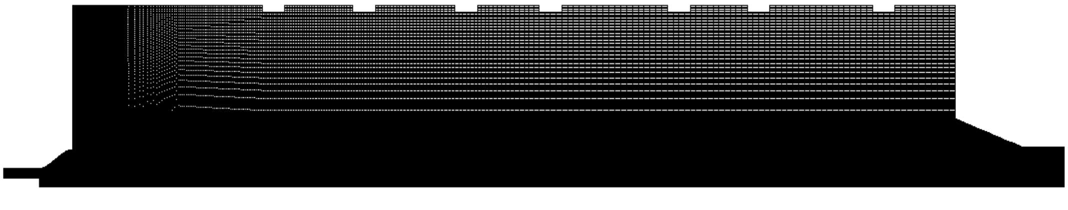

Figure 5.11. The 2D Grid for the IFRF case.

The wall boundary conditions were set according to estimates of Peters and Weber (1997) see Table 5.8, and the inlet conditions of the primary and secondary air streams, to the experimentally determined values, are shown in Table 5.9.

Table 5.8. Wall boundary conditions for the 2.4 MW IFRF case.

wall	temperature (°C)	emissivity
primary annulus	25	0.6
secondary annulus	300	0.6
burner core	527	0.6
quarl	1000	0.6
furnace front	1127	0.5
furnace cylinder	1127	0.5
furnace back	1027	0.5
exhaust duct	1027	0.5
cooling loops	727	0.4

Table 5.9. Inlet conditions for the 2.4 MW IFRF case.

	Primary	Secondary
coal mass flow (kg/s)	0.0731	---
air mass flow (kg/s)	0.1169	0.7456
temperature (°C)	25	300
axial velocity component	1	0.47
tangential velocity component	0	0.53
turbulent intensity (%)	10	20

The coal used was Göttelborn hvBb coal, and this was fed to the furnace dry. The ultimate and proximate analysis is shown in Table 5.10. The coal density was specified as 1000 kg/m^3, specific heat as 1100 J/kg K, and particle size distribution specified by the Rosin-Rammler distribution with 1 and 300 µm as the smallest and largest particle sizes, and the mean size was 45 µm.

Table 5.10. Ultimate and proximate analysis of the Göttelborn hvBb coal.

Ultimate	wt% (daf)
C	80.36
H	5.08
O	12.17
N	1.45
S	0.94

Proximate	wt% (dry)
Fixed Carbon	54.3
Volatile Matter	37.4
Ash	8.3

Particle devolatilisation was modelled with the Arrhenius type single rate model with pre-exponential factor of 4.2×10^{14} 1/s and activation energy of 230 kJ/mol, and the high temperature volatile yield set as 1.47. The devolatilising species were modelled as a single $C_xH_yO_z$ species with an average molecular weight of 50 g/mol. The char combustion model used was the Baum and Street (1971) kinetics/diffusion limited model with the rates defined by Peters and Weber (1997). Furthermore the volatile combustion was assumed to be governed according to the Eddy Dissipation Model of Magnussen and Hjertager (1977), and driven by the large eddy mixing time scale, k/ε.

The turbulence was modelled via the standard $k-\varepsilon$ model. Although the RNG version is found to be more appropriate for swirling flows, in this case a converged solution could not be obtained with the RNG or RSM models. This was thought to be due to the stiffness of these methods compared to the more numerically diffuse standard model, and that, according to ANSYS Inc. (2013). they are more sensitive to picking up transient behaviours, which may result in instabilities during steady state modelling.

The radiation was modelled via the Discrete Ordinates method with the theta and phi pixels of 2.

5.2.2 Results

Figure 5.12, Figure 5.13 and Figure 5.14 show a comparison of the axial velocity profiles measured at axial distances of 250, 500 and 850 mm away from the quarl exit. It is observed that the predicted trends are in good agreement with the experimental results. However, it should be noted that the peaks are in all cases are predicted to be significantly higher (approximately 50%) than the measured values. This may be a result of their location, as peaks situated between the measurement points simply are not be picked up. At the axial distance of 250 mm, the location of the peak is predicted to be approximately at the level of the burner quarl exit (which is 234 mm from the burner throat) and to gradually shift closer to the centreline at subsequent traverses. This is influenced by the exit curvature of the quarl, but primarily by the sufficiently high degree of swirl of the secondary air and the velocity difference between the primary and secondary streams. As a result, an adverse pressure gradient is set up which eventually results in a flow reversal and this is responsible for the formation of the internal recirculation zone (IRZ). The IRZ has a stabilising effect on the flame, as it convects heat back to the flame front. Also, it plays an important role in reducing the fuel NO_x emissions (which corresponds to ~80% of pulverised fuel NO_x emissions).

Figure 5.12 confirms the presence of the IRZ – corresponding to the negative values below the 100 mm radial distance from the centreline (although it is predicted with a somewhat higher intensity than the measured values). Figure 5.13 indicates that the tip of the IRZ is predicted to be located upstream of the 500 mm axial distance measurements and this corresponding well with the experimental results.

The presence of the external recirculation zone (ERZ) is also predicted by the model, and this is indicated by the negative axial velocities above the quarl exit line (234 mm). The ERZ is established by the swirling flow entering the chamber at the quarl exit, and this is due to the entrainment on the turbulent shear layer of the swirling jet boundary.

However, since the domain is bounded by the furnace walls, the fluid entrained into the jet is detrained from it further downstream. This recirculation pattern occurs up until the point where the stream of combustion products impinges on the furnace wall (indicated by Xp on Figure 4.14).

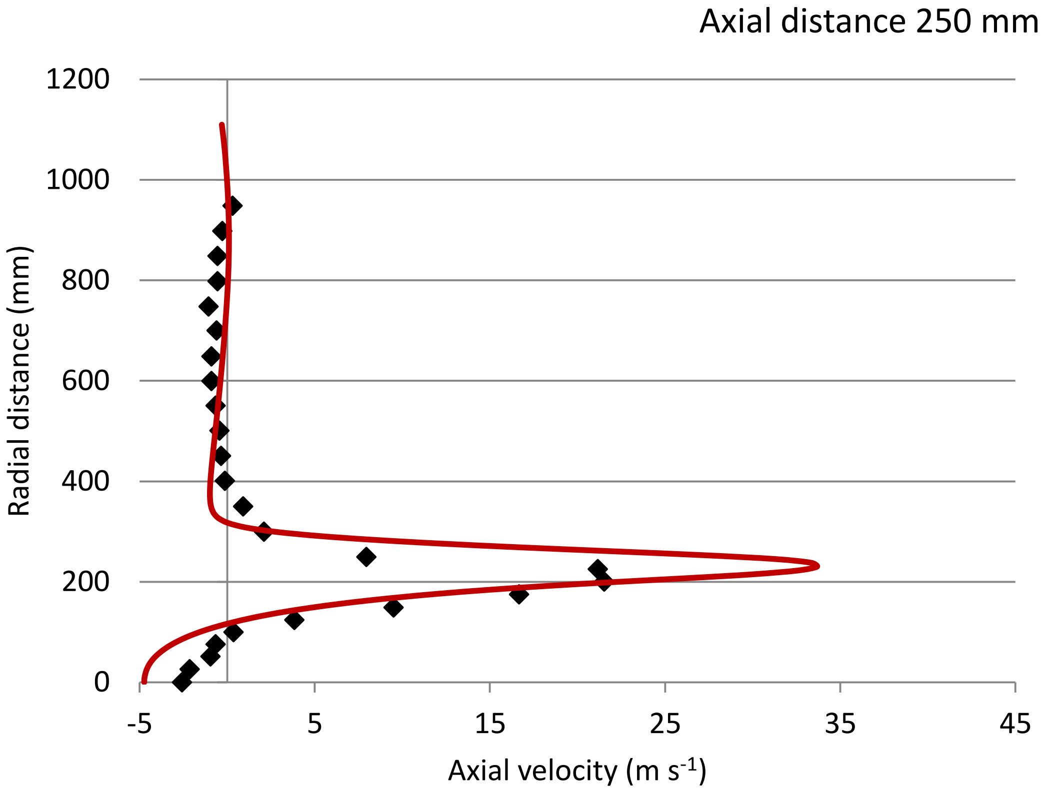

Figure 5.12. Axial velocities predicted (red line) and the experimental results (black dots) - at an axial distance of 250 mm.

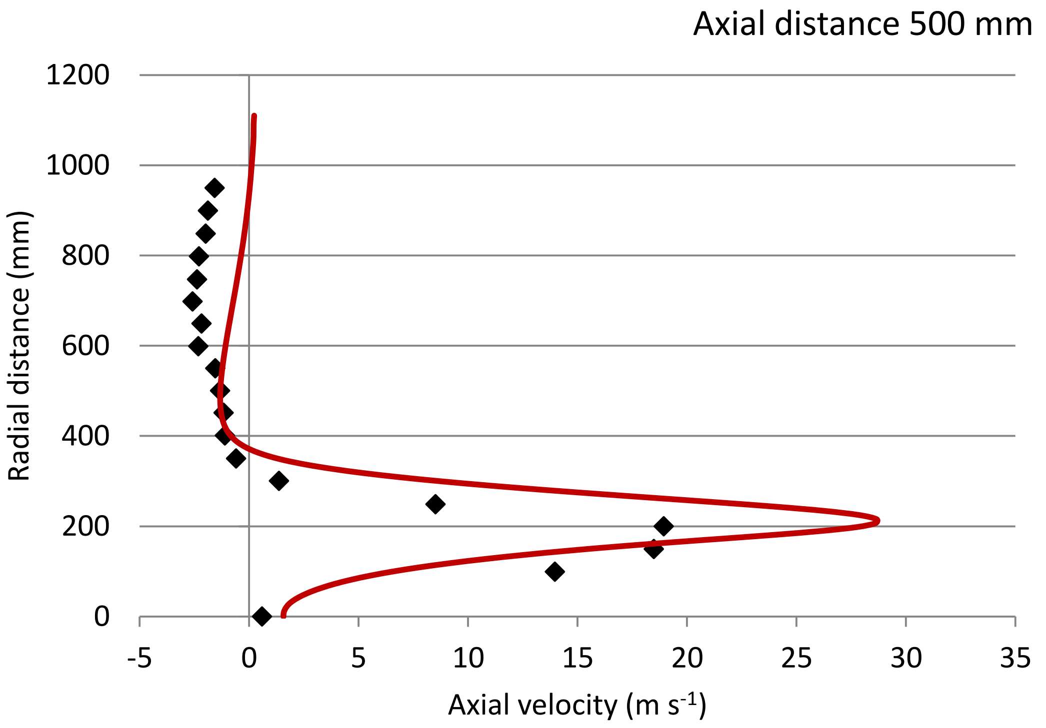

Figure 5.13. Axial velocities predicted (red line) and the experimental results (black dots) - at an axial distance of 500 mm.

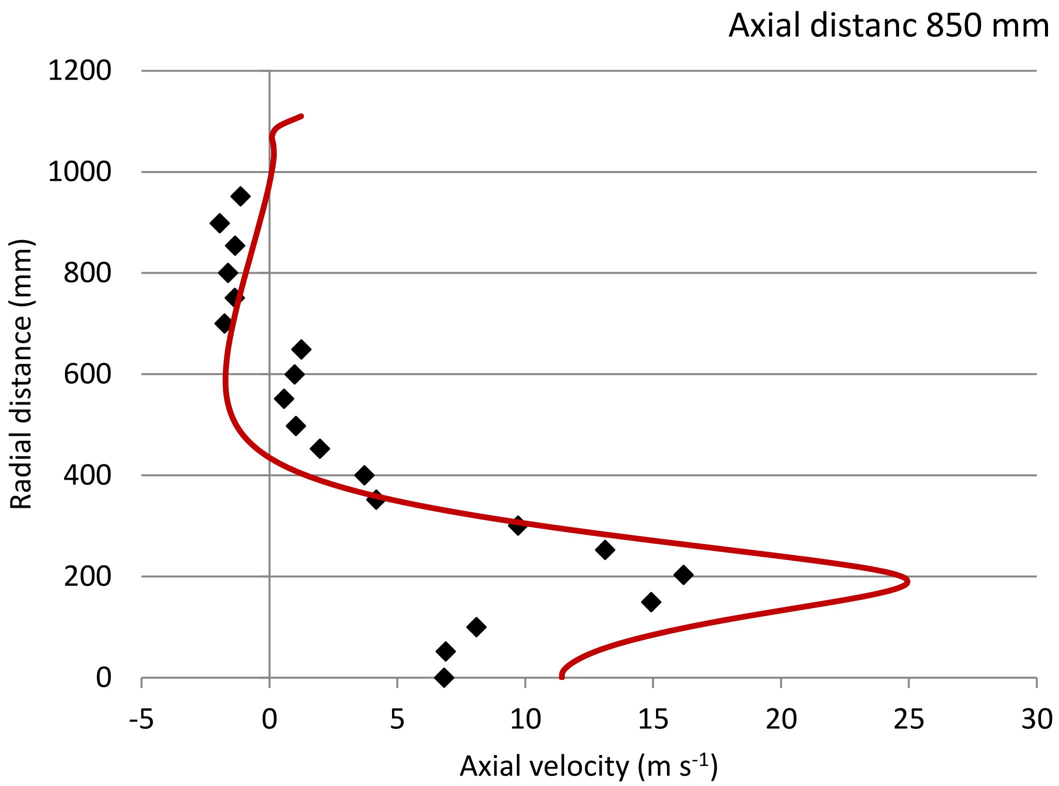

Figure 5.14. Axial velocities predicted (red line) and the experimental results (black dots) - at an axial distance of 850 mm.

The experimental results indicate that the eye of the recirculation zone is located close to the 850 mm traverse close to the radial distance of 700 mm, see Figure 5.14, corresponding to Xc on Figure 4.14), with a stronger recirculation closer to the walls. However it may be argued that the 2D results are not representative of the IRZ region due to the increased furnace diameter employed in order to maintain the cylindrical 2D cross sectional area to be the same as that of the rectangular 3D configuration. In contrast with the IRZ, which is influenced largely by the momentum of the incoming jet, and the dimensions of the burner and quarl, both of which were kept constant in the 2D case. Thus examination of the IRZ requires 3D modelling.

The effect of the particle trajectories greatly influences the overall NO_x emissions. When the particles devolatilise and burn in the shear mixing layer of the IRZ boundary (trajectories 1 and 2 in Figure 4.15), where O_2 is readily available, conversion pathways to NO_x are favoured. However, when particles follow the trajectories of paths 3 and 4, with an increased residence time inside the rich IRZ, the conversion of the evolved nitrogen containing species to molecular nitrogen is favoured (Smart *et al*., 1992).

A range of particle trajectories for particles of diameter 1, 70, 135 and 230 μm, are examined in Figure 5.15, where the devolatilisation process is indicated by the orange sections.

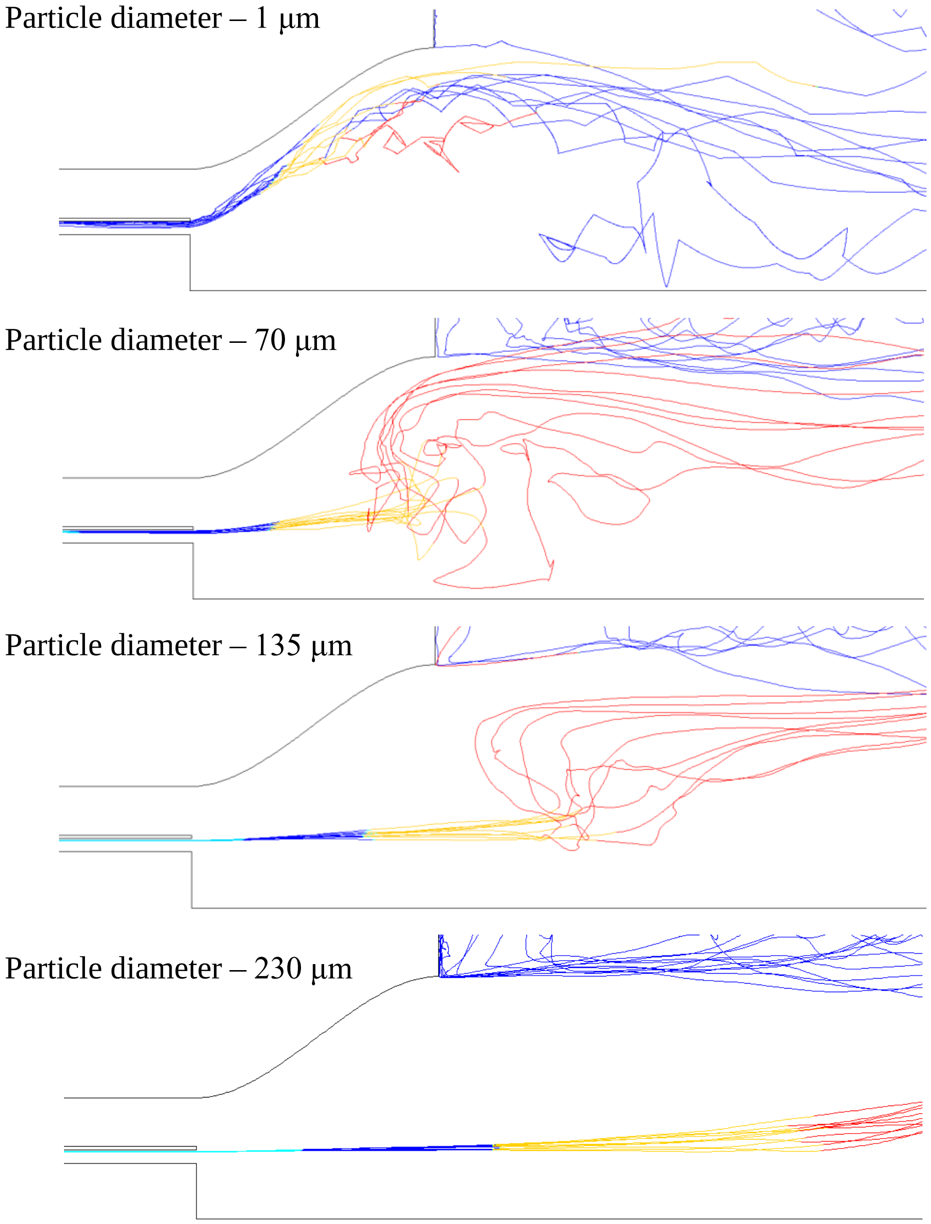

Figure 5.15. Trajectories of coal particles (single particle injections with 10 tries), coloured by steps of the combustion process (light blue – water evaporation, dark blue – inert heating, orange – devolatilisation, red – char combustion).

It is apparent that the smallest, 1μm, particles follow the flow closely and the devolatilisation indeed takes place in the turbulent mixing layer, favouring the conversion of volatile-N to NO. Weber *et al.* (1992) suggest that particles, up to 10 μm in diameter, follow the gas phase closely, whereas bigger particles, having larger inertia, retain their original momentum over longer distances and they are less effected by the turbulent fluctuations of the gas. Therefore they penetrate the IRZ and follow pathways 3 and 4 (as a function of their diameter), thus promoting the conversion of volatile-N to molecular N_2. Smart *et al*. (1992) concluded that particle trajectories can be shifted towards pathways 3 and 4 by pushing the coal gun inside the IRZ by up until 0.4 burner diameters. In this way, they achieved NO_x emission reductions by more than ~60% for a hvBb coal, and by ~25% for a less reactive lvBb coal.

O_2 outlet composition is predicted as 4.13% (dry), which is significantly different to the value of 3% given by Weber *et al*. (1992). However, later Peters and Weber (1997) argue that this 3% outlet O_2 measurement would be a result of the 16.4% excess air, and would result in close to 150 kg/h less air flow than at 22% excess air level maintained during the experiment. Thus they conclude that the O_2 concentration was measured erroneously, but do not list the possible reasons. Air ingress cannot be responsible for this as it would result in a higher exit O_2 concentration measured experimentally than the CFD result (not considering ingress). It is not a result of poor burnout either since both the experimental and CFD result predict similar char burnout. A possible contribution might be due to momentary variations in the firing rate and coal composition during the experiment, which can fluctuate by approximately 5% (as suggested by Williams *et al*. (2007) for another experimental test furnace, the RWA Combustion Test Facility. Though, due to the scientific nature of the facility, it is expected that these fluctuations are considered and their influence is minimised by reporting time averaged exit compositions. Therefore human error during the reading, or a fault in the measuring device are the most likely reasons.

In order to verify the exit O_2 concentration, a MS Excel mass balance table was used, assuming complete combustion of the fuel carbon, hydrogen and sulphur to CO_2, H_2O and SO_2, respectively (assuming that fuel N converted to N_2). Based on these assumptions, the stoichiometric O_2 requirement was determined. This was divided by 0.2315 to calculate the amount of stoichiometric air (on a mass basis), and then multiplied by the 1.22 to account for the excess air used. This resulted in 4.15% dry O_2, which compares well with the CFD predictions of 4.13%. The assumptions used in the MS Excel table have been previously verified by comparison with the results of an equilibrium combustion software, namely FLAME.

The 99.95% char burnout predicted by the model compares well with the 99.4% measured. Also the outlet temperatures are well matched with 807 °C measured, and 814°C predicted by the CFD model.

5.3 CFD modelling on a Commercial Scale Boiler

5.3.1 Introduction

Given the limited experience of firing 100% biomass in air, as well as firing coal and biomass under oxy-fuel conditions, in a full sized-utility boiler, CFD can play a valuable role in understanding some of the technical challenges involved in applying a CO_2 reduction technology to a utility boiler. CFD was used as a predictive tool to assess the oxy-fuel retrofit potential of a 500 MW_e coal-fired utility boiler, based at Didcot Power Station in the UK (see Section 0 for a detailed description). Furthermore, biomass co-firing cases were added. The CFD results were first validated against data available for the air-fired coal combustion case. These included empirical data, together with predictions from RWE npower's in-house model, were used for validating the CFD simulation of coal combustion in air. The empirical in-house model (based on Mobsby, 1984) has been optimized and validated by the power station operators to match the performance of the utility boiler. Then, for the same thermal input, the performance of the utility boiler was evaluated when coal, a 20% biomass blend, and 100% biomass is fired under air- and oxy-firing conditions.

5.3.2 Cases Investigated

The operating conditions for the validation case (coal combustion with air), are shown in Table 3.9. Also air in-leakage was considered. To allow for a comparable study of the results to the oxy-fuel conditions, where it is believed that efforts would be made to reduce leakage in a retro-fitted oxy-fuel plant, the value of 3% of the total air input was chosen, with leakage assumed to come through the hopper region. The ultimate and proximate analysis, CV and particle size and shape of the coal, Pittsburgh 8, and the modelled biomass are summarised in Table 3.5, Table 3.6 and Table 3.7.

Eight retrofit cases were investigated numerically for the combustion of coal, biomass, and a 20% biomass blend under both air- and oxy-firing conditions at 25 and

30% O_2 volumetric concentration (oxy25 and oxy30, respectively). The oxy-fired simulations discussed here were set-up, and run by Sandy Black.

The investigated conditions are summarized in Table 3.14. The thermal input, exit O_2 concentration, the number of firing burners, and air leakage were kept constant for all the cases. Pittsburgh 8 and pelletised wood were used for all the relevant cases involving coal and biomass. For the oxy-fuel cases, a wet-recycle was chosen and a 5% dry exit O_2 concentration was maintained. Furthermore the recycle ratios are shown in Table 3.14. The O_2 is assumed to be supplied by an Air Separation Unit (ASU) with a purity of 95%, containing 5% inert gases. The O_2 concentration in the primary register was fixed at 21% by volume, since further enrichment would increase the risk of fire and dust explosions (Toftegaard, 2010). Secondary and tertiary registers were enriched to achieve the desired overall O_2 concentration. The composition of the recycled flue gas for each case was calculated iteratively from the overall mass balance assuming complete combustion. See Section 3.7 for more details on the techniques used.

5.3.3 Computational Modelling

5.3.3.1 Computational Domain

The CFD calculations were performed using the commercial package ANSYS FLUENT 14.0 (ANSYS, 2013) with its user-defined functionality. The symmetry of the boiler allowed for only half of the furnace to be modelled. The modelled furnace geometry is shown in Figure 5.16, together with the location of the heat exchangers (platens 1 and 2, secondary superheater (SSH), and final reheater (FRH)). The outlet of the domain was located at the exit of the final reheater. Only 36 of the 48 burners were firing when the validation data was collected, and their location is clearly visible on the mesh. In order to conserve computational resources, the burner geometry was simplified, and the swirl vanes were modelled based on the relevant swirl angle (Table 3.10 and Table 3.11). The heat exchangers after the last part of the radiative section, the final reheater (FRH), were excluded from this investigation. This was because the convective heat exchangers were considered not to influence the combustion process and in-furnace heat transfer. However, in reality the flue gas flows past the convective reheaters, economisers, the air pre-heater, and gas cleaning units before being released through the stack.

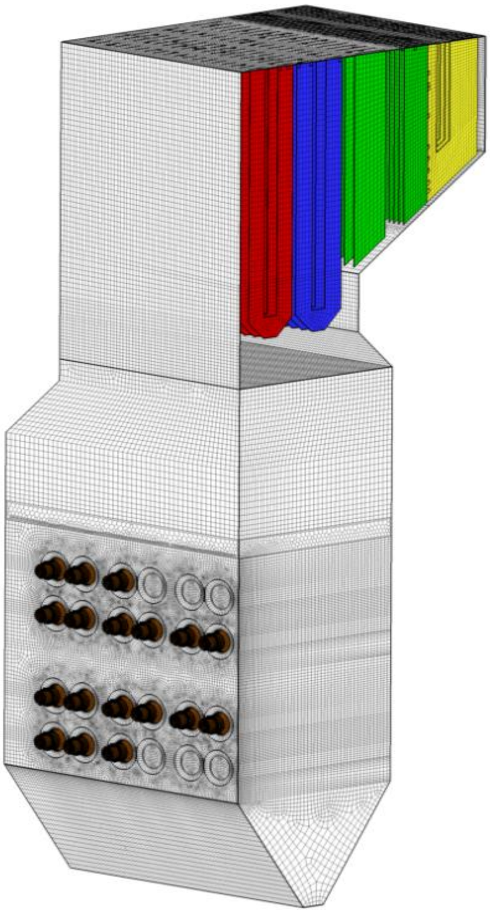

Figure 5.16. Modelled furnace geometry and mesh used, showing the location of the firing burners. The geometry is opened up to show the modelled heat exchangers (Platen 1 – red, Platen 2 – blue, Secondary Superheater – green, and the Final Reheater – yellow).

5.3.3.2 Grid Improvements

The original mesh was developed by RWE npower's CFD modelling team. This was improved by Edge (2011), who performed a grid independence study and identified the optimal mesh, which was adopted for this study. Further refinements targeting specific regions were made. These were done in two steps. Firstly, Dr. Alessandro Pranzitelli refined the mesh in the flame region, and improved the cell quality of the zone connecting the burner region with the top section of the boiler. This was done in order to assure the connectivity of the cells without recurring to non conformal interfaces, and instead a transition region of polyhedral cells was introduced. This produced a mesh of 3.2 million cells. Subsequently, I performed a grid refinement study focusing on the burner region. The mesh was refined near the burners walls in order to improve the wall treatment, where high gradients are expected. For this 2 other meshes were generated, consisting of 4.1 million cells (medium), and 4.8 million cells (fine). Predictions of heat transfer and furnace exit temperature were used as assessment criteria. While both offering improvements in the exit predictions, the medium and fine meshes performed similarly, and therefore the former was chosen for the study. The unstructured multiblock mesh consists mostly of swept hexahedral cells, with a small region of polyhedral cells present at the exit of the furnace section. An outline of the mesh employed can be seen in Figure 5.16.

5.3.3.3 Overall Modelling Approach

As previously justified in Sections 0 and 5.2, the continuous phase was modelled with the Eulerian treatment using a steady state Reynolds-Averaged Navier-Stokes (RANS) approach, where a Lagrangian frame of reference was used to track the motion of the fuel particles. The exchange of momentum, heat, and mass between the phases was accounted for using the source/sink terms in the governing equations for the two phases.

Turbulence was modelled by the realisable k-ε model, which has been used successfully in other oxy-fuel work modelling turbulent coal combustion with a swirl stabilised burner (Hjärtstam, 2012).

5.3.3.4 Heat Transfer

Since radiation is the dominant form of heat transfer in the furnace, and it is therefore important to model it correctly. As in the previous Sections 0 and 5.2, the radiative transfer equation (RTE) was solved using the Discrete Ordinates (DO) model (Murthy *et al.*, 1998) and the radiative properties of the gases were calculated using the Weighted Sum of Gray Gases (WSGG) approach (Hottel *et al.*, 1967; Smith *et al.*, 1982). The correlation proposed by Smith *et al.* (1982) has been successfully applied in numerous CFD studies involving the combustion of coal and biomass in air (see Ma *et al.*, 2007; Ma *et al.*, 2009).

However, in oxy-fuel conditions, high concentrations of strongly absorbing CO_2 and H_2O exist and this correlation is no longer applicable. The full spectrum correlated k-distributions (FSCK) model, developed by Porter *et al.* (2010) who have shown it to provide more accurate results for a typical oxy-fuel FGR environment compared to the WSGG model (Smith, 1982). However, a major limitation in implementing the FSCK model is the level of computational resources required (Porter *et al.*, 2010), and several authors have instead proposed new correlations for the WSGG model under oxy-fuel conditions (Johansson *et al*., 2010; Johansson *et al*., 2011; Kangwanpongpan *et al*., 2012; Krishnamoorthy *et al*., 2010). Based on the recommendation of Becher *et al*. (2012), who evaluated the available correlations in the literature, the values of Johansson (2011) were chosen for the oxy-fuel cases, implemented via a user defined function (UDF). This is in contrast with the earlier work of Black *et al*. (2012), who used the original WSGG model. The WSGG UDF was configured and implemented in the oxy-fuel simulations by Black. The original WSGG values suggested by Smith *et al*. (1982) were used for the air-fired cases. The effect of soot on radiation was considered (Sazhin, 1994) and the soot formation was modelled with the coal-derived Moss-Brookes model (Brookes *et al*., 1999; Brown *et al*., 1997).

Similar to the approach taken in Sections 5.1.3.3, in order to model the heat transfer through the walls, a partial overall admittance factor and temperature, based on the water/steam temperatures within the respective tube banks (Table 3.8), were used, Edge (2011).

5.3.3.5 Combustion Modelling

The combustion of volatile species from the devolatilisation of the particles was modelled using the Eddy Dissipation Model (EDM) (Magnussen *et al*., 1976) using a two-step global reaction mechanism as used previously in Sections 0 and 5.2, and in Gharebaghi *et al*. (2011), Ma *et al*. (2007) and Ma *et al*. (2009). The devolatilisation and burnout of the particles were modelled with the single kinetic rate (Badzioch *et al*., 1970) and intrinsic models (Smith, *et al*., 1982), respectively, with the model constants used, as before, for coal (Ma *et al*., 2009). The rate constants for the devolatilisation of wood and the intrinsic properties of the wood char were obtained from Ma *et al*. (2009) and Lu *et al*. (2008), respectively. The pulverised coal particles were assumed to be spherical in shape, and the Rosin-Rammler size distribution was calculated as 1 μm to 350 μm, with a mean diameter of 75 μm. The wood particles were assumed to be cylindrical, with lengths ranging from 90 μm to 3 mm. The cylindrical particles were modelled as equivalent volume spheres. This, however, yields a lower surface area than the surface area of the original cylindrical particle, which may lead to the under prediction of both the convective and radiative heat transfer to the particles, resulting in incorrect predictions of particle heat up times and location of the volatile release. In order to account for the differences in surface areas, a shape factor, *SF*, was used, defined as the ratio of surface area of an equivalent volume sphere to the surface area of a cylindrical particle. When calculating the heat transfer to and from the wood particles, the surface area of the equivalent spheres were modified according to the particle shape factor, where A_p and r_p are the area and spherical radius of the equivalent volume particle, respectively. It was assumed that the internal temperature gradients could be neglected, since the mean equivalent diameter of the wood particles was approximately 330 μm and over 75% were under 400 μm with an aspect ratio of 2 or more (Ma *et al.*, 2009). When assessing the temperature history of the particles, an accurate estimation of the particle trajectories is required in order to determine the time that the particle spends travelling through different gas temperature zones. The drag force, which affects the particle trajectory, is influenced by the particle shape. The method of Haider and Levenspiel (Haider *et al.*, 1989) was used to calculate the drag coefficient, C_D, of the wood particles using the particle shape factor (Ma *et al.*, 2009).

5.3.4 Validation Case

Temperature predictions taken at cross section along the third column of burners are shown in Figure 5.17. Heat transfer results, given by the summation of the heat transfer to the water walls and the radiative heat exchanger section (platens 1 and 2, SSH and FRH), are shown in Figure 5.18.

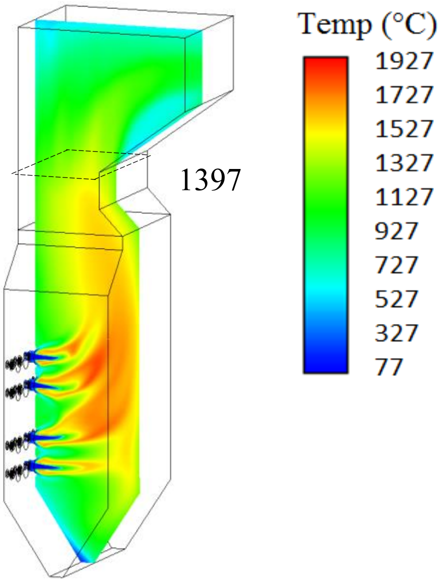

Figure 5.17. Temperature predictions taken at cross section along the third column of burners for the air-fired validation case.

The high temperature regions are produced by the combustion of the volatiles released from the coal followed by the combustion of char, where burnout is completed before the exit of the furnace. Within the furnace section, radiation to the surrounding water walls is the dominant form of heat transfer (Chedaille and Braud, 1972). Since there is a direct line of sight to the flames, radiation is a key part of the heat transfer to the superheaters, platen 1 and 2, see Figure 3.22. Downstream of these, where the direct line of sight to the flames is restricted by the boiler nose, convective heat transfer becomes increasingly important.

The cold region at the hopper shows the air in-leakage, which is entrained by the recirculation zone created by the bottom row of burners. This phenomenon has also been observed by a CFD study on a multi burner furnace by Lockwood and Parodi (1998). The CFD prediction and power station data of the furnace and heat exchanger exit temperatures are compared in Table 5.11. The exit temperature of 1397°C was within 5% of the experimental measurement of 1316°C, and in close agreement with the in-house model used by the power station (1393 °C).

Table 5.11. Exit plane temperatures for the air-fired validation case.

Section	Exp	In-house	CFD
Furnace	1316	1383	1397
Platen 1	-	862	935
Platen 2	-	1009	1026
SSH	-	900	867
FRH	-	781	821

Figure 5.18 and Table 5.12 show the predicted heat transfer results for the air-coal simulation. Compared to the total heat transfer of 861 MW given by the in-house code, the predictions differ by less than 2%. As the CFD results of the air-coal validation case correspond closely to the predictions of the in-house model used by the power station, the air-coal CFD case is used as a reference when evaluating the boiler performance for the investigated retrofit cases.

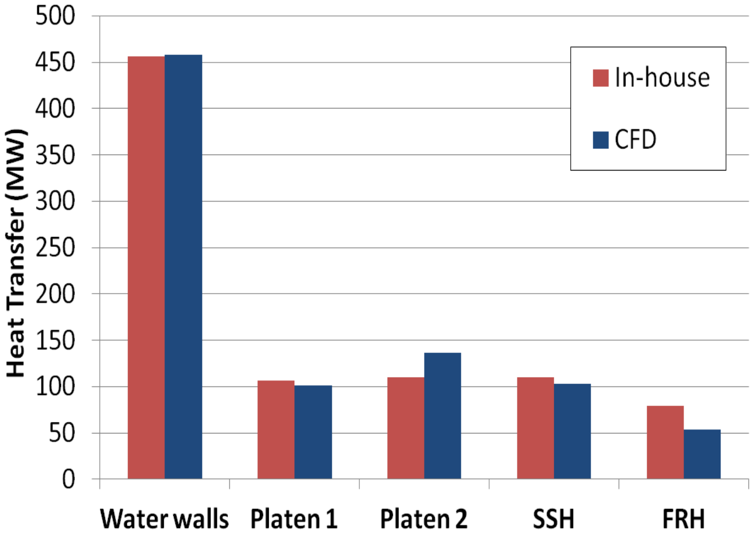

Figure 5.18 Heat transfer to the water walls and the radiative heat exchanger section for the air-fired validation case.

Table 5.12. Comparison of the heat transfer results of the RWE in-house and CFD codes for the air-coal validation case.

Section	In-house	CFD	Difference
Water walls	456	457	0 %
Platen 1	106	99	-7 %
Platen 2	110	136	24 %
SSH	110	101	-8 %
FRH	79	52	-34 %
Total	861	845	-2 %

5.3.5 Oxy-coal Modelling Study

Figure 5.19 shows the gas temperature contours under oxy-fuel conditions when firing coal. An increase in the inlet O_2 concentration is shown to increase the flame and furnace exit temperatures.

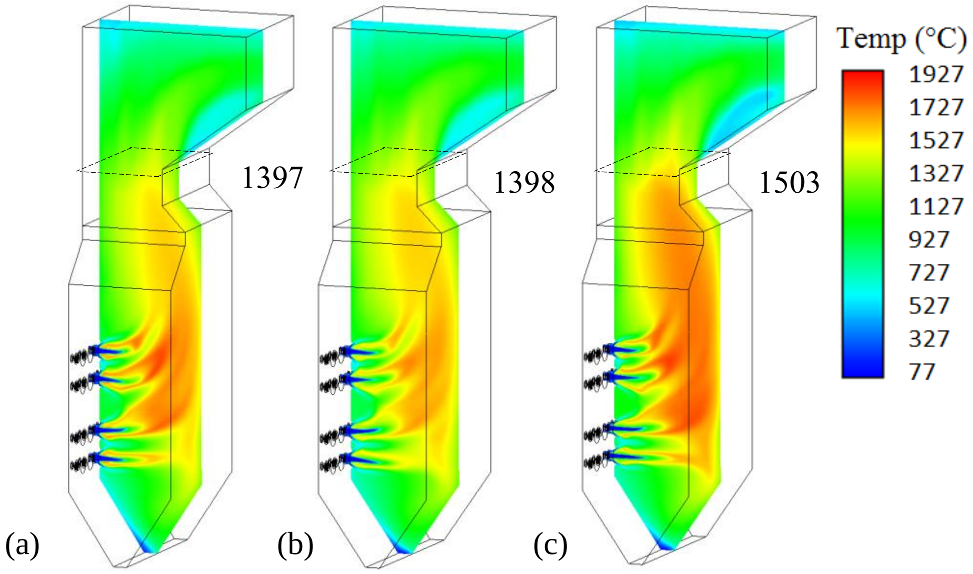

Figure 5.19. Temperature predictions taken at cross section along the third column of burners for the air-fired validation case and the oxy-coal cases – (a) air-coal, (b) oxy25-coal and (c) oxy30-coal.

To achieve a higher O_2 concentration, the flue gas recycle, and hence the dilution, is reduced and the adiabatic flame temperature is therefore increased (Smart *et al.*, 2009). The higher gas temperatures result in an increase in thermal radiation to both the water walls and the radiative heat exchangers, and as a result the total heat transfer increases in both of these sections (Figure 5.20 and Table 5.13).

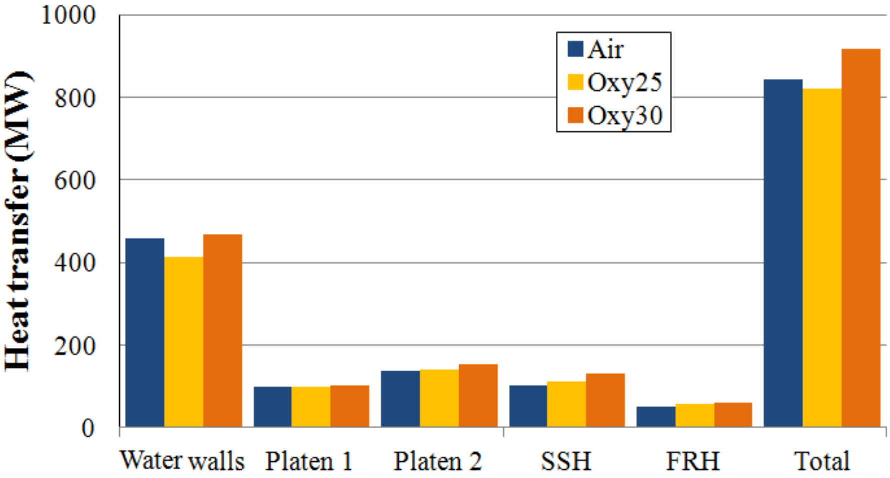

Figure 5.20. Heat transfer to the water walls and the radiative heat exchanger section for the air-fired validation case and the oxy-coal cases (air-coal, oxy25-coal and oxy30-coal).

Table 5.13. Comparison of the heat transfer results of the RWE in-house and CFD codes between the air and oxy fired coal cases.

Section	Air-Coal (MW)	Oxy25 diff.	Oxy30 diff.
Water walls	457	-10 %	2 %
Platen1	99	1 %	5 %
Platen2	136	3 %	13 %
SSH	101	9 %	28 %
FRH	52	10 %	19 %
Total	**845**	**-3 %**	**8 %**

The same trend was observed experimentally by Smart *et al.* (2010b) for a 0.5 MW experimental facility designed to replicate the flue gas path of a utility scale boiler. Their results found that a reduction in the level of the flue gas recycle led to an increase in radiative heat transfer, but the opposite effect was recorded in the convective section, which was attributed to the reduction in the flue gas mass flow. This suggests that heat transfer to the convective heat exchangers, outside the modelled domain, would be reduced as well.

When retrofit of oxy-fuel technology to an existing boiler, heat transfer characteristics and temperature profiles of the air firing design will have to closely match. The results suggest that, in order to achieve this, the optimum O_2 concentration lies between 25 and 30%. This value is in agreement with those summarised in Toftegaard *et al.* (2010).

5.3.6 Air and Oxy-fired Biomass Combustion

Predictions of biomass-firing behaviour under air- and oxy-fuel conditions for the coal-biomass blend cases and for the 100% biomass firing cases are presented in Figure 5.21 (b-d) and (e-g), respectively. For the air and oxy-fuel cases, the results show a reduction in furnace temperatures when compared with firing coal in the respective environments, see Figure 5.19. Moisture content and calorific value have been shown by Smart *et al.* (2010b) to affect flame temperatures. Although dried pelletised wood has a lower moisture content than coal (Table 3.5), the higher biomass

mass flow required to maintain the thermal input means that the total moisture introduced with both fuels is approximately the same. Therefore moisture content can, in this case, be discounted as the reason behind the lower temperatures observed in Figure 5.21.

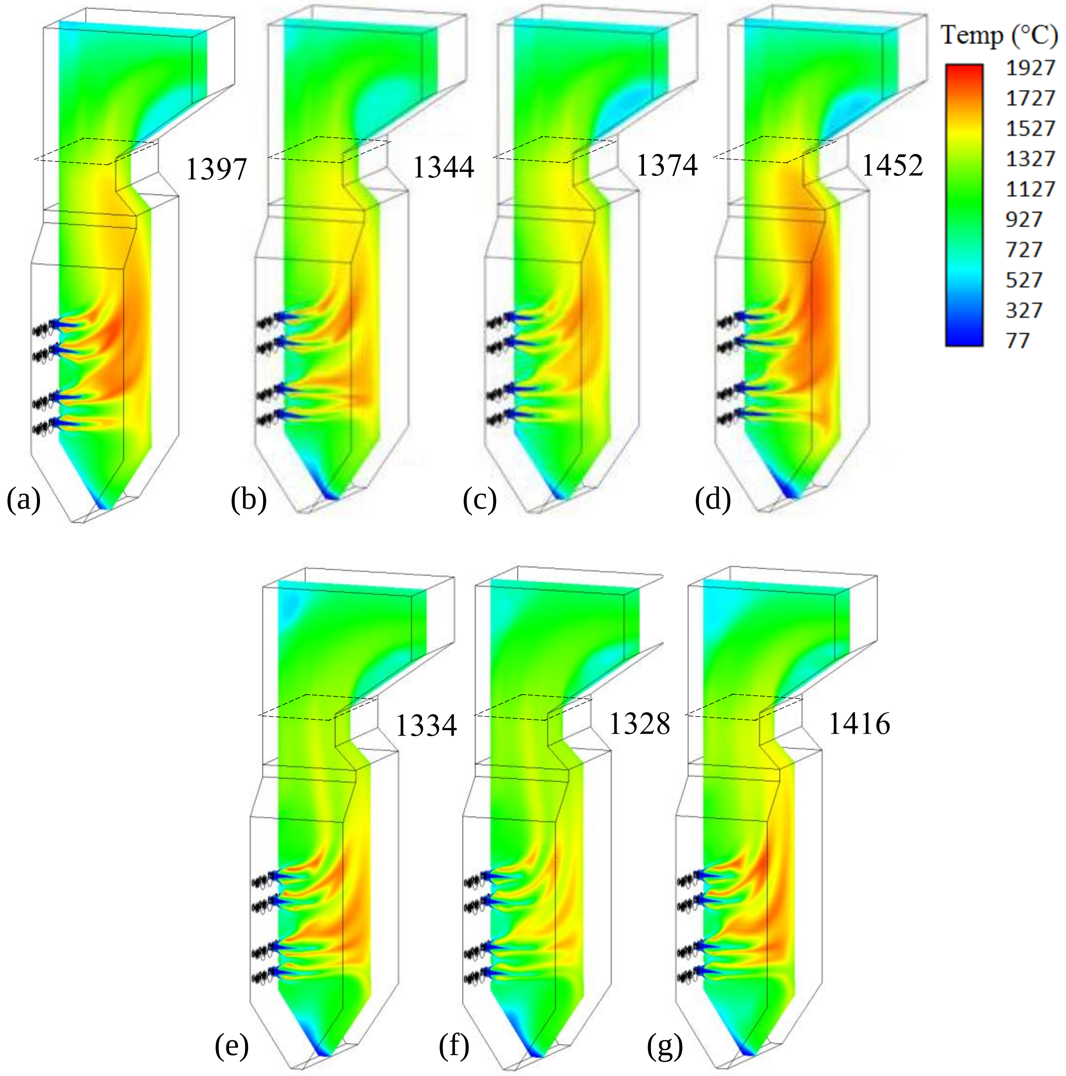

Figure 5.21. Temperature predictions taken at cross section along the third column of burners for the air-fired validation case and the oxy-biomass cases – (a) air-coal, (b) air-blend, (c) oxy25-blend, (d) oxy30-blend, (e) air-biomass, (f) oxy25-biomass and (g) oxy30-biomass.

Predictions of the carbon in ash (CIA) evaluated after the FRH section showed higher values for biomass than for coal, with values of 11% and 0.64% in air-biomass and air-coal cases, respectively. This means that some of the chemical energy remained within the fly ash particles. An increase in carbon in ash is expected when firing 100% biomass, due to the presence of larger particles, which heat up and burn out more slowly. However, it should be noted that, as the ash content is generally much lower for biomass, the remaining carbon would constitute a larger percentage of the fly ash when compared to coal ash. Although the gasification reactions for the coal and biomass chars were not included here, it is important to note that recent work by Edge *et al*. (2011) has shown that it has an effect on the overall char reactivity when moving to a oxy-fuel RFG environment. Reaction rates used for the biomass char include the possible catalytic effects on char burnout, but a much more detailed theoretical approach would be needed in order to assess its impact.

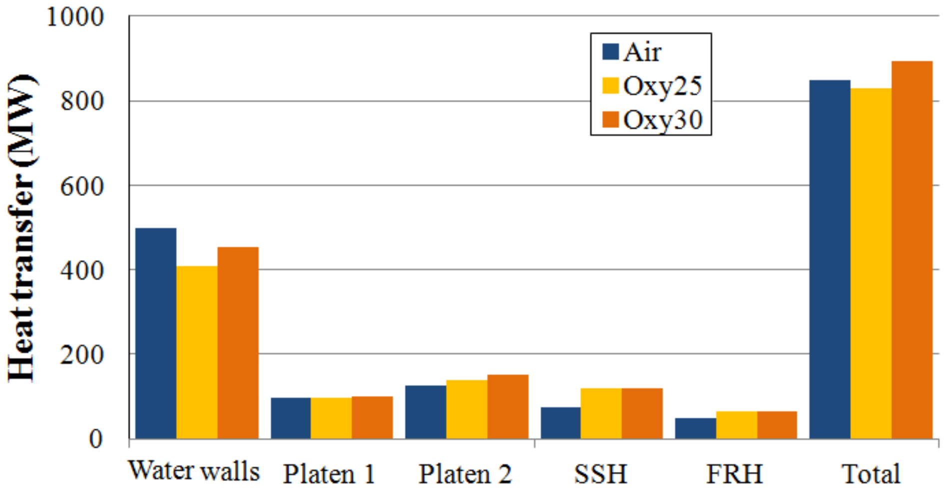

Figure 5.22. Heat transfer to the water walls and the radiative heat exchanger section for the air-fired blend case and the oxy-blend cases (air-blend, oxy25-blend and oxy30-blend).

Table 5.14. Comparison of the heat transfer results of the RWE in-house and CFD codes between the air and oxy fired coal and biomass cases.

Section	Air coal / blend	Oxy25 diff. coal / blend	Oxy30 diff. coal / blend
Water walls	457 / 499	-11 % / -18%	0 % / -9%
Platen1	99 / 97	-2 % / 1%	2 % / 5%
Platen2	136 / 127	2 % / 9%	11 % / 19%
SSH	101 / 76	19 % / 58%	20 % / 59%
FRH	52 / 50	23 % / 28%	24 % / 29%
Total	**846 / 849**	**-2 % / -2%**	**6 % / 5%**

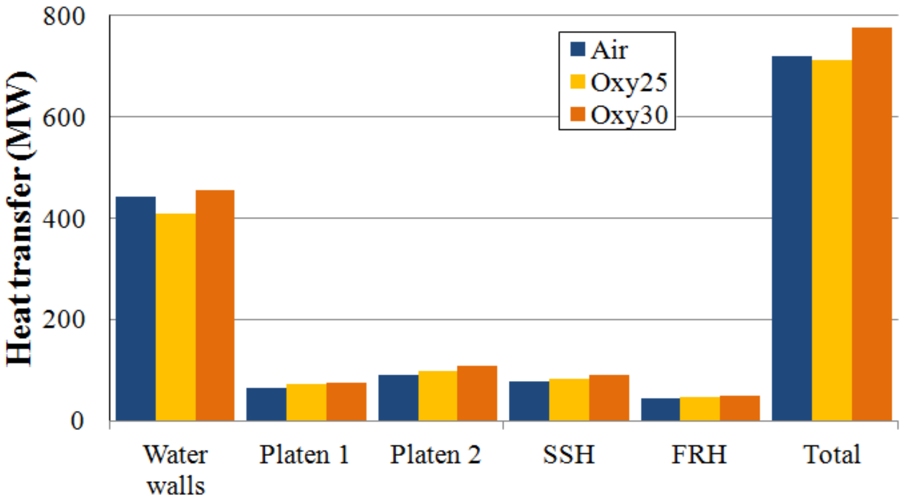

Figure 5.23. Heat transfer to the water walls and the radiative heat exchanger section for the air-fired biomass case and the oxy-biomass cases (air-biomass, oxy25-biomass and oxy30-biomass).

Table 5.15. Comparison of the heat transfer results of the RWE in-house and CFD codes between the air and oxy fired coal and biomass blend cases.

Section	Air		Oxy25 diff.		Oxy30 diff.	
	coal /	biomass	coal /	biomass	coal /	biomass
Water walls	457 /	441	-10 % /	-7%	-1 % /	3%
Platen1	99 /	65	-27 % /	12%	-23 % /	17%
Platen2	136 /	90	-28 % /	9%	-21 % /	19%
SSH	101 /	78	-17 % /	7%	-11 % /	15%
FRH	52 /	45	-9 % /	5%	-7 % /	7%
Total	**846 /**	**719**	**-16 % /**	**-1%**	**-8 % /**	**8%**

The biomass particles have an overall lower total surface area when compared to finely ground coal, and therefore radiative emissions due to the particles within the furnace are reduced. This was observed in the CFD simulations, Figure 5.24. Furthermore, as the amount of ash is significantly lower in the biomass, the radiative emissions from the fly ash particles passing through the superheater sections are also reduced.

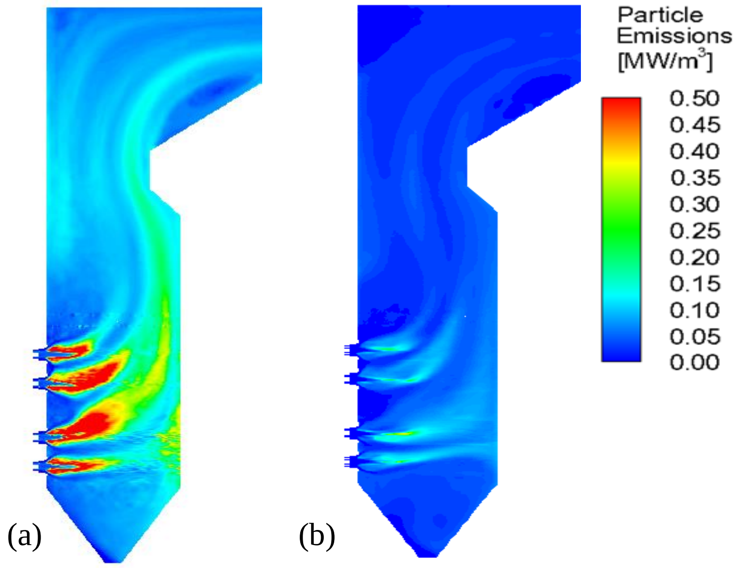

Figure 5.24. Radiative emissions from particles in the coal and biomass fired cases – (a) air-coal and (b) air-biomass results.

On the basis that particle emissions play a significant role in radiative heat transfer (Marakis *et al*., 2000), it can be argued that the reduction in particle emissions is another cause of the lower heat transfer observed in Figure 5.22 and Figure 5.23, when a biomass blend and 100% biomass is fired.

Retrofitting an existing boiler for biomass firing may require several modifications to improve burnout, and if oxy-biomass technology was considered, radiative heat transfer may be improved at O_2 concentration greater than 30%, although this may impact on the materials inside the boiler. To a lesser extent, the larger particles also affect the biomass-blend cases. However, coal dominates the overall combustion process and maintains temperatures required to sustain the combustion of biomass. As a result, the total heat transfer can be expected to be similar to that of coal firing. For retrofitting purposes, a blend may also be used as fuel for oxy-fuel combustion when an O_2 concentration between 25 and 30% is used. Another important consideration in retrofitting oxy-fuel technology is the impact on the performance of the burner. The release of volatile matter was found to occur closer to the burner region for both coal and biomass, bringing the flame nearer as O_2 enrichment increases. This is another important consideration in retrofitting oxy-fuel technology as this will impact on the performance of the burner with regards to flame shape, stability and emission control.

As a carbon capture technique, firing 100% biomass in an oxy-fuel capture plant can lead to carbon negative emissions. However, the results indicate that the heat transfer is lower than the design conditions (air-coal). For retrofitting, enriching O_2 above 30% could be used with oxy-fuel combustion to increase the heat transfer to both the water walls and radiative heat exchangers, although the increase in temperatures may impact negatively on the materials inside the boiler. It must be noted that the values reported are indicative of the performance trends and do not relate to quantitative values. Moreover, modifications that would likely be carried out during retrofitting, such as the use of dedicated biomass burners and changes to the firing arrangement to increase the particle residence time, would also help improve performance. Furthermore, it is important to note that CFD was used to model only a section of the whole power generation system and in order to more accurately assess the impact of oxy-coal combustion on the overall power plant performance, an integrated CFD-Process model would need to be used (Edge *et al*., 2012).

Firing coal results in the highest carbon balance but appears to have the least impact on the performance under oxy-fuel combustion, since predictions indicate that heat transfer and temperatures can be closely matched to that of air firing. Co-firing can be used to shift the carbon emissions balance of an oxy-coal plant from near neutral to negative, without significant penalties on the total heat transfer. When the deep emission reduction potential of 100% biomass firing is desired, further modifications would be necessary to achieve output closer to the original design of the boiler.

The results presented here indicate that a number of physical sub models will be required to allow the impact of the alternative fuels and oxidiser mixtures to be assessed accurately. For example, more advanced models are needed to deal with the catalytic influence of biomass char combustion on the overall burnout, char gasification, radiative heat transfer, as well as particle size, shape and internal temperature gradients of larger biomass particles.

5.4 Conclusions

CFD modelling was first undertaken on a 250 kW, air-fired coal rig, of the same dimensions to the PACT CTF, and with a theoretical scaled version of an IFRF burner. Modelling techniques from the literature (including turbulence, combustion, heat transfer modelling, grid generation and appropriate treatment of boundary conditions) were developed and then applied and validated on the 2.4MW IFRF furnace burning pulverised coal under air-firing conditions.

Building on the modelling work undertaken on small scale test facilities (Section 0 and 5.2), a commercial CFD code was employed to assess the suitability of modelling the performance of a 500 MW_e utility boiler in relation to furnace temperatures, heat transfer and burnout. Coal, a 20% biomass blend, and 100% biomass fired in air and oxy-fuel environments for a wet-recycle for the same thermal input was investigated.

Predictions showed that for the oxy-fuel cases, the higher O_2 concentration at the inlet increased the furnace exit temperature and heat transfer to the radiative sections of the boiler, for each of the respective fuels. For the biomass blend cases investigated, total heat transfer was similar to that of the coal-firing cases since coal dominated the combustion process. However, temperatures at the furnace exit and total heat transfer decreased when 100% biomass was used. This was attributed to the larger particle sizes and the reduction in particle radiation. The latter was due to the decrease in the total surface area of the biomass particles when compared to the much finer coal particles, as well as the lower ash content of the biomass.

The results suggest that for a wet recycle retrofit, the optimum O_2 concentration lies between the simulated range of 25 and 30%, where heat transfer characteristics of the air-fired design can be matched, when firing either 100% coal or the 20% biomass blend, but not when firing 100% biomass. Therefore, co-firing could be used to shift the carbon emissions balance of a coal fired oxy-fuel plant from near neutral to negative, without significant penalties on the total heat transfer. However, when the substantial emission reduction potential of 100% biomass firing is desired, further modifications may be necessary to achieve an output closer to the original design of the boiler.

Chapter 6

Conclusions and Future Work

It is clear, from numerous studies, that CCS has great potential to play a major role in reducing CO_2 emissions, and thus mitigating climate change. It will also enable the continued use of fossil fuels over the coming decades, while renewable, nuclear, or even fusion power generation technologies are developed to meet the world's total energy requirements.

Oxy-fuel is one of the leading carbon capture technologies. It has a major advantage in that it can be retrofitted to existing plants, as well as applied to newly-built power stations. Thus it promises to address future CO_2 emissions that are already locked into existing fossil fuel plants. However, before the technology can be made available, there is a need for further technological learning about the oxy-fuel combustion process, and the role that it might play in the development of technologies for Carbon Capture and Sequestration. Computational Fluid Dynamics can be used to model the complex physical and chemical processes taking place during combustion, and can provide reliable predictions of, for example, in-furnace temperature profiles, heat flux distribution, flame characteristics, and pollutant formation trends. Therefore, it is a useful tool in aiding burner and furnace design and development. However, the existing submodels available in commercial CFD packages were developed for the combustion of coal under air-firing conditions, and many of the assumptions are not valid when moving to oxy-fuel atmospheres. For example in radiation modelling methods, where the traditional grey gas treatment of combustion gases is invalid due to increased levels of triatomic gases, CO_2, H_2O, participating in radiative heat exchange actively absorbing and emitting radiation. Therefore, there has been ongoing developments of new submodels that are specific to oxy-firing conditions (e.g. FSCK model developed by the team at the University of Leeds – see Porter (2010)). Crucially, however, these new models need validation data from well defined, small-scale experimental studies.

This PhD dissertation has contributed to the development of CCS by presenting the results of an experimental programme conducted on a 250 kW solid fuel combustion test facility (located at the PACT national facilities near Sheffield), and investigating

CFD modelling for oxy-fuel combustion (of both coal and biomass), on both pilot and commercial-scale boilers. It also sets out a programme for future experimental work.

6.1 Significant Experimental Findings

Coal was fired in air under both non-preheated and preheated conditions, as well as under pre-heated oxy-firing conditions. A range of detailed measurements were taken, and the following major findings were identified.

6.1.1 Air-firing Conclusions

Preheating the combustion air increases the heat input to the burner, facilitating ignition and therefore stabilising the flame, and the additional heat also enhances devolatilisation and improves burnout, enhancing the efficiency of the process. When preheating, the radiative heat transfer from the flame also increases. This is significant because it is the main and most important form of heat transfer within furnaces. The largest increases were observed near the flame region. In commercial, multi-burner boilers, this would result in increased radiative feedback between adjacent burners, further increasing the radiative heat available to heat the fuel particles and having a beneficial effect on flame stability. Finally, preheating increases the efficiency of the power generation process by enabling low-grade sensible heat recovery from the flue gas, recycling it into the boiler.

The effect of burner staging on NO and CO emissions with both non-preheated and preheated combustion air was examined, and the optimal emissions performance of the burner for the non-preheated and preheated cases was identified. CO emissions decreased with preheating the combustion air, and also with increasing burner staging for both the non-preheated and preheated cases. The disadvantage of preheating combustion air was found to be that it increased thermal NO_x formation and evidence for increased fuel NO_x formation was also found, due to increased mixing of the IRZ and the staged combustion air streams. However a decreasing trend in NO emissions was observed in both preheated and non-preheated cases when the burner staging was increased. The optimal burner setup was identified for the non-preheated and preheated cases, respectively, with the lowest NO emissions. Changing the primary air ratio was found only to influence the emissions slightly. However the primary air ratio had a significant effect on flame stability when comparing the 18, 20 and 22%

primary air cases. Furthermore the flame stability decreased when the primary air was increased, corresponding to an increased primary air velocity and reduced particle residence time in the root region of the flame.

In-furnace suction pyrometry and heat flux results for the preheated combustion air case were also analysed, and evidence for the presence of the ERZ and the IRZ were identified in both the suction pyrometry results as well as in the heat flux measurements. This corresponded to the flame structure as described in the literature for similar burner setup fired in a confined furnace enclosure. The combustion air stream was found to follow the trajectory of the quarl angle as it enters the furnace, which was due to the swirling combustion air attaching to the quarl before it enters the furnace. The importance of the IRZ and ERZ on stabilising the flame was emphasised due to the recycling of heat to the root of the flame, thus increasing particle heat up and devolatilisation. The effect of IRZ on NO_x reduction was also discussed, as the volatile-N species evolving form coal, devolatilising in the reducing IRZ, tend to form N_2 instead of NO. Also, since the IRZ recirculates NO already formed, from downstream of the flame to the root rich in hydrocarbon radicals, the IRZ has an important role in the destruction of NO_x.

The radiative heat transfer followed the trend observed during the centreline temperatures measured with suction pyrometry, peaking between the 575 and 800 mm measurement ports. After the 800 mm location, as the gases within the combustion chamber cool, the radiative heat flux progressively decreased, with the lowest reading recorded at the last measurement location before the flue outlet. The location of the peak in total heat transfer is shifted from the radiative peak at the end of the flame, to be closer to the root of the flame. The trends observed suggest that the total heat transfer, which is the sum of the convective and radiative terms, is manly influenced by the thermal radiation in furnaces firing pulverised coal. Therefore the radiative heat flux data is of great importance to the validation of the newly developed CFD submodels on this furnace.

6.1.2 Oxy-firing Conclusions

The oxy-fuel experiments produced flue gas high in CO_2 concentration, which is required to enable carbon capture without chemical scrubbing processes. As the recycle rate reduced (corresponding to higher O_2 concentration cases), the exit concentrations of NO increased by 16%, largely due to the reduced oxidiser flow and the resulting reduction in dilution by CO_2. This was then confirmed by the much smaller increase in NO emissions indices (6%), on a mg/MJ basis, when moving from the oxy27 to the oxy30 case. The increase in the emissions indices was attributed to higher temperatures, and therefore the increased production of thermal NO.

Compared to the preheated air base case, the oxy27 and oxy30 cases resulted in a 53% and 51% reduction in NO emissions, respectively. This reduction was attributed to a number of factors, which included the low levels of atmospheric N_2 in the oxidiser (which may produce oversaturation of NO in the combustion atmosphere reversing the Zeldovich mechanism, and reduce prompt NO formation). Furthermore, a reduction in fuel NO formation (responsible for ~80% of the total NO in pulverised coal flames), which is affected by the fluid dynamics, via its effect on burner staging and mixing between the fuel rich primary and staged secondary and tertiary streams. Compared to the air-firing cases the burner velocities decreased significantly. This may then result in decreased mixing between the fuel rich flame root and the staged combustion air streams, allowing more residence time for the volatile-N in the reducing zones of the flame, significantly lowering fuel NO formation.

Evidence of higher volatile formation in oxy-fuel combustion was found in the literature, which was attributed to the heterogeneous gasification reaction of CO_2 with the char, which also affected N partitioning producing an increased volatile-N release. When Low-NOx burners are used, such as the one used in this investigation, increased volatile-N release may reduce fuel-NO formation due to more fuel-N being released in the staged fuel rich zones promoting volatile-N conversion to N_2.

As the recycle rate reduced (corresponding to higher O_2 concentration cases), the exit concentrations of SO_2 increased. The increase in exit SO_2 concentrations was attributed to the reduced oxidiser flow, and the comparison of air and oxy-fired emissions indices suggested that SO_2 emissions are independent of the combustion atmosphere used, and depend on the amount of sulphur supplied with the coal. Therefore the SO_2 emissions can be altered by the choice of coal used.

The results indicate that there are no significant issues in the control of CO emissions when moving to oxy-fuel combustion.

The effect of oxy-firing on the temperature profiles and on the heat flux characteristic of the flame was also investigated. The peak radiative heat transfer values of the air and oxy30 cases corresponded to the typical range predicted on a coal-fired boiler using the FURDEC heat transfer code, which is 340-500 kW/m^2.

For the oxy-cases, in furnace temperatures and heat flux increased with increasing total O_2 concentration. The results indicated that it is possible to match the air-fired temperature profiles when retrofitting for oxy-fuel combustion by modifying the recycle ratio, and the optimal recycle ratio lies between the investigated cases of 27% and 30% total O_2 concentrations (when dry recycle is used). The radiative heat flux profiles can also be adjusted, due to the dependence of thermal radiation on the temperature.

The temperature and heat flux measurements trends showed significant differences in the first furnace section between the air- and oxy-fired cases. This pointed to delayed combustion due to the higher heat capacity of CO_2; and delayed mixing between the Primary and Secondary/Tertiary streams, which may produce longer flames for the oxy-fired cases where the same burner is used for both firing modes.

The increased gas emissivity was found to increase the radiative heat transfer. Gas emissivity increases when replacing atmospheric N_2 with the tri-atomic CO_2, which actively participates in gas radiation and has a higher emissivity than N_2. Evidence for this was found in the second half of the furnace, where similar temperatures were measured for the preheated air and oxy27 cases, but these corresponded to significantly higher radiative heat transfer measurements for the oxy27 case than for the air case.

Comparing the findings with the literature showed that flame properties at the same recycle ratios may vary significantly with the type of coal used, and also depend on geometry and aerodynamics of the burners used. This confirmed the need for experimental trials using a range of coals with scaled versions of the burners to be used at commercial oxy-fired power stations.

The residence time within the furnace was higher for the oxy-fired cases, where the residence time increased with the total O_2 concentration. This is due to the reduction in recycle rate and therefore in the total oxidiser flow. Compared to the preheated air-fired cases, the oxy27 and oxy30 cases had a 26% and 34% increase in residence time, respectively.

The burnout is expected to improve with the reduction of recycle rate, which corresponds to higher volumetric O_2 concentrations, higher in furnace temperatures and higher residence times.

6.2 CFD Modelling Conclusions

CFD modelling was first undertaken on a 250 kW, air-fired coal rig, of the same dimensions to the PACT CTF, and then applied and validated on a 2.4 MW IFRF furnace burning pulverised coal under air-firing conditions. Building on this work, the performance of a 500 MW_e utility boiler was modelled, focusing on furnace temperatures, heat transfer and burnout. Coal, a 20% biomass blend, and 100% biomass fired in air and oxy-fuel environments for a wet-recycle for the same thermal input were studied.

The CFD predictions showed that for the oxy-fuel cases, the higher O_2 concentration at the inlet increased the furnace exit temperature and the heat transfer to the radiative sections of the boiler, for each of the respective fuels. For the blend cases studied, the total heat transfer was similar to that of the coal-firing cases. However, temperatures at the furnace exit and total heat transfer decreased when 100% biomass was used.

The results suggested that for a wet recycle retrofit, the optimum O_2 concentration lies between the simulated range of 25 and 30%, where heat transfer characteristics of the air-fired design can be matched, when firing either 100% coal or the 20% biomass blend, but not when firing 100% biomass. Therefore, co-firing could be used to shift the carbon emissions balance of a coal fired oxy-fuel plant from near neutral to negative, without significant penalties on the total heat transfer. However, when the deep emission reduction potential of 100% biomass firing is desired, further modifications may be necessary to achieve an output closer to the original design of the boiler.

6.3 Future Oxy-fuel Work and Recommendations

For the Oxy-fired trials, flow rates corresponding to different techniques in splitting the combustion air were identified. However, there is a gap in the literature that identifies the best available techniques for splitting the oxidiser between the burner registers. Moreover, the best approach may differ from burner to burner. Accordingly, plans for two different approaches have been drawn up:

(i) Fixing the primary volume flow, and therefore the primary velocity and the momentum of coal injected into the flame.

(ii) Fixing the volumetric split of the primary to total oxidiser, which results in a reduction in primary velocity and coal momentum injected into the flame. This approach increases the residence time of the coal within the primary zone, and increases flame stability.

To provide additional validation data the oxy-fuel trials can be extended to include measurements of flame temperature measurements using suction pyrometry, in-furnace gas compositions of O_2, CO, CO_2, SO_2 and NO, and coal burnout. In future experiments, radiative heat flux measurements should be undertaken using Ar gas purge instead of N_2, which might improve the accuracy of the measurements.

Furthermore, the combustion of biomass, which has the potential to deliver negative CO_2 emissions when combined with CCS technologies, should be investigated.

For both coal and biomass combustion, the extension of the studies to include the investigation of slagging would be beneficial, together with detailed characterisation of the produced ash and slag samples.

Advanced imaging studies, involving 2D and 3D camera probes, is scheduled to be undertaken in collaboration with the research team at the University of Kent. This will allow for the testing of their novel 3D imaging equipment on a turbulent, pulverised fuel flame.

In addition, the use of PIV laser imaging should be considered. This will provide invaluable data on the in-furnace velocities, which would also greatly aid the validation, and the use of LES turbulence models. Detailed in-furnace measurements of the gas species and temperatures close to the burner can also be used for the validation of the LES models.

The experimental programmes realised will contribute to an oxy-fuel database being available for CFD sub-model validation. Test results from the oxy-coal studies detailed above will constitute the basis for the validation of the FSCK model that is currently being further developed by the modelling team at the University of Leeds.

Bibliography

ABBAS, T., COSTEN, P.G. & LOCKWOOD, F.C. 1996. Solid fuel utilization: From coal to biomass. *Symposium (International) on Combustion,* 26**,** 3041-3058.

ABRAHAM, B.M., ASHBURY, J.G. & LYNCH, E.P. 1982. Coal Oxygen Process Provides CO_2 for Enhanced Oil Recovery. *Oil and Gas Journal,* 80**,** 68-75.

ANDERSSON, K., JOHANSSON, R., JOHNSSON, F.. 2011. Thermal radiation in oxy-fuel flames. *Int. J. Greenhouse Gas Control,* 5 (1), S58-S65.

ANSON, D., MOLES, F.D. & STREET, P.J. 1971. Structure and surface area of pulverized coal during combustion. *Combustion and Flame,* 16**,** 265-274.

ANSYS INC. 2013. FLUENT Theory Guide.

BACKREEDY, R.I., JONES, J.M., POURKASHANIAN, M. & WILLIAMS, A. 2006. Burn-out of pulverised coal and biomass chars[small star, filled]. *Fuel,* 82**,** 2097-2105.

BADZIOCH S., HAWKSLEY P.G.W. 1970. Kinetics of Thermal Decomposition of Pulverized Coal Particles. Ind. Eng. Chem. Proc. Des. Dev., 9 (4), 521-30.

BALLANTYNE, T.R., ASHMAN, P.J., MULLINGER, P.J. 2005. A new method for determining the conversion of low-ash coals using synthetic ash as a tracer. Fuel; 84 (14–15), 1980–1985.

BAUM, M.M. & STREET, P.J. 1971. Predicting the Combustion Behaviour of Coal Particles. *Combustion science and technology,* 3**,** 231 - 243.

BECHER V., GOANTA A., SPLIETHOFF H. 2012. Validation of spectral gas radiation models under oxyfuel conditions - Part C: Validation of simplified models. *Int. J. Greenhouse Gas Control*., 11, 34-51

BEÉR, J., & CHIGIER, N.A. 1972. *Combustion Aerodynamics,* London, Applied Science Publishers Ltd.

BLACK, S., SZUHÁNSZKI, J., PRANZITELLI, A., MA, L., STANGER, P.J., INGHAM, D.B., POURKASHANIAN, M. 2013. Effects of firing coal and biomass under oxy-fuel conditions in a power plant boiler using CFD modelling. *Fuel*, 113, 780-786.

BP. 2013. *BP Statistical Review of World Energy - June 2010* [Online]. Available: http://bp.com/statisticalreview [Accessed 10 December 2010].

BROOKES S.J., MOSS J.B. 1999. Prediction of Soot and Thermal Radiation in Confined Turbulent Jet Diffusion Flames. Combust. Flame, 116, 486–503.

BROWN A.L. 1997. Modelling Soot in Pulverized Coal Flames. PhD Thesis. Brigham Young University.

BUHRE, B.J.P., ELLIOTT, L.K., SHENG, C.D., GUPTA, R.P., WALL, T.F. 2005. Oxy-fuel combustion technology for coal-fired power generation. *Prog Energ Combust*, 31 (4) 283-307.

CHEDAILLE, J., BRAUD, Y. 1972. Inustrial flames - Volume 1 - Measurments in Flames. London: Edward Arnold (Publishers) Ltd.

CCC (COMMITTEE ON CLIMATE CHANGE). 2009. *Building a low-carbon economy – The UK's contribution to tackling climate change,* London, The Stationary Office.

CDIAC (CARBON DIOXIDE INFORMATION ANALYSIS CENTER). 2014. *Global CO_2 Emissions from Fossil-Fuel Burning, Cement Manufacture, and Gas Flaring: 1751-2007* [Online]. Available: http://cdiac.ornl.gov/ftp/ndp030/global.1751_2007.ems [Accessed 4 Feb 2011].

CHEN, L., YONG, S.Z., GHONIEM, A.F. 2012. Oxy-fuel combustion of pulverized coal: Characterization, fundamentals, stabilization and CFD modelling. *Prog Energ Combust*, 38 (2) 156-214.

CROISET E., Thambimuthu, K., Palmer, A. 2000. Coal combustion in O_2/CO_2 mixtures compared with air. Can J Chem Eng 78 (2) 402-407.

DECC. The Renewable Obligation (RO). 2012. [Online]. Available: http://www.decc.gov.uk/en/content/cms/meeting_energy/renewable_ener/renew_obs/renew_obs.aspx, [Accessed 29 September 2012].

DECC. UK Bioenergy Strategy. 2012. URN: 12D/077 London; 2012.

DARDE, A., PRABHAKAR, R., TRANIER, J.P. & PERRIN, N. 2009. Air separation and flue gas compression and purification units for oxy-coal combustion systems. *Energy Procedia*, 1**,** 527-534.

DAVIDSON, R.M. & SANTOS, S.O. 2010. Oxyfuel combustion of pulverised coal. IEA Clean Coal Centre.

DE NEVERS, N. 2000. *Air pollution control engineering,* London, McGrawHill.

DHUNGEL, B. 2010. *Experimental Investigations on Combustion and Emission Behaviour during Oxy-Coal Combustion*, PhD Thesis, University of Stuttgart.

EDGE, P.J. 2011. Modelling and simulation of oxy-coal fired power plants. PhD Thesis. University of Leeds.

EDGE, P., GHAREBAGHI, M., IRONS, R., PORTER, R., PORTER, R.T.J., POURKASHANIAN, M., SMITH, D., STEPHENSON, P. & WILLIAMS, A. 2011a. Combustion modelling opportunities and challenges for oxy-coal carbon capture technology. *Chem Eng Res Des*., 89, 1470-93.

EDGE, P., GUBBA, S.R., MA, L., PORTER, R., POURKASHANIAN, M. & WILLIAMS, A. 2011b. LES modelling of air and oxy-fuel pulverised coal combustion--impact on flame properties. *Proceedings of the Combustion Institute,* 33**,** 2709-2716.

EDGE, P.J., HEGGS, P.J., POURKASHANIAN, M., STEPHENSON, P.L., WILLIAMS, A. 2012. A reduced order full plant model for oxyfuel combustion. Fuel, 101, 234-43.

ELEXON. 2011. *BM Reports* [Online]. Available: http://www.bmreports.com/bsp/bsp_home.htm [Accessed 16 April 2011].

FLEIG, D., NORMANN, F., ANDERSSON, K., JOHNSSON, F. & LECKNER, B. 2009. The fate of sulphur during oxy-fuel combustion of lignite. *Energy Procedia,* 1**,** 383-390.

FLETCHER, T.H. & HARDESTY, D.R. 1992. Compilation of Sandia Coal Devolatilization Data: Milestone Report. *Sandia Report No. SAND92-8209.*

FLETCHER, T.H., KERSTEIN, A.R., PUGMIRE, R.J., SOLUM, M.S. & GRANT, D.M. 1992. Chemical percolation model for devolatilization. 3. Direct use of carbon-13 NMR data to predict effects of coal type. *Energy & Fuels,* 6**,** 414-431.

FLORIN, N. & FENNELL, P. 2010. *Carbon capture technology: future fossil fuel use and mitigating climate change* [Online]. Available: http://www3.imperial.ac.uk/climatechange/publications [Accessed 15 March 2011].

FOLGUERAS, M.B., DÍAZ, R.M., XIBERTA, J. 2004. Sulphur retention during co-combustion of coal and sewage sludge. *Fuel* 83 (10) 1315-1322.

FRY, A., ADAMS, B., PASCHEDAG, A., KAZALSKI, P., CARNEY, C., ORYSHCHYN, D., WOODSIDE, R., GERDEMANN, S., OCHS, T. 2011. Principles for retrofitting coal burners for oxy-combustion. *Int. J. Greenhouse Gas Control,* 5 (1), S151–S158.

GHAREBAGHI, M., IRONS, R.M.A., MA, L., POURKASHANIAN, M., PRANZITELLI, A. 2011. Large eddy simulation of oxy-coal combustion in an industrial combustion test facility. *Int. J. Greenhouse Gas Control*; 5:S100-S110.

GENETTI, D., FLETCHER, T. & PUGMIRE, R. 1999. Development and application of a correlation of ^{13}C NMR chemical structural analyses of coal based on elemntal Composition and Volatile Matter content. *Energy and Fuels,* 13**,** 60-68.

GRIFFITHS, J.F. & BARNARD, J.A. 1995. *Flame and Combustion,* London, Blackie Academic & Professional.

HAIDER A, LEVENSPIEL O. 1989. Drag Coefficient and Terminal Velocity of Spherical and Nonspherical Particles. *Powder Technol*., 58, 63–70.

HARKER, J.H., BACKHURST, J.R. 1981. *Feul and Energy.* London: Academic Press Inc.

HILL, S.C., SMOOT, L.D. 2000. Modelling of nitrogen oxides formation and destruction in combustion systems. Progress in Energy and Combustion Science; 26 (4–6), 417–458.

HJÄRTSTAM S., JOHANSSON R., ANDERSSON K., JOHNSSON F. 2012. Computational Fluid Dynamics Modelling of Oxy-Fuel Flames: The Role of Soot and Gas Radiation. Energy Fuels, 26, 2786-97.

HM GOVERNMENT 2009. The UK low carbon transition plan – National strategy for climate and energy. Norwich.

HOTTEL H.C., SAROFIM A.F. Radiative Heat Transfer. New York: McGraw-Hill; 1967.

HURT, R.H. 1998. Structure, properties, and reactivity of solid fuels. *Symposium (International) on Combustion,* 27**,** 2887-2904.

IEA. 2010. *World Energy Outlook 2010* [Online]. Available: http://www.worldenergyoutlook.org/ [Accessed 5 March 2011].

IFRF (International Flame research Foundation). 1994. IFRF Catalogue – Measurement Equipment: Suction Pyrometer.

IPCC. 2013. IPCC Fourth Assessment Report: Climate Change.

JERNIGAN, J.R. 2007. Chemiluminescence NO_x and GFC NDIR CO Analyzers for Low Level Source Monitoring. Thermo Environmental Instruments. [Online].

Available:
http://www.thermo.com/eThermo/CMA/PDFs/Various/File_2650.pdf
[Accessed 11 Oktober 2013].

JOHANSSON R., ANDERSSON K., LECKNER B., THUNMAN H. 2010. Models for gaseous radiative heat transfer applied to oxy-fuel conditions in boilers. Int. J. Heat Mass Transfer, 53, 220-30.

JOHANSSON R., LECKNER B., ANDERSSON K., JOHNSSON F. 2011. Account for variations in the H_2O to CO_2 molar ratio when modelling gaseous radiative heat transfer with the weighted-sum-of-grey-gases model. Combust. Flame, 158, 893-901.

JORDAL, K., ANHEDEN, M., YAN, J. & STRÖMBERG, L. 2004. Oxyfuel Combustion for Coal-Fired Power Generation with CO_2 Capture – Opportunities and Challenges. *GHGT-7 Conference.* Vancouver, Canada.

KANGWANPONGPAN T., SILVA R.C., KRAUTZ H.J. 2012. Prediction of oxy-coal combustion through an optimized weighted sum of gray gases model. Energy, 41, 244-51.

KATZER, J.R. 2007. *The future of Coal-Based Power Generation – MIT Energy Initiative* [Online]. Available: http://www.un.org/esa/sustdev/sdissues/energy/op/ccs_egm/presentations_papers/katzer_future_of_coal.pdf [Accessed 4 August 2010].

KOBAYASHI, H., HOWARD, J.B. & SAROFIM, A.F. 1977. Coal devolatilization at high temperatures. *Symposium (International) on Combustion,* 16**,** 411-425.

KRISHNAMOORTHY G. 2010. A new weighted-sum-of-gray-gases model for CO_2-H_2O gas mixtures. Int. Commun. Heat. Mass., 37, 1182-86.

LI, H, ELLIOTTA, L., ROGERS, H., AUSTIN, P., WALL, T. 2013. Coal burnout in a pilot-scale rig simulateing pulverised coal injection and a laboratory drop tube furnace. 10th Australian Coal Science Conference, Brisbane Queensland.

LOCKWOOD, F.C., PARODI, S.A. 1998. Burner-Burner interaction. Performance Prediction in Advanced Coal Fired Boilers .Contract No JOF3 - CT95 – 0005. Project Area 1 - Project 110. [Online]. Available: ftp://cemflam.org/pub/pdf/JOF3-CT95-0005-pdf-files/JOF3-CT95-0005-110-Lockwood-ICSTM.pdf [Accessed 10 July 2012].

LODGE JR., J.P. 1988. Methods of Air Sampling and Analysis. CRC Press LLC.

LU, G. & YAN, Y. 2009. Advanced Monitoring and Characterisation of Combustion Flames. *20th Annual Meeting and Meeting of the Combustion and Advanced Power Generation Division.* University of Leeds.

LU, H., WARREN, R., PEIRCE, G., RIPA, B., BAXTER, L.L. 2008. Comprehensive Study of Biomass Particle Combustion. Energy Fuels, 22, 2826–39.

MA, L., GHAREBAGHI, M., PORTER, R., POURKASHANIAN, M., JONES, J. M. & WILLIAMS, A. 2009. Modelling methods for co-fired pulverised fuel furnaces. *Fuel*, 88**,** 2448-2454.

MA, L., JONES, J.M., POURKASHANIAN, M., WILLIAMS, A.. 2007. Modelling the combustion of pulverized biomass in an industrial combustion test furnace. Fuel, 86, 1959-65.

MAGNUSSEN, B.F. 1989. Modeling of NO_x and soot formation by the Eddy Dissipation Concept. *Int.Flame Research Foundation - 1st topic Oriented Technical Meeting.* Amsterdam, Holland.

MAGNUSSEN, B.F. & HJERTAGER, B.H. 1977. On mathematical modeling of turbulent combustion with special emphasis on soot formation and combustion. *Symposium (International) on Combustion*, 16**,** 719-729.

MAN, C.K. & GIBBINS, J.R. 2011. Factors affecting coal particle ignition under oxyfuel combustion atmospheres. *Fuel*, 90**,** 294-304.

MARAKIS J.G., PAPAPAVLOU C., KAKARAS E. 2000. A parametric study of radiative heat transfer in pulverised coal furnaces. Int. J. Heat Mass Transfer, 43, 29-2971.

MCKINSEY & COMPANY. 2014. CO_2 abatement: Exploring options for oil and natural gas companies. [Online]. Available: http://www.mckinsey.com/insights/energy_resources_materials/co2_abatement_exploring_options_for_oil_and_natural_gas_companies [Accessed 15 February 2014].

MEDTHERM CORPORATION. 2012. Operating Instructions and Calibration Records. GTW-50-24-21584 Combination Furnace Heat Flux Probe.

MET OFFICE. 2011. *Record of past variations in CO_2 concentrations from ice core records* [Online]. Available: http://www.metoffice.gov.uk/climate-change/guide/faq?media=2030 [Accessed 4 February 2011].

MIT. 2014. *Power Plant Carbon Dioxide Capture and Storage Projects* [Online]. Available: http://sequestration.mit.edu/tools/projects/index.html [Accessed 4 April 2014].

MOBSBY, J.A.. 1984. Thermal Modelling of Fossil Fired Boilers. In 1st UK Heat Transfer Conference. I. Mech E. and I. Chem E., Leeds.

MURTHY J.Y., MATHUR S.R. 1998. A Finite Volume Method for Radiative Heat Transfer Using Unstructured Meshes. J.Thermophys.Heat Transfer, 12, 313-21.

NIMMO, W., LIU, H. 2010. Developments in NO_x Emission Control by 'Reburning' in Pulverised Coal Combustion. *in: Grace, C.T. (Ed.), Coal Combustion Research. 2010*

NORMANN, F., ANDERSSON, K., LECKNER, B., JOHNSSON, F. 2009. Emission control of nitrogen oxides in the oxy-fuel process. *Prog Energ Combust* 35 (5), 385-397.

OKAZAKI, K., ANDO, T. 1997. NO_x reduction mechanism in coal combustion with Recycled CO_2. *Energy* 22 (2-3) 207-215.

PORTER, R., LIU, F., POURKASHANIAN, M., WILLIAMS, A., SMITH, D. 2010. Evaluation of solution methods for radiative heat transfer in gaseous oxy-fuel combustion environments. *J. Quant. Spectrosc. Radiat. Transfer*, 111, 2084-94.

PALLARÉS, J., ARAUZO, I. & WILLIAMS, A. 2007. Integration of CFD codes and advanced combustion models for quantitative burnout determination. *Fuel,* 86**,** 2283-2290.

PALMER, M. 2014. Propagation of uncertainty. [Online]. Available: http://web.mit.edu/fluids-modules/www/exper_techniques/2.Propagation_of_Uncertaint.pdf
[Accessed 4 Oktober 2013].

PAUL, B., DATTA, A. 2008. Burner development for the reduction of NO_x emissions from coal fired electric utilities. *Recent Patents on Mechanical Engineering,* 1, 175-189.

PETERS, A.A.F. & WEBER, R. 1997. Mathematical Modeling of a 2.4 MW Swirling Pulverized Coal Flame. *Combustion science and technology,* 122**,** 131 - 182.

PICKARD, S., DAOOD, S.S., NIMMO, W., LORD, R., POURKASHANIAN, M. 2013. Bio-CCS: Co-firing of Established Greenfield and Novel, Brownfield Biomass Resources under Air, Oxygen-enriched Air and Oxy-fuel Conditions. Energy Procedia, 37, 6062–6069.

PIELKE, R.A. 2009. *The British Climate Change Act: a critical evaluation and proposed alternative approach* [Online]. Available: http://stacks.iop.org/ERL/4/024010 [Accessed 3 December 2009].

PIK (POTSDAM INSTITUTE FOR CLIMATE IMPACT RESEARCH). 2009. *Emissions cut of 40% below 1990 levels by 2020 needed for industrial countries for 2°C limit* [Online]. Available: http://www.pik-potsdam.de/news/press-releases/emissions-cut-of-40-below-1990-levels-by-2020-needed-for-industrial-countries-for-2b0c-limit [Accessed 3 December 2009].

PILLAI, K.K. 1981. The Influence of Coal Type on Devolatilization and. Combustion in Fluidized Beds. *J. Inst. Energy,* 54**,** 142-150.

RANZ, W.E. & MARSHALL, J.W.R. 1952a. Evaporation from Drops Part I. *Chem. Eng. Prog,* 48**,** 141-146.

RANZ, W.E. & MARSHALL, J.W.R. 1952b. Evaporation from Drops, Part II. *Chem. Eng. Prog.,* 48**,** 173-180.

ROOIJMANS, T. 2012. *Suction pyrometer user manual*.

ROYAL SOCIETY. 2005. *Ocean acidification due to increasing atmospheric carbon dioxide* [Online]. Available: http://royalsociety.org/Ocean-acidification-due-to-increasing-atmospheric-carbon-dioxide/ [Accessed 3 June 2009].

SAZHIN S.S. 1994. An Approximation for the Absorption Coefficient of Soot in Radiating Gas. Manuscript. Fluent Europe Ltd.

SCHEFFKNECHT, G., AL-MAKHADMEH, L., SCHNELL, U. & MAIER, J. 2011. Oxy-fuel coal combustion--A review of the current state-of-the-art. *International Journal of Greenhouse Gas Control,* In Press, Corrected Proof.

SCHMIDT, U., REXROTH, C.H. & CREMER, I. 2004. New trends in combustion simulation. *2nd (International) SBF568-Workshop.* Heidelberg, Germany.

SHADDIX, C.R. & MOLINA, A. 2009. Particle imaging of ignition and devolatilization of pulverized coal during oxy-fuel combustion. *Proceedings of the Combustion Institute,* 32**,** 2091-2098.

SHADDIX, C.R. & MOLINA, A. 2011. Fundamental investigation of NO_x formation during oxy-fuel combustion of pulverized coal. *Proceedings of the Combustion Institute,* 33**,** 1723-1730.

SHAH, M.M. 2006. Oxy-fuel Combustion for CO_2 Capture from PC Boilers. *31st Int. Conf. on Coal Utilisation and Fuel Systems.* Clearwater, (FL).

SIGNAL GROUP. 2008. 4000VMA Heated Non-Vacuum NO_x Analyser Operating Manual. Camberley, England.

SMART, J., LU, G., YAN, Y. & RILEY, G. 2010a. Characterisation of an oxy-coal flame through digital imaging. *Combustion and Flame,* 157**,** 1132-1139.

SMART, J.P., KNILL, K.J., VISSER, B.M. & WEBER, R. 1989. Reduction of NO_x emissions in a swirled coal flame by particle injection into the internal recirculation zone. *Symposium (International) on Combustion,* 22**,** 1117-1125.

SMART, J.P., MORGAN, D.J. & ROBERTS, P.A. 1992. The effect of scale on the performance of swirl stabilised pulverised coal burners. *Symposium (International) on Combustion,* 24**,** 1365-1372.

SMART, J.P. & MORGAN, M.E. 1992. The comparison between constant velocity and constant residence time scaling. *IFRF Doc No. F 37/y/28.*

SMART, J.P., O'NIONS, P. & RILEY, G.S. 2010b. Radiation and convective heat transfer, and burnout in oxy-coal combustion. *Fuel,* 89**,** 2468-2476.

SMART, J.P. & RILEY, G.S. 2011. On the effects of firing semi-anthracite and bituminous coals under oxy-fuel firing conditions. *Fuel,* In Press, Uncorrected Proof.

SMITH, I.W. 1982. The combustion rates of coal chars: A review. *Symposium (International) on Combustion,* 19**,** 1045-1065.

SMITH T.F., SHEN Z.F., FRIEDMAN J.N. 1982. Evaluation of Coefficients for the Weighted Sum of Gray Gases Model. ASME, 104, 602-8.

SMITH, J. D., LORRA, M., HIXSON, E.M. & ELDREDGE, T. 2003. CFD in Burner Development. *In:* BAUKAL, J. C. E. (ed.) *CFD in Burner Development.*

SNAPE C. 2014. Presentation, OxyCAP Workshop 2014. London.

STERN, N. 2006. *STERN REVIEW: The Economics of Climate Change* [Online]. Available: http://www.hm-treasury.gov.uk/sternreview_index.htm [Accessed 3 November 2009].

STOPFORD, P.J. 2002. Recent applications of CFD modelling in the power generation and combustion industries. *Applied Mathematical Modelling,* 26**,** 351-374.

STREET, P.J., WEIGHT, R.P. & LIGHTMANN, P. 1969. Further investigations of structural changes occurring in pulverised coal particles during rapid heating. *Fuel,* 48**,** 343.

SU, S., POHL, J.H., HOLCOMBE, D., HART, J.A. 2001. Techniques to determine ignition, flame stability and burnout of blended coals in p.f. power station boilers. Progress in Energy and Combustion Science, 27 (1), 78-98.

SZUHÁNSZKI, J., BLACK, S., PRANZITELLI, A., MA, L., STANGER, P.J., INGHAM, D.B., POURKASHANIAN, M. 2013. Evaluation of the Performance of a Power Plant Boiler Firing Coal, Biomass and a Blend Under Oxy-fuel Conditions as a CO_2 Capture Technique. *Energy Procedia,* **37**, 1413-1422.

TIAN, Z.F., WITT, P.J., SCHWARZ, M.P. & YANG, W. 2009. Comparison of Two-Equation Turbulence Models in Simulation of a Non-Swirl Coal Flame in a Pilot-Scale Furnace. *Combustion science and technology,* 181**,** 954 - 983.

TOFTEGAARD, M.B., BRIX, J., JENSEN, P.A., GLARBORG, P. & JENSEN, A.D. 2010. Oxy-fuel combustion of solid fuels. *Progress in Energy and Combustion Science,* 36**,** 581-625.

UBHAYAKAR, S.K. 1976. Burning characteristics of a spherical particle reacting with ambient oxidizing gas at its surface. *Combustion and Flame,* 26**,** 23-34.

USNOAA. 2011. *Trends in Atmospheric Carbon Dioxide* [Online]. Available: http://www.esrl.noaa.gov/gmd/ccgg/trends/global.html [Accessed 16 June 2011].

VAN DEN BROEK, M., HOEFNAGELS, R., RUBIN, E., TURKENBURG, W. & FAAIJ, A. 2009. Effects of technological learning on future cost and performance of power plants with CO_2 capture. *Progress in Energy and Combustion Science,* 35**,** 457-480.

VERSTEEG, H.K. & MALALASEKERA, W. 2007. *An introduction to computational fluid dynamics: the finite volume method,* London, Pearson Education.

WALL, T., LIU, Y., SPERO, C., ELLIOTT, L., KHARE, S., RATHNAM, R., ZEENATHAL, F., MOGHTADERI, B., BUHRE, B., SHENG, C., GUPTA, R., YAMADA, T., MAKINO, K. & YU, J. 2009. An overview on oxyfuel coal combustion--State of the art research and technology development. *Chemical Engineering Research and Design,* 87**,** 1003-1016.

WALL, T.F. 2007. Combustion processes for carbon capture. *Proceedings of the Combustion Institute,* 31**,** 31-47.

WALL, T., STANGERA, R., SANTOS, S. 2011. Demonstrations of coal-fired oxy-fuel technology for carbon capture and storage and issues with commercial deployment. Int. J. Greenhouse Gas Control, 5 (1) S5-S15.

WEBER, R. 1996. Scaling characteristics of aerodynamics, heat transfer, and pollutant emissions in industrial flames. *Symposium (International) on Combustion,* 26**,** 3343-3354.

WEBER, R. & DUGUÉ, J. 1992. Combustion accelerated swirling flows in high confinements. *Progress in Energy and Combustion Science,* 18**,** 349-367.

WEBER, R., DUGUÉ, J., SAYRE, A. & VISSER, B. M. 1992. Quarl zone flow field and chemistry of swirling pulverized coal flames: Measurements and computation. *Symposium (International) on Combustion,* 24**,** 1373-1380.

WILLIAMS, A., BACKREEDY, R., HABIB, R., JONES, J. M. & POURKASHANIAN, M. 2002. Modelling coal combustion: the current position. *Fuel,* 81**,** 605-618.

WILLIAMS, A., JONES, J.M. & POURKASHANIAN, M. 2007. Co-firing Coal/Biomass and the Estimation of Burnout and NO_x Formation. *BCURA Report.*

WILLIAMS, A., POURKASHANIAN, M. & JONES, J. M. 2000. The combustion of coal and some other solid fuels. *Proceedings of the Combustion Institute,* 28**,** 2141-2162.

WORLD COAL ASSOCIATION. 2014. Coal Statistics. [Online]. Available: http://www.worldcoal.org/resources/coal-statistics/ [Accessed 2 March 2014].

XIONG, J., ZHAO, H., ZHENG, C., LIU, Z., ZENG, L., LIU, H. & QIU, J. 2009. An economic feasibility study of O_2/CO_2 recycle combustion technology based on existing coal-fired power plants in China. *Fuel,* 88**,** 1135-1142.

ZEP. 2010a. *CO_2 Capture and Storage (CCS)* [Online]. Available: http://www.zeroemissionsplatform.eu/library/publication/101-ccs-powerpoint-presentation.html [Accessed 3 March 2011].

ZEP. 2010b. *Recommendations for research to support the deployment of CCS in Europe beyond 2020* [Online]. Available: http://www.zeroemissionsplatform.eu/library.html [Accessed 16 August 2010].

ZHANG, J., KELLY, K.E., EDDINGS, E.G., WENDT, J.O.L. 2011. CO_2 effects on near field aerodynamic phenomena in 40 kW, co-axial, oxy-coal, turbulent diffusion flames *Int. J. Greenhouse Gas Control,* 5 (1), S47-S57.

Appendix – Oxy-fired Commissioning

Figure A.1 shows the furnace temperatures recorded when carrying out oxy-fuel commissioning activates, and Figure A.2 shows the corresponding O_2 and CO_2 flue gas measurements. During this commissioning process, the primary oxidiser was kept as air. The activities began with the steady air-firing of coal at 160 kW thermal input, followed by transition of the secondary/tertiary combustion air streams to the mixture of synthetic O_2/CO_2, at 25% O_2 concentration, by volume. This was achieved by introducing O_2/CO_2 flows corresponding to 25 kW steps in thermal input, followed by the reduction in air corresponding to 25 kW reduction in the thermal input. This process was repeated until all of the tertiary combustion air was replaced with O_2/CO_2 mixture. After each steps, the flame stability was checked based on exit composition, furnace temperatures, and visual checks were also made though the observation port fitted on the first section of the furnace. No significant dimming in flame intensity was observed and the secondary/tertiary transition process was completed within ~30 minutes. Then the thermal input and corresponding primary air and secondary/tertiary O_2/CO_2 flows were ramped up to 200 kW, in 20 kW steps.

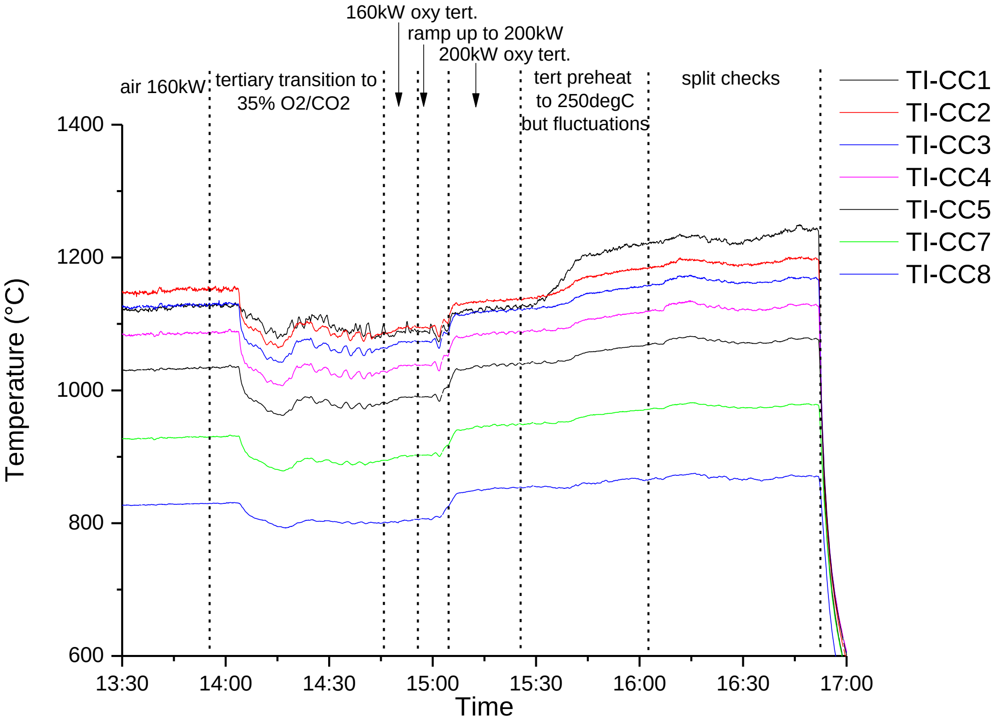

Figure A.1. Temperature measurements recorded during oxy-commissioning activities with the Type R sheathed thermocouples fitted within the furnace. Title of the activates undertaken are also shown.

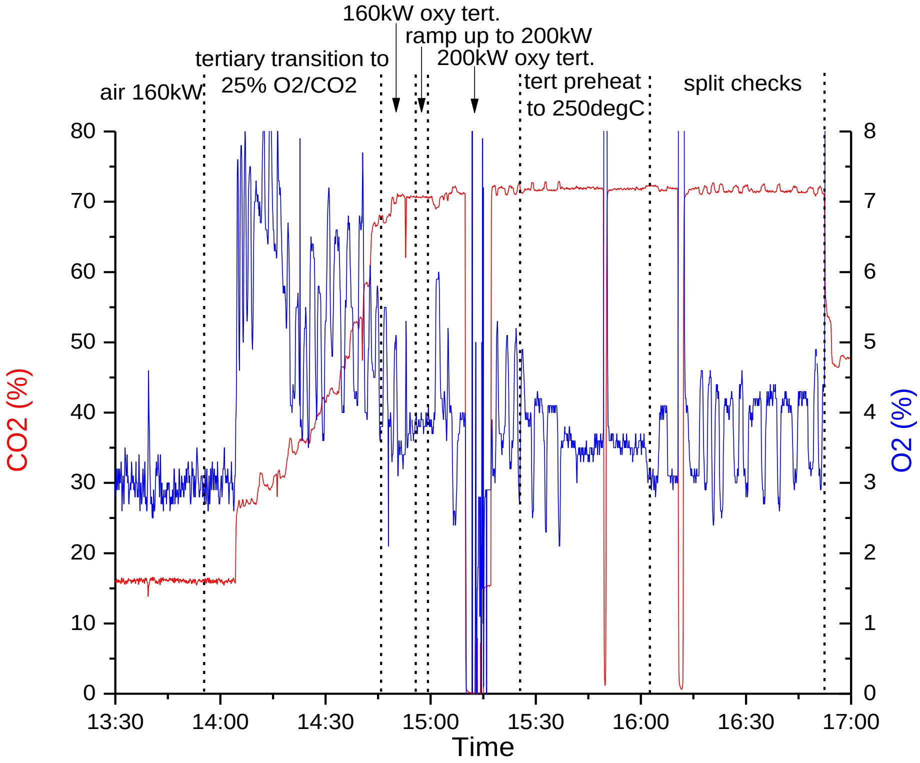

Figure A.2. O_2 and CO_2 trace recorded during the oxy-commissioning activities.

During the commissioning of the secondary/tertiary preheheater, up to 100°C fluctuations were observed in the preheater outlet temperature (Figure A.3), and the PID loop was identified as the most likely reason for this. Subsequent activities, involving the original programmer of the PLC (A&R Controls), revealed reprogramming issues, and required PID tuning of the system, after which steady operation of the preheaters was achieved.

The O_2 and CO_2 emissions traces also revealed an issue with the stability of the O_2 and CO_2 injections (Figure A.4), and the valve manufactures, Flowserve, was also involved in solving this issue.

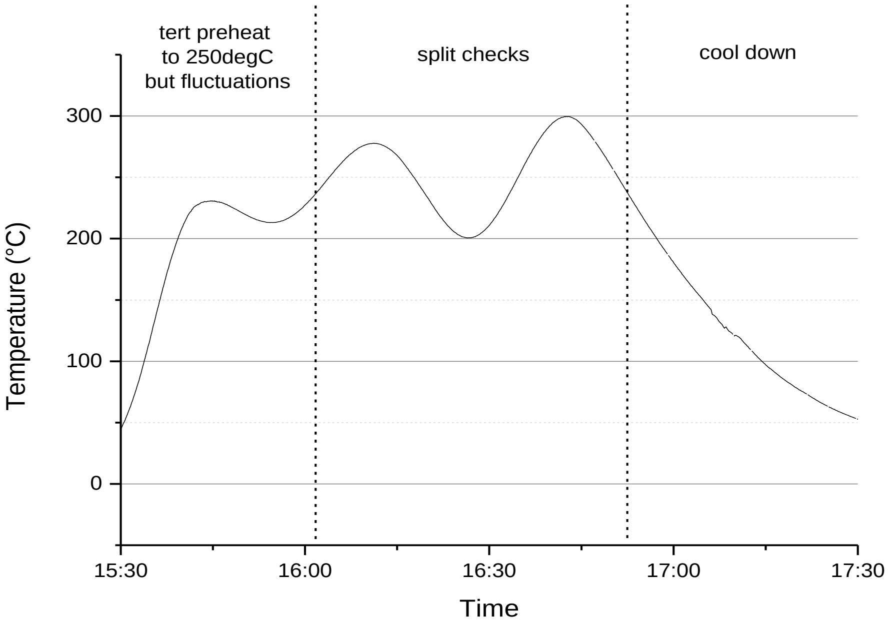

Figure A.3. Temperature measurements recorded during oxy-commissioning activities with the Type R sheathed thermocouples fitted within the furnace. Title of the activates undertaken are also shown.

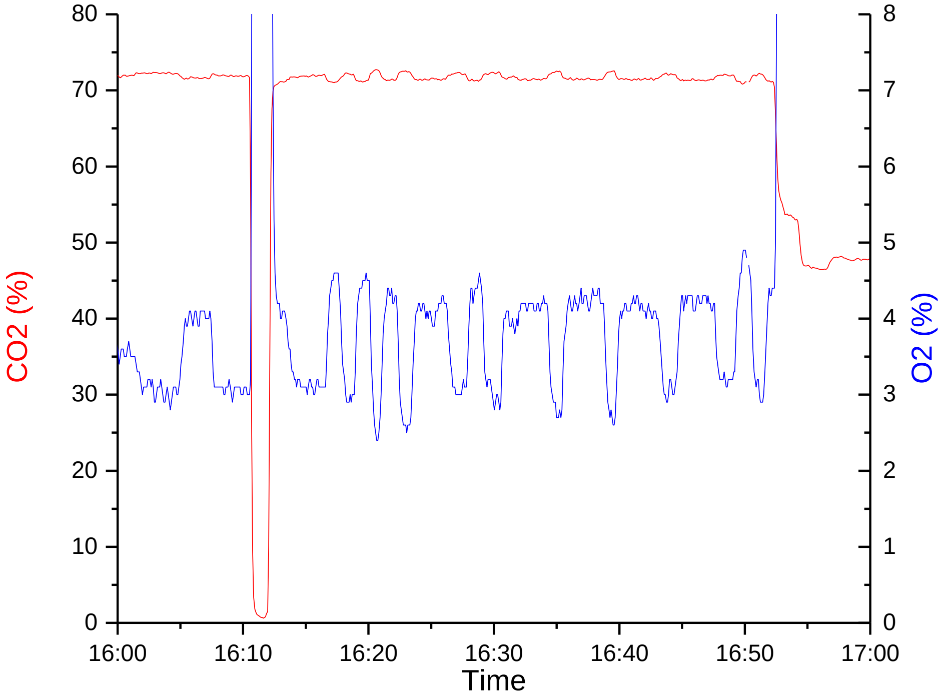

Figure A.4. O_2 and CO_2 measurements recorded during scoping exercise on burner optimisation undertaken as part of the oxy-commissioning activities.

Figure A.5. shows the CO_2 flow and valve opening % recorded during a cold commissioning oxy run. The CO_2 flow set point was 246 kg/hr:

- at 13:30, when the PID signal reached 40.3% opening there was a sudden increase in flow over the setpoint,
- the PID was gradually trying to close the valve but it only seemed to move at ~13:38 at 36.3% opening, producing a sudden drop in the flow,
- again, the flow only changed when the PID signal reached 39.99% opening but this time the increase took the flow very close to the setpoint.

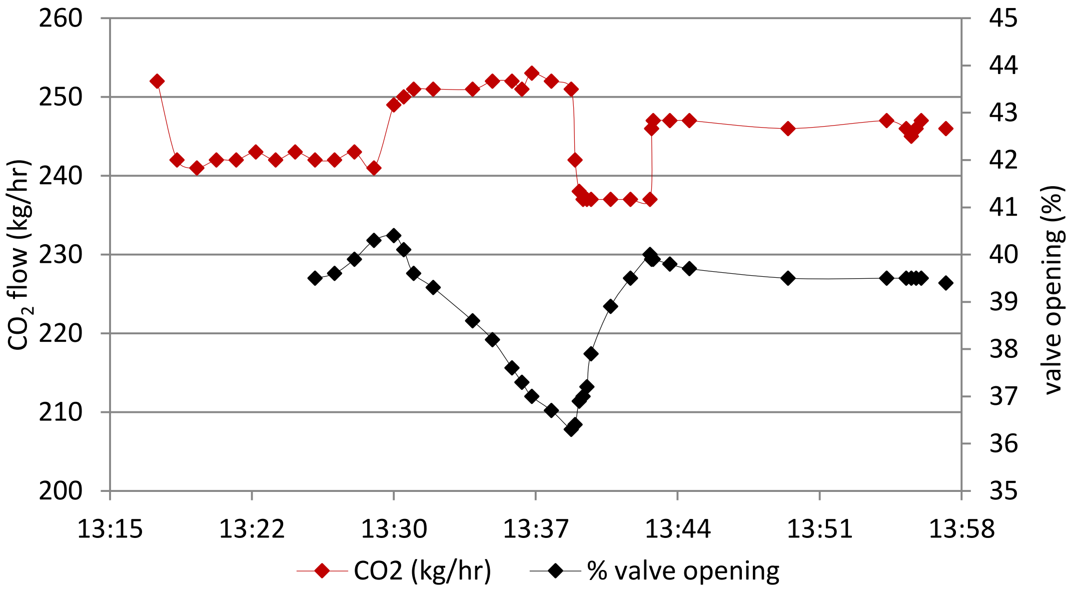

Figure A.5. CO_2 flow and valve opening % recorded during a cold commissioning oxy run.

After discussion with the valve manufacturer (Flowserve), it was concluded that the seals on the valve seats will require replacement, as the old once are likely to be deformed making the movement of the valve harder and resulting in sharp movements of the flow control vale producing the fluctuations seen. After servicing the valves stable flow was achieved and the oxy-fired experiments could resume.